Numerical acceleration methods for high cycle fatigue crack propagation with a phase-field model

Jaccon Adrien

N° d'ordre NNT : 2023ISAL0084

THÈSE de DOCTORAT de L'INSA DE LYON
Membre de l'Université de Lyon

École Doctorale MEGA (ED 162)
Mécanique, Énergétique, Génie Civil, Acoustique

Spécialité de Doctorat
Mécanique

Soutenue publiquement le 07/11/2023 par

Adrien Jaccon
Ingénieur

Numerical acceleration methods for high cycle fatigue crack propagation with a phase-field model

Devant le jury composé de

NOM, Prénom	Grade/Qualité	Établissement	Rôle
LORENTZ, Éric	Ingénieur HDR	EDF	Rapporteur
LEGRAIN, Grégory	Professeur	Centrale Nantes	Rapporteur
DE LORENZIS, Laura	Professeur	ETH-Zürich	Examinatrice
BERINGHIER, Marianne	Maître de conférence	ISAE-ENSAM	Examinatrice
YVONNET, Julien	Professeur	Université Gustave Eiffel	Examinateur
GRAVOUIL, Anthony	Professeur	INSA Lyon	Directeur de thèse
MOLNÁR, Gergely	Chargé de recherche	CNRS-LaMCoS	Co-directeur de thèse
PRABEL, Benoit	Ingénieur HDR	CEA Paris Saclay	Encadrant

INSTITUT NATIONAL DES SCIENCES APPLIQUÉES LYON

Département de la Formation par la Recherche et des Études Doctorales (**FEDORA**)

Bâtiment INSA direction, 1er étage
37, av. J. Capelle
69621 Villeurbanne Cédex
fedora@insa-lyon.fr

Référence : TH1021_JACCON Adrien

L'INSA Lyon a mis en place une procédure de contrôle systématique via un outil de détection de similitudes (logiciel Compilatio). Après le dépôt du manuscrit de thèse, celui-ci est analysé par l'outil. Pour tout taux de similarité supérieur à 10%, le manuscrit est vérifié par l'équipe de FEDORA. Il s'agit notamment d'exclure les auto-citations, à condition qu'elles soient correctement référencées avec citation expresse dans le manuscrit.

Par ce document, il est attesté que ce manuscrit, dans la forme communiquée par la personne doctorante à l'INSA Lyon, satisfait aux exigences de l'Etablissement concernant le taux maximal de similitude admissible.

INSA LYON
Campus LyonTech La Doua
20, avenue Albert Einstein - 69621 Villeurbanne cedex - France
Tél. +33 [0]4 72 43 83 83 - Fax +33 [0]4 72 43 85 00
www.insa-lyon.fr

Département FEDORA – INSA Lyon - Ecoles Doctorales

SIGLE	ECOLE DOCTORALE	NOM ET COORDONNEES DU RESPONSABLE
CHIMIE	**CHIMIE DE LYON** **https://www.edchimie-lyon.fr** Sec. : Renée EL MELHEM Bât. Blaise PASCAL, 3e étage secretariat@edchimie-lyon.fr	**M. Stéphane DANIELE** C2P2-CPE LYON-UMR 5265 Bâtiment F308, BP 2077 43 Boulevard du 11 novembre 1918 69616 Villeurbanne **directeur@edchimie-lyon.fr**
E.E.A.	**ÉLECTRONIQUE, ÉLECTROTECHNIQUE, AUTOMATIQUE** **https://edeea.universite-lyon.fr** Sec. : Stéphanie CAUVIN Bâtiment Direction INSA Lyon Tél : 04.72.43.71.70 secretariat.edeea@insa-lyon.fr	**M. Philippe DELACHARTRE** INSA LYON Laboratoire CREATIS Bâtiment Blaise Pascal, 7 avenue Jean Capelle 69621 Villeurbanne CEDEX Tél : 04.72.43.88.63 **philippe.delachartre@insa-lyon.fr**
E2M2	**ÉVOLUTION, ÉCOSYSTÈME, MICROBIOLOGIE, MODÉLISATION** **http://e2m2.universite-lyon.fr** Sec. : Bénédicte LANZA Bât. Atrium, UCB Lyon 1 Tél : 04.72.44.83.62 secretariat.e2m2@univ-lyon1.fr	**Mme Sandrine CHARLES** Université Claude Bernard Lyon 1 UFR Biosciences Bâtiment Mendel 43, boulevard du 11 Novembre 1918 69622 Villeurbanne CEDEX **sandrine.charles@univ-lyon1.fr**
EDISS	**INTERDISCIPLINAIRE SCIENCES-SANTÉ** **http://ediss.universite-lyon.fr** Sec. : Bénédicte LANZA Bât. Atrium, UCB Lyon 1 Tél : 04.72.44.83.62 secretariat.ediss@univ-lyon1.fr	**Mme Sylvie RICARD-BLUM** Institut de Chimie et Biochimie Moléculaires et Supramoléculaires (ICBMS) - UMR 5246 CNRS - Université Lyon 1 Bâtiment Raulin - 2ème étage Nord 43 Boulevard du 11 novembre 1918 69622 Villeurbanne Cedex Tél : +33(0)4 72 44 82 32 **sylvie.ricard-blum@univ-lyon1.fr**
INFOMATHS	**INFORMATIQUE ET MATHÉMATIQUES** **http://edinfomaths.universite-lyon.fr** Sec. : Renée EL MELHEM Bât. Blaise PASCAL, 3e étage Tél : 04.72.43.80.46 infomaths@univ-lyon1.fr	**M. Hamamache KHEDDOUCI** Université Claude Bernard Lyon 1 Bât. Nautibus 43, Boulevard du 11 novembre 1918 69 622 Villeurbanne Cedex France Tél : 04.72.44.83.69 **hamamache.kheddouci@univ-lyon1.fr**
Matériaux	**MATÉRIAUX DE LYON** **http://ed34.universite-lyon.fr** Sec. : Yann DE ORDENANA Tél : 04.72.18.62.44 yann.de-ordenana@ec-lyon.fr	**M. Stéphane BENAYOUN** Ecole Centrale de Lyon Laboratoire LTDS 36 avenue Guy de Collongue 69134 Ecully CEDEX Tél : 04.72.18.64.37 **stephane.benayoun@ec-lyon.fr**
MEGA	**MÉCANIQUE, ÉNERGÉTIQUE, GÉNIE CIVIL, ACOUSTIQUE** **http://edmega.universite-lyon.fr** Sec. : Stéphanie CAUVIN Tél : 04.72.43.71.70 Bâtiment Direction INSA Lyon mega@insa-lyon.fr	**M. Jocelyn BONJOUR** INSA Lyon Laboratoire CETHIL Bâtiment Sadi-Carnot 9, rue de la Physique 69621 Villeurbanne CEDEX **jocelyn.bonjour@insa-lyon.fr**
ScSo	**ScSo*** **https://edsciencessociales.universite-lyon.fr** Sec. : Mélina FAVETON INSA : J.Y. TOUSSAINT Tél : 04.78.69.77.79 melina.faveton@univ-lyon2.fr	**M. Bruno MILLY** Université Lumière Lyon 2 86 Rue Pasteur 69365 Lyon CEDEX 07 **bruno.milly@univ-lyon2.fr**

*ScSo : Histoire, Géographie, Aménagement, Urbanisme, Archéologie, Science politique, Sociologie, Anthropologie

Acknowledgements

(*in french*)

Je souhaite en premier lieu remercier Benoit Prabel, Gergely Molnár et Anthony Gravouil, qui m'ont accompagné sur l'intégralité de mon parcours scientifique et professionnel depuis quatre ans, à travers deux projets et cette thèse. Vous avez toujours été disponibles, pédagogues, rigoureux. Travailler à vos côtés à été un plaisir et un privilège. Joffrey Bluthé, merci à toi pour ton encadrement depuis quelques années, et ton amitié. A vous quatre, vous avez constitué une équipe d'encadrement disponible à toute heure, qui m'a accompagné avec autant de vigueur sur les aspects scientifiques qu'humains.

Je suis reconnaissant envers Éric Lorentz et Grégory Legrain d'avoir accepté la lourde tâche de rapporteur, ainsi que Laura De Lorenzis, Julien Yvonnet et Marianne Beringhier pour leur participation au jury de thèse.

Merci également à Julien Réthoré pour son organisation de l'activité benchmark à Prague qui a permis une réflexion intéressante sur la comparaison numérique-expérimentale. Par ailleurs, merci pour le partage des résultats expérimentaux qui a permis d'alimenter ce travail.

Il y'a quatre ans également que j'ai été accueilli chaleureusement au sein du LISN, et j'ai pu y voir passer tout un tas de gens qui m'ont inspirés, aidés, accompagnés. Je doute qu'il soit possible de trouver un environnement de travail plus sain, convivial, et je vous remercie tous pour celà: Marouane, Clémence, Cédric, Franck, Clément, Thierry et Thierry, Cécile, Julien et Julien, Nadège, Séverine, Manon (Marion?), Myriam, Jorge, Greg, Deborah, Ivan, Clémentine, Lonis, Ismaila et pleins d'autres. Merci également à Pascal Bouda pour son soutien à plusieurs reprises, et sa grande pédagogie. Mention spéciale aux amis des laboratoires avoisinants que je n'ai malheureusement rencontrés que trop tard. Matthieu, Quentin, et le binôme infernal Morgane et Guillaume. Votre humour, vos idées et nos discussions me manqueront. J'espère pouvoir rester en contact avec vous. Côté Lyon, je

n'ai pas beaucoup été présent mais je remercie Yvan et Julie pour leur support constant pendant ces trois ans, et nos rencontres en conférence.

Ce projet n'aurait également pas pu aboutir sans le support de mes amis, et plus particulièrement le noyau dur, la grande team LAR. Merci à vous tous avec qui j'ai pu m'éloigner du plateau le week-end et chaque été. De façon peu exhaustive, merci Romain, Louis, Vincent, Laura, Yassine, Adèle, Estelle, Rémi, Aurélien, François, Pierre, Théo, Mathieu et bien sûr Maxime, graphiste de talent qui m'a assisté sur la conception de figure. J'aimerai aussi souligner le soutien de Pierre, Yassine, Louis et dernièrement Théo pour leur multiples acceuils chaleureux dans leur appartement à Lyon. Je n'oublie également pas l'autre noyau dur, que je vois malheureusement plus rarement. Originaires de tous les horizons, ils trouvent quand même le moyen d'être là pour moi. A vous les amis de Zürich Bastien, Emile, Louis-Pierre, Pierre et Gabriele. Enfin, à vous les amis romains, à Michele, Yassine et Antoine.

Merci enfin à ma famille, à qui je dois tout. D'abord mes parents qui m'ont fait naître, grandir, mûrir et qui m'ont donné les moyens de faire ce qui me passionne dans les meilleures conditions. Ma soeur qui m'a accompagné, formé, qui m'a inspiré et m'inspirera. Á vous trois, car sans vous je ne serai rien. Je souhaite également remercier le reste de mon cocon familial, toujours présents, mes meilleurs supporteurs à vous Pépé, Mémé, Magali, Jean-Claude, Maxime, Carla. Je n'oublie pas Papy et Mamy que je prends moins souvent le temps de voir, mais qui comptent tout autant dans mon coeur.
Enfin je souhaite évidemment remercier ma complice de tous les jours, Feriel, qui a partagé avec moi le quotidien de cette thèse, qui m'a supporté sans vaciller dans mes moments les plus faibles, insupportables, végétatifs, et avec qui les bons moments sont devenus meilleurs.

Merci à vous tous, car c'est à travers vous que j'ai tiré toute la substance de ce travail, la possibilité de l'entreprendre et finalement la capacité de le réaliser.

Abstract:
Predicting the initiation and propagation of fatigue cracks in structures is a major challenge for the industry, aiming to move beyond the typically used conservative approaches to reduce costs, optimize designs, and ensure structural integrity over longer durations. Numerous numerical methods can be employed in this context, notably the phase-field approach, which offers significant flexibility in dealing with complex crack scenarios and addressing crack initiation and growth in a unified manner. However, the computational cost associated with applying this model to real-world cases is currently too high, limiting its application to academic scenarios. The objective of this thesis is to propose various acceleration approaches to mitigate this prohibitive computational cost, while maintaining the required precision and robustness. This is intended to make real-life application of the phase-field model feasible.

To achieve this goal, a phase-field fatigue model was implemented within the finite element code Cast3M. An approach based on toughness degradation was chosen and validated across several sample usual of the phase-field literature. Additionally, a new energy decomposition method was introduced to enhance efficiency and robustness of this critical step. Subsequently, several modifications of the initial implementation were suggested to accelerate computations. Firstly, the cycle calculation was optimized through the introduction of a staged solution scheme tailored for fatigue scenarios. Then, multiple cycle jump schemes were proposed to minimize the number of calculated cycles. Lastly, an adaptive mesh refinement approach was adopted to optimize the number of degrees of freedom considered during the simulation. These tools effectively address the various reasons behind the computational cost issues in phase-field fatigue modelling, including the need for the resolution of a non-linear coupled problem, on a large number of cycles, using a very fine mesh.

Subsequently, this accelerated phase-field framework was applied to several standard academic cases to validate its implementation and demonstrate the potential timesaving benefits. Furthermore, two numerical-experimental comparison cases were presented using the accelerated approach. These trials showcased the abilities of the accelerated model while also highlighting additional challenges associated with applying the model to real-life cases.

Résumé :
La prédiction de l'initiation et de la propagation de fissure de fatigue dans les structures constitue un enjeu majeur de l'industrie, qui cherche à limiter les approches habituellement conservatives pour diminuer les coûts, optimiser les formes, et garantir l'intégrité des structures sur des durées plus longues. Un nombre important de méthodes numériques peuvent être exploités dans ce contexte, et notamment l'approche champ de phase, qui bénéficie d'une grande flexibilité pour traiter des cas de fissuration complexe, et considérer l'initiation et la propagation de fissure de façon unifiée. Cependant, le coût numérique associé à l'application de ce modèle sur des cas réels est aujourd'hui trop important et limite donc son application à des cas académiques. L'objectif de ce mémoire est de proposer plusieurs approches d'accélération pour diminuer ce coût de calcul prohibitif, tout en maintenant le niveau de précision et de robustesse, dans le but de rendre possible l'application sur des cas réels du modèle champ de phase.

Pour ce faire, un modèle champ de phase étendu en fatigue est implémenté dans le code éléments finis Cast3M. Une approche par dégradation de la ténacité est choisie et validée sur plusieurs cas usuels de la littérature champ de phase. Par ailleurs, une nouvelle méthode de décomposition de l'énergie est également mise en place, permettant d'en améliorer l'efficacité et la robustesse. Nous proposons ensuite plusieurs modifications de cette implémentation initiale qui permet d'accélérer les calculs. D'abord, le calcul de cycle est optimisé à travers l'introduction d'un schéma de résolution étagée adapté au cadre en fatigue. Ensuite, nous introduisons plusieurs schémas de saut de cycle permettant de minimiser le nombre de cycles calculés. Enfin, une approche de raffinement adaptatif de maillage est mise en place, afin de permettre d'optimiser le nombre de degrés de liberté pris en compte pendant la simulation. Ces outils répondent en fait aux différentes raisons pour lesquelles le coût de calcul du modèle champ de phase en fatigue est prohibitif: la résolution d'un problème non-linéaire, sur un nombre très important de cycles, avec un maillage extrêmement fin dans la zone endommagée.

Ce cadre champ de phase accéléré est ensuite exploité sur plusieurs cas académiques usuels pour valider son implémentation, et montrer les gains en temps de calcul possibles. Puis, deux cas de comparaisons numériques-expérimentales utilisant l'approche accélérée sont proposés. Ces essais mettent en évidence les capacités du modèle accéléré tout en soulignant d'autres difficultés liées à l'application du modèle sur des cas réels.

Table of contents

List of figures

List of tables

General introduction

The precise prediction of crack initiation and growth in structures is of great interest for several industries (nuclear, aeronautic, railway), that seek to guarantee high safety standards, while optimizing their structure for cost and efficiency. In order to provide more accurate and robust predictions of the fracture cases encountered in the industry, the scientific community has developed several theoretical tools to model what experimental observations have shown about the physical mechanisms at play in the degradation of structures. The widespread development and use of these tools to study fracture is quite recent, as the first theoretical framework for crack propagation was born just after the first world war [93]. Five decades later came the rise of numerical simulations in structural engineering, with the development of the finite element method and its successful application to industrial cases. Understanding and predicting the fracture phenomenon is now commonly based on three intertwining tools: experimentation, theory and numerical simulation.

It is in this context that this work was mandated by the Laboratory for Integrity of Structure and Normalisation (LISN), at the Alternative Energies and Atomic Energy Commission (CEA). Using its expertise and high-end devices for fracture testing, the laboratory is centered on the analysis and sizing of components to guarantee the integrity of structures in normal and accidental conditions. In order to support these experimental tools, several numerical methods are also developed and implemented in the research finite element software of the CEA: Cast3M. Moreover, the design standards for pressurized water reactor are developed in this laboratory. These objectives lead to the need for the characterization of material integrity at the scale of the sample, all the way to the scale of the structure, in complex loading situations, and sometimes very challenging temperature and pressure environments.

To be more specific, this work is centered around the numerical modeling of high cycle fatigue fracture, *i.e.,* of the degradation caused by a repeated load characterized by a low

amplitude (leading to stresses below the material's yield stress) but a high number of cycles before fracture (typically about 10 000 - 10 000 000 cycles). This type of degradation of materials is found everywhere in the industry since the generalized introduction of rotating machines in the XIXth century. In this regard, a considerable amount of structural components today are subjected to fluctuating loadings, which led to the observation that a large majority of failure cases in the industry are due to fatigue [61]. Consequently, very high security margins are enforced on those structural components to avoid such incidents. However, in recent years the development of numerical modelling has enabled finer predictions of fatigue crack propagation, notably with the finite element method, which has been used in the present work as well. These methods allow engineers to optimize the design of new structural components, or to extend the service life of existing ones. Therefore, a large community of scientists work on the improvement of these methods, by upgrading their robustness, flexibility and accuracy to recover fracture cases in complex geometries, or loading conditions, while modelling the non linear behaviour of some materials. Moreover, a key aspect of the research led in this field is the search for gains in computing time, which still cripples the real-life application of most fine modelling frameworks.

One recurring issue of the numerical modelling of fracture is that the crack is a discontinuity in the considered domain. Most approaches used in the industry are based on a discrete representation of the crack, where this discontinuity is treated as a free boundary of the finite element mesh, which thus has to be explicitly modelled, and remeshed when the crack advances [208]. In a FEM context, this means that the mesh must be rebuilt at every propagation step, with a specific placement of nodes in the path of the crack. Furthermore, the fields defined on the initial mesh have to be transferred. These treatments can become very cumbersome in the case of complex crack geometries, and make the application of such approaches on real-life cases untractable. Some recent works have put forward ways to avoid these remeshing issues such as XFEM, which has successfully shown its ability to predict efficiently several fracture cases [83, 84, 188]. On the other hand, damage mechanics approaches brought another way to avoid remeshing issues [62, 120, 143] by describing the crack propagation as a material degradation. These approaches are however often limited to small crack advances.

Another recent approach is attracting a considerable amount of attention from the scientific community: the damage phase-field model. This approach originates from the variational approach for fracture by Francfort & Marigo [76], which recasted Griffith's criterion used to evaluate crack propagation, in a minimization problem. Then Bourdin et al. [38], have put forward the damage phase-field formulation as a regularization of this variational

problem to enable its numerical treatment. Therefore, a fracture mechanics approach resulted in a continuous damage model, bridging the gap between those communities. The resulting smeared representation of the crack enabled to recover crack initiation, growth, arrest, as well as several other complex fracture phenomena, such as branching, kinking, coalescence, without the need for additional criteria [38]. Moreover it benefits from a rigorously set thermodynamics framework [165]. Finally, since a smeared representation of the crack is used, it avoids remeshing issues altogether. This kind of model can hence be used to predict very complicated fracture scenarios with a relatively straightforward implementation [44, 172]. Considering these numerous advantages, the damage phase-field model could offer very interesting possibilities to model real life cases.

Nevertheless, the damage phase-field model is not yet used in the industry, because of several factors. First, the method is computationally very expensive, due to the need for a very fine spatial discretization in the zone where the crack propagates, in order to capture the steep gradient of the diffuse field representative of the crack. This requirement has a tendency to bound damage phase-field application to academic examples. The damage phase-field literature has already tackled this issue with several phase-field adaptive mesh refinement approaches, that have shown great abilities to accelerate computing time, especially when the crack path is not known beforehand [103].

Furthermore, unlike the standard finite element method for fracture, the damage phase-field model is characterized by two unknowns, which yields a coupled probel and can lead to convergence issues. These issues are less critical in fatigue, but a relevant solving strategy must still be chosen, such as a usual staggered strategy [44], or the use of BFGS on the staggered framework [129].

Moreover, most fatigue phase-field models require the need for an explicit computation of every single cycle [94], which means that the framework is untractable for very long fatigue lives, where the number of cycles can reach more than 10^7. The combination of those factors mean that real-life applications of the model are too expensive without the use of acceleration techniques.

Another barrier of the use of the damage phase-field model is the calibration of the numerical parameters to compare numerical and experimental results. A reflexion on the interpretation of the numerical parameter of the damage phase-field model has already been started [6, 171, 241], but would require further interrogations, especially in a fatigue context.

It is in this context that this work takes its roots: making the application of the fatigue phase-field model possible for industrial use, by accelerating computations, without affecting

the accuracy or the robustness of the method. With a relevant accelerated framework, the goal was then to conduct numerical-experimental comparisons in order to assess the predictive abilities and the robustness of the framework in front of experimental results. In order to accelerate the framework in a fatigue context, we put forward the idea of using adaptive mesh refinement (AMR), hence optimizing the number of degrees of freedom at a given propagation step. Moreover, we propose using cycle jump schemes, to avoid the explicit computation of every cycle, hence optimizing the number of cycle at which the problem must be solved. Both adaptive mesh refinement techniques (in a brittle context) [103, 244], and cycle jumps [130, 151], have been applied previously to accelerate damage phase-field computation, but they had never been used together before in a fatigue context. This constitutes the main original contribution of the present work. In the end, the application of the proposed accelerated framework for real-life samples will act as a proof of concept that this method enables a flexible, efficient, predictive and robust framework.

The structure of this work flows naturally from these objectives. First, a brief literature overview of fatigue fracture was provided in Chapter 1 with some of the theoretical and resulting numerical tools that were set for its characterization. Then, the choice of the damage phase-field model for high cycle fatigue was detailed in Chapter 2, by reviewing the different model's components and their different versions in the literature, thus offering an overview of the current issues in damage phase-field modelling. After detailing these components, a new spectral decomposition approach was proposed to add unilateral effects with the damage phase-field model. Finally, the proposed model was applied on several numerical benchmarks, in order to validate the model and showcase its ability to recover a fatigue phenomenology.

Then, the acceleration methods used to make the application of damage phase-field tractable for a larger range of application, were introduced in Chapter 3. First, the computation of a cycle was investigated by considering different approaches to solve the phase-field coupled problem. Then the cycle jump framework was introduced, before detailing the different steps of the AMR process. Then, a unified accelerated framework was proposed, and applied on several numerical benchmarks, in order to illustrate the possible computing gains, at a given level of accuracy.

Finally, this unified accelerating phase-field fatigue framework was used to create numerical-experimental comparison and showcase the ability of the model to be used for such applications. Several issues related to parameter identification and modelling of experimental setups have been treated in order to highlight the limitations of the application of the phase-field model on real-life cases.

1 Preliminaries

This chapter provides a concise literature review of the fatigue failure phenomenon, along with an exploration of the theoretical and numerical methods utilized for modeling and prediction.

Contents

In this first chapter, we started with the introduction of the fatigue degradation phenomenon, detailing the different stages, and different driving mechanisms identified at each stage. Some of the empirical and theoretical tools that were set up to study fatigue failure as a whole were then briefly introduced. Considering the design approach of the nuclear industry context, the focus was then shifted to the last stages of fatigue failure: fatigue crack propagation. To do so, the Linear Elastic Fracture Mechanics framework was introduced, along with its most known fatigue application, the Paris Erdogan Law. Then, we presented a literature review of the different numerical tools that were proposed to model fatigue crack propagation in a finite element framework, differentiating between two types of crack representations, discrete and diffuse models. In the end, special attention was given to the phase-field model and its extension to fatigue crack propagation.

1.1 Review of fatigue failure

1.1.1 Phenomenology of fatigue

Fatigue is the main mode of failure in the industry, as it is responsible for as much as 80% of all recorded industry failure cases [61]. It is however a very complicated failure mode as it results from a cyclic repeated load, that is usually very low compared to the monotonous load critical threshold. Furthermore, the rate at which this degradation occurs is very insidious as it starts progressively, with no obvious sign, before suddenly leading to complete failure. Considering how hard this phenomenon is to detect before it is too late, it is not surprising that it was discovered recently in the history of engineering and material sciences: in the wake of the industrial revolution, when automated machinery and repeated solicitations applications were developed and spread around the globe. The first concrete observations of this phenomenon were led in the railway industry and notably August Wöhler in Germany in the 1860's. After numerous large-scale incidents on the European railway system that the scientific community struggled to understand, this German engineer has put forward the first experimental device and procedure to quantify fatigue. By applying a cyclic repeated load on a train axle geometry, he showed that the amplitude of loading for fracture with these loading conditions was much lower than for a static monotonous load [254]. And so was born a new category of failure, so called fatigue failure.

The first experimental observations of fatigue have since led to an in depth characterization of the phenomenon [75, 213, 239]. Fatigue is usually separated in three phases, where the physical mechanisms driving degradation are different and material dependent.

The first phase is nucleation. The material is degraded at the scale of the micro-structure: the cyclic loading induces the irreversible movement of dislocations along favorable shearing planes [239]. This creates so-called persistent slip bands *i.e.,* localization of plastic deformations in these shear planes, favouring the creation of micro-cracks. Nevertheless, at this point, the macroscopic response of the material is unchanged.

In the second phase, these micro-cracks coalesce to form macro-cracks, reaching a size where the crack is detectable. It is hence usually called the coalescence phase, or stage I of crack propagation by Forsyth [75]. This phase is still highly dominated by micro-structural effects.

Then, the formed macro-cracks start aligning themselves to follow a given direction, and propagate in a stable manner. This level of degradation starts to have a measurable influence on the macro-structure.
The crack may propagate until it reaches a critical size at which point unstable crack propagation possibly leads to complete failure [75]. Those stages are illustrated in Fig. 1.1. Initiation of the fatigue crack occurs in the first two stages while stable crack propagation and the possible complete failure occur in the last stage.

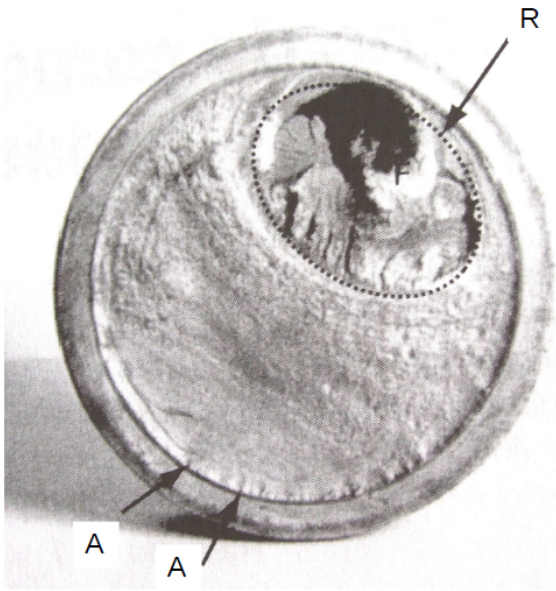

Figure 1.1: Fracture surface on a wind turbine blade in Lemaignan [141]: Initiation zone is marked by A, the striation zone of stable crack propagation is comprised between A and R. Finally R corresponds to ductile unstable fracture.

A typical fatigue loading is defined by the cyclic variation of external quantities $\Delta\hat{u}$ (*e.g.,* prescribed displacement, volume or surfacic forces, or temperature). This variation is

defined by its maximum and minimum values, leading to the load ratio: $R = \hat{u}_{\min}/\hat{u}_{max}$.

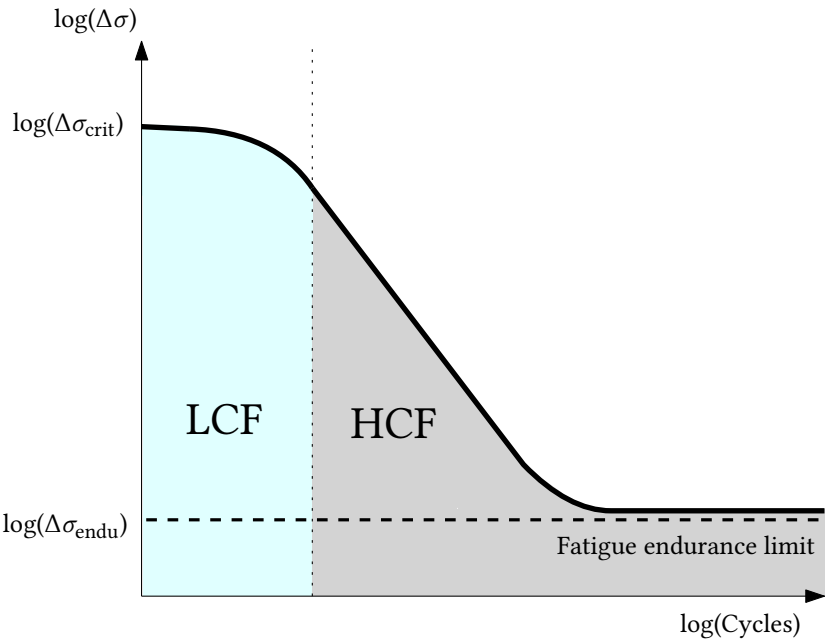

Figure 1.2: Typical S-N curve for metallic materials.

In Wöhler's initial work [254], the S-N curve was developed: it was illustrated in Fig. 1.2. Considering a cyclic uniaxial loading of amplitude $\Delta\sigma$ with an average stress of 0 ($R = -1$), the sample will break for a given number of cycles N, which is compiled in the S-N curve. The curve starts at $N = 1$ equivalent to the static critical loading $\Delta\sigma_{\text{crit}}$, corresponding to fracture in one cycle, and lower levels of stress are then applied to figure out how many cycles are required for nucleation or fracture. Note that for some materials, these curves seem to end asymptotically, as represented in Fig. 1.2 Consequently, it seems that we can define an endurance limit of materials: a load $\Delta\sigma_{\text{endu}}$ below which no fatigue degradation can occur, for an infinite number of cycles. However, S-N curves are usually limited to 10^7 cycles because of time and resource limitations linked to fatigue experiments. In this regard, several authors argue for the need to improve fatigue endurance characterization, as the behaviour at $N > 10^7$ can sometimes lead to sudden failure for $\Delta\sigma < \Delta\sigma_{\text{endu}}$ [19, 243].

Furthermore, the literature usually differentiates between two types of fatigue: low cycle fatigue (LCF), or olygocyclic fatigue, and high cycle fatigue (HCF), or polycyclic fatigue. Low cycle fatigue occurs for high loadings and relatively few cycles (under 10^5 cycles), whereas high-cycle fatigue takes place for low loadings and a high number of cycles (as far as 10^7 cycles). In the case of the former, plastic deformation usually plays a key role. Conversely, only marginal amounts of plastic dissipation appear for polycyclic fatigue.

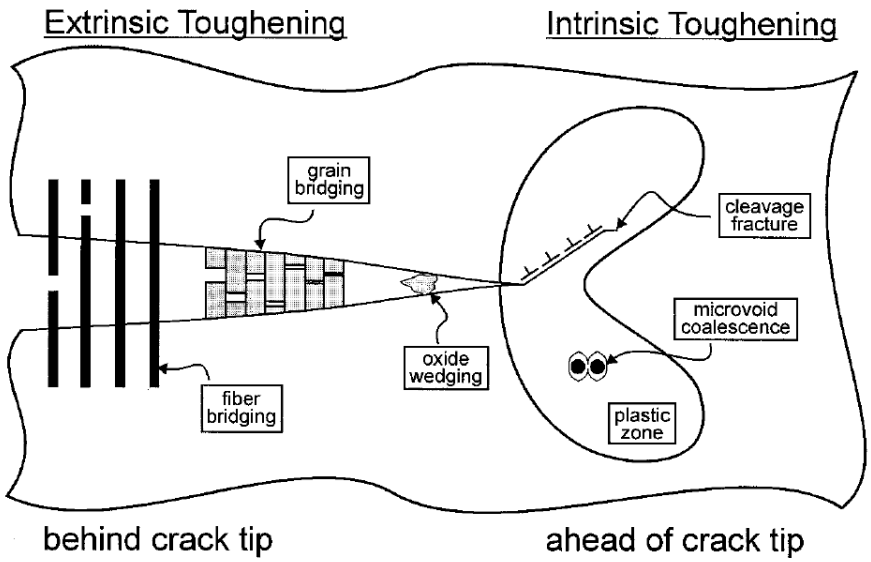

Figure 1.3: Visualization of some of the mechanisms driving, or preventing fatigue crack propagation from Ritchie [213].

This relative contribution of plastic effects is the fundamental difference between LCF and HCF. They are therefore usually studied separately because of the strong influence of plastic effects on the fatigue response. LCF was considered out of the scope of this work. Consequently, we direct the interested reader to Ref. [156], for a description of the usually observed phenomenologies in LCF.

Nevertheless, note that if at the macroscopic scale, plastic effects are considered negligible in HCF, degradation is still driven by irreversible dissipative mechanisms at the micro-scale. In fact, several effects are responsible for fatigue degradation as highlighted by Ritchie [213], and his illustration in Fig. 1.3, where fatigue fracture was described as the competition between multiple mechanisms. Some drive crack propagation ahead of the crack tip, *e.g.,* with micro-structural damage such as the formation of micro-voids and their coalescence or cleavage fracture, while other prevent crack propagation. Those shielding mechanisms can for example result from the formation of an inelastic zone in the wake of the crack or the structural contact, or oxidation of the crack lips [213]. The multi-physics and multi-scale nature of the phenomenon makes it particularly hard to model each of the components and their respective coupling explicitly. Consequently, in this work we focus on the macroscopic modelling of fatigue based on continuum mechanics. In this context, fatigue damage is seen as a dissipative phenomenon that encompasses all of these driving mechanisms.

1.1.2 Sizing for fatigue in the industry

There exist different approaches to size components for fatigue loadings in the industry. We can divide these approaches in two distinct categories: total life approaches, and defect tolerant approaches.

Total life approaches are all direct successors to Wöhler's sizing method, which is to search for a relationship between a critical stress criterion and the number of applied cycles. Since a single critical value acts as a threshold, we see that these approaches do not try to discriminate between the fatigue degradation phases: nucleation/coalescence and propagation. The critical values can alternatively be chosen as the number of cycles required to nucleate, start propagating or lead to complete failure [189]. We give a brief review of some of these total life approaches, but redirect the interested reader to Papadopoulos [189] and Weber [249].

The global idea is to construct an envelope, relating a critical load to a critical number of cycles. In the seminal work of Wöhler [254], this envelope is created in simple loading conditions: uniaxial load with a nil average stress. However, this created envelope is only valid for applications using these very specific loading conditions. Consequently, extensions have been proposed, to take into account the influence of the average stress [89, 232], or link the total life to plastic deformations [55], and the extension of this envelope in all directions of the stress space, hence considering multi-axial fatigue criteria [189, 249]. Developing these threshold envelopes can be performed empirically like Wöhler and a large part of the following literature [59, 91, 186], but also using specific theoretical frameworks. For instance we can mention criteria based on a model of the maximum shear stress, considering that the nucleation part of fatigue degradation takes place along favourable shear planes [58]. Additionally, a deeper connection to the physical mechanisms of fatigue degradation was set by Dang Van et al. [248], by considering a multi-scale model that takes into account the plastic effects at the micro-scale, while keeping an elastic framework at the macro-scale.

The second approach used in the industry to size components for fatigue loadings is the defect tolerant approach. where a defect is initially postulated in the studied component, and the objective is to quantify whether or not the fatigue loading induces a propagation of this defect, at which rate, in which direction and so on. It is therefore linked to the study of crack propagation, and was hence born with the advances in Linear Elastic Fracture Mechanics, driven by Griffith [93], Irwin [113], and their link to fatigue by Paris and Erdogan [190]. The industrial context of this work relies on the damage tolerant approach, as it is the norm in the nuclear industry, and the objective is the prediction of crack path in

complex geometries or complex loadings. Consequently, for the remainder of this section we focus on the second group of sizing approaches, using fracture mechanics theoretical tools.

1.2 Fatigue crack propagation

In order to study fatigue crack propagation, the fracture mechanics community relies on theoretical tools such as the critical energy release rate, and the stress intensity factors, which were therefore introduced in this section.

1.2.1 Linear elastic fracture mechanics

1.2.1.1 Energy-based approach

The first theoretical framework set to study crack propagation was put forward in 1921 by Griffith. In his seminal work [93], the author sets the problem as follows: given an initial crack in a structure, what conditions must be met, in order for the crack to propagate? In this context, an energetical criterion was set, following the idea that crack propagation happens when it becomes more energetically favourable than keeping the structure together. When a crack propagates by a given unit area dA, it "releases" potential energy $d\Pi$ at the crack tip. For Griffith, the crack propagates if this released energy is sufficient to create two new distinct surfaces: the crack lips. Therefore, the author linked the energy release at the crack tip (over an advance of crack surface), to a material dependent quantity, the surface energy usually named γ.

In this context, the author introduces the energy release rate G, defined as the energy released for a given advance of the crack:

$$G = -\frac{d\Pi}{dA} \tag{1.1}$$

Griffith's criterion can then be formulated as:

- $G < 2\gamma$ No crack propagation
- $G = 2\gamma$ Stable crack propagation
- $G > 2\gamma$ Unstable crack propagation

Note that 2γ is a material parameter, named the critical energy release rate, or tenacity of the material: G_c, a parameter that quantifies the resilience of a material to crack propagation.

1.2.1.2 Local fields approach

Following a local analysis of the mechanical fields around a crack tip (in linear elasticity) by Westergaard [250], Irwin [113, 114] put forward an analytical expression for the first terms of a Taylor expansion of asymptotic stress and strain fields at the crack tip. Since these asymptotic stress fields are singular (approaching infinity at the crack tip), the author introduced the so-called Stress Intensity Factors (SIF), that enable a quantification of the singularity. Furthermore, the author decomposed these expressions through the mode of fracture that describes the movement of the crack lips with respect to each other. Three modes are defined, based on kinematic arguments, they are illustrated in Fig. 1.4. Subsequently, we can write the expression of these asymptotic stress fields as a function of polar coordinates centered at the crack tip (r,Θ). Using the generalized notation of Ref.[202], we can write, for a specific stress component σ^{ij}:

$$\sigma^{ij}(r,\theta) \underset{r\to 0}{\simeq} \sum_m \frac{K_m}{\sqrt{2\pi r}} \cdot f_m^{ij}(\theta), \text{ with } m = I, II, III. \tag{1.2}$$

f_m^{ij} being an angular function of Θ and the considered mode. Furthermore, Irwin puts forward a link between Griffith's energy based approach, and this asymptotic field analysis approach by proving that the SIFs are related to G by the so-called, Irwin formula [114], which was since extended for mixed mode propagation [70, 86].

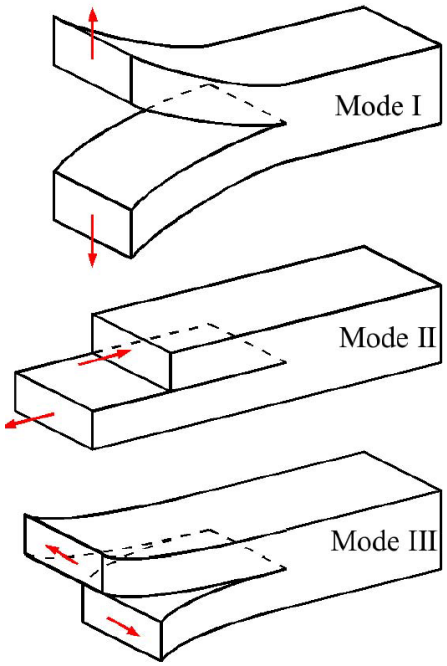

Figure 1.4: The three modes of fracture (figure from [202]).

Note that these singular fields are not representative of the reality of the stress state at the crack tip: instead, a plastic zone arises in the vicinity of the crack tip [42]. LEFM is valid when this plastic zone can be considered as "confined", in a very small radius around the tip, and hence, not affecting the macroscopic response [42]. In this case, the asymptotic fields are still dominant on a larger radius around the tip, the K-dominance zone. Additional theoretical tools have been developed to model the fields when the plastic zone cannot be neglected, such as the HRR fields [110, 212].

1.2.2 The Paris Erdogan Law

Following these developments in LEFM, Paris and Erdogan [190] very rapidly postulated that in a fatigue framework, the crack growth rate might be driven by the SIF, representative of the stress state at the crack tip. The authors plotted the crack growth rate (with respect to the number of cycles) $\frac{da}{dN}$, as a function of the SIF range ΔK during those elapsed cycles. This results in a curve with three distinctive domains shown in Fig. 1.5.

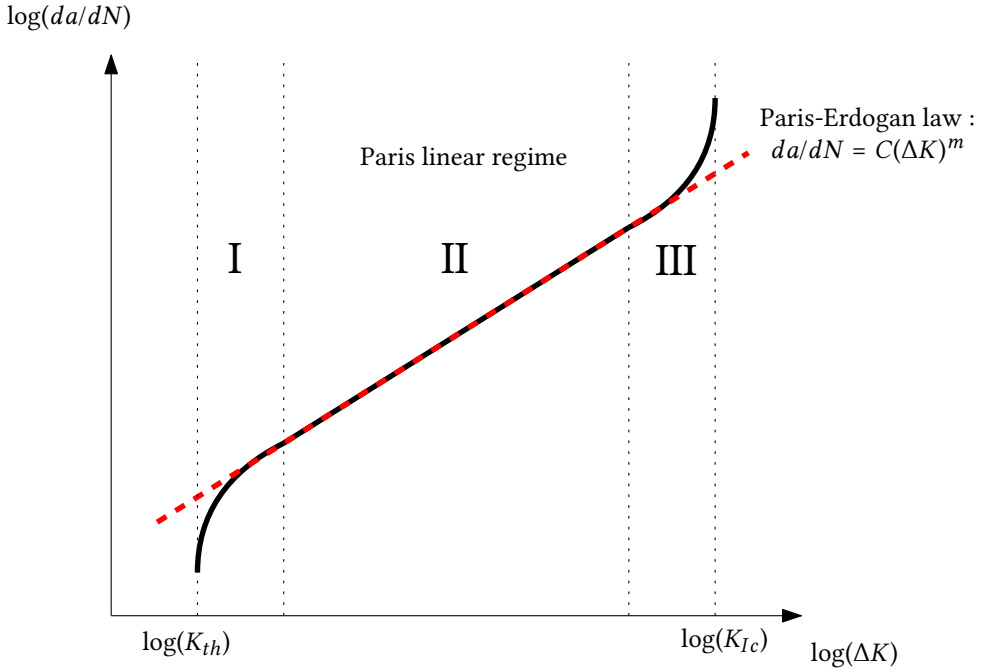

Figure 1.5: A typical plot of crack growth rate as a function of the stress intensity range. The Paris-Erdogan equation displays a decent fit with the central linear section of regime II.

On a logarithmic scale, we distinguish three domains: (I) is nucleation, where cracks tend to follow a rapid crack propagation rate above a specific ΔK_{th}, below which no crack propagation happens. (II) is the stable crack propagation regime. As it is linear in the logarithmic domain, it can be used to describe simple cases of crack propagation very reliably.

A so-called Paris-Erdogan law can be set as a power law model, driven by two coefficients, usually denoted m and C used to fit the behaviour to some given experimental results:

$$\frac{da}{dN} = C\Delta K^m. \tag{1.3}$$

(III) is the unstable failure regime where very rapid crack propagation is observed until K_{Ic}, the critical toughness of the material is reached, leading to complete failure.

Note that the range of SIF ΔK is simply defined as:

$$\Delta K = K_{max} - K_{min}, \tag{1.4}$$

with K_{max} being the maximal value of the SIF during a cycle, and K_{min} the minimal value during a cycle.

This approach has been extended to take further effects into account such as the influence of the average stress [74, 85, 252] or the effect of a non-negligible plasticity radius around the crack tip, which induce closure effect, discovered by Elber [67], or retardation effects [252]. All sorts of similarly ΔK driven crack growth rate curves have since been proposed, with very complex formulations and a high number of coefficients, such as the NASGRO curve, which is designed to recover the three steps of crack propagation [163]. Note also the troublesome case of small cracks [193], whose growth rates seem to be severely underestimated with usual Paris' Law approaches.

1.3 Numerical approaches for fatigue crack propagation

Following the description of theoretical tools for fatigue crack propagation analysis, we present a brief overview of the numerical approaches that were set up in the literature to model fatigue crack propagation in a finite element method (FEM) context.

For crack growth modeling in the FEM context, two modeling issues need to be considered: the representation of the crack, and the evolution law of crack growth. We chose to split this section in two, first considering models where the crack is a discrete object usually represented through the finite element mesh, and then approaches where the crack is a diffuse object, usually represented by a nodal field or internal variable. For each of these crack representations, we provided an overview of the different evolution laws that can be set up to drive crack growth. Finally, we reviewed existing phase-field fatigue models, which is the diffuse model chosen in this work.

1.3.1 Discrete crack models

A brief overview of the pros and cons of discrete crack models in a fatigue context is given here, but we direct the interested reader to a more complete analysis of the topic in Refs. [135, 208].

Discrete models usually rely on the explicit representation of the crack as a part of the finite element mesh. The load is then applied on the resulting cracked geometry to compute a specific criterion that estimates whether the crack propagates or not. For instance we can cite these references Ref. [57, 83, 84, 205], where J-integral based methods [63, 211] are used to compute ΔK values which are then injected as input of a Paris Law to deduce the crack growth rate. Alternatively, fatigue specific criteria can be used, developed by modeling fatigue damage accumulation at the crack tip, based on physical arguments [118, 134]. Nevertheless, in both cases, each propagation step can be summarized as [208]:

1. Computation of ΔK or fatigue threshold.
2. Evaluation of direction of the crack.
3. Remeshing for crack propagation.

Consequently multiple numerical frameworks must be built, namely the numerical computation of ΔK [63, 90, 227], the numerical computation of directional criterion [37, 42, 70, 228], and the numerical framework to enable remeshing and the transfer of fields [37, 45, 52, 219]. Each of these steps might introduce numerical errors, add layers of complexity to the implementation, and limit the domain of applicability of the model: indeed, ad-hoc

criteria are added to the formulation, which are usually deduced in very simple settings, rendering application of the approach in complex geometries or with multiple interacting cracks not tractable. However, these methods benefit from a large literature, years of applications in the industry, and the fact that accurate results can be recovered with a relatively coarse mesh [96, 208]. For instance, we can cite the nice improvements of FEM with remeshing applied to 3D crack propagation by Chiaruttini et al. [53].

In order to avoid the mentioned remeshing issues, a popular approach was put forward by Belytschko & Black [22], and supplemented by Moës et al. [170], the eXtended Finite Element Method (XFEM). The initial idea put forward by Belytschko & Black, was to use properties of partition of unity [231], to enrich the shape function basis with near crack-tip functions (using Irwin asymptotic fields [113], or HRR fields for plastic effects [69]). This way, a finer description of the field around the crack tip can be recovered for a much coarser mesh. Then, Moës et al. [170] added a discontinuous generalized Heaviside function in the basis of elements on the crack path, which enables discontinuity of the fields inside elements, hence uncorrelating the mesh and the crack. All these advantages come at the cost of the need for the selection of enriched elements (not all elements' basis functions are enriched to reduce the computing cost), and the consideration of this enriched basis in all steps of the propagation process (computation of ΔK, transfer of fields [83]). Nevertheless, interesting results have been recovered with this approach for fatigue crack growth analysis, first by Moës et al. [170], for 2D mixed mode cases, and for 3D cases [92, 168]. Then multiple comparisons with experimental results have shown the ability of the framework [25, 68, 238, 263]. Recently, an XFEM framework able to recover crack coalescence was put forward by Pali et al. [188]. In Fig. 1.6, we have illustrated the finite element meshes that could be put forward to model a crack, using FEM and XFEM.

Finally, another widely used approach for numerical prediction of fatigue crack growth is the Cohesive Zone Model (CZM), based on the work of Dugdale [66]. This framework introduces a force between the nodes at the crack tip and states an evolution law between crack opening displacement and stress at the crack tip. Fracture is hence limited to a local region ahead of the crack tip, and a progressive decohesion of crack tip nodes is induced by the external loading. Several fatigue extensions of this framework have been put forward, with different approaches to induce decohesion from a cyclic loading: considering a linear cyclic law [16], a plasticity driven degradation [180], or adding a damage parameter that influences this cohezive force as fatigue degradation occurs [99, 155], or other additional parameters to fit to Paris-like propagation laws [54]. Note that these approaches are usually less empirically driven than the former FEM-XFEM, as they consider different

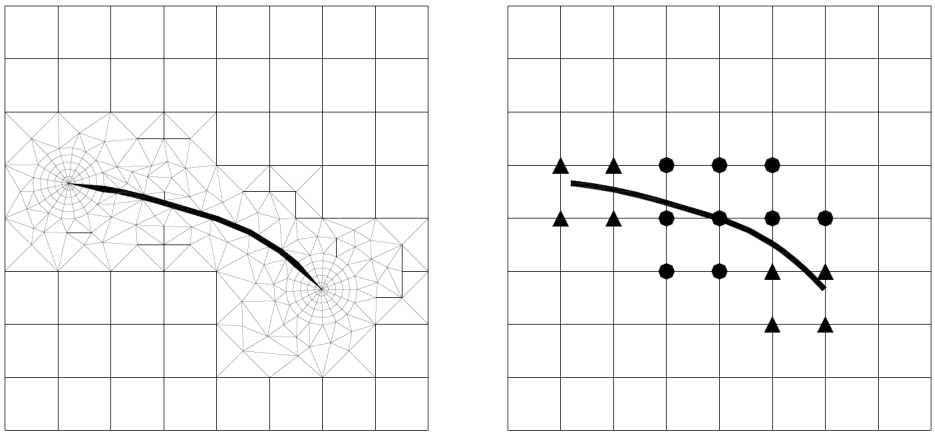

Figure 1.6: Comparison of FEM and XFEM mesh from [208].

driving mechanisms at the crack tip to elaborate the cohesive force and its degradation rather than explicitly using a Paris Law to drive crack propagation. However, it poses the same remeshing issues as with standard FEM approaches, which would also make its application untractable on complex 3D, interacting cracks, propagation cases.

1.3.2 Diffuse damage models

Another approach used to model a crack in a fatigue context comes from the damage mechanics community, where a scalar value is introduced to represent damage (a scalar or a tensor of higher dimension [62]). This damage influences the mechanical response, and propagates to neighboring elements following specific evolution laws. It is usually chosen between 0 and 1, considering that 1 yields a complete loss of rigidity. Contrary to discrete models, the crack is hence represented by a set of completely damaged elements. The first approach relying on a damage internal variable in a continuum mechanics context was proposed by Kachanov et al. [121], and since extended for several classes of materials, and fatigue *e.g.,* for ductile materials in Refs. [47, 144]. These approaches are very flexible to model complex crack patterns such as crack branching, coalescence and avoids issues of remeshing which leads to easy treatment of complex cases and 3D cracks. Furthermore they enable the consideration of initiation and propagation in a unified manner [142]. This means that both total life analysis and defect tolerant approaches can be used at once. However it induces a difficulty to identify the crack, and so can lead to issues, *e.g.,* for the consideration of friction of the crack lips or unilateral effects [160]. Most importantly, this kind of approach suffers from a dependency to the size of the mesh, as no spatial convergence can be reached [20, 36, 200].

To avoid this mesh dependency issue, several approaches have been proposed such as introducing gradient terms in the constitutive equations [35, 73, 194] or more directly non-local terms [119, 201]. Localization of strain and damage fields are thus regularized with the use of spatial derivatives in the case of the former, and the averaging of local driving forces in a defined neighborhood, in the case of the latter: In both cases, these corrections are based on the consideration of a local neighborhood and the definition of internal lengths. Further information on these models can be found in Refs.[62, 143, 196]. More recently, Moës et al. [169] have presented the Thick Level Set (TLS) model, which introduces a definition of the damaged zone with levels sets which uses a non-local treatment of the damage field. This enabled an easy to implement model with the robustness and flexibility of non-local damage models [26]. Delay effect damage models have also shown their ability to avoid localization issues, but are usually applied in a dynamic context [8, 237].

Finally, another diffuse approach is of increasing interest for the scientific community in the context of fracture: damage phase-field models. The crack is also represented by a scalar variable, yielding a diffuse representation of the crack. The damage evolution law can then be obtained through different means: namely as a regularization of the variational formulation of the Griffith criterion by the fracture mechanics community [38, 165], or deduced from Ginzburg-Landau evolution law by the physics community [132]. Alternatively it can be seen as a specific gradient enhanced model by the damage mechanics community [34, 176, 259]. Several applications of phase-field model to simulate fracture case have been developed in recent years. Since its initial use for brittle crack propagation [38, 165, 172], it has been extended to add ductile effects [5, 9, 31, 65, 164, 173], dynamic effects [39, 123, 173], anisotropic effects [146, 184, 242], or multiple damaging sources [28, 184] and fatigue effects [7, 30, 44, 148].

This approach yields a thermodynamically robust framework [165], with no mesh dependency issues, or the need for remeshing procedures. Furthermore it has shown its ability to recover accurately well-known fracture cases [11, 29, 241] as well as more complex crack patterns [172, 217] without the need to set additional criteria. However it suffers from its considerable computing cost that is usually linked to the fine discretization required for spatial convergence, and the numerical difficulties associated with the resolution of the phase-field and mechanical coupled problem [60].

The damage phase-field model was chosen in this work and most particularly its fatigue extension to consider high cycle fatigue crack propagation.

1.3.3 Phase-field for fatigue

In this section, we briefly review different approaches used to extend the phase-field formulation to induce fatigue effects. Note however that a more complete description of the damage phase-field model and the fatigue effects components will be provided in Section 2.1. In Refs. [38, 77], the damage phase-field model is viewed as the regularization of the variational approach for fracture. In this regard, the fracture problem is recast into an energy minimization problem. The modeling process then reduces to expressing a relevant free energy potential of the fracturing structure. From this definition, the evolution laws are derived by applying standard variational calculus arguments to the set energy: the unknown quantities are the ones that minimize the energy of the structure. In this context, the damage phase-field free energy potential can be written as:

$$\Pi_{int}(\boldsymbol{u}, d) = E(\boldsymbol{u}, d) + W(d). \tag{1.5}$$

where $\boldsymbol{u}$ is the displacement field, d the phase-field variable (which can be seen as a damage variable). This expression is representative of the regularization of the variational formulation of Griffith's criterion. It models crack propagation as the competition between elastic energy and a surface energy dependent upon the phase-field parameter.

This formulation can reproduce brittle unstable crack propagation, but does not see the influence of a cyclic loading of sub-critical amplitude. In order to add these fatigue effects, multiple proposals have been made in the literature, which can be summarized as the two following possible modifications of the free energy potential:

$$\Pi_{int}(\boldsymbol{u}, d) = E(\boldsymbol{u}, d) + W(d) + \int_0^t \dot{\mathcal{H}}(d, \bar{\alpha}(\tau))\, \mathrm{d}\tau \ (e.g., [13, 149]). \tag{1.6}$$

$$\Pi_{int}(\boldsymbol{u}, d) = E(\boldsymbol{u}, d) + \int_0^t f(\bar{\alpha}(\tau)) \cdot \dot{W}(d)\, \mathrm{d}\tau \ (e.g., [7, 44]). \tag{1.7}$$

Here we introduced a history dependent internal variable $\bar{\alpha}(\tau)$, representative of fatigue degradation. Consequently, we differentiate approaches where an additional term $\mathcal{H}$ is added to the brittle potential (1.6), and approaches where the dissipation potential $W(d)$ is modified (1.7). In both cases $\bar{\alpha}$ is cumulated through the fatigue loading, supplementing the crack driving force in the case of the latter and degrading the fracture threshold in the case of the former. Consequently, they lead to similar models where a cyclic load will yield fatigue-like degradation.

The first approach relies on the idea of adding a term to the free energy potential which

acts as additional driving forces of damage, as a function of accumulated fatigue variables, as written in eq. (1.6). This additional term is always representative of the work spent on microstructural effects [149, 150, 220]. Boldrini et al. [30] proposed the introduction of an additional phase-field variable to model the micro cracks that are representative of fatigue degradation. A well posed thermodynamic framework was set by deriving the expression of this fatigue phase-field internal variable from the pseudo-dissipation potential. Similarly, Amendola & Fabrizio [13] have put forward a thermodynamically consistent model, however using a single phase-field formulation. We can cite multiple approaches relying on added driving terms, such as Loew et al. [150] applied to the fatigue of rubber, where the fatigue law is built from micro-cracks growth arguments. Furthermore Schreiber et al. [220, 222] added an additional term built from Miner's rule [167]. Haveroth et al. [101] proposed a similar idea to Boldrini et al. [30] for elasto-plastic materials, by adding an additional phase-field variable, and fatigue potential, before deriving the evolution laws from thermodynamical consistency arguments.

The other types of approaches, materialized by eq. (1.6), can be labeled as toughness degradation methods. They are inspired by Alessi et al. [7] which have put forward a 1D formulation for the fatigue extension of the damage phase-field model. With these models, the toughness of the material, can be viewed as a new internal variable of the problem: it is degraded through the accumulation of the fatigue variable, also representative of micro-structural effects. By lowering toughness in a localized zone around the crack tip (or zones of stress concentration), the threshold for fracture is lowered, enabling crack propagation for sub-critical loads. This approach is purely phenomenological as there is no experimental evidence that fatigue fracture is the result of such an embrittlement of the material. Nevertheless, some authors argue for the physical validity of considering fracture toughness as a variable [6]. Additionally it provides a very straightforward model, that has shown interesting abilities to model fracture, such as the recovery of Wöhler like curve and a Paris linear regime [44] and also usual features of low cycle fatigue [100, 125, 224, 225, 247]. Note that all of these fatigue behaviors are reproduced without the need for an explicit introduction of empirical criteria such as the Paris Law.

Both approaches requires a definition of a fatigue internal variable, representative of cumulated microstructural effects that lead to fatigue fracture. In the initial formulation of Alessi et al. [7], the authors defined the fatigue variable as accumulated strains, but further investigations led to the adoption of an energy accumulation, using the non-compressive part of elastic energy density in order to avoid observed mesh dependency issues [44]. Most other implementations relied on this idea [87, 100, 125, 225, 247, 262], except for Seiler et al. [224]

where the local strain approach is considered. Note that the positive part of elastic energy was sometimes supplemented with plastic terms for elasto-plastic formulations [125, 247], and with phase transformation terms for a shape-memory extension by Simoes et al. [229].

Additionally, the work of Mesgarnejad et al. [162] proposed a similar approach, where some parts of the damage dissipation potential are degraded in a local zone around the crack tip. In fact, recent literature tends to rely more and more on crack tip dependent formulation as in Alessi et al 2023, [6] where an additional "fatigue threshold function" is introduced, to magnify fatigue degradation in a defined zone around the crack tip, and prevent (or slow down) degradation out of this so-called Fatigue Process Zone. Alternatively, Grossman-Ponemon et al. [94] put forward a formulation based on Mesgarnejad et al., with local toughness degradation around the crack tip. These crack-tip limited approach are rooted in the physical reality of fatigue degradation, as we know that dissipative phenomenon are mainly acting in such a zone, but it also limits the flexibility of the approach as it requires a localization of the crack tip, which is not always trivial. Furthermore, enabling degradation far away from the crack tip, *i.e.,* anywhere in the structure, may be key to recover crack nucleation cases and bridge the gap between fatigue crack growth and nucleation [6].

Finally, we can also mention other original approaches that were put forward in a damage phase-field context and don't correspond to either presented formulations (1.6) and (1.7). For instance, one of the first contribution for fatigue in a damage phase-field model was set by Amor et al. [14], by regularizing a variational fatigue model set in Ref. [116]. The free energy potential was written as a function of the variation of "crack length" - crack energy density with a damage phase-field model. This enabled to directly retrieve a Paris' like expression for crack growth, but was hence limited to crack growth. Alternatively, Lo et al.[148] have proposed to add fatigue effects by introducing a viscous term in the formulation.

In this work, we used a toughness degradation formulation, identical to the first approach of Carrara et al. [44]. As mentioned before, this model has proven its predictive abilities as well as being able to reproduce a fatigue-like behavior. Furthermore, these methods will benefit from recent literature which provides new constitutive choices to model more and more fatigue effects, and roots the model in sound theoretical foundations [6, 88].

Conclusion of the chapter

In this chapter, we have introduced the concept of fatigue degradation, *i.e.,* the degradation of materials under a cyclic loading. After detailing the stages of fatigue failure, we recalled that multiple conceptualization of sizing to cyclic loadings exist in the industry: total life approaches and defect tolerant approaches. With the former, all phase of fatigue degradation are considered as one, and the objective is to quantify critical loadings for which no fatigue degradation happens. For the latter, a defect is initially considered in the studied structure, and the objective is to ensure that the fatigue loading does not propagate this defect to complete failure.

In the present nuclear industry context, the defect tolerant approach is the most widely considered. Therefore, we followed with the description of the theoretical tools used to study fatigue crack propagation, which are based on Linear Elastic Fracture Mechanics (LEFM), and the Paris-Erdogan law, linking fatigue crack growth rate with the usual quantities defined in LEFM.

From these theoretical tools, multiple numerical approaches were proposed in the literature to model the fatigue crack propagation phenomenon in a finite element context. First discrete crack models were presented, where the crack is represented as a discrete discontinuity in the finite element space. We have explained that these approaches rely on the setup of multiple ad-hoc criteria to determine the modalities of crack propagation, *e.g.,* the crack growth rate or the direction of propagation, which were set up empirically, or with very simple analytical setup. This renders the applications of such models in the context of networks of cracks very tedious. Therefore, other models were presented, based on a diffuse representation of the crack, and the setup of specific evolution laws to drive crack propagation. Those approaches are usually more flexible to model complex crack patterns, with crack kinking, coalescing or branching. Multiple methods were introduced, with a special attention to the phase-field model, which was ultimately chosen in this work, considering its ability to recover very complex crack patterns without the need for additional criteria.

We finally introduced some of the different phase-field extensions to model fatigue crack propagation and we have shown the ability of the framework to recover cases of either relying on discrete representation of the crack, or diffuse representation through the introduction of damage variables. We have furthermore shown how these approaches could be seen as very promising frameworks to predict real life fatigue crack growth scenarios.

Nevertheless, we have mentioned some of the limitation of this phase-field framework, namely the high computational cost due to the need for a very fine mesh to capture the

steep gradient of the damage field, and the cycle-by-cycle formulation associated with these models that lead to the individual computations of millions of cycle for real life applications. We will discuss these issues further after detailing the setup of the model in the next chapter.

2

Phase-field model for fatigue fracture

In this section, the different ingredients of the phase-field model are detailed and a specific phase-field fatigue formulation is proposed and applied on typical fracture mechanics benchmarks.

Contents

Following the introduction of the fatigue degradation phenomenon, we have introduced several modeling framework setups to predict fatigue crack propagation in a finite element context. We have chosen the popular phase-field framework for its ability to handle complex crack patterns, and introduced the different extensions of the brittle formulation to model fatigue. In this section, we continued the description of the fatigue phase-field model with a more in-depth literature review of its components. Each of these components were described with a brief review of the different existing variants, and the justification of the constitutive choice made in the present work.

Special attention was then given to the energy split used in this work to model unilateral effects. A new method relying on a change of basis was presented to accelerate the decomposition scheme and avoid the rise of singular values during the decomposition operations.

Then, considering the previously set constitutive choices, we detailed the equations linked to the resolution of the resulting coupled phase-field problem, and the associated finite element implementation. The set model was then applied on several numerical samples to showcase the ability of the framework to reproduce typical fatigue phase-field benchmarks.

2.1 Phase-field model for fracture

2.1.1 Variational approach for fracture to phase-field regularization

Francfort and Marigo put forward a novel variational framework [77] to model brittle fracture, inspired by Griffith's energetic approach. In their seminal work, they underline the fact that even though several approaches relying on the energy release rate and Griffith's criterion have emerged through the years to predict fracture, a variational approach derived from this energetic analysis was still lacking. Such a formulation was furthermore pursued considering the deficiencies of the Griffith approach to model fracture, namely the inability to model crack initiation, unstable crack propagation and to give directional information about crack propagation.

Let us consider a domain Ω, and its boundary $\partial\Omega = \partial\Omega_u \cap \partial\Omega_t$. The domain is loaded by volume forces $\bar{\boldsymbol{b}}$ on Ω and surface tractions $\bar{\boldsymbol{t}}$, on $\partial\Omega_t$. Additionally, a displacement $\bar{\boldsymbol{u}}$ is prescribed on $\partial\Omega_u$. In this context, the authors study two types of unknown, the displacement $\boldsymbol{u}$, and the set of cracks Γ. From these definitions, the authors reframe Griffith's criterion in a variational form, by writing the internal energy functional as:

$$\Pi^0_{int}(\mathbf{u},\Gamma) = E_0(\mathbf{u},\Gamma) + W_0(\Gamma) = \int_\Omega \psi_0 \,\mathrm{d}V + \int_\Gamma G_c \,\mathrm{d}S. \tag{2.1}$$

This functional is the internal energy of a cracked structure. For instance $E_0(\mathbf{u},\Gamma)$ is the mechanical component with ψ_0 the elastic energy density, while $W_0(\Gamma)$ is a crack component, expressed as G_c, the fracture toughness of the material, integrated over the crack area Γ to represent energy dissipation in fracture. This formulation stems from Griffith's idea that crack propagation is a competition between elastic energy released at the crack tip, and the surface energy required to create two new crack surfaces. Consequently, the free energy of the cracked body is set as the sum of elastic energy and surface energy over the crack. Next, the external potential energy is set as:

$$\Pi^0_{ext}(\boldsymbol{u},\Gamma) = \int_\Omega \bar{\boldsymbol{b}} \cdot \boldsymbol{u} \,\mathrm{d}V + \int_{\partial\Omega_t} \bar{\boldsymbol{t}} \cdot \boldsymbol{u} \,\mathrm{d}S. \tag{2.2}$$

We can write the total potential energy of the system as:

$$\Pi^0(\boldsymbol{u},\Gamma) = \Pi^0_{int}(\boldsymbol{u},\Gamma) - \Pi^0_{ext}(\boldsymbol{u},\Gamma). \tag{2.3}$$

In a quasi-static framework, at each instant the solution is the one which induces equilibrium of the system, hence finding the admissible couple $(\boldsymbol{u},\Gamma)$ that minimizes the energy functional Π^0 (2.3). The fracture problem is thus recasted as a minimization problem. Note that considering that crack propagation is a purely dissipative phenomenon, an irreversibility constraint is set such that at t_1, t_2, two successive time steps:

$$\Gamma(s) \subseteq \Gamma(t) \text{ for } t_1 < t_2. \tag{2.4}$$

This model is able to counteract the mentioned limitations of Griffith's approach [48, 76]. However, the application of the described framework is complicated, as it requires to identify precisely the crack position and to take into account the jumps of the displacement field. Given the complexity of its implementation in a general numerical framework, a regularized version of this functional, originally introduced by Bourdin et al. [38], is used in this work.

A phase-field paradigm is applied to the functional (2.3) by Bourdin et al. [38], and then Miehe et al. [166] inspired by Ambrosio and Tortorelli [12], themselves inspired by Mumford and Shah [178], that considered a similar functional applied in an image segmentation context. This phase-field paradigm is defined as the regularization of the discontinuity, (*i.e.,* the crack), across a given width, in order to ease its numerical treatment. Indeed, as illustrated in Fig. 2.1, the initially considered sharp crack is smeared around

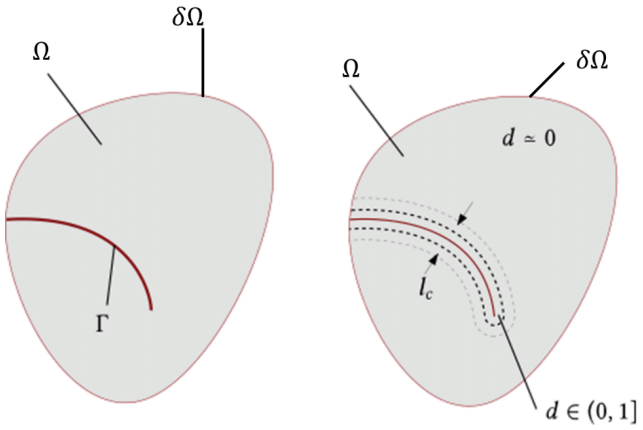

Figure 2.1: Sharp and diffuse crack topologies.

its sharp geometry by considering the crack as a scalar field d, ranging from 0 to 1. For $d = 0$ the material is intact, whereas for $d = 1$ it is fully broken. Furthermore, we can interpret the physical meaning of $0 < d < 1$ considering that here, the phase-field is representative of a crack, and that physically a crack is not a sharp object, but is emerging from micro-cracks in a diffuse damage zone. In this context, we can draw links between this phase-field approach and damage mechanics, where a scalar (or tensor) field, is introduced to be representative of a damage field. Henceforth, d will alternatively be referred to as a damage field or a phase-field. From the introduction of the phase-field, and its application in a fracture mechanics context, a regularized approximation of the free energy functional (2.1) is set in Refs.[38, 166]:

$$\Pi_{int}(\boldsymbol{u}, d) = E(\boldsymbol{u}, d) + W(d) = \int_\Omega \psi(\boldsymbol{u}, g(d))\, \mathrm{d}V \quad + \int_\Omega G_c.\gamma\left(d, \nabla d\right)\, \mathrm{d}V. \tag{2.5}$$

$E(\boldsymbol{u}, d)$ is the total damaged mechanical energy, and $\psi(\boldsymbol{u}, d)$, the damaged elastic energy density. Both are affected by the damage field through a degradation function $g(d)$. Then, $W(d)$ is the energy dissipated in fracture. It is still defined as G_c integrated over the crack surface, meaning that $\gamma(d, \nabla d)$ represents a regularized crack surface density. This term is the diffuse description of the crack surface: it is linked to the approximation of the sharp crack surface. Note that it is influenced both by d and ∇d, drawing another link with damage mechanics, where a gradient term is often introduced in the damage behavior law in order to avoid mesh dependencies. Finally note that the regularized setting is set on the same domain, as d is defined everywhere on Ω.

This approximation of the free energy functional is usually justified through Γ convergence [40], according to which the minima and minimizers of functional (2.5) converge to those

of functional (2.1) as lc approaches 0. As such, this regularized expression is proven to converge to the sharp brittle formulation: when l_c approaches 0, the domain Ω for which $d = 1$ approaches Γ [38, 49, 50]. This vision of the phase-field model means that l_c is a regularizing parameter, which should be chosen as close to 0 as possible to collapse back to a brittle formulation.

Similarly to the sharp variational formulation (2.3), in a quasi-static framework, the solution is the minimization of the regularized functional Π:

$$\Pi(\boldsymbol{u}, d) = \Pi_{int}(\boldsymbol{u}, d) - \Pi_{ext}(\boldsymbol{u}). \tag{2.6}$$

It follows that, the minimizing fields $(\boldsymbol{u}^*, d^*)$ can be solved by using standard arguments of variational calculus:

$$(\boldsymbol{u}^*, d^*) = \underset{\substack{u \in \mathcal{A}_u \\ d \in \mathcal{A}_d}}{\arg\min}\ \Pi(\boldsymbol{u}, d). \tag{2.7}$$

For $\mathcal{A}_u$, the set of all kinematically admissible displacement fields, and $\mathcal{A}_d$, the set of all irreversible phase-fields. For instance, $\boldsymbol{u} \in \mathcal{A}_u = \{\boldsymbol{u} \in H^1(\Omega) \mid \boldsymbol{u}_{\partial\Omega_u} = \bar{\boldsymbol{u}}\}$.

2.1.2 Model components

The expression of the regularized free energy functional (2.5) can be seen as the sum of a damaged mechanical term $E(\boldsymbol{u}, d)$ and the energy dissipated in fracture $W(d)$: we now expand the expression of these terms, using the generalized notations of Ref. [259]:

$$E(\boldsymbol{u}, d) = \int_\Omega g(d) \cdot \psi_0^+(\boldsymbol{u}) + \psi_0^-(\boldsymbol{u})\, dV, \tag{2.8a}$$

$$W(d) = \frac{G_c}{c_w} \cdot \int_\Omega \frac{w(d)}{l_c} + l_c \cdot |\nabla d|^2\, dV. \tag{2.8b}$$

Here all the components of the brittle phase-field model are listed:

- The degradation function $g(d)$
- The energy split as ψ_0^+ and ψ_0^-
- The dissipation function $w(d)$ and c_w

The following section is a literature review of those components along with the important treatment of the irreversibility constraint, and the constitutive choices related to fatigue effects.

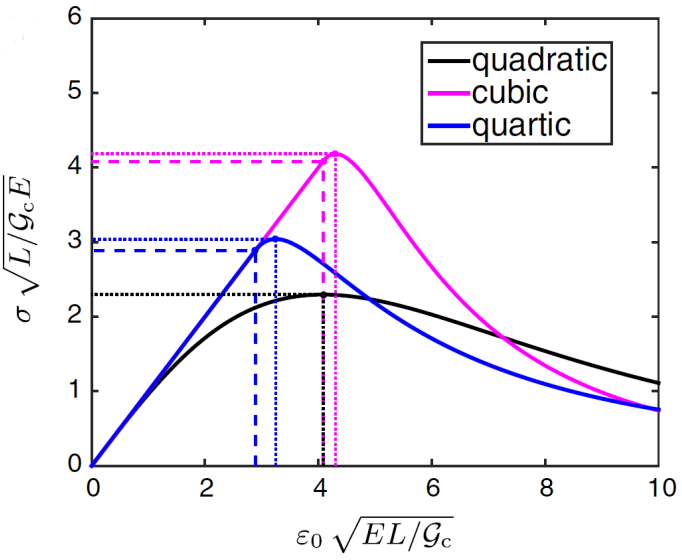

Figure 2.2: Normalized stress as a function of normalized displacement for several degradation function by Kuhn et al [133]. Dashed line indicate normalized stress and strain at which the elastic domain ends, while dotted lines show the critical values of these normalized parameter.

2.1.2.1 $g(d)$, degradation function

The degradation function is the term that enables the energy restitution as cracks propagate in the solid: as the phase-field increases, the mechanical response is softened. It is assumed to be a strictly decreasing continuous function, with values ranging between 0 and 1, for damage values ranging from 1 to 0. $g(d)$ is usually chosen as a polynom of d (*e.g.*, $g(d) = 1-d$). See Refs. [226] for a first order degradation function, Refs. [9, 38, 166, 172] for second order degradation functions, Refs. [31, 106] for third order, or Refs. [98, 105, 122, 124, 133] for fourth order degradation function. See [31, 133] for a comparison of the degradation functions and their respective influence on the phase-field model and see Fig. 2.2.

First order degradation functions are not very popular in the phase-field community because $g'(d)$ is then independent of d. Consequently, the force driving damage evolution is not reduced as damage increases. On the contrary, a second order degradation function offers a decreasing linear relation between d and its driving force. However, because of the fact that $g'(0) \neq 0$, any amount of loading induces an increase of the damage field, and hence a softening of the response: no elastic domain exists (note that with the AT1 formulation, an elastic threshold can still be reproduced, see Section 2.1.2.2). This observation is the main reason that has motivated authors to consider higher order degradation functions. Indeed, as reported in Kuhn et al. [133], higher order degradation functions can be tuned in order to satisfy $g'(0) = 0$, and hence offer an elastic threshold below which the response is perfectly linear. Note however, that such a choice for the

degradation function induces an abrupt softening of the mechanical response, and have been reported to pose a challenge to numerical solvers. Interestingly, Kuhn et al. [133] report that even though the computed mechanical response before crack initiation varies widely between those formulation, the mechanical response after initiation is the same.

The second main reasoning that led to the introduction of new degradation functions is the observation that the critical stress σ_c computed with a phase-field model is dependent on l_c. Hence, a parameter viewed as a regularization term has an influence on the material behaviour. While a part of the literature chooses to embrace this dependency and argue that it adds richness to the phase-field formulation [171], others have been designing phase-field models that are independent of l_c, in order to consider the term strictly as a regularization term, closer to Bourdin et al.'s [38] original vision. For instance we can cite Ref.[218] which puts forward a complex expression for the degradation function that allows very precise fine-tuning and that dissociates σ_c and l_c. Additionally Wu et al. [255] put forward a power based degradation function, inspired by the work of Lorentz et al. [152], tackling identical issues in the similar field of gradient damage modeling.

Considering ease of implementation, adaptivity of this work's implementations to the existing literature, a classic quadratic degradation function is chosen henceforth. It is expressed as:

$$g(d) = (1-d)^2 + k. \tag{2.9}$$

Note that following Miehe et al. [166], a small parameter k is introduced in order to avoid an ill-conditioned stiffness matrix by keeping a very small residual stiffness in damaged elements.

2.1.2.2 $w(d)$, geometric crack function

In the generalized expression (2.8b), we have adopted the formalism of Ref. [259], that considers that the crack surface density $\gamma(d, \nabla d)$ expressed in eq. (2.5) is described by a gradient term, and $w(d)$, a so-called geometric crack function, associated with the coefficient c_w. This function drives the crack topology, *i.e.,* the distribution of the damage field in the domain, as a diffused sharp crack geometry. A wide variety of geometric crack functions have been put forward in the literature, each associated with a specific c_w, chosen to recover results of Γ convergence.

In a phase-field framework, two main geometric crack functions have been widely used, so-called AT1 and AT2 (for Ambrosio and Tortorelli). Those denominations are representative

of a linear function, AT1: $w(d) = d$, and a quadratic function, AT2: $w(d) = d^2$, associated respectively with $c_w = \frac{8}{3}$, and $c_w = 2$. See Refs. [28, 117, 176, 199, 241] for application of the AT1 formulation, and Refs. [38, 166, 172] for application of the AT2 formulation. Furthermore, a comparison of several aspects of these density functions was led in Refs. [176, 259]. We can briefly describe the difference between those functions by saying that, on the one hand, AT2 offers a very convenient numerical framework, at the cost of a significant influence of damage in the "elastic" domain, while AT1 enables an elastic threshold at the cost of numerical efficiency. Indeed, AT2 is more efficient than AT1 because the phase-field is intrinsically bounded by 0 and 1, and that in a staggered framework (described in Section 3.1), the phase-field problem is linear. On the contrary, with an AT1 formulation, an additional constraint must be set-up in order to bound the phase-field. Considering these numerical efficiency advantages, an AT2 formulation was considered in this work. Note however that such a choice has several consequences on the topology of the damage field and the mechanical response. First as already mentioned, no elastic threshold exists: any prescribed displacement induces damage. Furthermore, $d \geq 0$ everywhere in the considered domain. Nevertheless, d remains very small in the domains of small solicitation.

We can also cite other propositions of geometric crack functions, such as Refs. [255, 256], where a linear combination of AT1 and AT2 is put forward, and the higher order approach for the phase-field model by Borden et al. [32], where a quadratic geometric crack function is chosen along higher order gradient terms, enabling a greater regularity of the crack topology solution and hence better convergence rates.

Remark 2.1: Damage topologies for AT1 and AT2
In this remark, we used Miehe's illustrating example of applying the variational arguments to a damage problem: a so-called "variational problem of regularized crack topology" [165]. In this example, the authors considered a 2D plate with an initial sharp crack as shown in Fig. 2.3. The phase-field was initialized at $\hat{d} = 1$ on the sharp crack's initial nodes, and the crack topology problem was solved to find the damage field on this domain. This way, we have illustrated the influence of the crack geometric function on damage diffusion. Additionally, we developed the equations linked to the energy minimization principle to show a part of the process used to deduce the phase-field model equations. This approach applied to the total Lagrangian in eq. (2.3) can be performed to deduce the coupled system strong form equations. Moreover, considering the straightforward implementation of this numerical experiment in Cast3M, we provided the code in Appendix B.2: indeed, we considered it would be relevant to the interested reader as it illustrates how the phase-field equations were solved by analogy using the thermal operators of Cast3M.

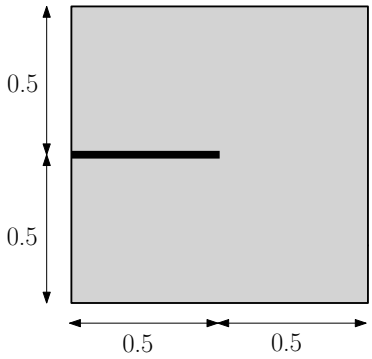

Figure 2.3: 2D cracked square, dimensions are in mm.

Following Ref. [165], we have solved a damage problem, with no influence of mechanics, by minimizing the Lagrangian with respect to d. Applying Dirichlet's condition of $\hat{d} = 1$ on the central node, and solving for this damage problem, we could then visualize the arrangement of damage depending on the used geometric crack function. First we write the crack surface density as:

$$\gamma(d, \nabla d) = \frac{1}{c_w} \left(\frac{w(d)}{l_c} + l_c \cdot |\nabla d|^2 \right). \tag{2.10}$$

Applying standard arguments of variational calculus we find the minimizing damage field by solving for a vanishing variational derivative of the damage functional $W(d) = G_c \cdot \int_\Omega \gamma(d, \nabla d) dV$:

$$\delta W(d) = 0 = \int_\Omega G_c \left(\frac{\partial \gamma}{\partial d} \delta d + \frac{\partial \gamma}{\partial \nabla d} \delta \nabla d \right) \, \mathrm{dV}. \tag{2.11}$$

Then, integration by parts and Ostrogradsky's theorem are used to get rid of the $\delta \nabla d$ terms, and we inject the generalized expression of the crack surface density (2.10):

$$\delta W(d) = \int_\Omega \frac{G_c}{c_w} \left(\frac{1}{l_c} \frac{\partial w(d)}{\partial d} - 2 l_c \cdot \Delta d \right) \delta d \, \mathrm{dV} + \int_{\partial \Omega} (\nabla d \cdot \boldsymbol{n}) \, \delta d \, \mathrm{dS}, \tag{2.12}$$

where $\boldsymbol{n}$ is the outward normal at the boundary. Therefore, we set the following strong form equation for this damage minimization problem, while enforcing $\nabla d \cdot \boldsymbol{n} = 0$ on the boundary:

$$\frac{G_c}{c_w} \left(\frac{1}{l_c} \frac{\partial w(d)}{\partial d} - 2 l_c \cdot \Delta d \right) = 0. \tag{2.13}$$

We develop for AT1 and AT2 respectively, $w(d) = d$, $w(d) = d^2$:

$$\textbf{AT1 model:}\quad \frac{3G_c}{8l_c} - \frac{3G_c}{4} l_c \cdot \Delta d = 0, \tag{2.14}$$

$$\textbf{AT2 model:}\quad \frac{G_c}{l_c} d - G_c l_c \cdot \Delta d = 0, \tag{2.15}$$

which can readily be solved in the described context for a 1D, and a 2D geometry (while enforcing $0 < d < 1$ for the AT1 model), yielding the topology illustrated in Fig. 2.5. Additionally, analytical solutions for these geometric function in 1D were provided in Fig. 2.4:

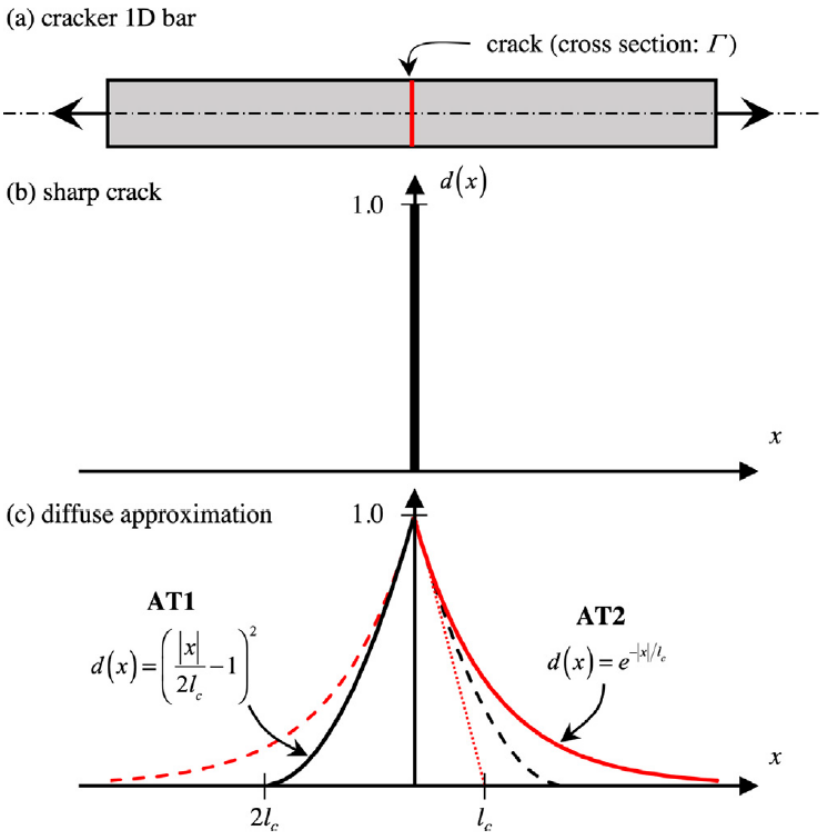

Figure 2.4: 1D crack topologies from Molnár et al. [176].

For the AT2 formulation, we see that the phase-field is strictly larger than 0: the structure started to damage everywhere. The AT1 geometric function induces a narrower localization band, for the same value of l_c, with undamaged zones $d = 0$, far from the prescribed $\hat{d} = 1$ nodes.

Note that these illustrations use a relatively large value of l_c, in order to differentiate clearly both geometric functions. Using the AT2 model, we then illustrated the influence

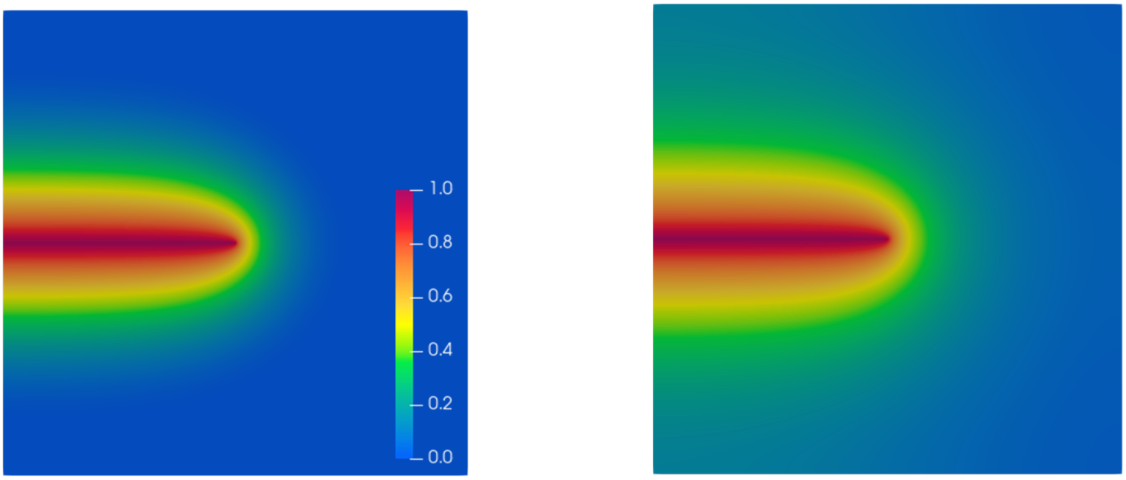

(a) 2D crack topology using the AT1 model.

(b) 2D crack topology using the AT2 model.

Figure 2.5: Influence of geometric crack function $w(d)$.

of l_c on damage topology. In Fig. 2.6, lower values of l_c are applied on the geometry to show the converging behavior of the model toward a sharp crack representation.

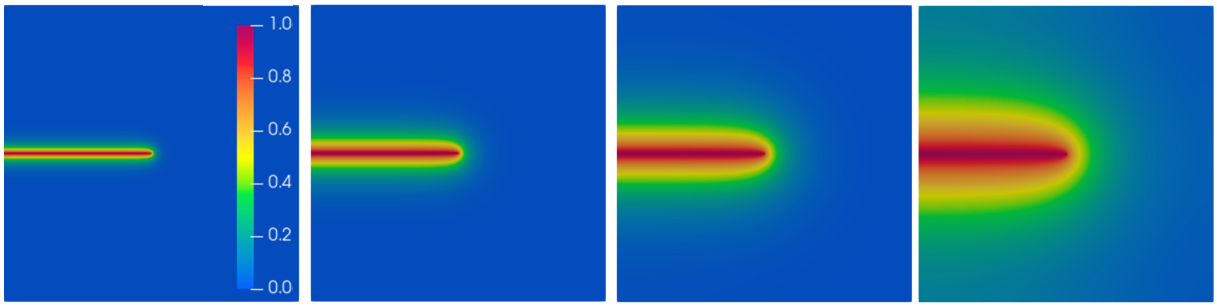

Figure 2.6: Topological influence of l_c: from left to right, with $l_c = 0.02$ mm, $l_c = 0.05$ mm, $l_c = 0.1$ mm, $l_c = 0.2$ mm.

2.1.2.3 Mechanical energy decomposition

In Bourdin et al.'s seminal work [38], the damaged mechanical energy density $\psi(\boldsymbol{u}, d)$ listed in eq. (2.5) was expressed as:

$$\psi(\boldsymbol{u}, g(d)) = g(d) \cdot \psi_0(\boldsymbol{u}), \tag{2.16}$$

with ψ_0, the usual elastic energy density. With this expression, the response is symmetric with respect to the prescribed displacement, meaning that the damage will increase similarly in tension and compression. However, this symmetric behavior is not representative of

experimental observations for most brittle and quasi-brittle materials.

This symmetric formulation could be employed if we limited ourselves to opened crack. However, considering that usual fatigue loadings can be defined by alternating compressive and tensile phases, we considered that the implementation of an asymmetric formulation was mandatory in order to model real-life fatigue specimens. In a cyclic loading context, Mazars et al. [160] have described and modeled the effect of those so-called unilateral effects: first, the restoration of the elastic stiffness in the zones where the crack lips are closed (hence avoiding crack interpenetration). Then, the setup of a damage evolution law, which is dependent upon the state of deformation.

The issue here, for most authors considering a damage mechanics or phase-field framework, has been to introduce an asymmetric behavior (often referred to as "anisotropic" in the literature, which should not be confused with material anisotropy: here it refers exclusively to a damage evolution anisotropy), while restricting the damage variable to a scalar. In this context, the most popular approach is the energy decomposition as introduced in eq. (2.8a). The elastic energy density is split in two distinct terms, the active term ψ_0^+ and the passive term ψ_0^-. In contrast to eq. (2.16), we write:

$$\psi(\boldsymbol{u}, g(d)) = g(d) \cdot \psi_0^+(\boldsymbol{u}) + \psi_0^-(\boldsymbol{u}). \tag{2.17}$$

The stored mechanical energy is split in an active contribution ψ^+, degraded by d, hence a part of the crack driving force, whilst ψ^- is not degraded and does not influence damage. The specific choice of these active and passive terms vary in the literature. We mention some of these approaches in the following section, but an extensive comparison of the existing approaches is made in Refs. [153, 259].

Considering this formulation we can reframe the initial symmetric energy density as:

$$\psi_0^+(\boldsymbol{u}) = \frac{\lambda}{2}[tr(\boldsymbol{\varepsilon})]^2 + \mu.tr(\boldsymbol{\varepsilon}^2) \text{ and } \psi_0^-(\boldsymbol{u}) = 0. \tag{2.18}$$

Such a formulation allows crack interpenetration and consequently yields unphysical responses when it is applied on cases where the crack lips are closed. The most popular example of such unphysical response is the simulation of the single-edge notched shearing sample, that was put in light by, *e.g.,* Refs.[10, 165]. The sample is illustrated in Section 2.4. The isotropic formulation predicts that two symmetric cracks propagate from the initial notch, implying crack interpenetration, while most decomposition approaches predict a single propagating crack, going toward the lower-right corner.

In order to take into account the unilateral effects, most authors put forward a specific split of the strain tensor, and choose which components of the tensor constitute the active and passive terms. Amor et al. [15], introduced a decomposition based on a volumic-deviatoric split of the strain tensor: damage is driven by positive volumetric component $\langle tr(\epsilon)\rangle^+$, and the deviatoric part of the tensor, representative of the shear state. Here, $\langle X\rangle^+ = 0$ if $X > 0$, and 0 otherwise. The passive term is constituted by the negative volumetric components $\langle tr(\epsilon)\rangle^-$. With this split, the sign of the volumetric term is driving the separation of tension and compression. However, note that in compression, the active term is still driven by the deviatoric part, hence enabling degradation. We can also cite Lancioni & Royer-Carfagni [139] for another version of a volumetric/deviatoric split, or the related "no-spectral" split, introduced for quasi-brittle material in Ref. [79].

$$\psi_0^+(\boldsymbol{u}) = \left(\frac{\lambda}{2} + \frac{\mu}{3}\right).\left(\langle tr(\boldsymbol{\varepsilon})\rangle^+\right)^2 + \mu.tr(\boldsymbol{\varepsilon}_{dev} : \boldsymbol{\varepsilon}_{dev})^2, \tag{2.19a}$$

$$\psi_0^-(\boldsymbol{u}) = \left(\frac{\lambda}{2} + \frac{\mu}{3}\right).\left(\langle tr(\boldsymbol{\varepsilon})\rangle^-\right)^2. \tag{2.19b}$$

Another very popular split is the spectral split introduced in Refs. [166]. This decomposition considers that crack propagation is driven by the positive part of the principal strains, hence using a spectral split of the strain tensor and using the sign of these principal components to discriminate between tension and compression.

$$\psi_0^+(\boldsymbol{u}) = \frac{\lambda}{2}\left(\langle tr(\boldsymbol{\varepsilon})\rangle^+\right)^2 + \mu.tr\left((\boldsymbol{\varepsilon}^+)^2\right), \tag{2.20a}$$

$$\psi_0^-(\boldsymbol{u}) = \frac{\lambda}{2}\left(\langle tr(\boldsymbol{\varepsilon})\rangle^-\right)^2 + \mu.tr\left((\boldsymbol{\varepsilon}^-)^2\right). \tag{2.20b}$$

Other approaches have been put forward in the literature such as a spectral split on the stress tensor in Wu et al. [257, 260]. Recently the deficiencies of these widely used energy splits are underlined in the literature. For instance, we observe unphysical stiffening on the shear case with Miehe's spectral split. Conversely, Amor's deviatoric split seems to carry its own issues when applied to compressive loadings [218]. One issue of these approaches is that the split is not an orthogonal decomposition of the strain tensor [102]. Notably Li et al. [147] have shown that this orthogonality principle was not satisfied with the spectral split. These issues also arise with all other splits when material anisotropic effects are added in the model [102]. Following from the orthogonal split of the strain tensor devised in He & Shao [102], multiple phase-field applications of these ideas have

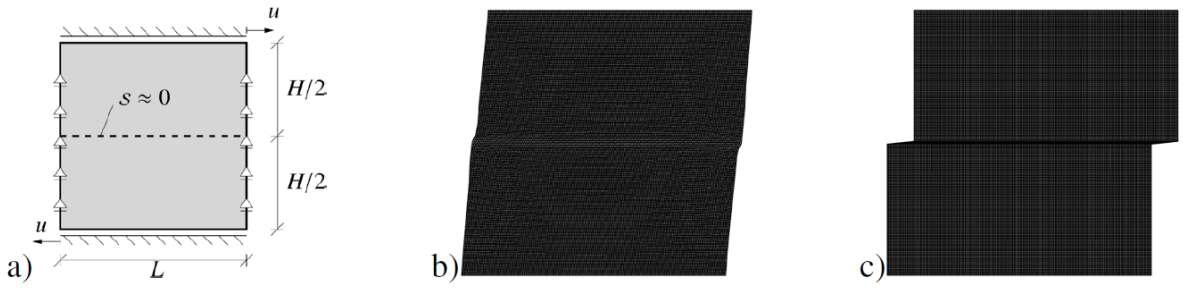

Figure 2.7: Numerical experiments by Strobl et al. [236]. (a) is the problem setting (b) is a deformed mesh with spectral decomposition (c) is a deformed mesh with a crack orientation dependent approach.

already been put forward in Refs. [185, 266].

Other authors view these discrepancies from another angle: usual energy splits induce unphysical energetical contributions in completely damaged material. Indeed, if $d = 1$, the formulation (2.17) induces $\psi(\boldsymbol{u}, d) \neq 0$ because it is equal to $\psi(\boldsymbol{u})^- \neq 0$. This is illustrated in [234–236] using a fully cracked square and applying a shear load on the upper corner as is illustrated in Fig. 2.7. With a perfect split, we should expect that the top side of the square would be displaced with no strain visible on either side of the crack. On the contrary, what we observe is the presence of unphysical stresses at the crack that induce a residual rigidity in shear. Hence Strobl et al. [235, 236] and later Steinke & Kaliske [234] have introduced formulations explicitly based on the direction of the crack and its normal. This enables to recover unilateral effects, and avoid these observed unphysical contributions at the cost of variational consistency and applicability on any given case, because of the difficulty to specify a crack orientation, for instance in cases of crack nucleation or at the crack tip.

Alternatively, a very popular approach was put forward in Ambati et al. [10], coined the hybrid approach. In a staggered context, (meaning that the minimization problem is split into two staggered minimization problems to solve for $(\boldsymbol{u}, d)$ separately, see Section 3.1) the resolution of the mechanical problem influenced by constant damage is trivial with the isotropic formulation. However, when a split of energy is adopted, it induces strong non-linearity, lengthening the search for a converged solution. Consequently, the authors keep the isotropic formulation during the mechanical resolution step to keep a linear elastic mechanical sub-problem. Then they apply the split before the damage step, meaning that the damage sub-problem is then only driven by the active contributions of mechanical energy. Additionally, the authors add a constraint on the damage field, $d = 0$ if $\psi^- > \psi^+$. This formulation enables to recover the unilateral effect and to recover results of other decomposition approaches with a more robust and efficient solver, at the

cost of losing variational consistency of the standard regularized formulation. In the end, it is a similar approach to Strobl et al. [235], or the following Refs.[258, 264], where the crack driving force is built to reproduce a specific phenomenology instead of being deduced from the phase-field minimization problem.

In this work, we used a spectral split inspired by Miehe et al. [165], Bernard et al. [26] and Molnár et al. [173]. This way we consider unilateral effects using a split of energy and induce non-linearity of the mechanical sub-problem. These issues of non-linearity were somewhat treated in Section 3.1.2, while the specific implementation of the spectral split was detailed in Section 2.2.

2.1.2.4 Damage irreversibility

Finally, the last component of the phase-field model is the irreversibility constraint that must be respected throughout computations: the crack cannot heal. In this work, the issue of irreversibility is scarcely investigated. We hence put forward this brief review of the numerical approach to solve the issue of irreversibility that was used in the literature. However, we direct the interested reader to De Lorenzis & Gerasimov [60], in which a rigorous mathematical setting is exposed to compare the most often implemented approaches. Furthermore, the authors use various numerical benchmarks to illustrate the influence of these approaches on the computed response.

The irreversibility condition can be seen as an additional constraint on the phase-field, such that $\dot{d} \geq 0$. It is hence often added in the form of usual constraint enforcing methods, trading this inequality condition for a larger system restricted to equality conditions. For instance, approaches relying on an augmented Lagrangian method [251], or the introduction of penalty terms [17, 81], or Lagrange multiplier's [103, 154, 176]. These methods allow for a rigorous enforcement of the irreversibility condition everywhere on Ω, at every time-step, while keeping variational consistency of the formulation. However, these approaches usually imply a substantial computing cost. In this context, several authors put forward solutions to reduce the computing cost, by limiting the constraint to specific sub-sets of the domain, as in the seminal work of Bourdin [38], or Gerasimov & De Lorenzis using a penalty term [82], or as was done in Lu et al. [154], with an accelerated Lagrange multiplier approach. In those works, a specific phase-field threshold (or variation of the phase-field) is chosen to define the constrained sub-set. Note that these approaches enable damage healing in all the zones not recognized as being part of the crack sub-set, or the varying sub-set.

Another approach was introduced by Miehe et al. [166] in a staggered resolution context

(see Section 3.1): the history field method. The authors put forward the substitution of the mechanical fields driving crack propagation by a so-called history field. This field is set to only increase during propagation meaning that the source terms seen in the damage problem should not decrease. Note that the history field is not just a source term/crack driving force term. In most formulations it is also coupled to damage in the minimizing system of equation as detailed in [60], and clearly expressed in Section 2.3. This newly introduced field is defined as the maximum value of ψ_0^+ over the computed time interval whose continuous and discretized expressions are:

$$H(t) = \max_{\tau \in [0:t]} \left(\psi_0^+(\tau) \right), \tag{2.21a}$$

$$H_{n+1} = \begin{cases} \psi_0^+(\boldsymbol{\varepsilon}) & \text{if } \psi_0^+(\boldsymbol{\varepsilon}) > H_n \ , \\ H_n & \text{otherwise,} \end{cases} \tag{2.21b}$$

where H_n is the history field computed at the previous step. This formulation enables H to satisfy the Karush-Kuhn-Tucker condition:

$$\psi_0 - H \leq 0, \quad \dot{H} \geq 0, \quad \dot{H}(\psi_0 - H) = 0 \ , \tag{2.22}$$

in loading and unloading, meaning that the driving force of fracture cannot decrease: a damaged zone will not recover even in unloading scenarios. This yields a very robust, efficient, and easy to implement approach to enforce irreversibility at the cost of complete loss of variational consistency, because not every argument of the formulation is derived from the energy minimization principle.

Considering the efficiency of this approach, and its widespread application in the phase-field literature, we decided to use the history field approach to enforce irreversibility in the fatigue phase-field approach.

2.1.2.5 Fatigue effects

Considering all the previously mentioned modeling choices for the degradation function, the geometric crack function, the energy split and the damage irreversibility condition, we can write the final free energy functional of the cracked body in a brittle framework as:

$$\Pi_{int}(\boldsymbol{u}, d) = \int_\Omega g(d) \cdot \psi_0^+(\boldsymbol{u}) + \psi_0^-(\boldsymbol{u}) \, \mathrm{d}V + \int_\Omega G_c \cdot \left(\frac{d^2}{2l_c} + \frac{l_c |\nabla d|^2}{2} \right) \mathrm{d}V. \tag{2.23}$$

These specific choices enable a very standard and flexible formulation, which corresponds to

the practical consideration of the phase-field model in this work. Indeed, the goal is to put forward accelerating tools that can be used on real-life cases, and be readily adapted to other phase-field contexts. In this regard the accelerating tools presented in Chapter 3 are here investigated with this standard formulation, widely documented in the literature, and easily transferable. Moreover, the quadratic degradation function and crack density function enable a very efficient numerical treatment as the phase-field is intrinsically bounded, and a smoother jump of the unknowns is recorded at the onset of fracture. Additionally the history field approach is also very efficient, and widely adopted in the literature.

Now, as mentioned in the previous section, this brittle formulation was transformed by applying a fatigue driven degradation of the fracture toughness, inducing crack propagation for sub-critical loadings in the zones where toughness has been degraded [44]:

$$\Pi_{int}(\boldsymbol{u}, d) = \int_{\Omega} g(d) \cdot \psi_0^+(\boldsymbol{u}) + \psi_0^-(\boldsymbol{u}) \, \mathrm{d}V + \int_{\Omega} \int_0^t f\left(\bar{\alpha}(\tau)\right) G_c \cdot \dot{\gamma}\left(d, \nabla d\right) \mathrm{d}\tau \; \mathrm{d}V, \quad (2.24)$$

where the newly introduced fatigue degradation function $f(\bar{\alpha})$ is driven by the fatigue history dependent internal variable $\bar{\alpha}(\tau)$.

In this work, we used straightforward expressions of $f(\bar{\alpha})$ and $\bar{\alpha}$, in order to propose easily extendable accelerating tools. However, note that these terms can be built to induce very complex experimentally observed fatigue effects, such as the influence on crack growth rate of the average stress, or the effect of crack closure [6]. Furthermore, their construction can be performed with numerical-experimental comparisons in mind, hence considering that their driving parameters can be fit to recover Wöhler's curve/Paris' Law slopes, endurance limits, values of ΔK_{thresh} [88], and even multiple domains of the Paris curve, like a NASGRO equation [6]. In this next subsection, we gave a brief overview of these chosen degradation function and fatigue history variable.

$\bar{\alpha}$, fatigue history variable

Following the original formulation of Alessi et al. [7] and Carrara et al. [44], fatigue degradation in this model is driven by a fatigue history variable, which is a macroscopic representation of the internal microscopic dissipative phenomenon, responsible for fatigue failure. This fatigue history variable is defined by the accumulation of a mechanical quantity during the cyclic loading characteristic of the fatigue phenomenon. Subsequently, in all fatigue extensions of the phase-field model, several constitutive choices must be made

regarding this quantity: which quantity accumulates, how does it accumulate and how can this accumulation model phenomenologies specific to fatigue, such as the influence of average stress or ductile effects [88].

We can write the fatigue history variable as the accumulation of a fatigue internal variable, thus, in a time discretized setting, at a given time-step n we use quantities computed at $n-1$ such that:

$$\bar{\alpha}_n = \bar{\alpha}_{n-1} + \int_{n-1}^{n} \chi(\alpha)\,\mathrm{d}t \ , \tag{2.25a}$$

$$\simeq \bar{\alpha}_{n-1} + \Delta\bar{\alpha} \ . \tag{2.25b}$$

Indeed, in this work, as already introduced earlier, we kept notations of Carrara et al's seminal work [44]. Namely we define α, the fatigue internal variable, which can be set as any non decreasing mechanical quantity that should be linked to fatigue degradation. In the first work on toughness degradation models [7], the authors put forward the use of an accumulated strain quantity (which would be analagous to damage mechanics approaches such as Kachanov's initial formulation [121]). However, (as in damage mechanics), this formulation induces mesh dependency issues that were corrected by Carrara et al.[44] using a fatigue variable of energetic nature. Furthermore, the authors put forward the coupling of this variable with the phase-field, so as to disable fatigue degradation in fully damaged zone. This, in turn, avoids issues of singularity at the crack tip, since no energy is accumulated on the singular points [88]. As stated previously, most approaches rely on this energetic approach, as was highlighted in Ref.[6], where an enlightening comparison of existing approaches is proposed. Since no plastic effects are considered, we can write the expression of α as it was chosen in this work, and the following references: [6, 87, 88, 100, 262]:

$$\alpha = g(d) \cdot \psi_0^+ . \tag{2.26}$$

Consequently, fatigue degradation is driven by the same quantity as the phase-field variable is: ψ_0^+, the non-compressive part of mechanical energy. Furthermore, note that the degradation function $g(d)$ is also reused, namely, the parabolic degradation function (2.9).

The next step is the setup of an accumulation scheme of the fatigue internal variable: hence the shape of χ, or $\Delta\bar{\alpha}$ introduced in eq. (2.25b). This function can be tweaked to add the influence of fatigue specific effects. First, we can cite the initial formulation of Carrara et. al, where no fatigue specific effects were taken into account, except for the

fact that no accumulation happens in unloading. In a time-discretized setting, considering the quantities between t^{n-1} and t^n:

$$\Delta\bar{\alpha}_1 = |\alpha_n - \alpha_{n-1}| \cdot \mathrm{H}\left(\frac{\alpha_\mathrm{n} - \alpha_{\mathrm{n-1}}}{\Delta \mathrm{t}}\right), \tag{2.27}$$

where, H is the Heaviside function, which yields 0 for negative values of energy increment. Additionally the authors put forward a formulation to take the influence of the average stress into account:

$$\Delta\bar{\alpha}_2 = \left(\frac{\alpha_n - \alpha_{n-1}}{\alpha_N}\right) \cdot \left(\frac{\alpha_n + \alpha_{n-1}}{2}\right) \cdot \mathrm{H}\left(\frac{\alpha_\mathrm{n} - \alpha_{\mathrm{n-1}}}{\Delta \mathrm{t}}\right). \tag{2.28}$$

With a normalization parameter α_N. Here, average stress effects are taken into account by the introduction of the average fatigue internal variable $(\alpha_n + \alpha_{n-1})/2$.

In Seleš et al. [225], the authors highlighted the fact that this formulation should not induce fatigue accumulation for a static load. However, nothing prevents energy from cumulating with a static load, which means that a poor choice of fatigue parameters can lead to "fatigue" degradation for monotonous load [44]. Consequently, the authors put forward the idea of restricting accumulation to the unloading phases. This way, an alternated cyclic loading will induce accumulation, while a static load will not. In discretized form, this yields:

$$\Delta\bar{\alpha}_3 = |\alpha_n - \alpha_{n-1}| \cdot \mathrm{H}\left[-\left(\frac{\alpha_\mathrm{n} - \alpha_{\mathrm{n-1}}}{\Delta \mathrm{t}}\right)\right]. \tag{2.29}$$

Note that these authors used a slightly different formulation for the fatigue internal variable (also used in Ref.[130]): choosing an undamaged energetic term instead of the term explicited in eq. (2.26). Furthermore, the authors report that for a given strain amplitude, the energetic response is highly dependent on the average strain value. Consequently, they showed how this formulation automatically recovers an average stress dependent method [225].

Finally we can mention the work of Golahmar et al. [88], which has recently proposed a more complex formulation of this accumulation, in order to add a significant amount of fatigue specific effects. Namely the authors state the need to model: (a) the average stress effect, (b) the endurance limit of the materials (asymptotic response for a large amount of cycle on the Wöhler curve), and (c) the dependency of the approach to specific parameters that enable the fit with a specific slope of S-N curve. This yields the following formulation:

$$\Delta\bar{\alpha}_4 = \left(\frac{\alpha_{max}}{\alpha_N}\right)^n \cdot \left(\frac{1-R}{2}\right)^{2\kappa n} \mathrm{H}\left(\alpha_{\max}\left(\frac{1-\mathrm{R}}{2}\right)^{2\kappa} - \alpha_{\mathrm{e}}\right), \tag{2.30}$$

with R defined as the load ratio, here defined as $\sigma_{I,min}/\sigma_{I,max}$ the ratio of maximum and minimum principal stresses, α_N a normalization parameter as in eq. (2.28), and n, κ, α_e, as experimentally fitted coefficients for S-N slopes and endurance limit. Note also the definition of α_{max} which is representative of the maximum amplitude of α during the considered cycle. This term comes from a very interesting aspect of this formulation, inspired by Seleš et al. [225]. Indeed, the authors highlight the fact that accumulating fatigue only in the unloading phases has a tendency to yield accumulation behind the crack tip (because of local unloading in the wake of the crack [88].) Consequently, the authors put forward the idea of driving accumulation only with one maximal variation of α, hence considering one peak to valley load, for each loading cycle. As well as correcting the cited issue with a static load, this approach yields accelerated computations because only one time-step per cycle is computed, where this maximum load is applied.

Note also the work of Alessi et al [6], where a generalized expression of this accumulation is proposed, as the combination of four state functions all responsible for different fatigue specific phenomenologies:

$$\chi(\alpha) = \chi_4(\chi_1(\alpha)) \cdot \chi_3(\chi_1^p(\alpha)) \cdot \chi_2(\chi_1(\alpha)). \tag{2.31}$$

Such that χ_1 is used to induce a fatigue process zone (FPZ): it magnifies α in the zone and reduce its influence outside of it. It can be seen that this FPZ was imposed in every term. χ_2 is used to discriminate between tensile and compressive terms (hence analog to the choice of ψ_0^+, instead of ψ). χ_3 is chosen so as to induce the effect of the average stress with the exponent p. Finally, χ_4 is a function that decides how much each loading and unloading phase plays a part in fatigue accumulation. The author hence gives the opportunity of devising a method where in unloading, a part of the fatigue internal variable is accumulated. This accumulation can, for example, be linearly decreasing during the unloading phase. With such a framework, the author shows that it is possible to model crack closure effects, as it is possible to control the relative contribution of the fatigue internal variable during loading and unloading phases.

Note that as the influence of these fatigue specific phenomenologies was not studied in this work, we used the very basic formulation stated in eq. (2.27).

$f(\bar{\alpha})$, fatigue degradation function

The second main ingredient of this fatigue extension is the fatigue degradation function, *i.e.,* the function linking the fatigue history variable with the local degradation of the critical toughness of the material. This function should follow a specific set of rules to be applicable in this context [44]: It should be strictly decreasing, continuous and (at-least) piece-wise differentiable. Furthermore, it should be bounded by 1 and 0, ideally approaching 0 for $\bar{\alpha} \to \infty$, and mandatorily approaching 1 for $\bar{\alpha} \to 0$, as it should coincide with a brittle behavior in this case, *i.e.,* G_c is unaffected when the fatigue history variable is 0. Several degradation functions have been proposed in the literature that induce different fatigue behaviors.

These functions are built differently in the literature, to account for different crack phenomenologies [6, 7, 44, 88, 225, 262]. The authors grant different characteristics to the fatigue degradation functions.

The first characteristic is the presence of a threshold before which no fatigue degradation can happen, usually driven by a specific parameter, here called α_T, which acts as a threshold of the fatigue internal variable. In a fatigue framework, this parameter could be linked to the endurance limit of a material or ΔK_{thresh}. In Carrara et al. [44] every proposed function has such a threshold, while in Seleš et al., some functions induce toughness degradation, even for an infinitesimal amount of fatigue history accumulation.

In a similar fashion, one can induce a lower threshold of degradation, meaning that there exists a constant C such that $f(\bar{\alpha}) > C$ for any $\bar{\alpha}$. This lower threshold could also be linked to an endurance limit of the material, and enables a residual toughness of the material, even as $\bar{\alpha} \to \infty$.

Finally, the last characteristic is the number of degrees of freedom driving this degradation function, which enables to control the decreasing slope of the function, and the described thresholds. In most formulations, only one degree of freedom is used, namely α_T [7, 44, 88, 225]. Then, some logarithmic formulations have been proposed where the threshold value and the slope of the function are degrees of freedom [7, 44, 225]. Finally a more recent formulation for elastomers materials has proposed three degrees of freedom [262].

Following Refs. [7, 44] we used two fatigue degradation functions, starting with a one parameter asymptotic degradation function, only driven by its threshold α_T:

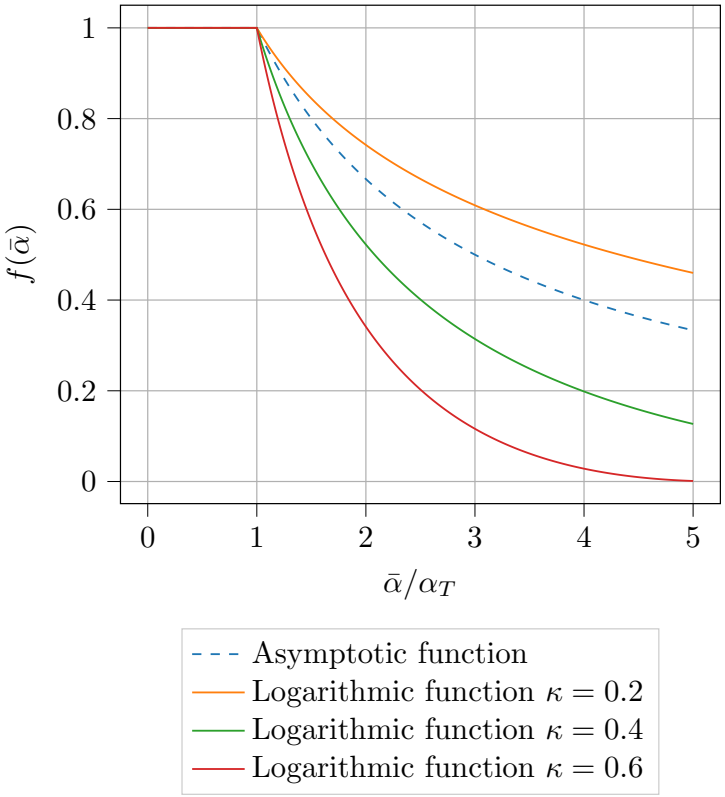

Figure 2.8: Visualization of the fatigue degradation functions used in this work.

$$f(\bar{\alpha}) = \begin{cases} 1 & \text{if } \bar{\alpha} < \alpha_T \ , \\ \left(\frac{2\alpha_T}{\bar{\alpha}+\alpha_T}\right)^2 & \text{if } \bar{\alpha} > \alpha_T . \end{cases} \tag{2.32}$$

Then, a second degradation function, also introduced in Ref. [7, 44], was investigated as it is driven by two parameters, α_T and κ (enabling a practical fit in a Paris Law framework, see Chapter 4), a logarithmic degradation function.

$$f(\bar{\alpha}) = \begin{cases} 1 & \text{if } \bar{\alpha} < \alpha_T \ , \\ \left(1 - \kappa \log(\frac{\bar{\alpha}}{\alpha_T})\right)^2 & \text{if } \alpha_T < \bar{\alpha} < \alpha_T 10^{1/\kappa} \ , \\ 0 & \text{if } \bar{\alpha} > \alpha_T 10^{1/\kappa} . \end{cases} \tag{2.33}$$

They are illustrated in Fig. 2.8. Note that the asymptotic degradation function never reaches 0, while the logarithmic degradation functions reaches zero for $\bar{\alpha} > \alpha_T 10^{1/\kappa}$.

2.1.3 Other questions

2.1.3.1 Pre-existing cracks

In the phase-field model, the definition of the crack is very ambiguous. The phase-field parameter is representative of a regularization of the sharp crack geometry, as well as being interpreted as a scalar damage indicator, with a damage mechanics vision. However, in the fracture mechanic community, it is used to initialize cracks as free boundaries in the finite element mesh, which can lead to multiple crack representations in the same domain. This issue usually arises because of the need to initialize cracks in the simulated geometries. Indeed, most studied fracture benchmark in the literature are pre-cracked (considering the need for an initial crack in LEFM), which means that this initial defect must be modeled.

This topic is scarcely discussed in the phase-field literature, even though most authors need to set initial cracks in their model. However, in Klinsmann et al. [128], this issue was discussed further, and a novel initialization strategy was proposed. Previously, this issue was also mentioned by Borden et al. [33].

The author first recalls the different usual initialization approaches, which were illustrated in Fig. 2.9. First, he mentioned the *mesh-induced* initialization, which is largely based on discrete representation of cracks, where the object is modeled by following the crack lips with the used mesh, and defining those lips as free-boundaries of the mesh. For instance, this can be done by representing the crack by a line of node, which are then doubled to enable the movement of those nodes with respect to each other: effectively allowing an opening of the crack when the structure is loaded. This approach hence takes a strict discrete representation of the crack as considered in LEFM, or with the phase-field model for $l_c \to 0$. However, it can be difficult to setup for complex initial crack patterns. Furthermore, it leads to multiple crack representations in the same model.

An alternative approach could be labeled as a *phase-field induced* initialization, where the initial crack is described with the damage field. The idea is usually to enforce $\hat{d} = 1$ on nodes following the crack geometry, and solve the damage problem to find the resulting damage topology which approximates the discrete crack geometry. Note that the specific application of this approach depends on the treatment of irreversibility that one chooses. Indeed, if a straightforward bound constrained optimization method is used, then an initial definition $\hat{d} = 1$ on the crack nodes can be used. However using the history field approach, one can expect that the phase-field would decrease to 0 at each new step computation considering that initially $H = 0$ everywhere. In this case, the enforcement $\hat{d} = 1$ on the initial crack nodes must be kept at each step of the simulation (which increases computing

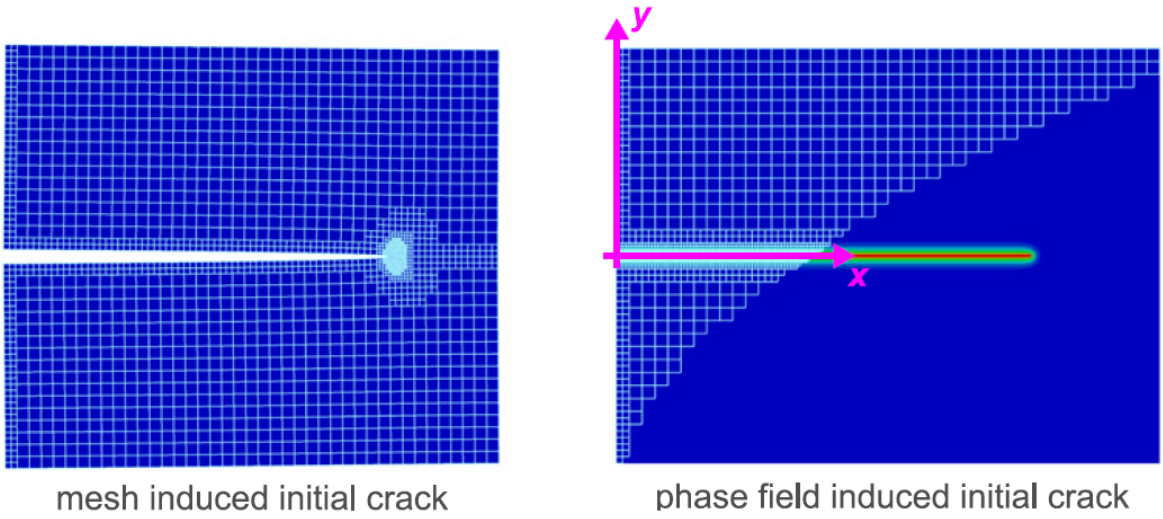

Figure 2.9: Crack initialization with the phase-field model, from Ref. [128].

time). Note that, as for the mesh-induced strategy, this kind of approach can be complex to setup for complicated crack geometry, as the mesh must also be constructed around these nodes which define the geometry of the crack.

With a history field approach for irreversibility, it is in fact strange to think about the initialization of H. It is representative of the "history" of the sample. However for pre-cracked samples, this history was not simulated, and so it is usually initialized at $H = 0$, even if it is not representative of the real "history" of the sample. It is in this context that the authors in Refs. [33, 128] have proposed another approach to consider an initial crack: the *history field induced* formulation (also considered as a phase-field induced in the cited work, since it corresponds to a diffuse description of the initial crack). The idea is to set an initial H that leads to the creation of a crack in the first steps of the simulation. Since irreversibility is driven by this field, the resulting crack will never vanish. This yields a very flexible method since there is no need to build the mesh around the crack geometry, or to enforce some boundary conditions during propagation.

The only remaining issue is to find an expression of H_0 that is relevant to recover a specific damage topology, for instance, the one recovered after the application of Dirichlet conditions on the crack nodes. Or, seeking an expression of H_0 that resembles the expression that would have resulted from the initiation of this crack, hence effectively modeling the pre-cracking of the sample with this field. In order to model the localization of the history field that would have happened if the initial crack was simulated rather than created, Klinsmann et al. [128] put forward an exponential function, similar to the

analytical expression of the 1D crack by Miehe et al. [165]. Contrary to this qualitative assessment of the initial history field, Borden et al. [33] put forward an expression derived from the 1D homogeneous examples. Both of these history field initiation methods have led to a very accurate recovery of the phase-field induced results, validating this approach.

Note that a similar issue of unknown history of the pre-cracked samples exists in fatigue. Indeed, $\bar{\alpha}$, representative of the fatigue history of the sample, is also usually initialized at $\bar{\alpha} = 0$, even with the presence of initial cracks. In a similar manner, we could imagine considering an initial value of $\bar{\alpha}$ to represent the energy accumulation of the pre-cracking process, and hence degrade G_c in the domain of the initial crack.

In this work, most pre-existing cracks were initialized using the mesh-induced method. For one numerical sample (see Section. 3.4.3), we instead enforced Dirichlet conditions $\hat{d} = 1$ on the relevant nodes, at each computed propagation steps. Using a mesh or phase-field induced initial crack has a significant influence on the computed mechanical response, depending on the value of l_c. These effects were considered out of the scope of this work, but note that initial testing seemed to show that a phase-field induced formulation usually displayed a lower critical strength compared to mesh induced initialization. Furthermore, we registered a less abrupt transition between the softening regime and the unstable regime for brittle crack propagation cases, with the phase-field induced formulation.

2.1.3.2 Discussions on l_c

As mentioned in Section 1.3, a purely local formulation of damage models leads to mesh dependent results. These issues led to the introduction of non-local terms, through a gradient term, or the influence of the neighborhood of each point [196], which always requires the introduction of an internal length. Another example is the Thick Level Set approach [26, 169], where the level sets act as markers of the damaged zone, within which the evolution of damage is defined on a specific width based on an internal length. In this sense, the internal length acts as a regularization parameter of purely local damage models.

In phase-field modeling, the characteristic length l_c fulfills a similar role: it was introduced to regularize the sharp crack free-energy potential formulation. This regularization is furthermore justified by the fact that for $l_c \to 0$, the regularized formulation approaches the sharp-crack formulation: Γ convergence. Therefore, the phase-field formulation can be seen as a regularized Griffith criterion, which means that l_c should always be chosen as small as possible in order to recover sharp crack results.

However, other authors argue for a different interpretation of this length: it can be seen as a material parameter. With this vision authors argue for the fact that it is representative of the internal length of the material [199]. Several works have established a relationship between the critical stress and the characteristic length, *e.g.,* [33, 241], and used these relationships to fit l_c and reproduce experimental observations, *e.g.,* [181, 183, 241].

Furthermore, these applications have permitted to show that the introduction of the internal length enabled a better reproduction of some experimental effects. For instance, consider the size effect highlighted by Bažant [21], where the critical load is dependent on the crack length. The Griffith criterion predicts an infinite critical load when the crack length approaches 0, not consistent with experimental observations. The phase-field model on the other hand, regularizes this infinite prediction, with the stabilization around a given σ_{crit} when the initial length of the crack approaches 0, which is in line with experimental observations [171, 241]. In this sense, the introduction of the characteristic length enriches the Griffith criterion which means that l_c is not only a regularization parameter, and the phase-field model is not only a regularized formulation which has to recover LEFM results: the model is a richer formulation to take fracture into account, where l_c is a material parameter. In the end, we could argue for the fact that a diffuse representation of the crack is more realistic than a discrete one, considering that damage operates in a process zone around the crack.

Finally, note that the choice of l_c also drives the computational cost of the simulation, considering the need for a very fine h/l_c in order to guarantee the spatial convergence of the solution, in the zone were the phase-field undergoes steep variations (h being the characteristic size of an element of the finite element mesh).

2.1.3.3 Solver for the non linear coupled problem

In order to solve the phase-field coupled problem, multiple solver types have been explored in the literature for the case of brittle phase-field fracture and its extensions. Two main approaches are considered: monolithic or staggered. A monolithic approach considers a strong coupling between damage and displacement, thus solving for $\boldsymbol{u}$ and d simultaneously. A staggered approach, on the other hand, uncouples both unknown fields and solves separately for each component while keeping the other constant.

In the case of brittle phase-field models, a monolithic approach was rarely adopted in the literature. This preference for a staggered resolution scheme stems from the non convexity of the brittle energy functional (2.6) with respect to ($\boldsymbol{u}$,d). This non-convexity means that

iterative solvers may have difficulty converging toward a single coupled solution. Specifically the usually adopted Newton-Raphson process can diverge, as noted by Gerasimov and De Lorenzis [60, 82]. Nevertheless, multiple authors have put forward solutions to this monolithic limitation, such as arc length method [159, 230], or line search processes [82].

Conversely to the strongly coupled formulation, the energy functional is convex with respect to $\boldsymbol{u}$ and d separately. Consequently, staggered approaches are more robust, but yield a slower convergence rate. Those solvers are usually variations of the alternate minimization scheme of Bourdin's work [38], where a mechanical, and damage problem are solved successively. Such a process can be seen as the sequential minimization of two sub-problems: first the minimization of Π_{int} with respect to $\boldsymbol{u}$ at a constant d, then the minimization of Π_{int} with respect to d at a constant $\boldsymbol{u}$.

At each time-step, the sub-problems are solved until a global convergence criterion is reached. This fixed point iterative search can be very slow, especially in the case of unstable crack propagation because the solution changes drastically across the domain. Hence, even though staggered approach are considered robust and efficient, they can also become untractable because of convergence issues.

Other authors [166, 172] employ a different staggered strategy: only one iteration of the staggered search is computed at each time step. Hence, global convergence is not verified for each computed step. This yields a very robust and efficient method, whose results are however very dependent upon the prescribed time-step. Note that adaptive time-step approaches have been put forward based on the enforcement of a maximum energy increment per computed time-step, as is for example implemented in Ref. [171], or a maximum damage increment in Ref. [129]. In this work, this variant of the staggered alternate minimization scheme is called the *explicit staggered scheme*, or one-pass scheme. Conversely, the strategy where global convergence is checked at each computed step is called the implicit staggered scheme. Depending on the fracture case that is being modeled, it is very hard to know whether the implicit scheme or the explicit scheme is best suited in terms of efficiency. Indeed, the former yields precise results for a small number of time steps but a large number of iterations, while the latter yields precise results for a large number of single iteration time-steps.

The specific implementation of a staggered scheme can be very flexible and allows modifications to accelerate convergence rates and reduce computing time. For instance, we can cite Kristensen et al. [129], where a BFGS approach was used to approximate a staggered tangent operator. In Lu et al. [154] multiple implicit staggered schemes were compared,

along with ideas for modified Newton schemes and convergence acceleration tools. In Wu [256], a path following method was put forward to accelerate convergence rate. In Farrell and Maurini [71], the standard alternate minimization approach is accelerated by adding an over-relaxation step in the minimizing process. Furthermore, the authors put forward a composite formulation, using an over-relaxed alternate minimization process that guides the solution robustly "within the basin of convergence of a Newton-type method", where applying a monolithic approach is efficient.

Considering the plurality of resolution schemes available in the literature, a special attention was given to the choice of a relevant solver in a fatigue framework in Section 3.1.

2.2 Energy spectral decomposition: A change of basis approach

After setting a fatigue phase-field model, we investigated the implementation of the spectral energy decomposition described in 2.1.2.3. We specifically worked on the robustness and efficiency of the approach implemented in Ref. [173], inspired by Ref. [26]. Considering the fact that singular values can appear in the computation of the terms linked with usual spectral decomposition methods, a novel framework was put forward and published in the work of Molnár et al. [176].
As introduced previously, unilateral effects are added by separating the mechanical energy term. Following Ref. [173], inspired by Bernard et al. [26], we write the elastic energy density $\psi(\boldsymbol{u}, d)$ as the sum of the following active and passive component:

$$\psi_0^+(\boldsymbol{u}) = \frac{\lambda}{2}\left(\langle tr(\boldsymbol{\varepsilon})\rangle^+\right)^2 + \mu\sum_{k=1}^{3}\left(\langle\varepsilon_k\rangle^+\right)^2, \tag{2.34}$$

$$\psi_0^-(\boldsymbol{u}) = \frac{\lambda}{2}\left(\langle tr(\boldsymbol{\varepsilon})\rangle^-\right)^2 + \mu\sum_{k=1}^{3}\left(\langle\varepsilon_k\rangle^-\right)^2, \tag{2.35}$$

with λ and μ being Lamé constants and the components ε_k being the principal terms of the strain tensor. In this section we write $\hat{\boldsymbol{\varepsilon}}$ for the strain tensor and $\hat{\boldsymbol{\sigma}}$ for the stress tensor expressed in their principal basis. To select the positive and negative parts of the strain tensor components, expressed respectively as $\langle\cdot\rangle^+$ and $\langle\cdot\rangle^-$, we follow Bernard et al. [26] by introducing the following switch variables:

$$\begin{cases} \beta_k = 1 \text{ if } \varepsilon_k > 0, \\ \beta_k = 0 \text{ otherwise.} \end{cases} \tag{2.36}$$

$$\begin{cases} \beta = 1 \text{ if } tr(\boldsymbol{\varepsilon}) > 0, \\ \beta = 0 \text{ otherwise.} \end{cases} \tag{2.37}$$

The expression of the energy density in a general 3D form becomes:

$$\psi(\boldsymbol{u}, d) = \frac{\lambda}{2}\cdot g(d\cdot\beta).tr(\boldsymbol{\varepsilon})^2 + \sum_{k=1}^{3}\left(\mu\cdot g(d\cdot\beta_k).\varepsilon_k^2\right). \tag{2.38}$$

From this expression we can deduce the associated stress tensor $\boldsymbol{\sigma}$, and damaged stiffness

tensor $\boldsymbol{C}$ by differentiating $\psi(\boldsymbol{u}, d)$ with respect to the components of the strain tensor:

$$\boldsymbol{\sigma} = \frac{\partial \psi}{\partial \boldsymbol{\varepsilon}} \text{ and } \boldsymbol{C} = \frac{\partial \boldsymbol{\sigma}}{\partial \boldsymbol{\varepsilon}} = \frac{\partial^2 \psi}{\partial \boldsymbol{\varepsilon}^2}. \tag{2.39}$$

Considering that the active and passive terms (2.34), (2.35) are only expressed with respect to the principal terms ε_k, Bernard et al. [26] applied the chain rule to the derivatives (2.39) such that for the stress tensor we write:

$$\boldsymbol{\sigma} = \frac{\partial \psi}{\partial \boldsymbol{\varepsilon}} = \frac{\partial \psi}{\partial \hat{\boldsymbol{\varepsilon}}} \frac{\partial \hat{\boldsymbol{\varepsilon}}}{\partial \boldsymbol{\varepsilon}}. \tag{2.40}$$

Additionally they introduced a principal stiffness term, $\hat{\boldsymbol{L}}$ which links principal stresses and principal strains as $\hat{\boldsymbol{\sigma}} = \hat{\boldsymbol{L}}\hat{\boldsymbol{\varepsilon}}$. It is expressed as:

$$\hat{\boldsymbol{L}} = \frac{\partial^2 \psi}{\partial \hat{\boldsymbol{\varepsilon}}^2}, \tag{2.41}$$

which, following eq. (2.38), can be written in a 3D context in matrix form using Voigt's notation as:

$$\hat{\boldsymbol{L}} = \begin{bmatrix} \lambda \cdot g(d \cdot \beta) + 2\mu \cdot g(d \cdot \beta_1) & \lambda \cdot g(d \cdot \beta) & \lambda \cdot g(d \cdot \beta) \\ \lambda \cdot g(d \cdot \beta) & \lambda \cdot g(d \cdot \beta) + 2\mu \cdot g(d \cdot \beta_2) & \lambda \cdot g(d \cdot \beta) \\ \lambda \cdot g(d \cdot \beta) & \lambda \cdot g(d \cdot \beta) & \lambda \cdot g(d \cdot \beta) + 2\mu \cdot g(d \cdot \beta_3) \end{bmatrix}. \tag{2.42}$$

Expression (2.40) can then be rewritten as:

$$\boldsymbol{\sigma} = \hat{\boldsymbol{\varepsilon}}^T \hat{\boldsymbol{L}} \frac{\partial \hat{\boldsymbol{\varepsilon}}}{\partial \boldsymbol{\varepsilon}}, \tag{2.43}$$

and the stiffness tensor $\boldsymbol{C}$ can be written as:

$$\boldsymbol{C} = \left(\frac{\partial \hat{\boldsymbol{\varepsilon}}}{\partial \boldsymbol{\varepsilon}} \right)^T \hat{\boldsymbol{L}} \frac{\partial \hat{\boldsymbol{\varepsilon}}}{\partial \boldsymbol{\varepsilon}} + \hat{\boldsymbol{\epsilon}} \hat{\boldsymbol{L}} \frac{\partial^2 \hat{\boldsymbol{\varepsilon}}}{\partial \boldsymbol{\varepsilon}^2}. \tag{2.44}$$

In Refs. [26, 173], the first and second derivative of the principal terms are derived through the invariants of the strain tensor and the analytical expression of the eigenvalues. As reported by the mentioned authors, the expression of those derivative terms can become singular in a wide variety of cases (such as uni-axial or equibiaxial loadings). This comes from the fact that, in 3D, if two eigenvalues out of three are equal, the denominator of some derivative term's expression becomes 0. In Molnár et al. [173], small perturbation terms are added to the denominators to guarantee the robustness of the method. Additionally in Ref. [175], the same author computed the terms numerically with a finite difference

approach to avoid these issues.

Inspired by those works we put forward a novel approach to compute $\boldsymbol{C}$ that relies on the terms introduced in the formulation. The interesting idea is that since the energy density is only expressed in terms of the eigenvalues of the strain tensor, we can write a principal stiffness term $\hat{\boldsymbol{L}}$ that links the principal basis terms. From this tensor we can find the complete principal stiffness term $\hat{\boldsymbol{C}}$, that is representative of the stiffness tensor written in the principal basis, and rotate it into the working basis, using standard change of basis operators.

In the principal basis we trivially express the stiffness tensor components related to the three principal terms: it is the second derivative of $\psi(\boldsymbol{u}, d)$ with respect to those terms, *i.e.*, $\hat{\boldsymbol{L}}$. However, it is harder to interpret the meaning of the shear components of the principal stiffness tensor, since there are no shear strains in the principal basis. Consequently, these terms were deduced from numerical experiments in Ref. [176] yielding a diagonal shear matrix that is expressed in a 3D Voigt's notation as:

$$\hat{\boldsymbol{S}} = \begin{bmatrix} \mu \cdot \frac{|\varepsilon_1| \cdot g(d \cdot \beta_1) + |\varepsilon_2| \cdot g(d \cdot \beta_2)}{|\varepsilon_1| + |\varepsilon_2|} & 0 & 0 \\ 0 & \mu \cdot \frac{|\varepsilon_1| \cdot g(d \cdot \beta_1) + |\varepsilon_3| \cdot g(d \cdot \beta_3)}{|\varepsilon_1| + |\varepsilon_3|} & 0 \\ 0 & 0 & \mu \cdot \frac{|\varepsilon_2| \cdot g(d \cdot \beta_2) + |\varepsilon_3| \cdot g(d \cdot \beta_3)}{|\varepsilon_2| + |\varepsilon_3|} \end{bmatrix}. \tag{2.45}$$

The authors showed that using these shear terms yield results that are identical to the previously introduced formulation. The principal stiffness tensor in 3D Voigt's notation can be written as:

$$\hat{\boldsymbol{C}} = \begin{bmatrix} \hat{\boldsymbol{L}} & \boldsymbol{0} \\ \boldsymbol{0} & \hat{\boldsymbol{S}} \end{bmatrix}. \tag{2.46}$$

After obtaining this principal stiffness matrix, the last step is to find its components in the working basis using change of basis operators. Considering the strain and stress tensor represented as a 3 by 3 matrix, in the working basis $\boldsymbol{\varepsilon}_M$, $\boldsymbol{\sigma}_M$, and in the principal basis, $\hat{\boldsymbol{\varepsilon}}_M$, $\hat{\boldsymbol{\sigma}}_M$, we can write:

$$\boldsymbol{\varepsilon}_M = \boldsymbol{Q} \hat{\boldsymbol{\varepsilon}}_M \boldsymbol{Q}^T \text{ and } \boldsymbol{\sigma}_M = \boldsymbol{Q} \hat{\boldsymbol{\sigma}}_M \boldsymbol{Q}^T. \tag{2.47}$$

with $\boldsymbol{Q}$, a rotation matrix defined by the eigenvectors of the strain tensor. However, in this numerical implementation, strain and stress tensor are not represented by 3 by 3 matrices but by a vector of 6 components: Voigt's notation. For instance, in Cast3M,

in two dimensions, the strain tensor in Voigt's notation is written as: $\boldsymbol{\varepsilon} = (\varepsilon_{11}, \varepsilon_{22}, 2\varepsilon_{12})$ Consequently, two new rotation matrices $\boldsymbol{T}_\varepsilon$, and $\boldsymbol{T}_\sigma$ are introduced to enable such basis transformation with Voigt's notation so that for $\hat{\boldsymbol{\varepsilon}}$, $\boldsymbol{\varepsilon}$, and $\hat{\boldsymbol{\sigma}}$, $\boldsymbol{\sigma}$ in Voigt's notation we write the equivalent of eq. (2.47):

$$\hat{\boldsymbol{\varepsilon}} = \boldsymbol{T}_\varepsilon \, \boldsymbol{\varepsilon} \text{ and } \hat{\boldsymbol{\sigma}} = \boldsymbol{T}_\sigma \, \boldsymbol{\sigma}. \tag{2.48}$$

This formulation induces the following expression for $\boldsymbol{T}_{\boldsymbol{\varepsilon}}$, from the components of the 3 by 3 rotation matrix $\boldsymbol{Q}$:

$$\boldsymbol{T}_\varepsilon = \begin{bmatrix} Q_{11}^2 & Q_{21}^2 & Q_{31}^2 & Q_{21}Q_{11} & Q_{31}Q_{11} & Q_{21}Q_{31} \\ Q_{12}^2 & Q_{22}^2 & Q_{32}^2 & Q_{22}Q_{12} & Q_{32}Q_{12} & Q_{22}Q_{32} \\ Q_{13}^2 & Q_{23}^2 & Q_{33}^2 & Q_{23}Q_{13} & Q_{33}Q_{13} & Q_{23}Q_{33} \\ 2Q_{12}Q_{11} & 2Q_{22}Q_{21} & 2Q_{32}Q_{31} & Q_{22}Q_{11}+Q_{12}Q_{21} & Q_{31}Q_{12}+Q_{11}Q_{32} & Q_{22}Q_{31}+Q_{32}Q_{21} \\ 2Q_{13}Q_{11} & 2Q_{23}Q_{21} & 2Q_{33}Q_{31} & Q_{11}Q_{23}+Q_{21}Q_{13} & Q_{31}Q_{13}+Q_{11}Q_{33} & Q_{23}Q_{31}+Q_{33}Q_{21} \\ 2Q_{13}Q_{12} & 2Q_{23}Q_{22} & 2Q_{33}Q_{32} & Q_{22}Q_{13}+Q_{23}Q_{12} & Q_{13}Q_{32}+Q_{12}Q_{33} & Q_{23}Q_{32}+Q_{33}Q_{22} \end{bmatrix}, \tag{2.49}$$

and the following expression for $\boldsymbol{T}_\sigma$:

$$\boldsymbol{T}_\sigma = \begin{bmatrix} Q_{11}^2 & Q_{21}^2 & Q_{31}^2 & 2Q_{21}Q_{11} & 2Q_{31}Q_{11} & 2Q_{21}Q_{31} \\ Q_{12}^2 & Q_{22}^2 & Q_{32}^2 & 2Q_{22}Q_{12} & 2Q_{32}Q_{12} & 2Q_{22}Q_{32} \\ Q_{13}^2 & Q_{23}^2 & Q_{33}^2 & 2Q_{23}Q_{13} & 2Q_{33}Q_{13} & 2Q_{23}Q_{33} \\ Q_{12}Q_{11} & Q_{22}Q_{21} & Q_{32}Q_{31} & Q_{22}Q_{11}+Q_{12}Q_{21} & Q_{31}Q_{12}+Q_{11}Q_{32} & Q_{22}Q_{31}+Q_{32}Q_{21} \\ Q_{13}Q_{11} & Q_{23}Q_{21} & Q_{33}Q_{31} & Q_{11}Q_{23}+Q_{21}Q_{13} & Q_{31}Q_{13}+Q_{11}Q_{33} & Q_{23}Q_{31}+Q_{33}Q_{21} \\ Q_{13}Q_{12} & Q_{23}Q_{22} & Q_{33}Q_{32} & Q_{22}Q_{13}+Q_{23}Q_{12} & Q_{13}Q_{32}+Q_{12}Q_{33} & Q_{23}Q_{32}+Q_{33}Q_{22} \end{bmatrix}. \tag{2.50}$$

Note that the transformation matrices associated respectively with the strain and stress tensors are not equal because of the coefficients associated with shear strains in Voigt's notation.

From eq. (2.48), we can find the expression of the stiffness tensor in the working basis, as a function of the stiffness tensor expressed in the principal basis $\hat{\boldsymbol{C}}$ and the introduced transformation matrices:

$$\begin{aligned} \hat{\boldsymbol{\sigma}} &= \hat{\boldsymbol{C}}\hat{\boldsymbol{\varepsilon}}, \\ \rightarrow \boldsymbol{T}_\sigma \, \boldsymbol{\sigma} &= \hat{\boldsymbol{C}}\boldsymbol{T}_\varepsilon \, \boldsymbol{\varepsilon}, \\ \rightarrow \boldsymbol{\sigma} &= \boldsymbol{T}_\sigma^{-1}\hat{\boldsymbol{C}}\boldsymbol{T}_\varepsilon \, \boldsymbol{\varepsilon}, \end{aligned} \tag{2.51}$$

yielding a straightforward expression for the change of basis of the principal stiffness matrix:

$$\boldsymbol{C} = \boldsymbol{T}_\sigma^{-1}\hat{\boldsymbol{C}}\boldsymbol{T}_\varepsilon. \tag{2.52}$$

This results in a straightforward implementation of the method, where the introduced change of basis operators are used after computing the eigenvalues/eigenvectors associated

with the strain tensor. As mentioned in Ref. [176], the method is robust, accurate, and it yields faster computations than the original approach.

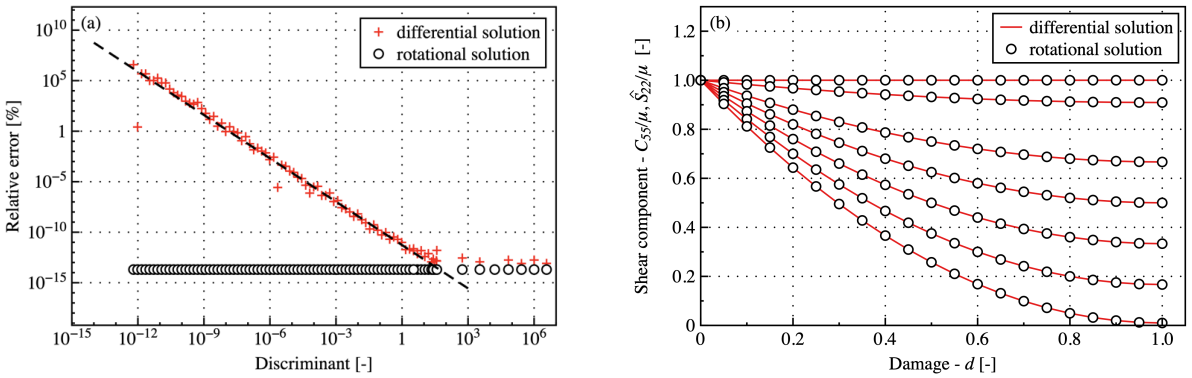

(a) **(b)**

Figure 2.10: (a) Maximum relative error between the decomposed and theoretical stiffness matrices (d= 0). The error is shown as a function of the discriminant of the third-order polynomial equation to calculate principal strains [173]. (b) Normalized shear component of the stiffness matrix determined using the differential and the rotational techniques". Figure and caption by Molnár et al. [176].

As was illustrated in Miehe et al. [166] and Ambati et al. [10], we showed the effect of the decomposition by applying a specific alternate loading (Fig. 2.11a) on the homogeneous sample (see Ref. [172] and Fig. 2.12). The sample was successively loaded in traction and compression. We showed the resulting stress-strain response of the homogeneous sample in Fig. 2.11b.

With an isotropic formulation, we observe that the response is degraded in traction. Then after the unloading phase, a damaged stiffness is maintained in compression (the slope in unloading is identical as the slope in compression) until the response is degraded further.

Conversely, with the spectral decomposition, the behavior is very different. After the initial traction and unloading phase, the undamaged stiffness is recovered in compression. Indeed, we can see that the slope in compression is the same as the initially elastic slope. This is representative of clack closure effects, and non-interpenetration of the crack lips. Then, we notice that in compression, the response is never degraded, regardless of the used loading, as crack propagation is driven only by positive principal strains. This is representative of the experimental observation that degradation is not identical for traction or compression in most studied materials. Moreover, this degradation evolution is usually much slower in compression.

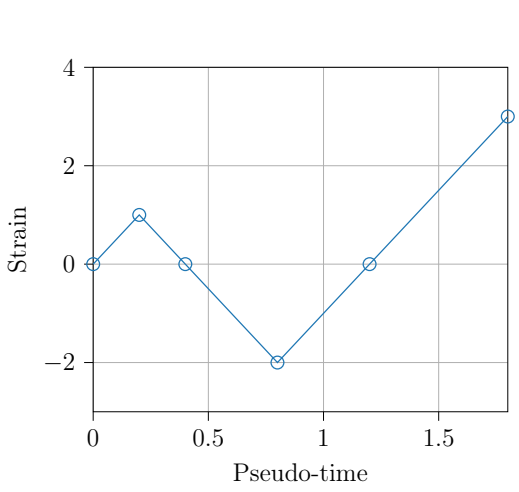

(a) Prescribed strain.

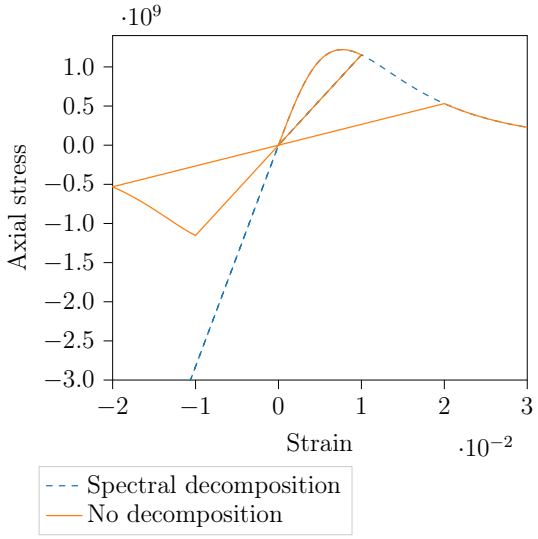

(b) Stress-strain response.

Figure 2.11: Influence of the decomposition on the homogeneous response.

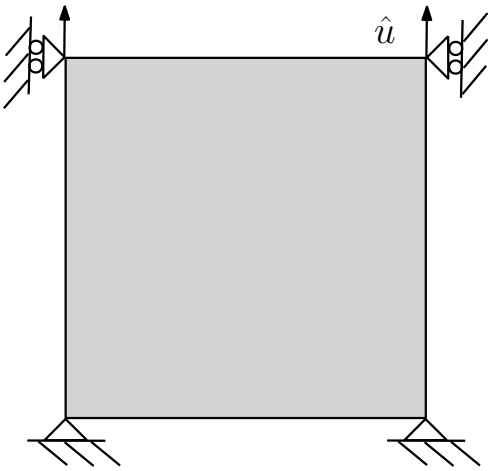

Figure 2.12: Geometry and boundary conditions of the homogeneous case.

2.3 Equations and implementation

Following the expression of all the components of the chosen fatigue phase-field model, we detail the formulation of the resulting model's governing equations. Furthermore, those formulations are rewritten in the framework of the finite element method, and the staggered phase-field fatigue solver is thus explicited.

2.3.1 Governing equations

The phase-field fatigue free energy functional (2.24), can be rewritten by considering that:

$$\dot{\gamma}(d, \nabla d) = \frac{\partial \gamma}{\partial d}\dot{d} + \frac{\partial \gamma}{\nabla d}\nabla \dot{d}, \tag{2.53}$$

yielding the following expression:

$$\begin{aligned}\Pi_{int}(\boldsymbol{u}, d) = &\int_\Omega (1-d)^2 \cdot \psi_0^+(\boldsymbol{u}) + \psi_0^-(\boldsymbol{u})\, \mathrm{d}V \\ &+ \int_\Omega \int_0^t f\left(\bar{\alpha}(\tau)\right) G_c \cdot \left(\frac{1}{l_c} d\dot{d} + l_c \nabla d \cdot \nabla \dot{d}\right) \mathrm{d}\tau \ \mathrm{d}V.\end{aligned} \tag{2.54}$$

Following Carrara et al.'s work [44], we switch to a power formulation to avoid the time dependency of this formulation. Using similar chain rule arguments as in eq. (2.53), the internal power reads as:

$$\begin{aligned}\dot{\Pi}_{int}(\boldsymbol{u}, d) = &\int_\Omega \left((1-d)^2 \cdot \frac{\partial \psi_0^+(\boldsymbol{u})}{\partial \boldsymbol{\varepsilon}} + \frac{\partial \psi_0^-(\boldsymbol{u})}{\partial \boldsymbol{\varepsilon}}\right) \dot{\boldsymbol{\varepsilon}} + \frac{\partial (1-d)^2}{\partial d} \cdot \psi_0^+(\boldsymbol{u}) \cdot \dot{d} \\ &+ f\left(\bar{\alpha}\right) G_c \cdot \left(\frac{1}{l_c} d\dot{d} + l_c \nabla d \cdot \nabla \dot{d}\right)\ \mathrm{d}V.\end{aligned} \tag{2.55}$$

Here, we introduced the strain tensor $\boldsymbol{\varepsilon}$. Note that small perturbations are assumed, such that displacements are small and the strain tensor is linear: $\boldsymbol{\varepsilon} = \frac{1}{2}\left(\nabla \boldsymbol{u} + \nabla \boldsymbol{u}^T\right)$. We can further introduce the damaged Cauchy stress tensor as:

$$\boldsymbol{\sigma}(\boldsymbol{u}, d) = (1-d)^2 \cdot \frac{\partial \psi_0^+(\boldsymbol{u})}{\partial \boldsymbol{\varepsilon}} + \frac{\partial \psi_0^-(\boldsymbol{u})}{\partial \boldsymbol{\varepsilon}}. \tag{2.56}$$

Furthermore, the external power can be written as:

$$\Pi_{ext}(\boldsymbol{u}) = \int_\Omega \boldsymbol{b} \cdot \dot{\boldsymbol{u}}\, \mathrm{d}V + \int_{\partial \Omega_t} \boldsymbol{t} \cdot \dot{\boldsymbol{u}}\, \mathrm{d}S\ . \tag{2.57}$$

As stated in Section 2.1.1, in a quasi-static context, the solution of the fracture problem is finding the admissible couple $(\boldsymbol{u}, d)$ that minimizes the Lagrangian constituted by

the internal and external energy functionals. Using a power formulation, it is equivalent to the principle of virtual power, that for any admissible couple $(\dot{\boldsymbol{u}}, \dot{d})$, we have the following balance:

$$\dot{\Pi}_{int}(\boldsymbol{u}, d) = \dot{\Pi}_{ext}(\boldsymbol{u}). \tag{2.58}$$

We perform integral by parts in order to eliminate the highest derivative order terms. Note a particular expression of a triple term integral by part due to the product with space varying $f(\bar{\alpha})$:

$$\int_\Omega \boldsymbol{\sigma} : \dot{\boldsymbol{\varepsilon}} \, \mathrm{d}V = \int_\Omega \mathrm{div}(\boldsymbol{\sigma} \cdot \dot{\boldsymbol{u}}) \, \mathrm{d}V - \int_\Omega \mathrm{div}(\boldsymbol{\sigma}) \cdot \dot{\boldsymbol{u}} \, \mathrm{d}V, \tag{2.59}$$

$$\begin{aligned} \int_\Omega f(\bar{\alpha}) \cdot \nabla d \cdot \nabla \dot{d} \, \mathrm{d}V = &\int_\Omega \mathrm{div}(f(\bar{\alpha}) \cdot \nabla d \cdot \dot{d}) \, \mathrm{d}V - \int_\Omega f(\bar{\alpha}) \cdot \Delta d \cdot \dot{d} \, \mathrm{d}V \\ &- \int_\Omega \nabla f(\bar{\alpha}) \cdot \nabla d \cdot \dot{d} \, \mathrm{d}V. \end{aligned} \tag{2.60}$$

And from Ostrogradsky's theorem, we have:

$$\int_\Omega \mathrm{div}(\boldsymbol{\sigma} \cdot \dot{\boldsymbol{u}}) \, \mathrm{d}V = \int_{\partial\Omega} \boldsymbol{\sigma} \cdot \boldsymbol{n} \cdot \dot{\boldsymbol{u}} \, \mathrm{d}S, \tag{2.61}$$

$$\int_\Omega \mathrm{div}(f(\bar{\alpha}) \cdot \nabla d \cdot \dot{d}) \, \mathrm{d}V = \int_{\partial\Omega} f(\bar{\alpha}) \cdot \nabla d \cdot \boldsymbol{n} \cdot \dot{d} \, \mathrm{d}S. \tag{2.62}$$

with $\boldsymbol{n}$ is the outward normal vector on the boundaries. We can rewrite the balance of power (2.58) as:

$$\begin{aligned} 0 = &- \int_\Omega (\mathrm{div}(\boldsymbol{\sigma}) + \boldsymbol{b}) \cdot \dot{\boldsymbol{u}} + \int_{\partial\Omega_t} (\boldsymbol{\sigma}.\boldsymbol{n} - \boldsymbol{t}) \dot{\boldsymbol{u}} \, \mathrm{d}S + \int_{\partial\Omega} (\nabla d.\boldsymbol{n}) \cdot \dot{d} \, \mathrm{d}S \\ &+ \int_\Omega \left[2 \cdot (d-1) \cdot \psi_0^+ + f(\bar{\alpha}) \cdot G_c \left(\frac{1}{l_c} d - l_c \Delta d \right) - G_c l_c \nabla f(\bar{\alpha}) \cdot \nabla d \right] \cdot \dot{d} \, \mathrm{d}V. \end{aligned} \tag{2.63}$$

This balance yields the following strong form equation system for the phase-field fatigue coupled problem:

$$\mathrm{div}(\boldsymbol{\sigma}) + \boldsymbol{b} = 0 \text{ on } \Omega, \tag{2.64a}$$

$$\boldsymbol{\sigma}.\boldsymbol{n} = \boldsymbol{t} \text{ on } \partial\Omega_f, \tag{2.64b}$$

$$\boldsymbol{u} = \hat{\boldsymbol{u}} \text{ on } \delta\Omega_u, \tag{2.64c}$$

$$2.(d-1)\cdot\psi_0^+ + f(\bar{\alpha})\left[\frac{G_c}{l_c}\cdot d - G_c l_c\cdot\Delta d\right] - G_c l_c \nabla f(\bar{\alpha})\cdot\nabla d = 0 \text{ on } \Omega, \tag{2.64d}$$

$$\nabla d.\boldsymbol{n} = 0 \text{ on } \partial\Omega. \tag{2.64e}$$

Considering the chosen treatment of irreversibility (see Section 2.1.2.4), we can switch the expression of the damage problem (2.64d) as:

$$2.(d-1)\cdot H + f(\bar{\alpha})\left[\frac{G_c}{l_c}\cdot d - G_c l_c\cdot\Delta d\right] - G_c l_c \nabla f(\bar{\alpha})\cdot\nabla d = 0 \text{ on } \Omega. \tag{2.65}$$

2.3.2 Finite element framework

We first set the finite element discretization framework, in order to detail the equations linked to this staggered implementation. First, the unknown fields are approximated as vectors of discrete nodal value, using the shape functions $\mathbf{N}$ and gradient $\mathbf{B}$, associated with $\boldsymbol{u}$ and d respectively. In Voigt notation, we write:

$$\boldsymbol{u} = \mathbf{N}_u\cdot\mathbf{u} \quad , \qquad \nabla\boldsymbol{u} = \mathbf{B}_u\cdot\mathbf{u}\ , \tag{2.66}$$

$$d = \mathbf{N}_d\cdot\mathbf{d} \quad , \qquad \nabla d = \mathbf{B}_d\cdot\mathbf{d}. \tag{2.67}$$

From the set balance of power (2.63) and the history field irreversibility treatment, we can write, in a discretized framework:

$$\int_\Omega \mathbf{B}^T.\boldsymbol{\sigma}(\mathbf{u})\,\mathrm{d}V - \int_\Omega \mathbf{N}^T\mathbf{b}\,\mathrm{d}V - \int_{\partial\Omega_t}\mathbf{N}^T\mathbf{t}\,\mathrm{d}S = \mathbf{R}_u, \tag{2.68a}$$

$$\int_\Omega \left[\mathbf{N}_d^T\left(2H + f(\bar{\alpha})\cdot\frac{G_c}{l_c}\right)\mathbf{N}_d + \mathbf{B}_d^T\left(f(\bar{\alpha})\cdot G_c l_c\right)\mathbf{B}_d\right]\cdot\mathbf{d} - \mathbf{N}_d^T 2H(\boldsymbol{\varepsilon})\,\mathrm{d}V = \mathbf{R}_d, \tag{2.68b}$$

with $\mathbf{R}_u$ defined as the mechanical residual and $\mathbf{R}_d$ defined as a damage problem residual.

Considering a staggered resolution scheme, we solve this coupled system of equation

sequentially. First a mechanical sub-problem at constant damage, then a damage sub-problem for constant mechanical fields. In order to solve the mechanical sub-problem, we used a Newton-Raphson formalism because of the non-linearity introduced by the spectral decomposition of Section 2.1.2.3. Conversely, considering the modeling choices of the phase-field model that were set in this chapter, the phase-field sub problem remains linear with respect to d. Let us describe these sub-problem resolution schemes, and their respective finite element formulation:

Mechanical problem

At every step $n+1$, the iterative Newton-Raphson scheme searches for the increment of displacement $\Delta\mathbf{u}$ such that $\mathbf{u}_{n+1}$ minimizes the mechanical residual.

$$\mathbf{u}_{n+1} = \mathbf{u}_n + \Delta\mathbf{u}. \tag{2.69}$$

Numerically, we break down this increment estimation into multiple iterations i:

$$\mathbf{u}_{n+1}^{i+1} = \mathbf{u}_{n+1}^{0} + \sum \delta\mathbf{u}^i = \mathbf{u}_{n+1}^{i} + \delta\mathbf{u}^{i+1}. \tag{2.70}$$

The residual is linearized around the solution at iteration $i+1$. To approach mechanical equilibrium we want:

$$\mathbf{R}_u^{i+1} \simeq \mathbf{R}_u^i + \frac{\partial \mathbf{R}_u^i}{\partial \mathbf{u}}.\delta\mathbf{u}^{i+1} = 0. \tag{2.71}$$

Injecting the expression of the residual (2.68a), this linearization can be expressed as:

$$\left(\int_\Omega \mathbf{B}^T.\frac{\partial \boldsymbol{\sigma}}{\partial \epsilon}.\mathbf{B}\,\mathrm{d}V\right).\delta\mathbf{u}^{i+1} = -\int_\Omega \mathbf{B}^T.\boldsymbol{\sigma}(\mathbf{u})\,\mathrm{d}V + \int_\Omega \mathbf{N}^T\mathbf{b}\,\mathrm{d}V + \int_{\partial\Omega_t} \mathbf{N}^T\mathbf{t}\,\mathrm{d}S. \tag{2.72}$$

In order to simplify notations, let us rename the terms of this equation as internal forces $\mathbf{F}_{int}$, external forces $\mathbf{F}_{ext}$, and the mechanical tangent operator $\mathbf{K}^u$:

$$\mathbf{F}_{int} = \int_\Omega \mathbf{B}^T\boldsymbol{\sigma}\,\mathrm{d}V, \tag{2.73}$$

$$\mathbf{F}_{ext} = \int_\Omega \mathbf{N}^T\mathbf{b}\,\mathrm{d}V + \int_{\partial\Omega_t} \mathbf{N}^T\mathbf{t}\,\mathrm{d}S, \tag{2.74}$$

$$\mathbf{K}_u = \int_\Omega \mathbf{B}^T.\frac{\partial \boldsymbol{\sigma}}{\partial \epsilon}.\mathbf{B}\,\mathrm{d}V = \int_\Omega \mathbf{B}_u^T\mathbf{C}\mathbf{B}_u\,\mathrm{d}V, \tag{2.75}$$

where $\mathbf{C}$ corresponds to a damaged material's stiffness matrix whose computation was

detailed in Section 2.2. We can then rewrite the mechanical residual (2.68a) as the usual static formulation:

$$\mathbf{R}_u = \mathbf{F}_{int} - \mathbf{F}_{ext}, \tag{2.76a}$$

$$= \int_\Omega \mathbf{B}_u^T \boldsymbol{\sigma} \, \mathrm{d}V - \int_\Omega \mathbf{N}_u^T \mathbf{b} \, \mathrm{d}V + \int_{\partial\Omega_t} \mathbf{N}_u^T \mathbf{t} \, \mathrm{d}S, \tag{2.76b}$$

And the mechanical sub-problem (2.72) solved at iteration i can be rewritten as:

$$\mathbf{K}_u^i \delta\mathbf{u}^{i+1} = \mathbf{F}_{ext} - \mathbf{F}_{int}^i. \tag{2.77}$$

Remark 2.2 - Prescribing displacement in Cast3M
As mentioned before, this work is implemented in Cast3M. In this finite element software, prescribed displacements are enforced using the Lagrange's multiplier. Accordingly, we introduce the linear relations matrix $\mathbf{A}$ that links displacement $\mathbf{u}$ and the imposed displacement $\mathbf{u}_{imp}$, such that $\mathbf{A} \cdot \mathbf{u} = \mathbf{u}_{imp}$. Moreover, we write the Lagrange multiplier vector as $\boldsymbol{\lambda}$. Considering this approach, we can rewrite the mechanical residue as:

$$\mathbf{R}_u = \begin{cases} \mathbf{F}_{int} - \mathbf{F}_{ext} - \mathbf{A}^T.\boldsymbol{\lambda}, \\ \mathbf{A}.\mathbf{u} - \mathbf{u}_{imp}. \end{cases} \tag{2.78}$$

Similarly, taking into account the described Newton-Raphson formalism, we write the full mechanical sub-problem:

$$\mathbf{K}_u \delta\mathbf{u}^{i+1} - \mathbf{A}^T.\delta\boldsymbol{\lambda}^{i+1} = \mathbf{F}_{ext} - \mathbf{F}_{int}^i + \mathbf{A}^T.\boldsymbol{\lambda}^i, \tag{2.79a}$$

$$\mathbf{A}.\delta\mathbf{u}^{i+1} = \mathbf{u}_{imp} - \mathbf{A}.\mathbf{u}^i. \tag{2.79b}$$

or, in matrix form:

$$\begin{bmatrix} \mathbf{K}_u & -\mathbf{A}^T \\ -\mathbf{A} & 0 \end{bmatrix} \begin{bmatrix} \delta\mathbf{u}^{i+1} \\ \delta\boldsymbol{\lambda}^{i+1} \end{bmatrix} = \begin{bmatrix} \mathbf{F}_{ext} - \mathbf{F}_{int}^i + \mathbf{A}^T.\boldsymbol{\lambda}^i \\ \mathbf{A}.\mathbf{u}^i - \mathbf{u}_{imp} \end{bmatrix}. \tag{2.80}$$

Phase-field damage problem

In this weakly coupled finite element setting, the damage problem stays linear, with respect to $\mathbf{d}$, such that we can recast the damage residual (2.68b) as a linear problem. At each time step n we solve:

$$\mathbf{K}_d \cdot \mathbf{d}_n = \int_\Omega \mathbf{N}_d^T 2H \, \mathrm{d}V, \tag{2.81}$$

with a phase-field stiffness matrix at the time step n defined as:

$$\mathbf{K}_d = \int_\Omega \mathbf{N}_d^T \left(2H + \frac{G_\mathrm{F}}{l_c}\right) \mathbf{N}_d + \mathbf{B}_d^T \left(G_\mathrm{F} \cdot l_c\right) \mathbf{B}_d \, \mathrm{d}V. \tag{2.82}$$

Here, we introduced the degraded toughness, defined as:

$$G_\mathrm{F} = f(\bar{\alpha}) \cdot G_c. \tag{2.83}$$

2.3.3 Staggered algorithm for fatigue

Considering the previously described finite element framework, we can set a first approach for a phase-field fatigue solver. For each computed time-step, the mechanical sub-problem is solved at constant d. Then the obtained mechanical fields are used to compute the history field H, accumulated fatigue variable $\bar{\alpha}$, and thus determine the associated fatigue degradation function $f(\bar{\alpha})$ and degraded toughness G_F. Next follows the resolution of the damage sub-problem influenced by (H, G_F).

With an explicit staggered approach, one pass of this procedure is applied at each computed time-steps. However, with the implicit approach, a global convergence criterion is checked. The choice of this criterion remains open in the literature with approaches usually relying on the convergence of damage as in Bourdin et al. [38], or convergence of the mechanical residual or phase-field residual with respect to the updated values of damage and displacement in Helfer et al. [104].

In this work, a damage dissipation convergence criterion was used. Internal iterations are stopped when the amount of brittle dissipated energy converges *i.e.,* when the area of the crack area stabilizes in the internal loop. Indeed, in a brittle phase-field context we saw that damage energy is directly linked to the crack area in Section. 2.1. Here, in spite of the fatigue context, we use this brittle energy indicator, as it makes for a very reliable damage global quantifier. We chose to normalize the criterion by the current

value of dissipated energy $W^j(d)$, taking j for staggered internal iteration index. The convergence criterion can be written as:

$$|W(d)^{j+1} - W(d)^j| < W(d)^0 \cdot 10^{-6}. \tag{2.84}$$

Note that the "global" mechanical residual, meaning $\mathbf{R}_u^{j+1}(\mathbf{u}^{j+1}, \mathbf{d}^{j+1})$, is computed along with this convergence criterion to initialize the next step's residual. It could be used as an indicator of global convergence as well.

A visual representation of this first approach for an implicit staggered scheme was given in Algorithm. 1. Once again, we clarify that the explicit version of this algorithm, mentionned thereafter, is just a one-pass version, where the global convergence check is considered to be true at each computed time-steps. This yields a robust but time-step dependent staggered scheme. Furthermore note that there are two imbricated internal loops: one of them for the minimization of the mechanical problem with indicator i, and one of them for the minimization of the global problem with indicator j.

It is also interesting to note that in this staggered framework, the mechanical sub-problem considers damage as a constant defined at the integration point of the finite element mesh. This is because in this setting, it is only linked to the damaged stress $\boldsymbol{\sigma}$. As such, the finite elements' stiffness is only influenced by the value of d at integration points, which means that a damage topology with a nodal peak at $d = 1$ will not fully degrade the neighboring elements. This in turn has implication on the spatial discretization required to ensure an accurate localization of the phase-field, and will be more specifically discussed in Section. 3.3.

Algorithm 1: Staggered alternate minimization scheme

Input: $\mathbf{u}^n, \mathbf{d}^n, H^n, \bar{\alpha}^n, \psi_+^n$

Output: $\mathbf{u}^{n+1}, \mathbf{d}^{n+1}, H^{n+1}, \bar{\alpha}^{n+1}, \psi_+^{n+1}$

Initialization: $(\mathbf{u}, \mathbf{d}, H, \bar{\alpha}, \psi_+)^{j=0} = (\mathbf{u}, \mathbf{d}, h, \bar{\alpha}, \psi_+)^n$

while *No global convergence* **do**

  Minimization of mechanical problem (2.77,2.80):

  • $\mathbf{u}^{j+1} \leftarrow \mathbf{u}^j + \sum \delta\mathbf{u}^i$ (influenced by $\mathbf{d}^j$)

  Internal irreversibility check: $H^{\text{int}}(\mathbf{u}^{j+1}) > H^n$ as eq. (2.21b)

  Update of fatigue degradation state $\bar{\alpha}^{\text{int}}$, $f(\bar{\alpha}^{\text{int}})$

  Solve the phase-field sub-problem (2.81)

  • $\mathbf{d}^{j+1}$ (influenced by $f(\bar{\alpha}^{\text{int}})$, H^{int})

  Global convergence check eq. (2.84)

  • Computation of mechanical residual $\mathbf{R}_u^{j+1}(\mathbf{u}^{j+1}, \mathbf{d}^{j+1})$

  • Update of $\mathbf{K}_u^{j+1}$ with eq. (2.46) and rotation (2.52)

  if *Global convergence* **then**

    $\mathbf{u}^{n+1} \leftarrow \mathbf{u}^{j+1}$

    $\mathbf{d}^{n+1} \leftarrow \mathbf{d}^{j+1}$

    $H^{n+1} \leftarrow H^{\text{int}}$

    $\psi_+^{n+1} \leftarrow \psi_+^{\text{int}}$

    $\bar{\alpha}^{n+1} \leftarrow \bar{\alpha}^{\text{int}}$

    Next time step

  else

    Next internal iteration: $j \leftarrow j + 1$

    $\mathbf{u}^j \leftarrow \mathbf{u}^{j+1}$, $\mathbf{d}^j \leftarrow \mathbf{d}^{j+1}$

    $\mathbf{K}_u^i \leftarrow \mathbf{K}_u^{i+1}, \mathbf{R}_u^i \leftarrow \mathbf{R}_u^{i+1}$

    No update of H or $\bar{\alpha}$

2.4 Numerical validation

In the following section, Algorithm 1 was used to compute several usual phase-field benchmark tests in order to validate our proposed model and implementation and demonstrate its ability to recover brittle and fatigue crack propagation cases.

2.4.1 Single-edge notched tensile sample

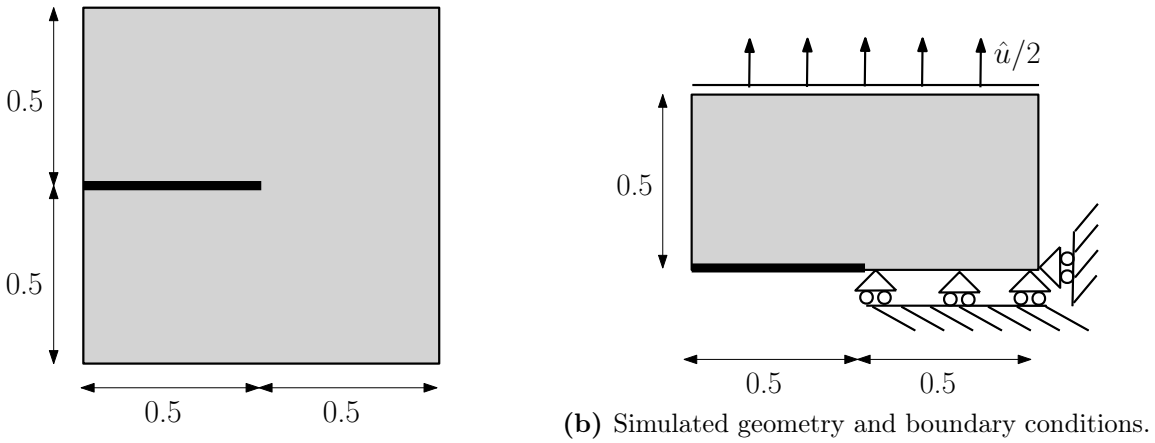

(a) Geometry (in mm).

(b) Simulated geometry and boundary conditions.

Figure 2.13: Geometry and boundary conditions of the SEN tensile sample.

The single-edge notched tensile sample is widely used in the literature notably for brittle fracture in Refs. [166, 172], and for fatigue fracture in Refs. [44, 129]. The complete geometry and its reduced model were illustrated in Fig. 2.13. We first investigated this sample with a monotonous load that induces unstable crack propagation. The following material parameters were used: $E = 210$ GPa, $\nu = 0.3$, $G_c = 2.7$ N/m, $l_c = 0.015$ mm. Note that the isotropic energy decomposition was applied here, and the fatigue effects were omitted. The crack propagated in a straight line so we enforced a fine mesh on the expected crack path, such that the characteristic length h of the finer elements was $h < l_c/8$. In Fig. 2.14, we plotted the computed reaction force as a function of prescribed displacement, with the proposed implementation. Results were in line with the cited literature. The slight difference between those results is due to the different staggered solver that were used. Indeed, Miehe et al. [166] and Molnár & Gravouil [172] used an explicit staggered scheme (see Section 2.1.3.3), while we used an implicit staggered scheme, with a global convergence check at the end of each computed time-step. Furthermore, in

Molnár & Gravouil [172], limited by Abaqus UEL tools, the authors required a smaller prescribed displacement step, in order to converge to a finer unstable regime solution.

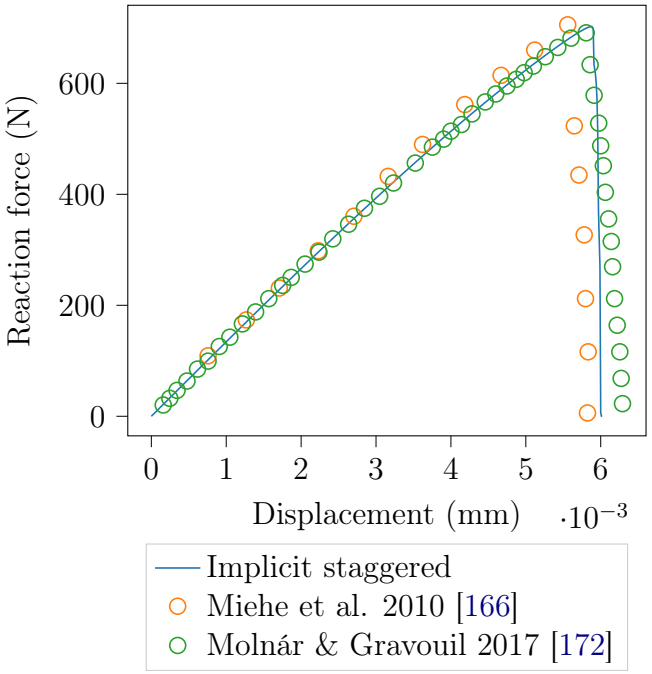

Figure 2.14: Comparison with phase-field brittle literature.

Then, we used the same geometry with a different load, following Ambati et al. [10], that have highlighted the deficiencies of the isotropic model with the SEN sample in pure shear: $\hat{u}$ was prescribed on the same boundary but in the x direction. Consequently, we successively applied the isotropic degradation scheme and the spectral decomposition model on this sample and observed the resulting crack pattern in Figs. 2.15a and 2.15b. In order to obtain those crack patterns, we applied the following material properties: $G_c = 2.7$ N/mm, $l_c = 0.0075$ mm, $E = 210$ GPa, $\nu = 0.3$, and no fatigue effects. The fact that there is two symmetric cracks when unilateral effects are not added, means that the crack lips inter-penetrate, and that the decomposition must be included to represent realistic physics.

In Ref. [44], the authors introduced a fatigue version of the SEN sample. The prescribed displacement is cycling, alternating and has a much lower maximum amplitude. The load ratio is -1, and the prescribed peak to peak amplitude is $\Delta\hat{u} = 0.002$ mm. Used material properties are almost identical to the previous case with $l_c = 0.004$ mm, and $\alpha_T = 56.25$ N/mm^2 with the fatigue degradation function (2.32). This fatigue loading results in a crack propagating for 200 cycles until complete failure of the sample. We provided a comparison between the described implementation and the cited literature in

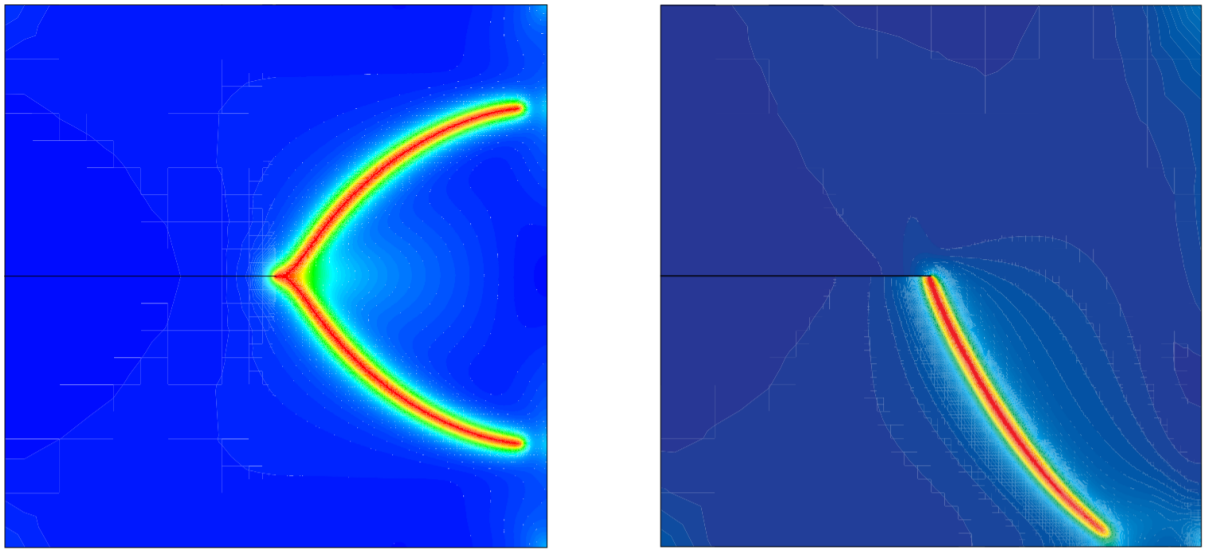

(a) Isotropic model computed damage field. **(b)** Spectral decomposition model.

Figure 2.15: Influence of the decomposition on the pure shear SEN sample.

Fig. 2.16. It can be seen that all these results deviate only slightly from each other. In this case, the solver types used by each group were very close. For instance Carrara et al. [44] and our work, used an implicit staggered scheme, while Kristensen et al. [129] used a BFGS staggered approach, which is still very similar the used implicit staggered algorithm.

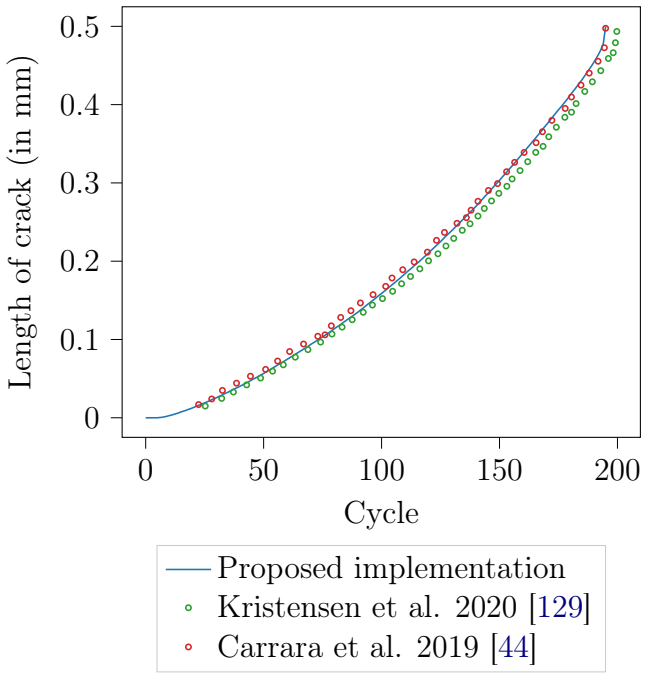

Figure 2.16: Comparison with phase-field fatigue literature.

Finally, as in Carrara et al. [44], we plotted the normalized accumulated fatigue variable

α_T as a function of computed cycles in Fig. 2.17. We compared results for the isotropic model, and the spectral decomposition formulation, using the material properties cited in Ref. [44]. As mentioned in Section 2.1.2.5, the fatigue degradation law is driven by the active part of the energy density in order to induce this decomposition effects in the fatigue framework. On this mode I fracture crack propagation case where the load ratio is -1, it yields a rate that is halvened by the fact that in compression, no energy is cumulated. Since the decomposition approach is not perfect, and since some zones of the sample see traction, we observe that a small amount of energy is cumulated in the compression phases.

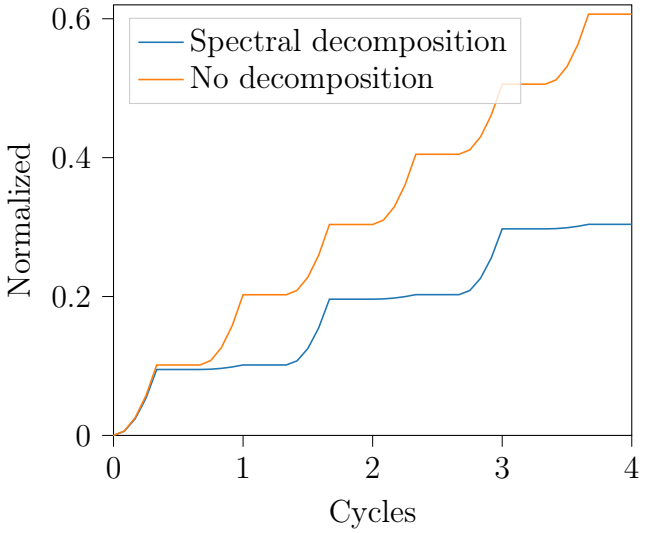

Figure 2.17: Influence of spectral decomposition on the cumulated fatigue variable.

2.4.2 Paris-like behaviour

An interesting feature of this model is that it is able to reproduce a phenomenology described by Paris Law, without the need to enforce the behavior explicitly. Indeed, as shown in Carrara et al. [44], if we apply the model on a given geometry, for multiple prescribed loads, a material dependent linear crack growth rate regime can be identified. We reproduced this observation on a generic fatigue fracture case: mode I crack propagation in an infinite domain, whose geometry was illustrated in Fig. 2.18. This crack case was chosen because of the very simple expression of the SIF. The material parameters chosen for this sample were $E = 210$ GPa, $\nu = 0.3$, $l_c = 0.1$ mm, $G_c = 2.7$ N/mm, $\alpha_T = \frac{G_c}{12 \cdot l_c}$, with no energy split. As was the case previously, since the crack path is known beforehand, we set a pre-refined mesh on the crack path that with smaller elements having a characteristic size h such that $h < l_c/8$. The size of simulated domain was taken as width $= 20 \cdot a_0 = 500 \cdot l_c$, which was considered large enough to treat the plane as infinite with respect to the crack

dimensions. A cyclic alternating load was enforced, with four different peak to peak amplitudes, and a -1 load ratio. Those different amplitudes induced four different fatigue lives illustrated in Fig. 2.19a. These data can be plotted in terms of the crack growth rate $\frac{da}{dN}$ (where a is the length of the crack) and the variation of SIF ΔK, here defined as $K_I^{max} - K_I^{min}$, with $K_I = \sigma\sqrt{a \cdot \pi}$. A material dependent linear regime can be observed in Fig. 2.19b, which is in line with a Paris-Erdogan phenomenology. On this specific example we have identified the following Paris law coefficients $C =$, and $m =$.

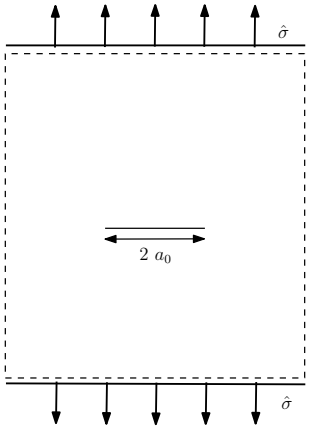

Figure 2.18: Geometry of the considered model.

Fatigue crack propagation literature usually approximates that this linear regime is independent of the considered geometry and load. It follows that we can use this linear characterization to fit numerical parameters to a specific experimentally observed crack growth rate. This will be extensively used in Chapter 4 in order to conduct numerical-experimental comparisons.

2.4.3 Crack branching

As one of the goal of the present implementation is to be able to recover complex crack propagation patterns, such as mixed mode propagation and networks of interacting cracks, we investigated the ability of the present framework to recover crack branching. Therefore, we introduced a case study inspired by Molnár & Gravouil [172], where a notched bi-material sample was used to display crack branching. Here, the bi-material illustrated in Fig. 2.20a consisted of two fictive materials differentiated by their fatigue threshold α_T. During cyclic loading, we anticipated crack propagation to occur perpendicular to the load direction until the interface between the upper and lower materials was reached.

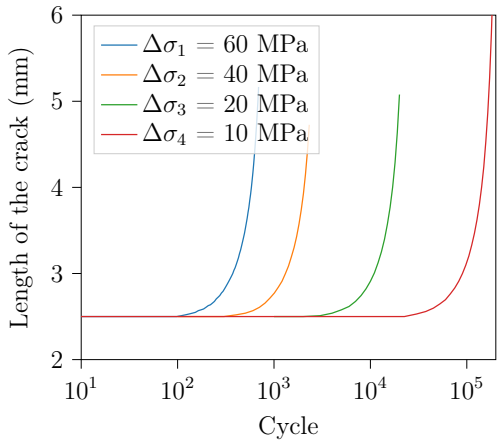

(a) Crack length as a function of computed cycle for different loadings.

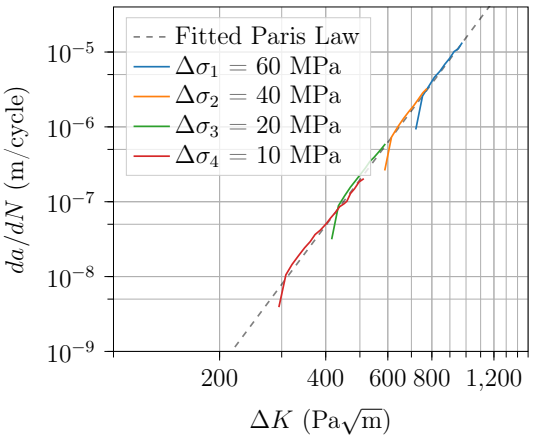

(b) Same result in the Paris domain.

Figure 2.19: Recovery of Paris Law behaviour.

Once this point was attained, crack branching was observed due to the inability of damage to occur in the much tougher upper material.

Other than α_T, both materials had the same properties: $E = 210$ GPa, $\nu = 0.3$, $l_c = 0.3$ mm, $G_c = 1$ N/mm. A cyclic loading of maximum amplitude $4 \cdot 10^{-3}$ mm and load ratio 0 was applied.

The mesh was refined on the expected crack path and the bi-material interface with $h < l_c/2$ in the refined zone. An illustration of this 2D mesh was provided in Fig. 2.20b.

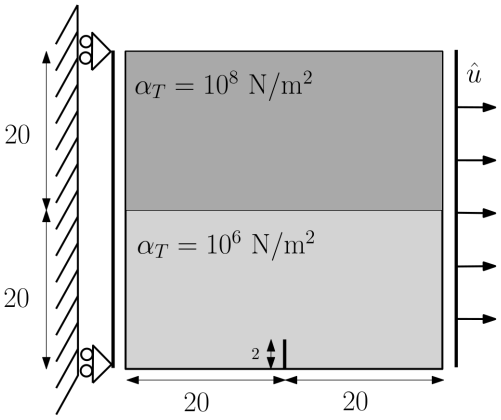

(a) Geometry (in mm).

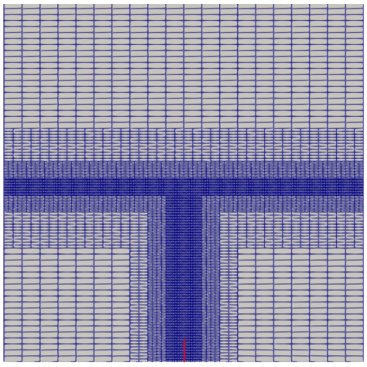

(b) Simulated geometry and boundary conditions.

Figure 2.20: Geometry and boundary conditions of the SEN tensile sample.

In order to give an idea the crack growth rate, we plotted the evolution of $W(d)$, the brittle crack dissipation term, in Fig. 2.21b. We can see that a stable crack propagation

regime turned into unstable crack propagation at a given critical length, around cycle 9000. In Fig. 2.21a, we have given the final crack pattern. The crack initiated at the notch and proceeded in mode I until the critical length. At this point, it propagated to the interface in one cycle. Then a stable fatigue crack propagation regime followed with two branching crack tips. Therefore, we have shown that this framework is able to recover crack branching as well as to capture a brittle and fatigue behavior, an unstable and a stable crack propagation regime in a unified manner.

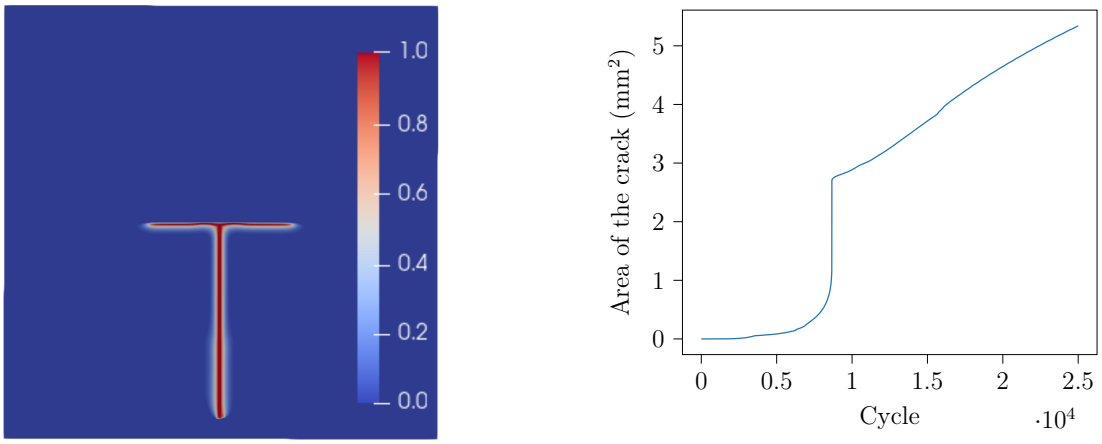

(a) Branching crack pattern.

(b) Area of the crack.

Figure 2.21: Topology of damage and evolution of its area.

2.4.4 Crack initiation

The numerical sample of a perforated plate illustrated in Fig. 2.22a was studied to show that the current framework was able to recover cases of crack nucleation with no initial crack tip, notch or damaged zone. Indeed, the ability to model fatigue crack nucleation and growth in a single framework could bridge the gap between usual complete fatigue life analysis and fatigue crack propagation methods. In order to trigger crack nucleation in a homogeneous unbroken structure we mirrored the following references [44, 182, 214, 240], that investigated crack nucleation on a periodically perforated plate. The material properties were $E = 12$ GPa, $\nu = 0.3$, $l_c = 0.01$ mm, $G_c = 1.4$ N/mm, $\alpha_T = 6.48$ N/m^2. A cyclic displacement was enforced on the upper edge which compressed the structure, $\hat{u}_{\max} = -2 \cdot 10^{-3}$ mm with a load ratio of 0. On this sample, the spectral split was used.

A mesh pre-refinement equivalent to $h < l_c/8$ was enforced around the holes. Fig. 2.23 shows an image of the damage field after crack initiation. As was observed experimentally, vertical crack patterns emerged in most holes. However, spurious zones of damage were

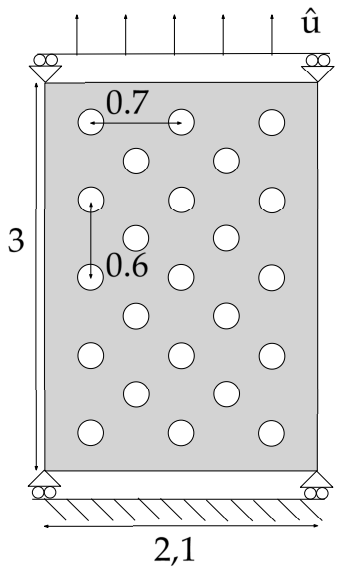

(a) Geometry in mm and boundary conditions.

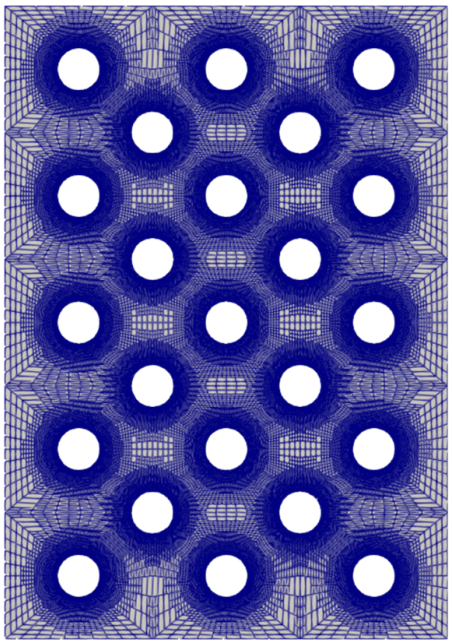

(b) Fixed mesh, refined prior to the simulation around the holes.

Figure 2.22: Geometry and mesh of the perforated plate.

also seen perpendicular to the applied loading and on a cross pattern centered on the hole. These results were in line with Ref. [182] (where a spectral split was also used, on a brittle fracture case *i.e.*, with a monotonous loading).

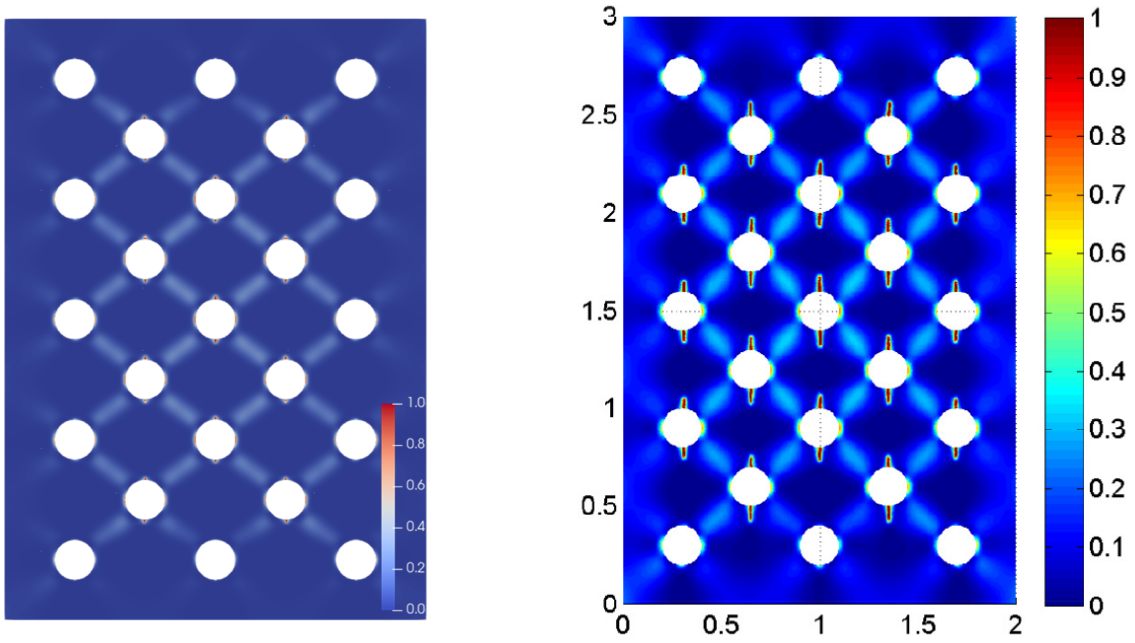

(a) Damage field after 1600 cycles.

(b) Computed damage field in Ref. [182].

Figure 2.23: Comparison of this fatigue version of the perforated plate with Nguyen et al [182].

By contrast, experimental studies of such a geometry on a quasi-brittle material only showed vertical cracks [240]. In fact, these spurious damaged zones were due to the adopted spectral split, which, as observed in the literature, is not always well suited to discriminate between compressive and tensile loadings [102], [236]. In Carrara et al. [44], a so-called "no tension" split [80], was used to model quasi brittle materials. As opposed to the spectral split, it enabled a good recovery of experimental data on this specific geometry: vertical cracks were observed, with no spurious damage in the compressive zones.

These results pointed at the fact that crack nucleation and crack growth were indeed recovered by the proposed framework in a unified manner. Moreover, this sample highlighted the limitations of the spectral split, as well as the need for a relevant energy decomposition scheme to reproduce specific experimental results.

Conclusion of the chapter

In this chapter, we detailed the different components of the phase-field model and explicited their influence on the resulting numerical framework. The constitutive choices for the implemented model were detailed along with the resulting governing equations and their implementation in a finite element context. Furthermore, we presented the spectral decomposition method used in this work to introduce unilateral effects. A novel change of basis approach was added to the formulation employed in Bernard et al. [26]. The resulting procedure yielded faster computation and eliminated the issues of singular values [176]. Finally, we applied the staggered framework on several numerical benchmarks that are often used in the phase-field literature to demonstrate this model's abilities. So indeed, it was shown that the model recovers complex fracture phenomenologies such as branching and crack nucleation, as well as fatigue crack propagation and properties approaching a Paris crack growth rate law. As was shown in the seminal work of Carrara et al. [44], Paris law behaviour, Miner law, Wöhler curve regimes can be reproduced, as well as crack nucleation and unstable crack propagation, all in a single unified framework. Usually those fracture phenomenologies are studied using separate tools. This is of course expected when all those different fracture cases are driven by very different physical mechanisms. But it is still very practical to have such a generalized tool in the numerical analysis toolbox. Such a flexible and easy to use formulation was bound to enable very interesting applications, and have the impact it has in the fracture mechanics community. However, such a compact methodology means that the application of the framework on real-life cases can become very difficult to conceptualize. A very small number of parameters is responsible for these very differently driven mechanisms. Consider for instance α_T, the threshold parameter of the fatigue degradation function. This fatigue parameter should be linked to a fatigue nucleation criteria, as well as the Paris coefficient, as well as the Griffith criterion. A theoretical framework is lacking to unify these methodologies, or maybe impossible to set. These questions are discussed further in Chapter. 4.

However flexible this approach may be, its direct application to industrial application is still out of the question for another reason: its computational cost. We have discussed before about the cost associated with the requirement of an extremely fine mesh in the damage zone to capture the steep gradient of the phase-field. In addition, this fatigue crack propagation numerical strategy implies the explicit computation of each individual cycles of the total fatigue life of a structure, in order to compute the non-linear accumulation of $\bar{\alpha}$. However, as mentioned before, high cycle fatigue applications, can yield a total life that ranges from 10^5 to 10^7 cycles. This is why, in the next chapter, we propose the

implementation of accelerating tools to solve the issues of excessive spatial discretization linked with the phase-field model and the excessive temporal discretization linked with this phase-field fatigue approach.

3

Acceleration tools

Following the definition of the model, we present multiple ways to accelerate the phase-field computations in a fatigue context.

Contents

In this section, we regrouped the investigations led to accelerate the phase-field model simulations when applied in a fatigue crack propagation context. Indeed, this approach is hindered by several efficiency issues that makes for a difficult application on large-scale models. These hindrances are discussed in this section along with solutions to accelerate their treatment, while keeping a given level of accuracy. First, the acceleration of the computation of a cycle was tackled by comparing different time-integration schemes. Then we put forward a cycle jump method in order to avoid the explicit computation of a large amount of cycle in a high cycle fatigue context. Finally, the issue of the excessive refinement linked with the diffuse representation of the crack was treated with the introduction of an adaptive mesh refinement process. Each of the proposed tools were then unified and applied on typical phase-field fracture benchmarks to showcase their accelerations abilities.

3.1 Staggered phase-field fatigue algorithm

In the light of the plurality of solving strategies that are available in a phase-field framework (Section 2.1.3.3), this section was dedicated to the analysis and choice of a suitable phase-field fatigue solver, and multiple convergence acceleration techniques.

3.1.1 Explicit and implicit scheme for fatigue fracture

At a first glance, the solver issues associated with the phase-field model do not seem to be predominant in the case of high cycle fatigue. Indeed, at the time scale of one cycle, the unknown fields change very slowly and thus should neither be a challenge to the implicit strategy iterative search, nor need a large number of time-steps to converge with an explicit strategy. This section explored this question by applying both strategies to basic numerical samples. Furthermore, a choice between the explicit and implicit approach was made in order to apply the solving strategy best suited to high cycle fatigue crack propagation.

First we illustrated the application of the explicit scheme in a brittle fracture case (by enforcing $f(\bar{\alpha})$=1), on a very basic sample: the homogeneous response in plain strain from Ref. [172]. For this simple case, an analytic solution is trivial and can be compared to the computed results. For instance, the damage equation (2.65) is considerably simplified with no gradient terms, yielding the following expression for damage:

$$d_{\text{ana}} = \frac{2H}{2H + f(\bar{\alpha}) \cdot \frac{G_c}{l_c}}. \tag{3.1}$$

Furthermore, σ^{yy}_{ana} is defined as $\sigma^{yy}_{\text{ana}} = g(d_{\text{ana}}) \cdot c_{22} \cdot \varepsilon$, with c_{22}, defined as the uniaxial

traction component of the stiffness matrix such that, in plain strain: $c_{22} = \frac{E(1-\nu)}{(1+\nu)(1-2\nu)}$. When $f(\bar{\alpha})$ is at 1, the analytical expression of the stress component σ^{yy} can directly be found from this relationship, while for a cyclic load, with $f(\bar{\alpha}) < 1$, an incremental solution is computed with a very fine du<10^{-9} to estimate the analytical solution.

The geometry and boundary conditions were illustrated in Fig. 2.12. The size of the square's side was 1 mm . Material properties were $E = 210$ GPa, $\nu = 0.3$, $l_c = 0.1$ mm, $G_c = 5$ N/mm. Initially, $f(\bar{\alpha}) = 1$ in order to neglect fatigue effects. Note that as the response is homogeneous, there is no need to reach a given l_c/h in order to converge spatially. A staggered explicit strategy was applied for different values of Δu, the displacement step. In Fig. 3.1a, we plotted the stress-strain response for these different displacement steps, underlining the dependency and convergence of the computed response. We also plotted the convergence rate of the average computed stress error in Fig. 3.1b defined as:

$$Err_\sigma = \frac{1}{n} \cdot \sum_{k=1}^{n} \frac{|\sigma^{yy}(\varepsilon^k) - \sigma^{yy}_{\text{ana}}(\varepsilon^k)|}{\sigma^{yy}_{\text{ana}}(\varepsilon^k)}. \tag{3.2}$$

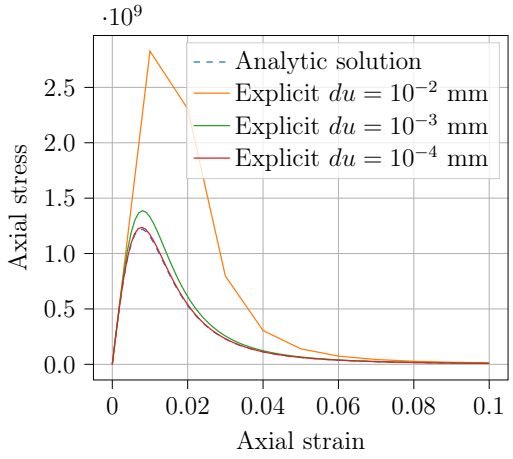

(a) Stress strain response in brittle fracture.

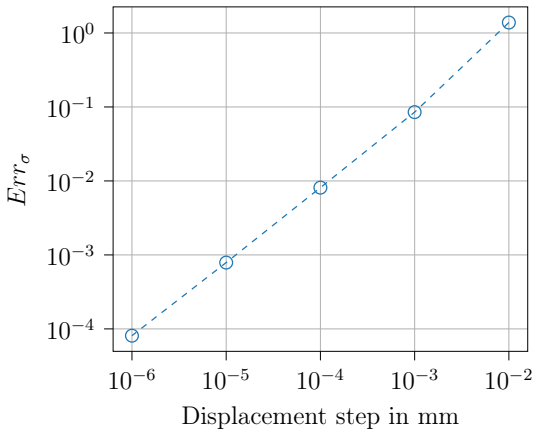

(b) Average error convergence rate.

Figure 3.1: Influence of the displacement step for an explicit staggered solver in brittle fracture.

Note that for this simple case, the implicit scheme (not plotted here for the sake of conciseness) converged to the exact solution very fast (1-3 iterations), almost independently of the used time-step (provided that the load extremum was captured).

After this measure of the brittle fracture error convergence, we set a framework related to high cycle fatigue conditions. In such conditions, the load is very small compared to the ones reported in brittle fracture. Furthermore, we can assume that the variation of the cumulated field in one cycle is very small compared to the fatigue threshold *i.e.*,

$\Delta\alpha << \alpha_T$. Hence we can neglect the variation of the fatigue degradation function in one cycle *i.e.*, $\Delta f(\bar{\alpha})/\Delta N \simeq 0$. In light of these assumptions, we studied the convergence of error with respect to the displacement step in a simulated high cycle fatigue context. To do so a loading u_{fat} is set as $u_{\text{fat}} = (1/100) \cdot u_{max}$, and we enforce $\Delta f(\bar{\alpha}) = 0$. However, we can expect fatigue degradation to play a large role in the convergence of the explicit scheme. Consequently, we set a constant value to the fatigue degradation function to simulate a specific state of fatigue degradation, and observe its influence on error convergence. Note that a cycle here is thought as one loading phase: the unloading is not taken into account. We plotted the analytic "fatigue" stress strain curve in Fig. 3.2a for different fatigue degradation states. Additionally, we plotted the rate of convergence of average error defined as eq. (3.2) with respect to the displacement step for the different fatigue degradation states in Fig. 3.2b. As expected, when there is no fatigue degradation we recovered the convergence rate of the brittle case. Since a high cycle fatigue modelling would be set with a very low loading, a fine displacement step would not require many computed steps per cycles. However, we see that as fatigue degradation increases, so does the non-linearity of the stress response, hence requiring more and more sub-steps to reach convergence. For instance, notice that in Fig. 3.2b, when $f(\bar{\alpha})$ is divided by 10, one must compute 10 times more steps per cycle in order to achieve a similar precision. This observation explains how an explicit staggered scheme can become inefficient even in conditions of very low loading amplitude, stable crack propagation and very slow evolution of the computed fields. From these observations, we can assume that this specific scheme is mostly applicable before the cumulated variable overcomes the fatigue threshold.

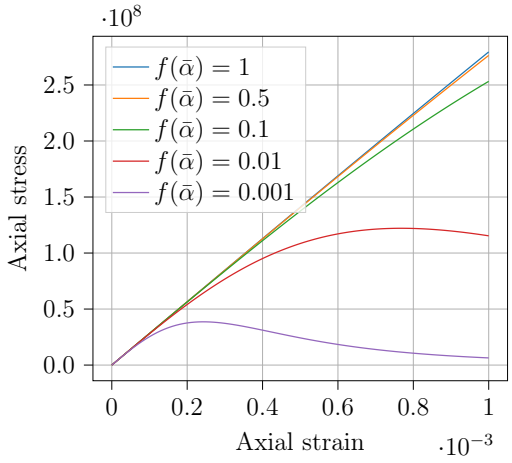

(a) Stress strain response in fatigue fracture.

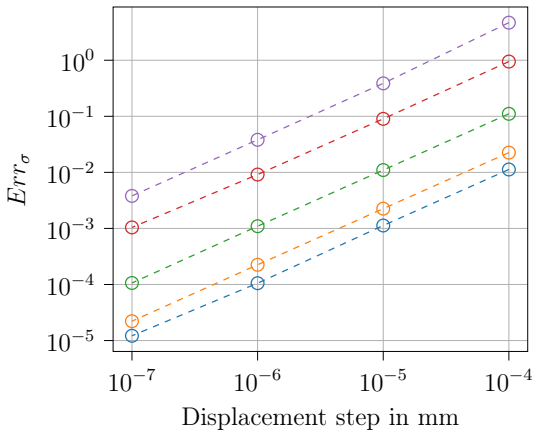

(b) Average error convergence rate.

Figure 3.2: Influence of the displacement step for an explicit staggered solver in fatigue fracture.

Finally we checked on the influence of the variation of $f(\bar{\alpha})$ on error convergence. Even

though we can assume that this variation is very small in the span of one cycle, we observed that on the homogeneous response, this variation influences the number of iterations per computed steps of the implicit staggered scheme. Therefore, we assumed it would also have an impact on the error convergence rate in an explicit framework. The numerical parameters were fine tuned in order to obtain a specific variation $\Delta f(\bar{\alpha})$, that always reach $f(\bar{\alpha}) = 0.5$. This enabled us to uncouple the error due to fatigue degradation, from the error due to the variation of the fatigue degradation function. Indeed, with this procedure, we compared the error convergence obtained for $f(\bar{\alpha}) = 0.5$, and $\Delta f(\bar{\alpha}) = 0$, to error convergence where $f(\bar{\alpha}) = 0.5$, and $\Delta f(\bar{\alpha}) = 0.1$, or $\Delta f(\bar{\alpha}) = 0.01$. We plotted the obtained variation of $f(\bar{\alpha})$ in Fig. 3.3a. Furthermore, the error convergence rate of those simulated scenarios are compiled in Fig. 3.3b. Unlike what was expected, we observed that this variation seems to have a very low influence on error convergence with respect to the displacement step for an explicit scheme.

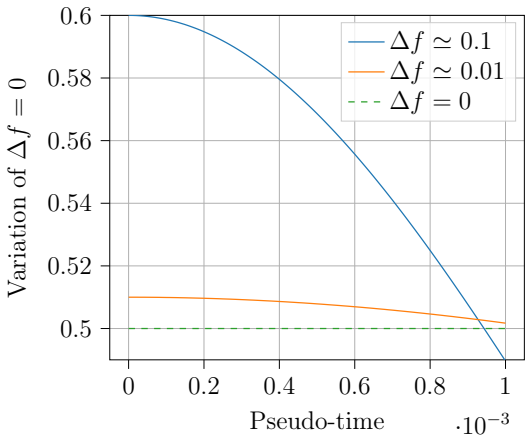

(a) Visualization of the enforced variations of $f(\bar{\alpha})$ during the fatigue loading.

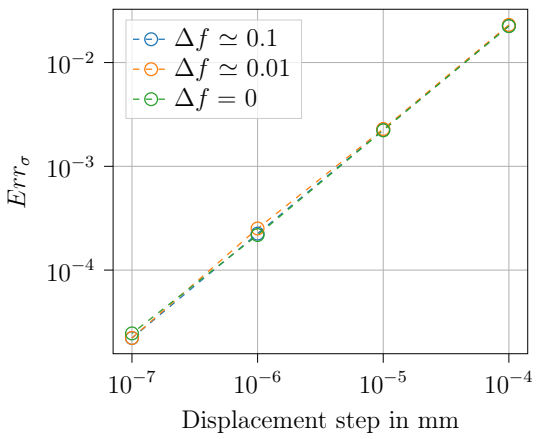

(b) Average error convergence rate.

Figure 3.3: Influence of the variation of $f(\bar{\alpha})$ on error convergence.

From these observations, we could argue for a hybrid explicit-implicit scheme, that uses alternatively those solving strategies depending on the value of the fatigue degradation function, or another damage or energy based criterion. However such a hybrid scheme was not attempted because the behaviour of the model before reaching the fatigue threshold is linear and does not require a cycle by cycle solver scheme: a large jump until the start of the fracture toughness G_c degradation can be performed [145, 225], as detailed in Section 3.2.

Note that the implicit scheme yielded very efficient results on this numerical sample, with very fast converging rate, and precise results almost independently of the used displacement

step and the fatigue degradation status. Indeed as stated before, it is only the variation of $f(\bar{\alpha})$ that seemed to have an influence on the number of iterations to convergence in the implicit framework. Since the variation of $f(\bar{\alpha})$ during a cycle in high cycle fatigue is very small, we can expect fast convergence rates of the implicit strategy.

However, this very simple case is not representative of the fracture cases that we will encounter: we can expect slower convergence rate on inhomogeneous cases. We have therefore evaluated the performance of those staggered schemes on a different numerical sample: the single-edge notched (SEN) tensile sample. This sample is widely used in the literature notably for brittle fracture in Refs. [166, 172], and for fatigue fracture in Refs. [44, 129] The geometry used was directly taken from these references and plotted in Fig. (2.13). On this inhomogeneous case, we expected that the implicit scheme would need more internal iterations to achieve convergence. In this context, the goal is to evaluate whether the quantity of internal iterations overcomes the number of computed steps of a converged explicit framework. The material properties, and prescribed loading are inspired by the study sample by Kristensen & Martinez-Pañeda [131]: $E = 210$ GPa, $\nu = 0.3$, $l_c = 0.04$ mm, $G_c = 2.7$ N/mm, $\alpha_T = 56.25$ N/mm^2, and the applied load was $\Delta\hat{u} = 0.002$ mm, and a load ratio of -1. Furthermore, no energy decomposition was used at first: the isotropic model is assumed. These material properties, along with the used loading enable a fatigue behavior in a very small number of cycles. Additionally the choice of a large characteristic length enables the use of a coarse mesh. All these parameters cause the sample to be very time efficient, making it a fitting test sample to evaluate the performance of our implementation in a fatigue context. Furthermore, this efficient tuning of the sample allows for a stable crack propagation that is nevertheless very fast, hence challenging the staggered solvers.

Both staggered strategies were employed on this sample and we compared the computed length of the crack in Fig. (3.4a). Moreover, the number of internal iterations per cycle in the implicit framework was plotted in Fig. (3.4b).

As can be seen in Fig. 3.4a, for an explicit scheme, a very fine time-step is necessary in order to reach convergence. Specifically, on this numerically challenging sample, we observed that as much as 2000 computed steps per cycle, hence using a displacement step of $\delta u = 1 \cdot 10^{-6}$ mm, is not fine enough to converge. These results are in line with the work of Kristensen et al. [129], and Khalil et al [125]. In a high cycle fatigue crack propagation context, such a time discretization applied to thousands, or millions of computed cycle is not computationally viable. The implicit staggered scheme on the other hand only needs a very limited amount of computed steps per cycle in order to converge: only the peaks of

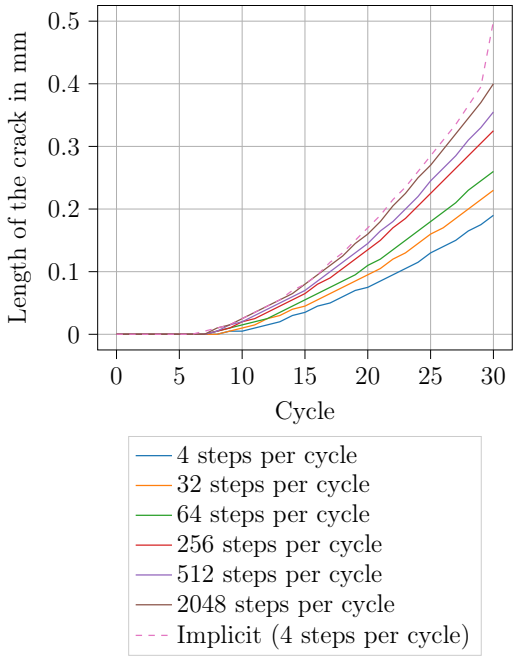

(a) Computed crack length with respect to cycles.

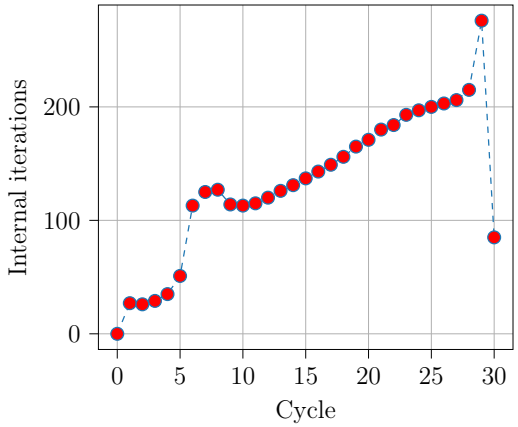

(b) Number or iterations per computed cycles.

Figure 3.4: Comparison of explicit and implicit staggered schemes.

loading need to be captured. However, we see in Fig. 3.4b that a large amount of internal iterations are computed per cycle: tens of iterations before crack propagation, to hundreds of iterations during the stable crack propagation regime. Still, we see that the implicit scheme is the more efficient approach, as a maximum of two hundred iterations per cycles is required in the fatigue regime, when thousands are required in an explicit framework.

Note that a peak of iterations is reported for the last step of the crack propagation, where we can consider that the phenomenology is closer to brittle fracture than high cycle fatigue. Indeed, as reported in the literature, an implicit approach has trouble converging in unstable crack propagation conditions [154]. However, as this work focuses itself around high cycle fatigue crack propagation, we can assume that these conditions are out of the scope. Nevertheless, since this model is based on brittle crack propagation, we can view this fatigue propagation as localized unstable crack propagation, limited to the fatigue-degraded zone. This is part of the explanation as to why it is such a challenge to reach the converged prescribed displacement with the explicit approach.

A general assessment concerning the case dependency of these observations is very complex here. These numerical experiments are no definitive proof that the explicit scheme is always less efficient. For instance by changing the used parameters on the SEN sample,

other conclusions can be drawn: Fig. 3.5a illustrates the computed crack length, and its convergence with respect to the number of computed time-steps, using $\alpha_T = 1125$ N/mm^2 and a maximum load of $\hat{u} = 0.001$ mm (all other parameters were kept constant). As in Fig. 3.4a, the explicit schemes requires a very large amount of time-steps to converge. However, the numerical error before convergence is very low, making it so that we could argue for an explicit scheme over an implicit scheme in these conditions of slower crack propagation rate. Then, taking the numerical values used in Refs. [44, 129]: $\alpha_T = 56.25$ N/mm^2, $l_c = 0.004$ mm, $G_c = 2.7$ N/mm yielding a crack propagation rate of the same order, for a lower value of l_c, we find back results in line with Kristensen et al. [129] as illustrated in Fig. 3.5b: the explicit scheme is very inefficient, since the implicit approach converges in 10 to 50 internal iterations. This is an illustration of the material dependency of the efficiency of a given solving strategy, but note that other sources could affect it, such as geometry or loading.

In the end, even with this lack of a general proof, we followed the observations in Ref.[129], and most results of the section: we chose to use the implicit scheme, as it guarantees an accuracy that is independent from the used-time step. Furthermore, it enables a straightforward generalized global convergence criterion, conversely to the explicit scheme that would require the setup of a specific criterion to ensure convergence.

3.1.2 Acceleration of the implicit scheme

After having chosen a relevant staggered strategy, we worked on the acceleration of the alternate minimization scheme in a fatigue context. These investigations were inspired by the work of Helfer et al. and Lu et al. [104, 154], where the implicit scheme was accelerated in a brittle fracture context. In these articles, a so-called "one-loop" alternate minimization scheme is described: at each Newton Raphson iteration of the mechanical sub-problem (2.77), damage is recomputed and integrated to the next mechanical iteration. This process can be seen as computing only one Newton-Raphson iteration per implicit steps. The authors applied it in a brittle fracture framework and underlined that in this context, such a process increases the coupling between the unknown fields, and eases the implementation of modified Newton approaches or convergence acceleration techniques [154].

In this section, we investigated the efficiency of this one-loop scheme, and other acceleration techniques in the fatigue phase-field framework. As in the previous part, the SEN tensile sample was used with a fatigue loading. However, the spectral energy decomposition was introduced in the formulation, in order to induce non-linearity of the mechanical

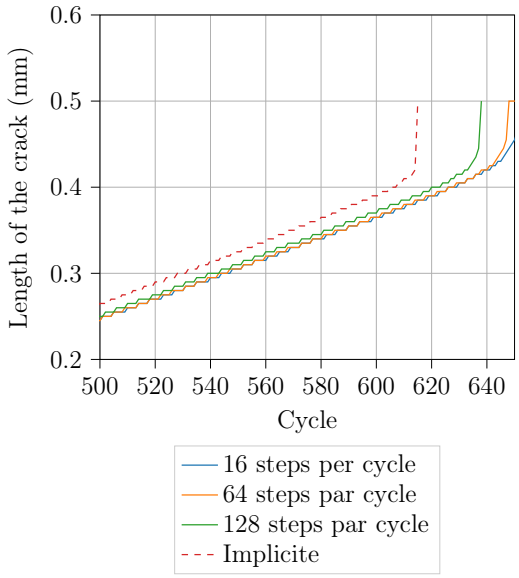

(a) Last part of crack propagation on SENT in fatigue.

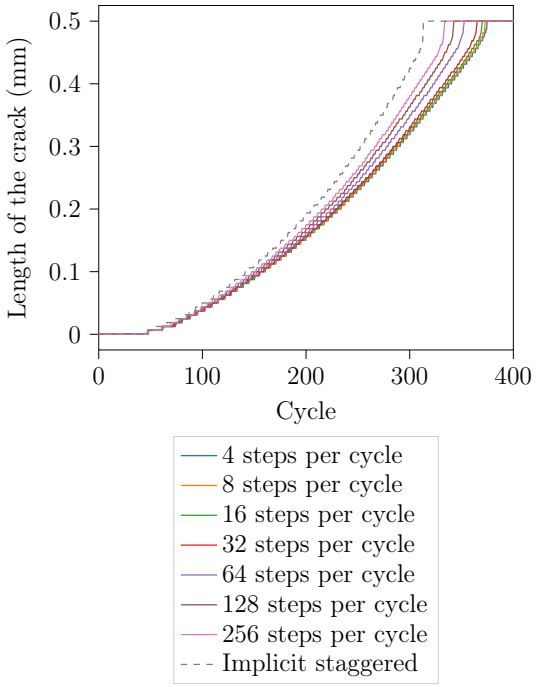

(b) Comparison between explicit and implicit on SENT with parameters from Ref. [44].

Figure 3.5: Influence of material parameters on efficiency of one scheme over the other.

sub-problem. Indeed, if an isotropic degradation is considered, the alternate minimization scheme and the one-loop scheme are equivalent: one iteration of the mechanical sub-problem is sufficient. The same material properties and loading were used for this investigation. However, here 60 cycles are simulated in order to achieve the same crack length, considering that with spectral decomposition the compression phases of the loading do not affect degradation.

In Fig. 3.6 we plotted the convergence of the mechanical residual with respect to the internal iterations of the implicit scheme of cycle 30 at point A and B of the loading, illustrated in Fig. 3.7.
The chosen cycle is located during the stable crack propagation regime (Fig. 3.8a), and was hence considered relevant to evaluate the efficiency of the schemes, by being representative of the majority of computed cycles (in a high-cycle fatigue context). Furthermore, point A and B are the critical point of the cycle computation, being respectively peak of the traction phase and peak of the compression phase. Note that the plotted iterations are representative of the staggered iterations, not taking the internal Newton-Raphson loops into account. As could be expected, the convergence at point A was very similar with both approaches because the behavior is almost linear in traction. Conversely, a slower convergence of the

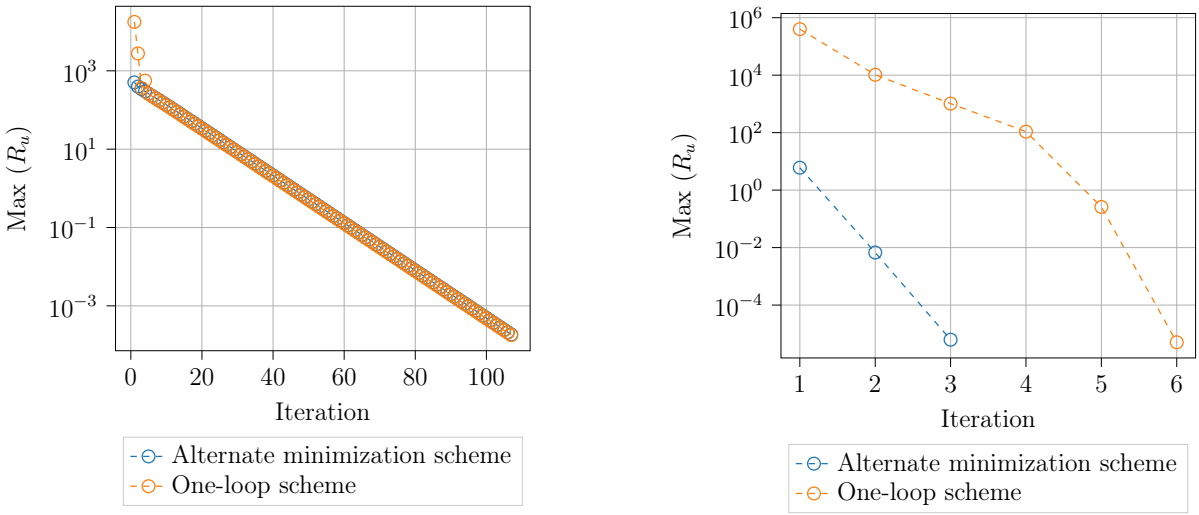

(a) Convergence of the residual at A.

(b) Convergence of the residual at B.

Figure 3.6: Residual convergence at A and B.

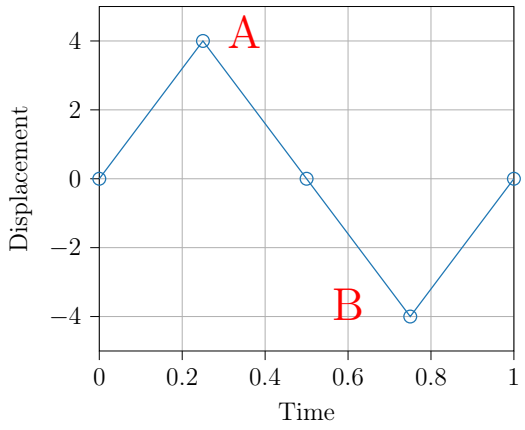

Figure 3.7: Loading used for these investigations.

one-loop scheme was observed at point B. Nevertheless, each of the alternate minimization scheme iterations contained multiple Newton-Raphson iterations. For instance, considering the convergence of the residual at A in Fig. 3.6a, we observed a similar convergence rate but an average of 2 internal iterations with the alternate minimization scheme. Note also that we did not display the last step where crack propagation becomes unstable until total failure of the sample. For the standard alternate minimization scheme, it converged in 1779 internal iterations while the one-loop scheme converged in 796 internal iterations. In the end, when considering the total number of computed iterations, we observed that the one-loop scheme was more efficient on this sample, Fig. 3.8b.

There could be multiple sources for this deficiency of the standard alternate minimization scheme compared to the one-loop formulation in a fatigue framework. One of them is

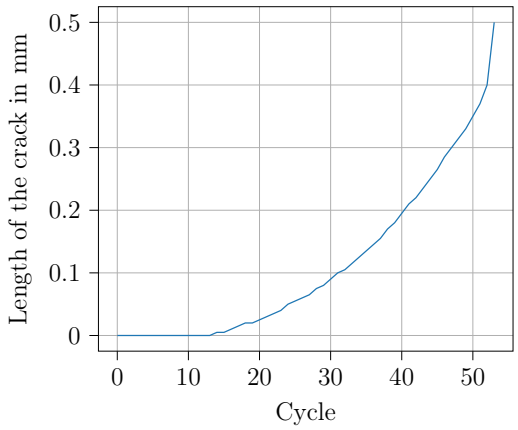

(a) Computed crack length with respect to cycles.

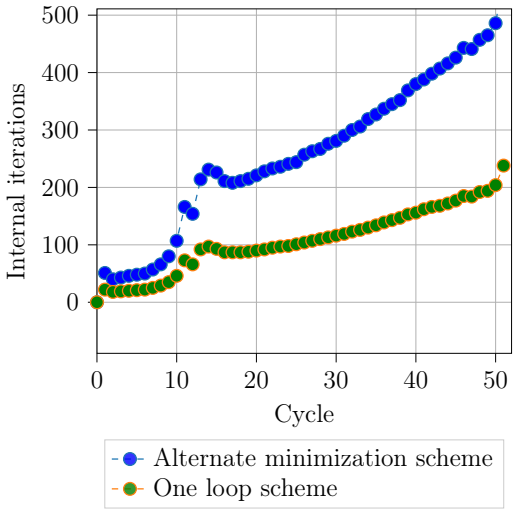

(b) Number or iterations per computed cycles.

Figure 3.8: Investigation of implicit schemes.

that, as stated by the authors in Refs.[104, 154], a better coupling between both unknown fields is achieved with the one-loop scheme. This effect might be magnified with the proposed fatigue implementation, by the fatigue effects that influence the damage problem and are computed between the mechanical and damage sub-problem. Furthermore, this implementation limits the quantity of loops contained in other loops, which can amount to a very large quantity of internal iterations when the convergence rate is slow. In addition, the one-loop scheme enables easier implementation of acceleration techniques as underlined by Lu et al. [154].

Consequently, we experimented multiple usual acceleration techniques: a modified-Newton formulation and acceleration of convergence. First, let us introduce the implemented modified-Newton framework. As is usual in Newton-Raphson framework, most of the computing time is spent in the inversion of the tangent operator. Therefore, it is not uncommon to use an efficiently computable approximation of the tangent operator instead of the so-called consistent operator. For instance, in this work we implemented an approach where the consistent operator is only updated every X iterations of the implicit loop. Alternatively, a scheme considering an undamaged stiffness operator was attempted. However, as is reported by Lu et al. in a brittle framework [154], such implementation usually lacks robustness: on the previous sample, non-convergence of the scheme was observed at cycle 10, which corresponds to crack initiation. Note that before cycle 10, the modified-Newton implementation was not always the most efficient, as computing time is gained at the operator numerical inversion step, while it is lost in all other operators

because of the increase of internal iterations. Note that no tuning of the update frequency X of the operator made the scheme more efficient than the consistent Newton scheme, or robust enough. Recently, a robust modified Newton approach was put forward in Kristensen et al. [130]. This specific implementation was not tested.

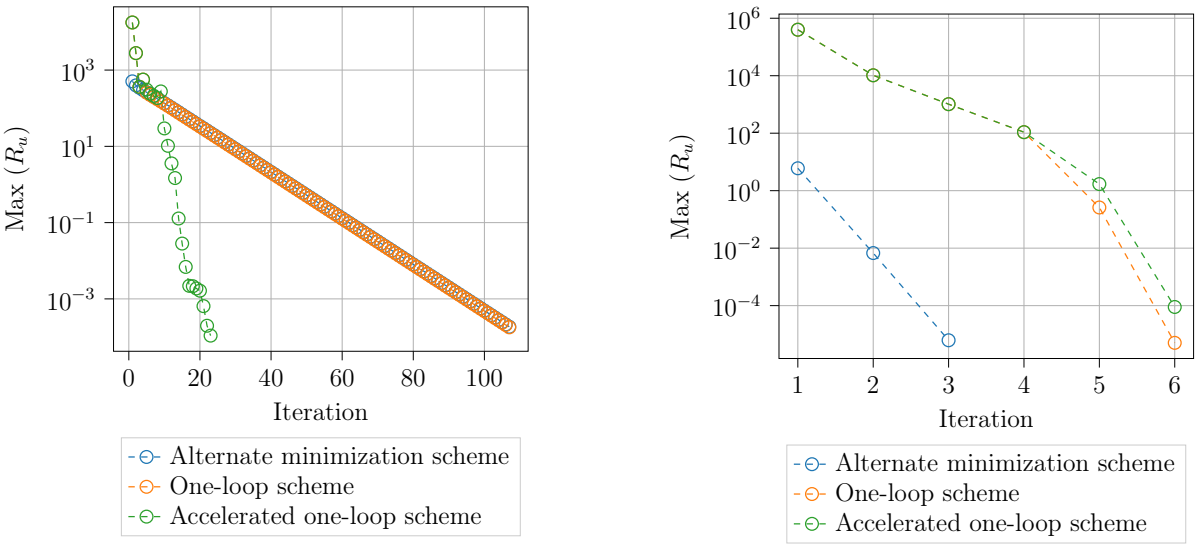

(a) Convergence of the residual at A.

(b) Convergence of the residual at B.

Figure 3.9: Influence of acceleration of convergence.

Then, a fixed point acceleration method was applied on the presented framework in order to accelerate convergence of the modified-Newton and Newton approaches, as it was reported in Ref. [104]. As all the implementation conducted in this work were made in Cast3M, we used an available acceleration method: Aitken's approach [3], which relies on the properties of the terms of a converging sequence. With this kind of approach, linear combinations of the successive residual obtained with the fixed-point staggered solver, are deduced to accelerate convergence. More details on these methods in Ref. [206]. This approach was not able to solve the robustness issues of the modified-Newton implementations, however it enabled a significant acceleration of the convergence with a consistent operator. In order to quantify this acceleration we used the previously set SEN geometry, in the previously cited loading conditions, and once again we plotted the convergence of the residual with respect to internal iterations at cycle 30 at A and B in Fig. 3.9, and the number of computed iterations per cycles during propagation in Fig. 3.10. The acceleration method enabled significant gains in computing time, as most computed cycles converged for less than half the required internal iterations. On this specific sample, the computing time between cycle 1 and 51 has been divided by three by using this acceleration method. However,

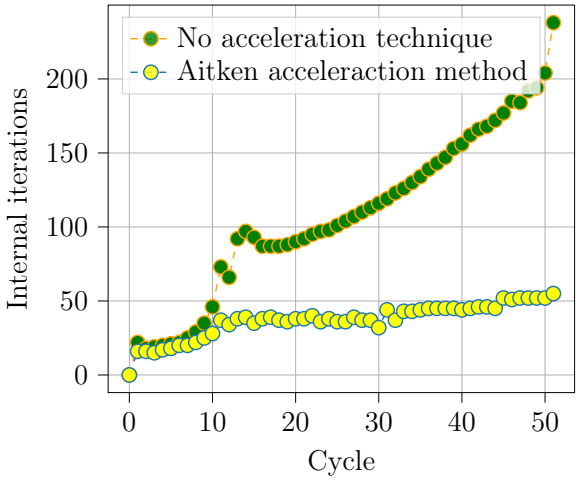

Figure 3.10: Iterations per computed cycles.

we see that the method can also yield slower convergence rate, such as at point B, where the accelerated convergence is slightly slower.

Considering the changes that were brought to the initial formulation of the staggered phase-field fatigue Algorithm (1), we can rewrite and detail it as Algorithm (2). It corresponds to a staggered implicit strategy, with a one-loop scheme. The usual alternate scheme can be recovered by applying more than one iteration of the mechanical sub-problem.

Algorithm 2: Staggered phase-field fatigue implementation

Input: $\mathbf{d}^n, H^n, \bar{\alpha}^n, \psi_+^n$

Output: $\mathbf{d}^{n+1}, H^{n+1}, \bar{\alpha}^{n+1}, \psi_+^{n+1}$

Initialization $\mathbf{u}^j \leftarrow \mathbf{0}$, $\mathbf{K}_u^j$, $\mathbf{R}_u^j$

- $(\mathbf{d}, H, \bar{\alpha}, \psi_+)^{j=0} = (\mathbf{d}, H, \bar{\alpha}, \psi_+)^n$

while *No global convergence* **do**

  One mechanical step of minimization (2.77,2.80):

  - $\mathbf{u}^{j+1} \leftarrow \mathbf{u}^j - (\mathbf{K}_u^j)^{-1} \cdot \mathbf{R}_u^j$ (influenced by $\mathbf{d}^j$)

  Internal irreversibility check: $H^{\text{int}}(\mathbf{u}^{j+1}) > H^n$ as eq. (2.21b)

  Update of fatigue degradation state $\bar{\alpha}^{\text{int}}$, $f(\bar{\alpha}^{\text{int}})$, $G_{\text{F}}^{\text{int}}$

  Solve the phase-field sub-problem (2.81):

  - $\mathbf{d}^{j+1}$ (influenced by $G_{\text{F}}^{\text{int}}$, H^{int})

  Global convergence check:

  - Check on damage dissipation eq. (2.71)
  - Computation of mechanical residual $\mathbf{R}_u^{j+1}(\mathbf{u}^{j+1}, \mathbf{d}^{j+1})$
  - Update of $\mathbf{K}_u^{j+1}$ with eq. (2.46) and rotation (2.52)

  if *Global convergence* **then**

    $\mathbf{d}^{n+1} \leftarrow \mathbf{d}^{j+1}$

    $H^{n+1} \leftarrow H^{\text{int}}$

    $\psi_+^{n+1} \leftarrow \psi_+^{\text{int}}$

    Next time step

    $\bar{\alpha}^{n+1} \leftarrow \bar{\alpha}^{\text{int}}$

    Next time step

  else

    Next internal iteration: $j \leftarrow j + 1$

    $\mathbf{u}^j \leftarrow \mathbf{u}^{j+1}$, $\mathbf{d}^j \leftarrow \mathbf{d}^{j+1}$

    $\mathbf{K}_u^j \leftarrow \mathbf{K}_u^{j+1}, \mathbf{R}_u^j \leftarrow \mathbf{R}_u^{j+1}$

    No update of H or $\bar{\alpha}$

Note that conversely to the initial algorithm, the displacement field is initialized as the nil vector, because this treatment is better suited to the next accelerations tools (adaptive mesh refinement, and cycle jump). Consequently the initialization of $\mathbf{K}_u$ and $\mathbf{R}_u$ is trivial. Then, those terms are updated during the global convergence check.

3.2 Cycle jump method in a phase-field framework

3.2.1 Accelerating fatigue time discretization

The need for cycle-by-cycle computation is not common to all numerical approaches for fatigue crack propagation. For instance, when fatigue is modeled through an empirical model, such as the Paris' law [68, 83, 84], "time" advancement is driven by Δa [68] or ΔK [83], which tends to regroup thousands of cycle, in one crack advance. On the contrary, if it is modeled through the phenomenological representation of the physical mechanisms driving crack propagation (which is usually the case with CDM or PF models), it requires the explicit computation of all cycles. Furthermore, as those fatigue models tend to yield complex non-linear evolution laws, the cycles must be divided into several load steps. In this regard, fatigue is a two-time scale approach. On the one hand, understanding the changes operating at the scale of a single cycle is crucial and influences the behavior at the macroscale. On the other hand, this macro time scale is composed of as much as 10^7 cycles which means that a cycle by cycle approach can result in excessively long computing times. Consequently, several approaches have been put forward by the concerned literature to treat this multi-scale issue.

In this context, continuum damage mechanics benefits from a large literature of several model reductions approaches, that seek to compute a minimal amount of small time scale operations while recovering the large time scale behavior. One of the largest category of such methods are based on the partition of the different difficulties of the formulation. For instance separation of local/global equations and linear/nonlinear systems in the LATIN approach [4, 27, 136–138, 210], where the whole time-frame is treated as one. Or separating micro and macro-time such as with temporal homogenization methods [64, 95]. Inspired by material homogenization approaches, these approaches drive the evolution of macro-time scale quantities with the homogenization of the micro-time scale quantities [204].

Then, we can also mention the approaches developed in a ductile framework, where the idea is to reach an approximation of the asymptotic state without the explicit computation of all cycles: so-called direct cyclic methods [23, 157, 197, 233]. Note that these approaches usually rely on the decomposition of the model, and model reduction as in the LATIN method.

Then, a very popular approach is the cycle jump, or cycle skipping technique. The idea is to skip large blocks of ΔN cycles by extrapolating the behavior computed over N "control cycles". Computing these control cycles provide insight into the evolution of quantities. Based on this information, a specific extrapolation method must be selected to maintain

the accuracy of the solution. Considering that the global behavior of high cycle fatigue remains stable during a large part of the crack propagation phase, authors expect to obtain large computing savings while maintaining an acceptable level of precision. One of the first work on this matter was put forward by Lemaitre & Doghri [145], with a first order extrapolation scheme and where ΔN is driven by the increment of the internal variables in order to keep a set level of accuracy. Then, Kiewel et al. [126] proposed a Runge-Kutta extrapolation scheme, and Fish and Yu [72] a forward Euler one-step scheme. Several other continuum damage approaches where accelerated with such methods, for example see Refs. [56, 187, 195, 216, 246].

Recently, considering the cycle by cycle treatment of most phase-field fatigue extensions, multiple authors have proposed the application of cycle jump schemes with the phase-field model [130, 151, 221, 225, 261]. Each of these approaches use different extrapolation schemes, and a specific accuracy criterion in order to jump an appropriate amount of cycles. Inspired by these authors, this section is dedicated to the introduction of a cycle skipping scheme that is relevant to the present phase-field fatigue extension and the application of two extrapolation schemes on simple numerical samples.

Note that another alternative approach to these model reductions methods already exists in the phase-field fatigue literature to avoid the explicit computing of every cycles. For some authors, the idea is to express the phase-field equations as a function of the cycles [94, 148, 162, 221]. Furthermore, other authors proposed to avoid computing multiple time-steps per cycle by considering the "envelope" of the cyclic loading [130, 221, 261]. In these works, the extrema of the loading are used to setup an equivalent load, which summarizes the cycle loading in one single time step. For instance in Kristensen et al. [130], a "constant load accumulation method" is put forward. The accumulation of the fatigue internal variable is computed in one time step at each cycle, by taking the value of the load ratio and the loading amplitude into account. This approach enables the author to significantly decrease computing time by reducing the number of increment per cycle. However, as is stressed in the mentioned work, this is only applicable for very simple periodical loadings. Note also that these approaches can easily be coupled to cycle skipping techniques, and could hence be adopted along the proposed framework.

3.2.2 Implementation of a cycle jump scheme

We can reduce the setup of a cycle jump scheme to two steps. First the choice of the quantities being extrapolated, and then the choice of the extrapolation scheme.

3.2.2.1 Choice of extrapolated quantities

Some authors argue for the extrapolation of all unknown quantities [1, 126, 151, 246]. However these approaches are based on more complex phase-field formulations, with plastic effects for LCF, and additional internal variables for elastomers in Loew et al. [151]. With the chosen elastic fatigue context, we opted for a simpler approach, where only one variable is extrapolated, in order to reduce the error due to the cycle jump extrapolation. In the proposed context, only two variables are not directly computable from the other quantities: $\bar{\alpha}$ and H. The fatigue history variable can be used alone to find all other unknowns *i.e.,* $\bar{\alpha}$ yields a value for $f(\bar{\alpha})$ from which d and then u can be computed back. On the other hand, the history field H at $N + \Delta N$ is not needed to initialize the problem: only its value at N is needed in order to check irreversibility by comparing it to the newly computed $H_{N+\Delta N}$.

We therefore chose to drive cycle jump with one parameter: the fatigue history variable. This was also performed in a continuum damage mechanics context using a damage parameter in Refs. [145, 187, 196], and in a phase-field context using the phase-field parameter or the fatigue history variable in Refs.[130, 221, 225, 261].

Note that the choice of the fatigue history variable was also motivated by the fact that it is a very appropriate variable to use in a cycle jump context. First, it evolves in a regular manner with respect to elapsed cycles, making a single control cycle representative of its general behavior. This is not true for the damage field, which has a tendency to remain almost constant, before localizing abruptly in the zones where the toughness of the material has been degraded. Secondly, the fatigue history variable has no threshold, which has to be numerically induced. Again this statement is not verified for the damage field which has to be artificially bounded if it is used as an extrapolated quantity to avoid $d > 1$. This artificial threshold is mostly problematic with the iterative scheme put forward in Loew et al [151], that is proposed in the next part. In this iterative context, where prediction is based on Δd, inducing a threshold yields abrupt variations of Δd which are not compatible with an iterative scheme.

3.2.2.2 Forward Euler extrapolation scheme (FE)

One of the simplest approach to estimate the evolution of the fatigue history variable is to consider its variation at current cycle N and extrapolate on ΔN cycle, therefore, a forward Euler scheme analogous to a first order Taylor development:

$$\bar{\alpha}_{N+\Delta N} = \bar{\alpha}_N + \Delta N \left(\dot{\bar{\alpha}}_N\right) \ , \tag{3.3}$$

This scheme was used by a large part of the literature, *e.g.,* [130, 145, 151]

3.2.2.3 Trapezoidal iterative extrapolation scheme (TI)

Inspired by Loew et al.'s application of implicit cycle jump for their phase-field elastomers approach [151], an implicit extrapolation scheme was introduced. Here, implicit means that we use information from one control cycle at N, before the cycle jump, and information from one control cycle at $N + \Delta N$, after the cycle jump. As performed in Ref. [151], we employ a trapezoidal extrapolation scheme:

$$\bar{\alpha}_{N+\Delta N} = \bar{\alpha}_N + \frac{\Delta N}{2} \left(\dot{\bar{\alpha}}_N + \dot{\bar{\alpha}}_{N+\Delta N}\right) \ , \tag{3.4}$$

with the quantities represented in Fig. 3.11, a scheme of the used cycle jump approach, we can define the terms of this expression as follows:

$$\dot{\bar{\alpha}}_N = \bar{\alpha}_{N+1} - \bar{\alpha}_N \ , \tag{3.5}$$

$$\dot{\bar{\alpha}}_{N+\Delta N} = \bar{\alpha}_{N+\Delta N+1} - \bar{\alpha}_{N+\Delta N}. \tag{3.6}$$

A Newton-Raphson scheme is implemented to search iteratively an extrapolated value of $\bar{\alpha}_{N+\Delta N}$ that enforces this trapezoidal extrapolation rule. Equation (3.4), combined with eq. (3.5) and (3.6) gives us the following cycle jump residual:

$$R_{cj} = \bar{\alpha}_N \cdot \left(1 - \frac{\Delta N}{2}\right) + \left(\bar{\alpha}_{N+\Delta N+1} + \bar{\alpha}_{N+1}\right) \cdot \left(\frac{\Delta N}{2}\right) - \bar{\alpha}_{N+\Delta N} \cdot \left(1 + \frac{\Delta N}{2}\right) = 0 \ , \tag{3.7}$$

and the next estimate of the Newton-Raphson scheme, with iterations of index k, is given by:

$$\bar{\alpha}^{k+1}_{N+\Delta N} = \bar{\alpha}^{k}_{N+\Delta N} - \left(\frac{\partial R_{cj}}{\partial \bar{\alpha}}|_{N+\Delta N}\right)^{-1} \cdot R_{cj}. \tag{3.8}$$

The residual operator from the Newton-Raphson scheme, a tangent operator used in the iterative search, is expressed as follows:

$$\frac{\partial R_{cj}}{\partial \bar{\alpha}}|_{N+\Delta N} = \frac{\partial \bar{\alpha}_{N+\Delta N+1}}{\partial \bar{\alpha}_{N+\Delta N}} \cdot \left(\frac{\Delta N}{2}\right) - \left(1 + \frac{\Delta N}{2}\right). \tag{3.9}$$

As in Ref. [151], the only remaining unknown term is $\frac{\partial \bar{\alpha}_{N+\Delta N+1}}{\partial \bar{\alpha}_{N+\Delta N}}$, meaning the variation of the extrapolated quantity at the end of a cycle with respect to the variation of the Newton-Raphson estimate of the quantity at the beginning of the cycle. Using eq. (2.27), we can express the cumulated mechanical energy α_{N+1} at the end of a cycle as:

$$\bar{\alpha}_{N+1} = \bar{\alpha}_N + \int_N^{N+1} \langle \dot{\alpha} \rangle^+ \, \mathrm{d}t. \tag{3.10}$$

We neglect the influence of $\bar{\alpha}_N$ on the evolution of α during a cycle, which is small compared to its cumulated value, yielding a very simple expression for the tangent operator (3.9) as $\frac{\partial \bar{\alpha}_{N+\Delta N+1}}{\partial \bar{\alpha}_{N+\Delta N}} = 1$.

The full algorithm for this iterative cycle jump scheme is presented in Alg. 3. At the first step, we only have information on the control cycle N. The first estimation is considered with a FE extrapolation scheme 3.3 to obtain a first estimate at $N + \Delta N$.

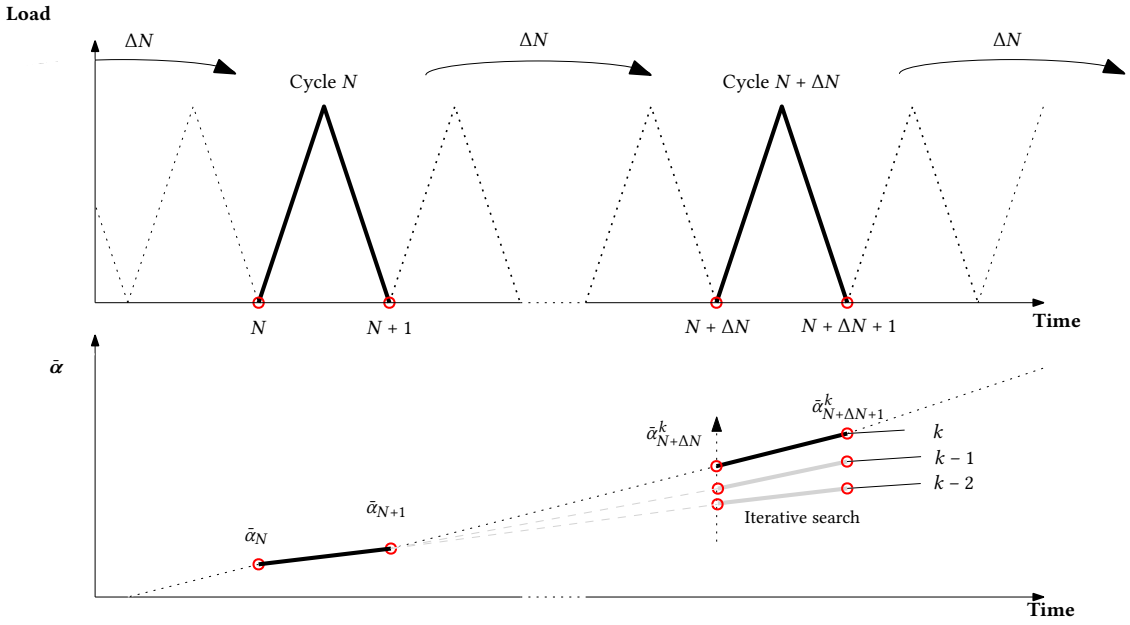

Figure 3.11: Illustration of the iterative cycle jump scheme with two graphs. We first represent the cyclic loading, with the computed cycles in bold (upper figure) and then the evolution of $\bar{\alpha}$ with respect to the elapsed cycle (lower figure). Two control cycles are initially computed, after which, the iterative scheme is used to search for $\bar{\alpha}_{N+\Delta N}$, yielding a new control cycle.

From this estimate, a control cycle at $N + \Delta N$ is computed to obtain an initial residual and start the presented Newton-Raphson iterative scheme. The iterative scheme is stopped when the maximum value of R^{cj} on the whole domain reaches a specific threshold. The user can then choose at which precision the trapezoidal extrapolation scheme is enforced. We

chose this precision criterion to be normalized by the initial value of $\bar{\alpha}_N^0$. The convergence criterion can be written as:

$$\max[R_{cj}^{\text{CONV}}] < \max[\bar{\alpha}_N^0] \cdot 10^{-6}. \tag{3.11}$$

Algorithm 3: Cycle jump scheme

Input: $\bar{\alpha}_{N+1}$, $\bar{\alpha}_N$

Output: $\bar{\alpha}_{N+\Delta N+1}$, $\bar{\alpha}_{N+\Delta N}$

Explicit prediction with eq. (3.3) to estimate $\bar{\alpha}_{N+\Delta N}^0$
Compute one cycle to obtain $\bar{\alpha}_{N+\Delta N+1}^0$
Deduce residual R_{cj}^0 with eq. (3.7)
$\bar{\alpha}_{N+\Delta N}^k \leftarrow \bar{\alpha}_{N+\Delta N}^0$ and $R_{cj}^k \leftarrow R_{cj}^0$
while *Criterion (3.11) is not respected* **do**
    Find a new estimate $\bar{\alpha}_{N+\Delta N}^{k+1}$ with eq. (3.8)
    Compute one cycle to obtain $\bar{\alpha}_{N+\Delta N+1}^{k+1}$
    Deduce residual R_{cj}^{k+1} with eq. (3.7)
Next computations initialized with
$\bar{\alpha}_{N+1} \leftarrow \bar{\alpha}_{N+\Delta N+1}$ and $\bar{\alpha}_N \leftarrow \bar{\alpha}_{N+\Delta N}$

It is interesting to note that for most simulated cases the initial step of fatigue crack propagation can be skipped with a very large ΔN. Indeed, until the fatigue degradation function $f(\bar{\alpha})$ becomes activated, *i.e.,* while $\bar{\alpha} < \alpha_T$, the evolution of $\bar{\alpha}$ is linear. This is used in Refs. [145, 225] to accelerate the initial phase of the simulation. In these works, the authors compute N control cycles to determine $\dfrac{\Delta\bar{\alpha}}{\Delta N}$ in this domain (which remains constant until degradation occurs). From this estimation, $N_{\text{deg}} = \dfrac{\alpha_T}{\Delta\bar{\alpha}}$, the cycle at which non linearity triggers, can be computed. Accordingly, we can jump to $N \leq N_{\text{deg}}$ without loss of accuracy [145, 225].

3.2.2.4 Investigation

As in the previous section, we have an explicit/implicit comparison: the issue is to quantify whether the trapezoidal iterative approach is more efficient than a forward Euler scheme. The former enabling to jump larger blocks of cycle, slowed by the consideration of multiple control cycles. While the latter provides a robust and efficient extrapolation scheme burdened by the limited amount of cycle that can be jumped at a given level of accuracy. We first illustrated the influence of those cycle jump schemes on the homogeneous sample, onto which, analytical expression of damage was detailed in eq. (3.1). A fatigue loading of

amplitude $\Delta\hat{u} = 10^{-3}$ mm and load ratio $R = 0$, was used: it was tuned to reach $d = 0.8$ at $N_{\text{tot}} = 10000$ cycles. The forward Euler scheme was first applied on the sample for jumps ranging from $\Delta N = 10$ to $\Delta N = 1000$. The average error on the damage field as a function of ΔN is illustrated in Fig. 3.12. This error was computed for $n = N_{\text{tot}}$ as:

$$Err_d = \frac{1}{n} \cdot \sum_{i=1}^{n} \frac{|d_{cj}^N - d_{\text{ana}}^N|}{d_{\text{ana}}^N}. \tag{3.12}$$

With this scheme, error is very dependent on the value of ΔN, but we see that as $\Delta N/N_{\text{tot}}$ decreases, a satisfactory level of precision can be reached.

Similarly, the trapezoidal iterative scheme was applied on the sample, and the average error as a function of prescribed ΔN was plotted in Fig. 3.12. For $\Delta N > 300$, convergence issues are reported with this iterative scheme. With lower values of ΔN, the prescribed threshold of eq. (3.11) enabled a steady error of 0.3%, regardless of the used ΔN. However, with this scheme, multiple iterations are required at each cycle jumps in order for the trapezoidal scheme to converge. Consequently we introduce ΔN_{eff}, the effective cycle jump, expressed as the ratio between total life and the number of computed cycles N_{calc}:

$$\Delta N_{\text{eff}} = N_{\text{tot}}/N_{\text{calc}}. \tag{3.13}$$

With a FE scheme, $\Delta N = \Delta N_{\text{eff}}$, but with the TI approach we can modify Fig. 3.12 by considering the effective cycle jump. Note that for the higher values of ΔN, the scheme's ΔN_{eff} stabilizes at 150. In order to reach this level of precision with the FE scheme, $\Delta N_{\text{eff}} = 20$ should be prescribed, yielding a less efficient cycle jump scheme on this specific sample.

Following this simple case, we investigated a non-homogeneous sample, already introduced in Section 2.4: the mode I crack in an infinite medium. A fixed mesh was used, refined prior to the simulation on the expected crack path. A cyclic stress was enforced on its upper boundary with a loading ratio of 0 and a load amplitude of $\Delta\sigma_2 = 40$ MPa. As in the previous case, we compared both extrapolation schemes. The resulting crack area for trapezoidal extrapolation and forward Euler were illustrated in Fig. 3.13a and Fig. 3.14 respectively. On Fig. 3.14 we see a strong dependency of the accuracy of the solution on the prescribed ΔN with the FE scheme. Conversely, the TI scheme is able to recover cycle by cycle results almost independently of ΔN, as observed previously and in Ref. [151]. However, it suffers from convergence issues if a large ΔN is used, as shown in Fig. 3.13b. Indeed, for larger number of jumped cycles, a larger number of implicit iterations is

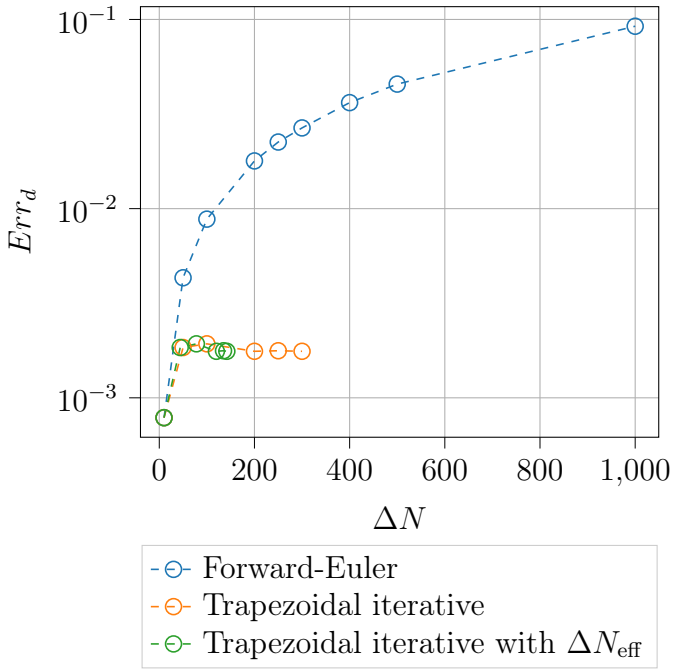

Figure 3.12: Error as a function of the jump ΔN and ΔN_{eff} to reach $N_{\text{tot}} = 10000$ cycles.

required. At ΔN values of 240 and 120, which correspond to approximately 10% and 5% of the computed lifetime respectively, non-convergence issues were observed at 700 cycles and 1700 cycles. The non-convergence issues observed at these cycles indicate an acceleration in the rate of fatigue crack propagation. This finding highlights the potential benefits of setting an adaptive value for ΔN using a criterion such as the one described in Ref. [151]. However, we used a simpler approach here: in the event that non-convergence was observed in the cycle jump iteration scheme, we reset the computed time step by using a smaller ΔN value. The value of the prescribed cycle jump was hence driven by the number of iterations of the trapezoidal scheme. Using this adaptive ΔN, we compared both schemes on $N_{\text{tot}} = 2500$ cycles. The error was defined as:

$$Err_{A(d)} = \frac{1}{N_{\text{tot}}} \cdot \sum_{N=1}^{N_{\text{tot}}} \frac{|A(d)_{cj}^{N} - A(d)_{\text{cycle}}^{N}|}{A(d)_{\text{cycle}}^{N}}, \tag{3.14}$$

hence simply substituting damage in eq. (3.12), by the area of the crack, and comparing, results with a cycle by cycle approach, to results with cycle jump. Furthermore, in order to get a better idea of error in the last stages of fatigue crack propagation, we also use the maximal value of this error during propagation. These data were compiled in Table 3.1. Note that we used the concept of ΔN_{eff} to provide a suitable comparison between both extrapolation schemes. We observed that the ΔN_{eff} of the trapezoidal scheme was always

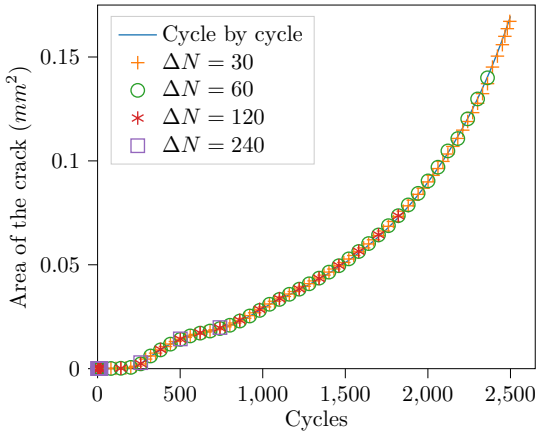

(a) Area of the crack computed for different ΔN with a TI scheme.

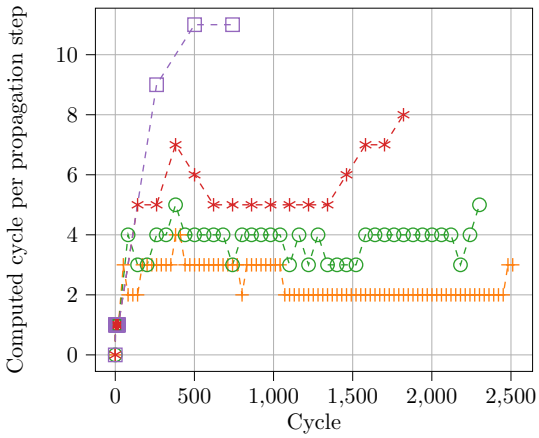

(b) Cycles computed per propagation step.

Figure 3.13: Study of the influence of ΔN with TI scheme.

around $\Delta N_{\text{eff}} = 12$, and yielded an average error bounded by $0.6\% < Err_{A(d)} < 1\%$. With the forward Euler scheme, an average error below below 1 % is reached for $\Delta N_{\text{eff}} < 10$. Both scheme hence enabling to significantly reduce computing time drastically. In this table, the acceleration factor was defined as a cycle by cycle computing time T^0 over cycle jump accelerated computing time T^{cj}.

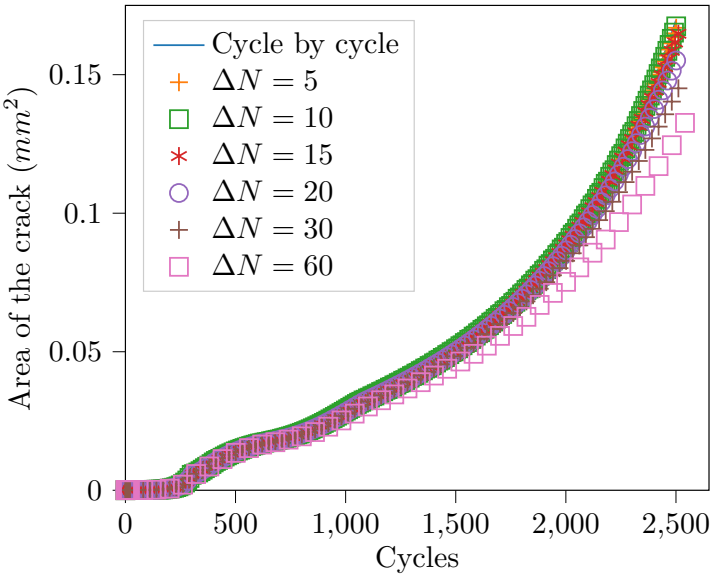

Figure 3.14: Area of the crack computed for different ΔN with a FE scheme.

Notice that ΔN_{eff} is not directly related to the gains in computing time for trapezoidal and forward Euler scheme. This means that the application of the cycle jump schemes lengthen some steps of the procedure. This is the result of a combination of factors: a longer

convergence of some individual cycles after the jump, length of diverse operations linked with cycle jump, and the time used for data transfer between these diverse subroutines.

With this analysis we see that both approaches are viable to accelerate significantly computing time as shown in multiple work aiming for the acceleration of phase-field fatigue computation [130, 151, 225]. Nevertheless, we want to stress the fact that the iterative scheme benefits from its implicit nature in multiple ways. First, as can be observed in Fig. 3.14, and with the maximum error, the forward Euler scheme starts to deviate significantly from the solution at the end of the computed lifetime. Average error with this scheme is largely influenced by the initial stages where the scheme provides very accurate prediction. However, it seems to be much less adapted to the last stages of fatigue crack propagation than the proposed iterative scheme. The application of this approach in a general framework would hence require the design of an adaptive ΔN approach, which is directly available with the trapezoidal extrapolation scheme. Nevertheless, note that the trapezoidal criterion is not absolute, and that a large enough ΔN value can lead to an overshoot of the computed solution, yielding completely spurious results. But its implicit nature has a tendency to stabilize the solution.

Further investigations on the extrapolation scheme and ΔN criterion, for the acceleration of the cycle jump process, were led in the context of cycle jump with AMR in Section 3.4. We refer the interested reader to the following Refs.[43, 130, 151, 216], which explore these questions without the AMR framework. In the same vein, we save the application of these extrapolation schemes on more complicated cases for the next section, as this work's novelty comes from the application of cycle jump in the AMR context.

Table 3.1: Efficiency improvements compared to cycle-by-cycle calculation, on a fixed mesh.

Loading case	ΔN	ΔN_{eff}	Average error	Maximum error	Acceleration factor (T^0/T^{cj})
TI	30	11.40	0.6%	2.4%	7.76
TI	60	12.1	0.4%	2.1%	6.92
TI	120	13.1	0.7%	2.1%	7.07
TI	240	12.5	1.0%	4.9%	6.24
FE	5	/	0.8%	2.2%	4.01
FE	10	/	0.7%	2.7%	6.45
FE	15	/	1.3%	4.2%	9.28
FE	20	/	2.6%	8.2%	12.04
FE	30	/	5.2 %	15%	17.04
FE	60	/	10.5 %	24%	28.41

3.3 Adaptive mesh refinement in a phase-field framework

Adaptive mesh refinement strategies are frequent in crack propagation modeling with a finite element framework because of the very local nature of the damage mechanics. Only a limited part of the structure under study exhibits nonlinear behavior, with high gradient zones localized in that area. To capture the mechanisms driving crack propagation, different levels of mesh refinement are used: coarser elements far away from the damaged zone and finer elements in the vicinity of the crack. For instance, we have been applying this method on all used mesh, as a pre-refinement was prescribed around the a-priori known damaged zone, while coarser elements were set on the rest of the domain. Such a compromise must be made between the discretization error and the computing ressources at hand, for real life application of the approach. This adaptive method leads to a significant increase in computational efficiency by allowing the optimization of the number of degrees of freedom while maintaining the accuracy of the numerical solution.

Furthermore, since the path of the cracks is often unknown in advance, the ability to adapt the mesh during crack propagation is a valuable technique for further reducing computational effort. The idea in this case is to refine or coarsen the finite element mesh during the propagation based on error estimators [267], or other physically based criteria [83]. For instance, we can cite multiple references that use mesh optimization methods to model crack propagation, such as a combination of XFEM and a localized multi-grid approach [191, 207], or XFEM and adaptive mesh refinement [83].

In phase-field modeling different refinement levels should also be used, as d varies between 0 and 1 very abruptly in a local zone whose size is driven by l_c. Multiple analyses of the numerical errors related to space discretization of the phase-field model can be found in the literature [165, 176]. In this last reference, the authors cite two sources of discretization error: the usual approximation error (that originates from the discrete approximation of a continuous domain), and the strain localization error, (both illustrated in Fig. 3.16).

A fine mesh size is required in the damaged zone to capture the gradient of d, as was analyzed in Miehe et al. [165], where the author showed that $l_c/2 > h$ suffices to recover analytical results. For instance we have reproduced the test carried by the cited authors, with the damage analysis of the cracked square plate as explained in remark 2.1 of Section 2.1.2.2. Γ_0 stands for the analytical crack area, while Γ is the phase-field computed crack area. We illustrated the computed error as Γ_0/Γ in Fig. 3.15. The converging ratio

$l_c/2$ was recovered along with the influence of the relative size of h and l_c to the size of the sample: for larger l_c, Γ convergence is not recovered, yielding a deviation with the analytical result, which is not linked to a discretization error.

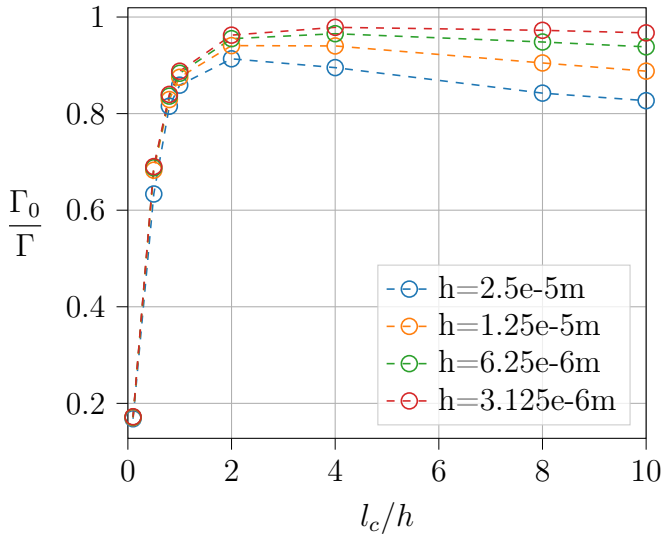

Figure 3.15: Illustration of numerical approximation as a function of l_c/h, as in Ref. [165].

Moreover, when damage interacts with the mechanical problem, it does so through the integration points of the finite element mesh, creating a new source of mesh dependent error, labeled as strain localization error in Ref. [176]. Applying deformation on a nodally induced damaged mesh will not yield a strictly broken material because damage in the mechanical response is taken into account at the integration point of the mesh. Consequently, the elements conserve a residual stiffness until d has reached 1 in the whole element. This induces a mesh dependent increase of the crack area [176]. The localization error can be minimized by enforcing larger l_c/h ratios, as far as 8.

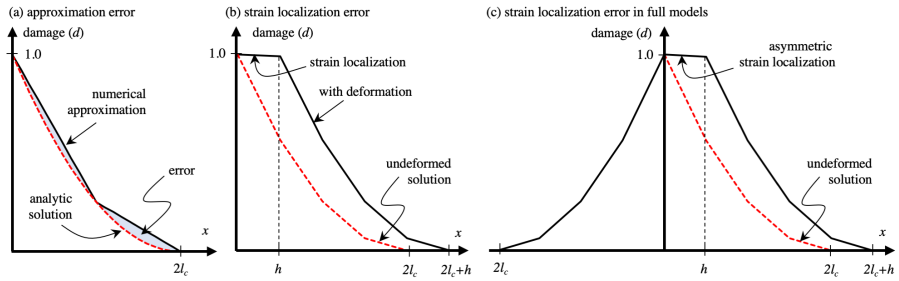

Figure 3.16: Visualization of usual discretization approximation error (a), and integration point coupling induced localization error (b), by Molnár et al. [176].

In this context we illustrated what $l_c/8$ refinement level means in term of required mesh

refinement on a standard benchmark in Fig. 3.17. Here we applied it on the single-edge notched sample with the parameters used in Section 2.4. Here $l_c/8$ is prescribed in a specific radius around the crack. Note the huge ratio between coarse and finer elements. This illustrates why adaptive mesh refinement tools have been implemented to make the method practical for industrial applications. We recall that as crack path is usually a-priori unknown, such a high level of refinement can be necessary across the entire numerical sample, yielding unpractically long computing time.

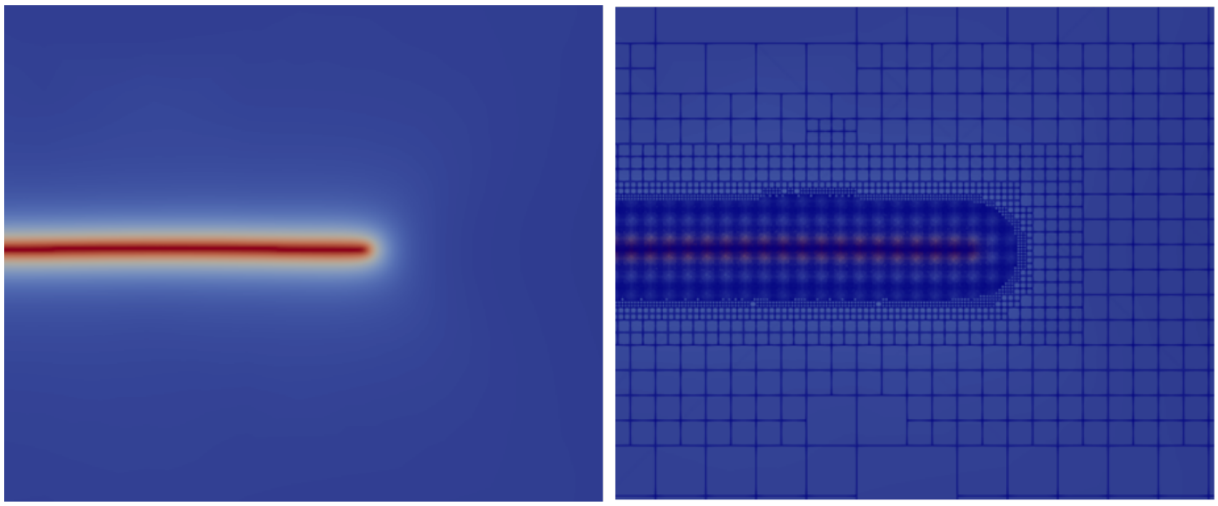

Figure 3.17: Illustration of the level of refinement required around the crack for a phase-field model.

In order to avoid this issue, several authors proposed AMR in a phase-field context. Heister et al. [103], used AMR on a phase-field model for brittle fracture. In this work, a predictor-corrector approach driven by a damage criterion was used and has shown its ability to maintain accuracy, even in the challenging context of unstable crack propagation. Thereafter, similar predictor-corrector approaches were proposed, that also reliant on a damage criterion [140], or on a mechanical energy criterion [128]. Following these initial works, a plethora of damage-driven methods have since been proposed such *e.g.,* [2, 18, 177, 179, 265], along with Ref. [127, 215], where multiple damage thresholds were defined to smooth out the mesh transition. In Tian et al. [244], a novel a-priori approach was introduced, that relies on the localization of the crack tip, to build a relevant fine mesh around the crack tip. Note that mesh coarsening is used in this last work. It is used to coarsen elements, which were initially predicted to be part of the process zone, but where damage has not localized. On the contrary, the authors estimate that the rest of the damaged zone has to remain finely mesh to capture the gradient of d. This contrasts with

usual AMR approaches for discrete applications of fracture mechanics, where coarsening operations can fully be applied in the wake of the crack tip [84]. Consequently, no coarsening was attempted in this work, even though a finer investigation of the possibilities of mesh coarsening could greatly increase computing gains.

More recently, several energy-based criteria specific to phase-field simulations have been highlighted [78, 97, 107]. Furthermore, sophisticated phase-field specific error estimators, in line with usual AMR estimators, have been studied [17, 108, 158, 253]. These approaches require the creation of additional fields to estimate the discretization error, but benefits from an optimal convergence rate of the mesh. They were not attempted in this work.

The following section describes the mesh refinement tools that have been implemented to combine the cycle jump scheme with adaptive mesh refinement in the context of phase-field fatigue simulations. The refinement method and projection operator are introduced, followed by the specification of the refinement criterion that was used during the mesh adaptivity process.

3.3.1 Mesh refinement method

Following Ref. [83], we used hierarchic h refinement: to obtain a given mesh size, coarser elements were subdivided into 2^D finer elements. In 2D, one square element was divided into $2^2 = 4$ elements, in 3D, it was divided into $2^3 = 8$ elements. An illustration of this type of refinement is provided in Fig. 3.18a.

Furthermore, it should be noted that this hierarchic refinement is non-conforming, meaning that every new subdivided element adds a number of so-called "hanging-nodes", *i.e.,* nodes that do not respect the continuity of the finite element mesh. They are illustrated in Fig. 3.18b. To enforce the compatibility of these nodes with the rest of the mesh we set displacement and damage to be linear combinations of the neighboring nodes displacement and damage using Lagrange multipliers. More details on the used operations can be found in references [83, 108]. This Lagrange multipliers approach for the treatment of continuity is used in Cast3M mesh refinement operators [46]. Note that this hierarchic approach is very similar to other works in phase-field AMR [103, 107, 108, 127]. Alternatively, other authors use hierarchic non-conformal refinement with a Nitsche approach to enforce continuity [177]. The hierarchic, non-conforming refinement approach presents numerous benefits within the context of an adaptive mesh refinement framework. Firstly, it makes it possible to keep a memory of original coarse elements, and their different subdivided parts, enabling easy implementation and data structure [107, 203]. Moreover, this refinement technique

simplifies the transfer of fields when restricted to mesh refinement, as each finer element is fully contained within a coarser one. Indeed, as field transfers are supported by the finite element shape functions, we find that the hierarchic refinement method enables a trivial link between the shape functions of coarse and fine elements.

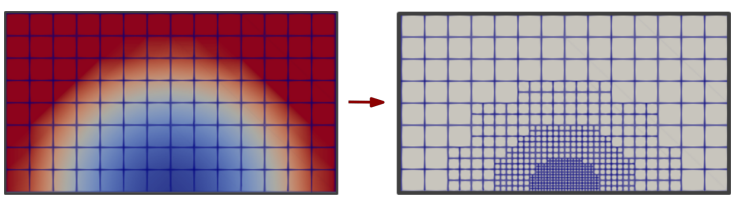

(a) Visualization of the hierarchic refinement tool, with an initially coarse mesh and associated element density (left) and the resulting successively subdivided refined mesh (right).

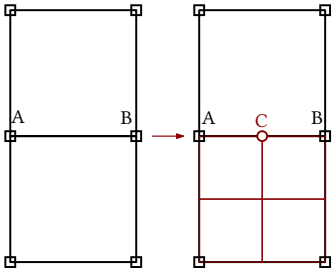

(b) Illustration of the hierarchic h refinement and resulting hanging node C.

Figure 3.18: Figures illustrating non-conforming hierarchic h refinement.

3.3.2 Projection process

As the crack propagates, new successive meshes are built to optimize the number of degrees of freedom in real time. This means that for every new refinement steps, all quantities defined in the phase-field fatigue framework have to be transferred or re-computed on each new successive mesh patterns. Multiple considerations enter in this choice of which field to transfer. First, note that projection operations are usually much faster than the resolution of a propagation step (which is necessary when recomputing rather than projecting). However, usual projection approaches entails that the resulting fields do not satisfy the balance equations, which can yield inaccurate results. In this work, such approaches were initially not attempted because the elastic framework and the choice of the hierarchic refinement method yielded very accurate transfer of the fields that did not disrupt significantly the accuracy of the computed solution.

In fact, we notice that field transfer are scarcely mentioned in the AMR phase-field literature, surely because this step has not yet proven to be an issue with the tested phase-field models. Nevertheless, is might arise in ductile contexts or with more specific couplings. For instance, authors report the need for balancing steps [83, 161], or more complex projection approaches [24, 41, 83] where the unification of balancing equations is integrated to the projection process.

As mentioned in the previous section, all fields can be recomputed except for $\bar{\alpha}$ and H, which hence have to be projected. Furthermore, d was projected as well considering the

computing gains of projecting over re-computing. Therefore, two kinds of fields have to be projected: nodal fields and internal variables defined at the integration points of the finite element mesh. The former can be trivially interpolated on the newly defined nodes, using their shape function support [24, 198]. However, the integration point quantities required a specific projection operator, because they are not supported by the shape functions, and are hence only defined on the integration points.

In the elastic small displacement context, we followed the work in Ref. [198], where shape functions of the coarse elements were used to interpolate integration points quantities. Thus, we first transformed those fields into nodal equivalents, and used the coarse element shape function to interpolate the nodal components. Algorithm 4 illustrates this procedure which is a built-in function of Cast3M. The implementation was facilitated by the fact that refined elements are always contained within a larger coarse one [84]. Additionally, Fig. 3.19 illustrated the chosen process.

Algorithm 4: Projection of integration point quantities $\mathbf{a}$
$\rightarrow$ from a coarse mesh M^l to a finer mesh M^{l+1}

Input: $\mathbf{a}^l = (\bar{\alpha}_{M^l}, H_{M^l})$

Output: $\mathbf{a}^{l+1} = (\bar{\alpha}_{M^{l+1}}, H_{M^{l+1}})$

1 Coarse mesh M^l is refined into M^{l+1}

2 Integration point of coordinate $\mathbf{x}^{l+1}$ is contained into a coarse element E^l:

- with shape function vector $\mathbf{N}_l$

3 Nodal vector $\hat{\mathbf{a}}^l$ is constructed by solving $\int_{E^j} \mathbf{N}_l^T \mathbf{N}_l \hat{\mathbf{a}}^l \, \mathrm{d}V = \int_{E^l} \mathbf{N}_l^T \mathbf{a}^l \, \mathrm{d}V$

4 $\mathbf{a}^{l+1}$ is interpolated at $\mathbf{x}^{l+1}$ using $\hat{\mathbf{a}}^l$ and $\mathbf{N}_l$: $\mathbf{a}^{l+1}(\mathbf{x}^{l+1}) = \mathbf{N}_l(\mathbf{x}^{l+1})\hat{\mathbf{a}}^l$

The remaining fields were computed back from the interpolated quantities. In the context of cycle-by-cycle refinement, this projection process resulted in highly accurate outcomes. However, if this approach were to be applied to coarsening operations, a more sophisticated projection strategy would need to be developed.

Note that in the published article where we presented the simultaneous use of cycle jump and adaptive mesh refinement [115], we reported the need for a balancing step, after this transfer procedure. Indeed, conversely to the cycle-by-cycle context, the use of cycle jump induced a ΔN magnification of the inaccuracies of the field transfer, which we initially thought to have a large influence on accuracy in initial tests. However, after further investigation, we noticed that in a large majority of cases (namely the samples tested in the next section), this balancing step did not improve the accuracy of the solution in a significant way. Moreover, the implementation of the "recycling process" described

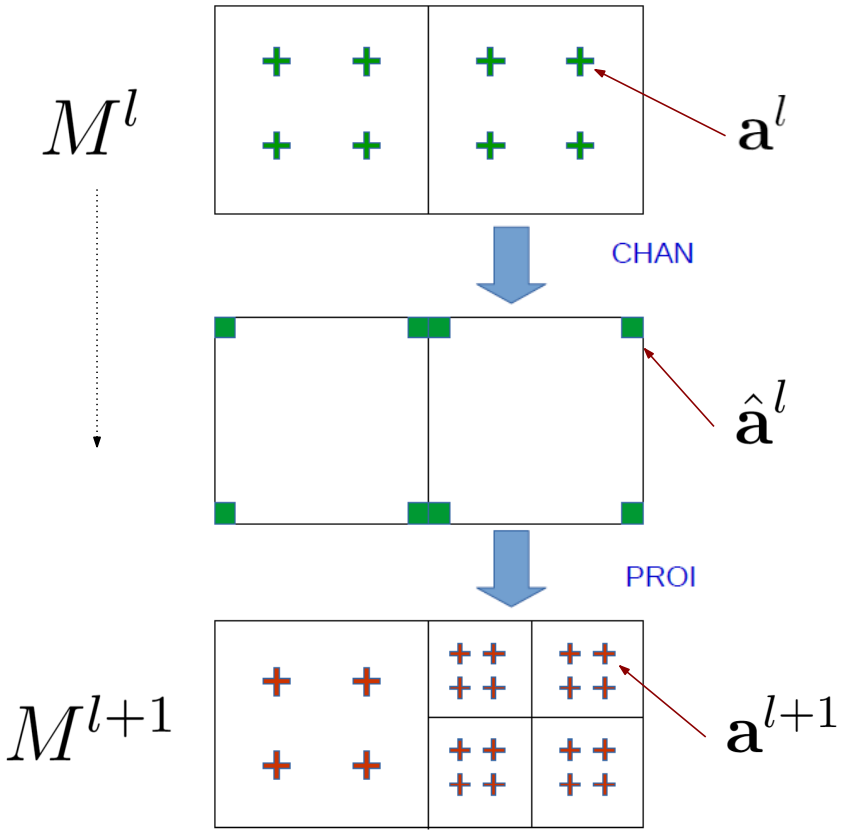

Figure 3.19: Schematics of the projection process for integration points defined quantities **a**, modified from Ref. [84]. "CHAN" is the subroutine performing step 3 and "PROI" is the subroutine performing step 4 of Algorithm 4 in Cast3M [46].

in the next Section. 3.4.2.3, avoids the issue of the ΔN magnification of the error with the trapezoidal scheme, by removing the initial forward Euler estimation after a mesh refinement step. Therefore, we did not need any balancing step in this work.

As irreversibility is enforced through the history field method introduced in Section 2.1.2.4, H is continuously compared to the computed mechanical energy to check irreversibility. However, such a local irreversibility verification is impossible from one mesh to another, as we cannot compare values on nodes/integration points that did not previously exist. As such, every time a new mesh is built, and the fields projected, we checked that $W(d)$ did not decrease. This verification was done on the global quantity $W(d)$ as we were unable to get local corrections on the history field. In practice, no reversibility of the damage field was observed in the application done in this work with adaptive mesh refinement.

3.3.3 Refinement criterion

Finally, it is necessary to establish a refinement criterion that, given a particular crack topology, will allow for the determination of a target mesh density that balances the number of degrees of freedom with an appropriate level of precision. In a finite element framework, one traditionally uses estimators relying on gradient quantities [267]. However, as noted before, in a phase-field framework we can assess that the critical field to describe is damage, and that most non-linear, high gradient evolution of the other fields (notably fatigue related internal variables) are located in this zone. These estimations allowed us to avoid using usual error estimators which usually requires the creation of additional fields to estimate discretization error during propagation [107, 158, 253, 267].

Instead, a simpler and more efficient criterion was thus set, as in most previously cited AMR phase-field references. As stated, high l_c/h ratios have to be reached in the zone where damage localizes in order to minimize the discretization error. In this fatigue context, we could also have used the fatigue related internal variables as a similar estimation of the damaged zone. However, such a choice would have hindered the application of the approach for brittle crack propagation, as fracture can occur in a zone where $\bar{\alpha} = 0$ (notably, in the last phase of fatigue crack propagation). Consequently, we set the following refinement criterion: if $d \geq d_{\text{AMR}}$, then $h = h_{\text{AMR}}$, with the parameters:

1. d_{AMR}: a threshold of damage that defines the boundary of the damaged zone,
2. h_{AMR}: a mesh size prescribed in this damaged zone.

At cycle N every element of the finite element mesh where at least one nodal value of d exceeds d_{AMR}, has to be of size h_{AMR}. Note that the illustrating Fig. 3.17 used these criteria. In this figure, we have set $d_{\text{AMR}} = 0.1$ and $h_{\text{AMR}} = l_c/8$. A smooth transition between the coarse area and the refined damage zone was achieved by refining successive layers of elements along the damaged zone, as described in the next Section 3.3.4. Therefore, it should be noted that elements for which d is under the threshold d_{AMR} may also be refined.

To choose the relevant criteria, we applied the material properties and loading defined in Section 2.4 for fatigue crack propagation on the SEN cyclically loaded sample. These criteria were checked at the end of each computed cycles, until the resulting mesh converged. This predictor-corrector approach inspired by Heister et al. [103] in a brittle phase-field context, will be further discussed in the next section. We studied the influence of both AMR criteria on the relative error in the crack area between AMR and initially refined meshes (PR). This relative error was defined as:

$$Error_{A(d)} = \frac{|A_{\mathrm{PR}}(d) - A_{\mathrm{AMR}}(d)|}{A_{\mathrm{PR}}(d)}. \tag{3.15}$$

Fig. 3.20 illustrates the error convergence rate with respect to d_{AMR} and h_{AMR} criteria. The plotted data in Fig. 3.20a suggests that the h_{AMR} criterion significantly impacted the accuracy of computed results. However, Fig. 3.20b shows that the precision was less affected by the d_{AMR} criterion as opposed to the h_{AMR} criterion. These results were expected [166, 172], as a very fine mesh size relative to the length scale was required in order to reach a decent precision. On the other hand, strong refinement further away from the damaged zone was less relevant in order to precisely compute the crack propagation, as illustrated by the low influence of d_{AMR} for $d_{\mathrm{AMR}} < 0.5$.

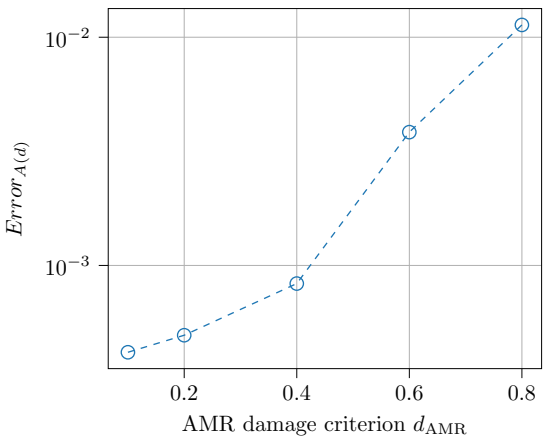

(a) Error convergence rate with respect to d_{AMR} ($h_{\mathrm{AMR}} = l_c/8$).

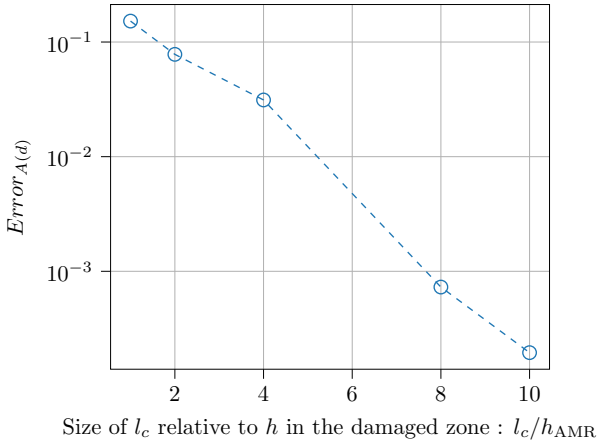

(b) Error convergence rate with respect to h_{AMR} ($d_{\mathrm{AMR}} = 0.1$).

Figure 3.20: Error convergence rate with respect to the mesh refinement criteria.

3.3.4 Smoothening process

In a hierarchic refinement setting, a coarse element might be divided into n smaller elements while its neighboring element remains coarse. This would introduce strong mesh distortion and yield less precise results, as is shown thereafter. To ensure a smooth progression of subdivisions in neighboring elements, we implicitly enforced a "2-to-1" constraint: if a fine element was divided into $n \cdot 2^D$ smaller elements, then its neighboring elements would be divided into $(n \pm 1) \cdot 2^D$. This results in only one "hanging node" (a node on a finer element that is not connected to a node on a coarser element) at each refinement transition.

Note that this smoothing process yielded asymmetric patterns of refined mesh even in the case of a seemingly symmetric damage field (Figs. 3.17, 3.24). Indeed, it was based on the

selection of elements bordering the located damaged zone. Such an automatic selection means that any small asymmetry of the damage field or initial mesh was magnified by the smoothing process. Nevertheless, as will be shown, this versatile implementation means that it can recover complex crack patterns without needing to locate the crack tip. This process was illustrated in Fig. 3.21. Applying this process in a context where a very important $h_{\text{coarse}}/h_{\text{fine}}$ ratio is used can yield meshes which do not respect the 2-to-1 ratio. Nevertheless, we have found that this approach was providing smooth transitions on a large amount of applications.

Using the accelerated properties cited in the previous section for the single-edged notched sample (hence, the fatigue crack propagation in 30 cycles from Ref. [131]), we plotted the influence of the number of layers used in this process on the computed crack propagation in Fig. 3.22. We see that the smoothening process is fundamental to recover accurate results, as the result computed without such transitions deviates significantly from the expected result. Notably, it delays nucleation at the initial notch. However, we see that the crack propagation rate remains analogous after this initial deviation. Furthermore, it seems that as much as four layers have to be used in order to fully converge with this mesh arrangement.

This result is surely dependent on the mesh structure and the $h_{\text{coarse}}/h_{\text{fine}}$ ratio. Therefore, on some of the cases presented in this work, you can notice that the enforced 2-1 ratio is not always satisfied. This is because in the context of very small l_c, compared to the size of the numerical sample (usually the case for real-life applications), this ratio is very important. With the used smoothening process, a layer of very coarse elements can be selected to be refined finely which yields very inefficient refined meshes (because large patches, far from the damaged zone, are refined finely). A compromise has to be found with the uniform mesh initially used at the beginning of the simulation to reduce $h_{\text{coarse}}/h_{\text{fine}}$, and avoid the formation of these fine patches, as in Fig. 3.24. Note however that using fine enough initial meshes, yielded very good robustness and accuracy of the scheme in all further applications, without further need for parameter adjustement.

3.3.5 Cyclically loaded single-edged notched with AMR

To end this subsection, we applied the adaptive mesh refinement tools, with converged AMR criteria, hence enforcing $h_{\text{AMR}} < l_c/8$ $d_{\text{AMR}} = 0.1$. We plotted the evolution of the crack in Fig. 3.23, and compared them to results computed on a pre-refined mesh, and results of the literature [44, 129]. We observed that the proposed mesh refinement tools

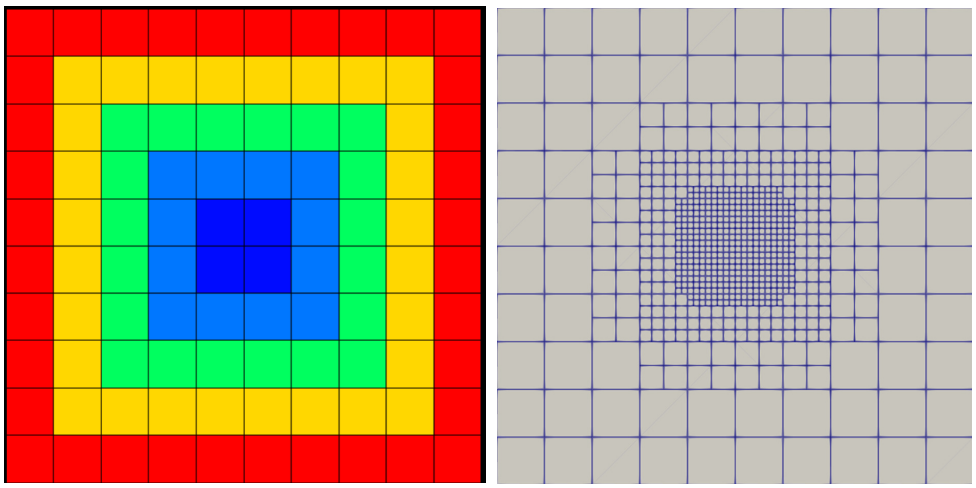

Figure 3.21: Vizualization of the smoothening process. The dark blue central zone is designated to be refined at $l_c/8$, while layers of elements are chosen around this zone to be subdivided at intermediate levels of refinement. These selected layers were here represented by different colors on the initially coarse mesh. On the left, is the refined mesh resulting from this process.

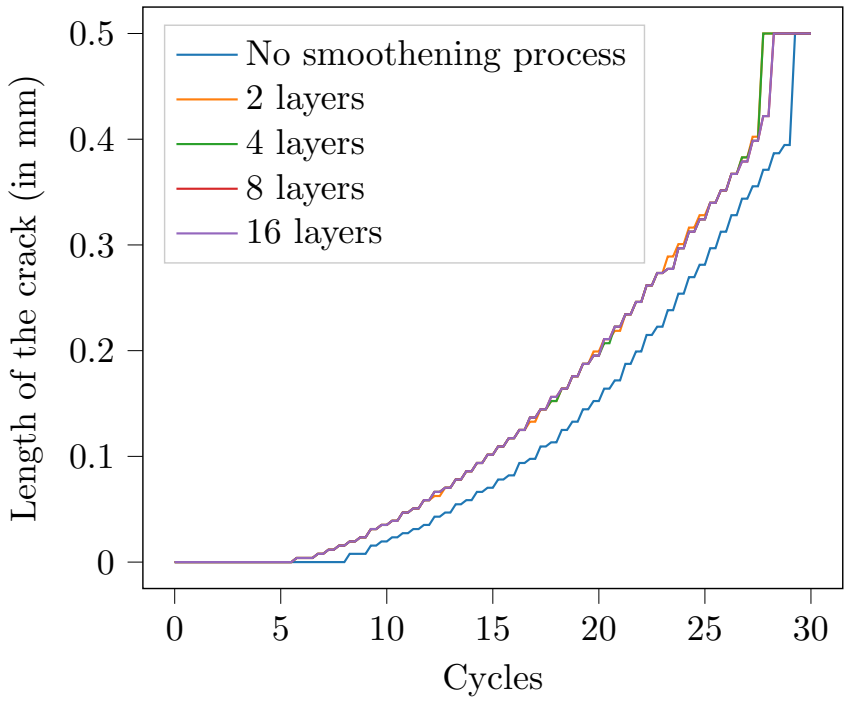

Figure 3.22: Influence of the smoothening process on computed crack propagation.

enabled a very accurate recovery of pre-refined results, while enabling to divide computing time by $\simeq 3.3$. This gain could be higher if we had considered that the propagation zone was not known in advance. Some illustrations of the refining mesh, and the compared pre-refined mesh were provided in Fig. 3.24. Note a small deviation between adaptively refined result and pre-refined result at the end of crack propagation, as crack growth rate is the most critical, and one AMR check per cycle may be too slow.

The application of the AMR framework on more complex cases is preserved for the next section where AMR and cycle jump are used at the same time.

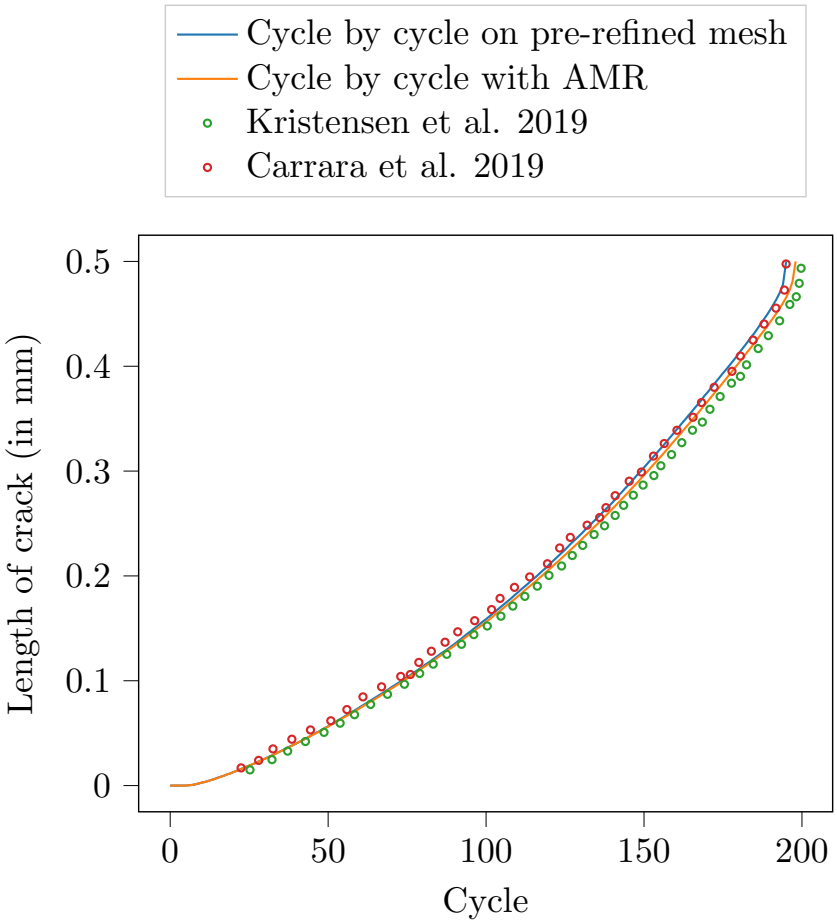

Figure 3.23: Length of the crack - comparison with fatigue phase-field literature (Refs. [44, 129]).

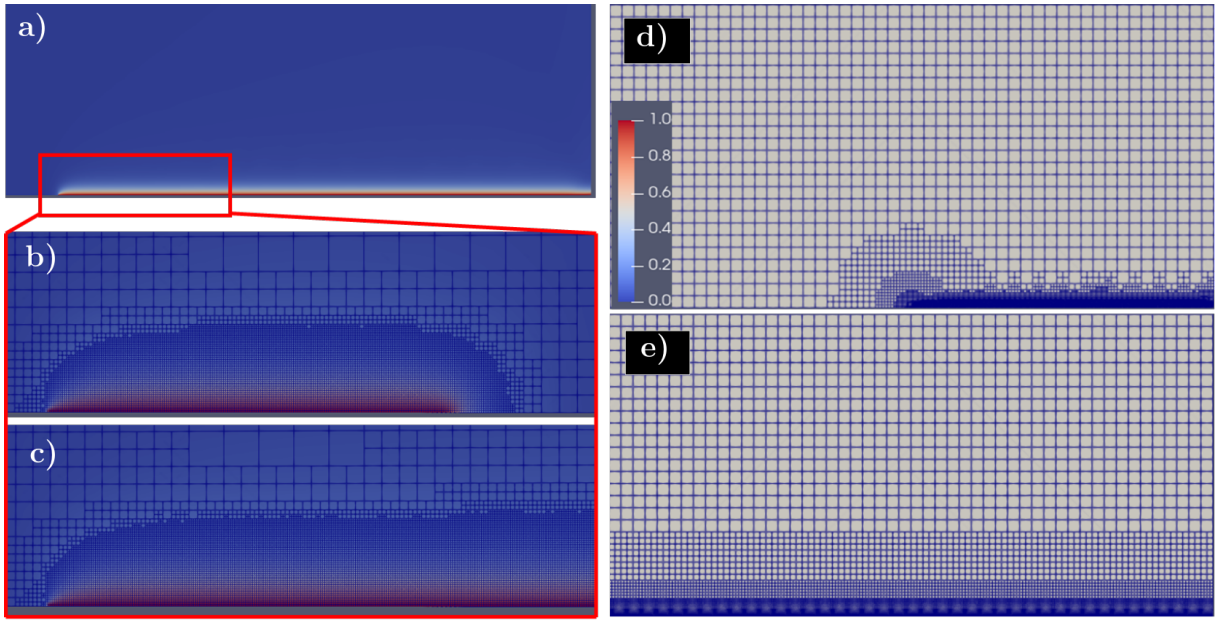

Figure 3.24: Visualization of the adaptive mesh refinement tools on the single edge notched specimen. a,b,c,d illustrate the adaptively refined solution. a) Damage field on the half-specimen b) Damage field and adaptive mesh in the red zone at cycle N = 50 c) Damage field and adaptive mesh in the red zone at cycle N = 100 d) Adaptively refined mesh at N=200 e) Fixed mesh refined prior to the simulation.

3.4 Adaptive mesh refinement and cycle jumps

In this section, we put forward the idea of combining cycle jump schemes with adaptive mesh refinement: the mesh is adaptively changed in order to reduce the number of degrees of freedom, while a minimal amount of cycles are computed on these reduced meshes. Optimization of space discretization and time discretization is thus executed simultaneously. Enabling this coupling in an efficient, robust and accurate manner is not trivial, and we will thus discuss the specifics of the implementation, accelerations tools, and limitations of the proposed framework. First, we set the propagation algorithm coupling these acceleration tools, then we compared efficiency and precision obtained for the two implemented extrapolation scheme. Then, additional ways to accelerate the coupling were put forward. Finally we observed the influence of this chosen scheme on the numerical samples investigated in Section 2.4, and some additional ones.

3.4.1 Proposed implementation

In a cycle by cycle fatigue framework, we could argue for the fact that an a-priori refinement criterion could be set-up considering the slow rate of crack propagation [244]. Meaning

that the defined criterion would be checked at the beginning of computed cycle to build a relevant mesh. However, using a cycle jump approach during the adaptive mesh refinement procedure could lead to accuracy issues with a-priori estimators, considering that in one AMR step a considerable amount of cycle are simulated, yielding important advances of crack propagation. In this context, using an a-priori strategy, such as in Refs. [83, 84, 244], we would run the risk of validating the convergence of the coupled phase-field problem, and the cycle jump procedure, on a non-converged mesh. Therefore, we employed the usual strategy that is applied in a brittle framework to capture unstable crack propagation [18, 103, 127]: an iterative AMR procedure that checks the mesh refinement criteria after the cycle jump procedure, in order to ensure that all operations carried out at a given propagation steps have converged spatially.

Note that an a-priori estimator could still be set up, but would likely require a considerable amount of parameter fine-tuning to guarantee accuracy of the solution on any given geometry. Considering that we are designing acceleration tools to be used in the context of complex crack patterns, we preferred an iterative strategy, which guarantees spatial and temporal convergence with the help of a-posteriori estimators. Additionally, with an a-posteriori estimator based on models for unstable crack propagation, we can expect to recover brittle and fatigue results in a unified framework: a property that the current fatigue model holds [44], and that would be interesting to keep with the accelerating framework.

Therefore, we propose the procedure illustrated in Algorithm 5, which is based on the verification of AMR criteria on quantities computed after the cycle jump, and an iterative approach until convergence of the mesh.

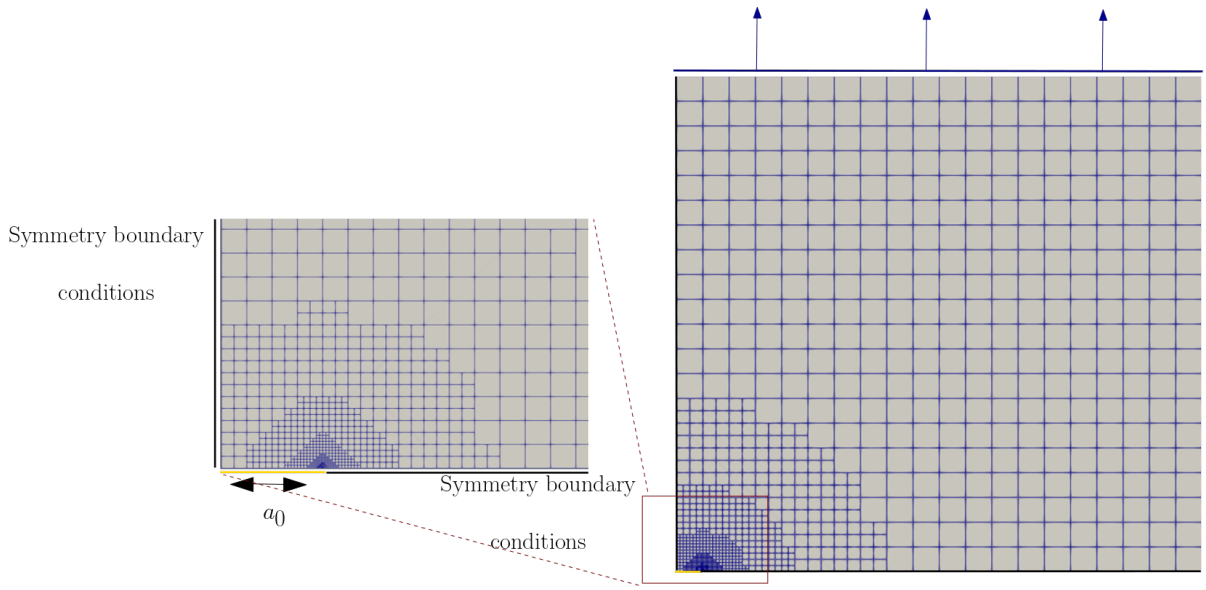

Figure 3.25: Mesh and used symmetries. Initial notch is indicated in yellow.

Algorithm 5: Cycle jump crack propagation with AMR

Input: $\bar{\alpha}_{N+1}$, $\bar{\alpha}_N$
Output: $\bar{\alpha}_{N+\Delta N+1}$, $\bar{\alpha}_{N+\Delta N}$
for $N = 1, N_{\max}$ **do**
  while *Refinement criterion is not respected* **do**
    Computation at cycle N: Alg. 2
    Cycle jump scheme to $N + \Delta N$: Alg. 3
    Check refinement criterion at $N + \Delta N$
    if *Remeshing is needed* **then**
      Remeshing operations
      Projection of the fields at N : Alg. 4
      Restart step (3) at N
    else
      Go to next computation step $N + \Delta N$ **quit**

3.4.2 Numerical investigation

3.4.2.1 Trapezoidal vs. Forward Euler

In a similar fashion to the cycle jump section, two extrapolation schemes were compared. However, this time, we added the adaptive mesh refinement framework. Therefore, the same numerical sample of a mode I crack in an infinite medium was used with the same

loading conditions, on a different initially refined mesh, illustrated in Fig. 3.25. The initial notch was refined at $h < l_c/8$, and then the mesh was refined during crack propagation, following $d_{\text{AMR}} = 0.1$ and $h_{\text{AMR}} < l_c/8$.

We compared the evolution of the crack area in Fig. 3.26a and Fig. 3.26b for the trapezoidal scheme and forward Euler scheme. Additionally the number of computed cycle per propagation steps for both schemes was plotted in Fig. 3.27. Finally a table comparing the computing gains and accuracy of both approaches was set-up in comparison to Table 3.1, in Table 3.2, where the acceleration factor was defined as unaccelerated computing time T^0 over cycle jump and AMR accelerated computing time $T^{\text{cj+R}}$.

In this section we extended the concept of $\Delta N_{\text{eff}} = N_{tot}/N_{computed}$ to the cycle jump and AMR context, in order to efficiently compare all the proposed implementations. Considering the described a-posteriori approach, it is possible to have multiple computed time-step per cycle. This means that a cycle by cycle approach yields a $\Delta N_{\text{eff}} < 1$. Furthermore, the forward Euler extrapolation scheme does not always yield $\Delta N = \Delta N_{\text{eff}}$.

As in the cycle jump section it is clear that the FE scheme's accuracy is highly dependent on the prescribed ΔN, while the TI scheme is able to recover accurate result almost independently of this parameter. Furthermore, the same non-convergence issue as in the cycle jump section was reported here, as with $\Delta N = 120$, the TI scheme chose a lower ΔN at $N \simeq 1700$. Furthermore, we noticed that a slightly larger error was made with cycle jump and AMR, as could be expected from this combination of acceleration tools. However, the average error is kept under 5% with all considered example, while the maximum error is almost doubled (compared to Table. 3.1): showing that the coupled scheme yield accurate result on average, but can deviate significantly in the last stages of fatigue crack propagation. These results seem to show a slight advantage of the TI scheme in this context, considering that it yields more precise results, for a given acceleration factor. Nevertheless, both schemes enable large computing gains, with low average error, provided that a relevant ΔN value is chosen.

3.4.2.2 Scalability of the approaches

Following this analysis with the loading $\Delta\sigma_2$, we investigated the scalability of the framework by applying the other loadings introduced in Section 2.4 on this sample: $\Delta\sigma_1$, $\Delta\sigma_3$, $\Delta\sigma_4$. Considering these different loadings, we plotted the evolution of the area of the crack in Fig. 3.29, and the resulting accuracy, gains in computing time,

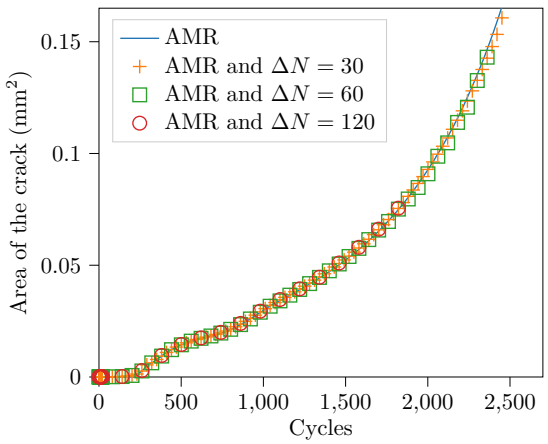

(a) Area of the crack computed for different ΔN on an adaptively refined mesh with TI scheme.

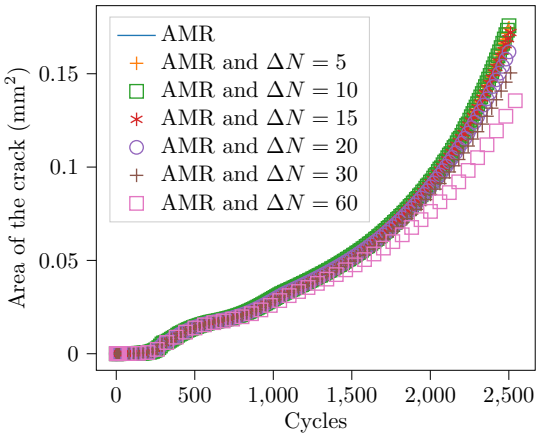

(b) Area of the crack computed for different ΔN on an adaptively refined mesh with FE scheme.

Figure 3.26: Study of the influence of ΔN on an adaptively refined mesh.

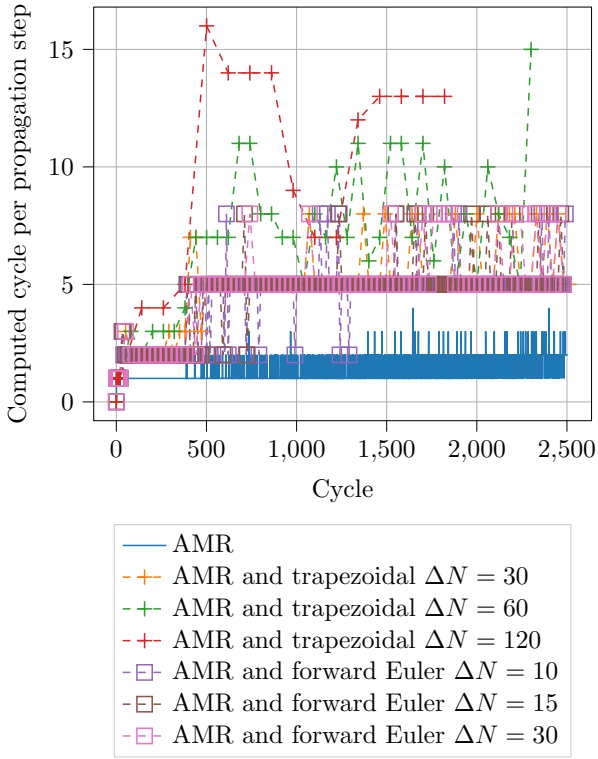

Figure 3.27: Number of cycle computed per propagation steps.

Table 3.2: Efficiency improvements compared to cycle-by-cycle calculation, on a fixed mesh.

Scheme	ΔN	ΔN_{eff}	Average error	Maximum error	Acceleration factor $(T^0/T^{\text{cj+R}})$
Cycle by cycle	1	0.41	1.5%	2%	3.63
TI	30	4.65	2.8%	4.9%	11.61
TI	60	5.58	1.8%	3.5%	11.72
TI	120	5.64	2.7%	5.1%	10.96
FE	10	1.86	2.73%	8.1%	10.96
FE	15	2.62	3.4%	11.8%	13.77
FE	30	4.42	5.2%	17.6%	17.94

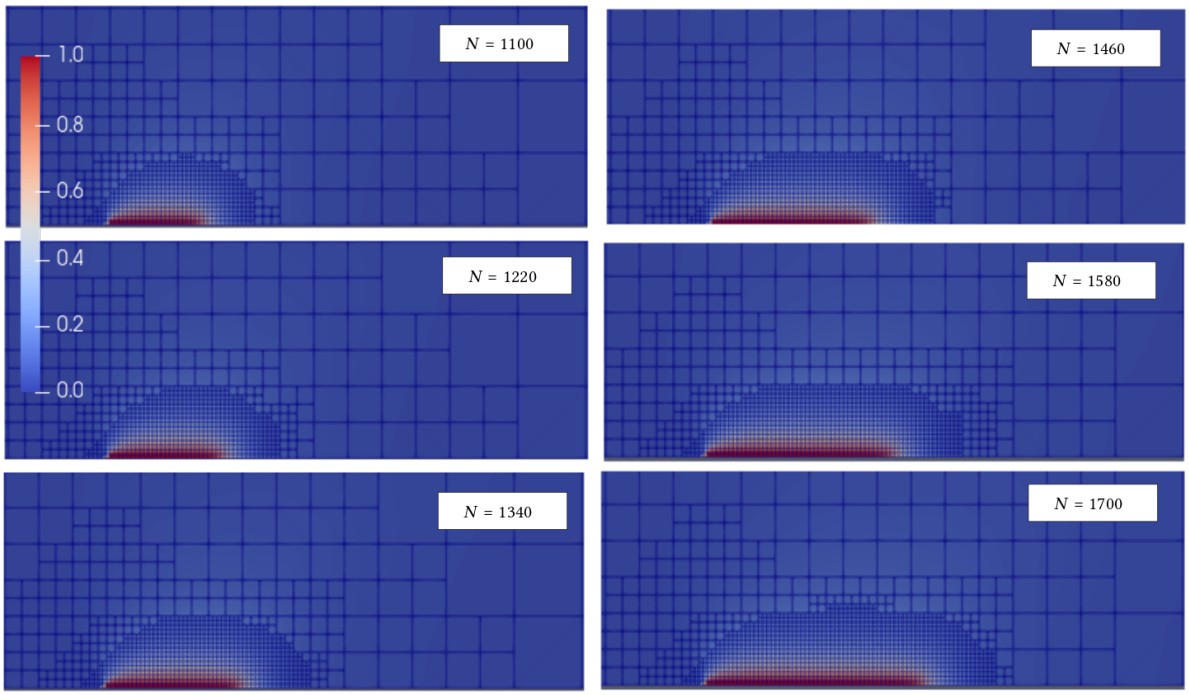

Figure 3.28: Visualization of the adaptive mesh refinement coupled with cycle jump tools on the crack in an infinite plane.

ΔN_{eff} in Table 3.3. Here accuracy was defined as the maximum error registered during crack propagation such that:

$$\text{Max}(Err_{A(d)}) = \text{Max}\left(\frac{|A(d)^N_{CJ+R} - A(d)^N_{\text{AMR}}|}{A(d)^N_{\text{AMR}}}\right), \tag{3.16}$$

hence comparing results accelerated with cycle jump and AMR (CJ+R), with results accelerated with AMR, and a cycle by cycle treatment. No comparison with unaccelerated results were led because of the untractable computing time associated with $\Delta\sigma_4$ and

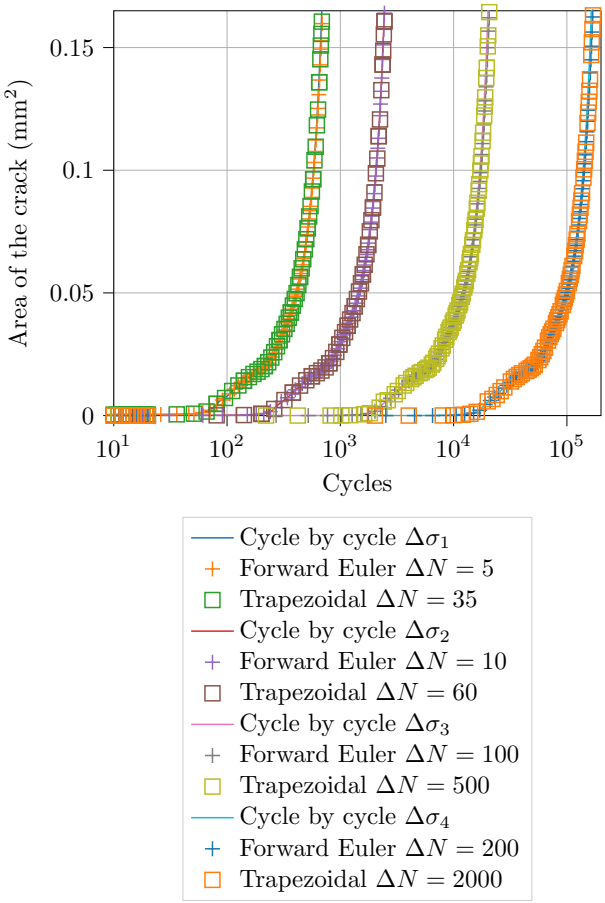

Figure 3.29: Area of the crack for the tested loadings.

$\Delta\sigma_3$ (yielding a large amount of cycle). Consequently, the acceleration factor was here defined as AMR accelerated computing time T^{R} over cycle jump and AMR accelerated computing time $T^{\mathrm{cj+R}}$. The values of maximum error and acceleration factor, along with the corresponding ΔN_{eff}, obtained in each case, were provided in Table 3.3.

Considering these four different loading amplitudes, we see that a larger fatigue life yields larger possible computing gains with the cycle jump framework. This is ideal for high cycle fatigue applications where fatigue life can go up to tens of millions of cycles. Additionally note that these computing gains are obtained by comparing with cycle-by-cycle computations, already accelerated with AMR. We can hence expect much larger computing gains if we had compared with results on a fixed mesh.

This investigation highlights multiple other properties of the proposed framework. First, it seems that the iterative scheme scales better than the FE extrapolation scheme, as for longer fatigue lives, we see that for similar computing gains, one scheme is 3-4 times more accurate than the other (for $\Delta\sigma_3$ and $\Delta\sigma_4$). This motivated us to use the trapezoidal

scheme in the rest of this work, as it seem to be better suited to this AMR and cycle jump framework. Nevertheless, we see that the trapezoidal scheme can also lead to inaccuracies: as much as 11% for $\Delta N = 500$ on $\Delta\sigma_3$. Indeed, as stated before, the trapezoidal criterion is not absolute, and can lead to an overshoot of the accurate result for large values of ΔN.

Table 3.3: Efficiency improvements compared to cycle-by-cycle calculation, on an adaptively refined mesh.

Loading	Scheme	ΔN	ΔN_{eff}	Maximum error	Acceleration factor ($T^R/T^{\text{cj+R}}$)
$\Delta\sigma_1$	Cycle by cycle	1	0.6	/	/
$\Delta\sigma_1$	TI	10	1.70	4.8%	1.21
$\Delta\sigma_1$	TI	15	1.84	6.5%	1.20
$\Delta\sigma_1$	FE	5	0.96	15%	1.51
$\Delta\sigma_1$	FE	10	1.68	30%	2.14
$\Delta\sigma_2$	Cycle by cycle	1	0.7	/	/
$\Delta\sigma_2$	TI	30	4.65	3.2%	3.22
$\Delta\sigma_2$	TI	60	5.58	4.1%	3.23
$\Delta\sigma_2$	TI	120	5.64	6.5%	3.01
$\Delta\sigma_2$	FE	10	1.86	6.4%	3.07
$\Delta\sigma_2$	FE	15	2.62	13.3%	3.79
$\Delta\sigma_2$	FE	30	4.42	25.7%	4.94
$\Delta\sigma_3$	Cycle by cycle	1	0.91	/	/
$\Delta\sigma_3$	TI	100	20.49	2.1%	11.26
$\Delta\sigma_3$	TI	200	37.27	6.8%	18.1
$\Delta\sigma_3$	TI	500	51.11	11.4%	17.6
$\Delta\sigma_3$	FE	10	2.89	8%	3.9
$\Delta\sigma_3$	FE	50	11.81	13.1%	11.4
$\Delta\sigma_3$	FE	100	20.00	17.2%	18.0
$\Delta\sigma_4$	Cycle by cycle	1	0.98	/	/
$\Delta\sigma_4$	TI	1000	210.08	3.5%	87.82
$\Delta\sigma_4$	TI	2000	263.50	7.9%	116.60
$\Delta\sigma_4$	FE	500	112.4	9.7%	85.49

3.4.2.3 Recycling data with trapezoidal scheme

With the chosen iterative procedure, several cycle jumps can be performed per computed cycles, themselves composed of multiple cycle computations. Indeed, we considered that if the mesh needs refinement, then the previously computed cycle jump was performed on a domain where spatial discretization convergence was not reached, hence it has to be performed again. While this assessment is true, we can still consider that the computed values after the cycle jump $\bar{\alpha}_{N+\Delta N}$ still holds some predictive value. Furthermore,

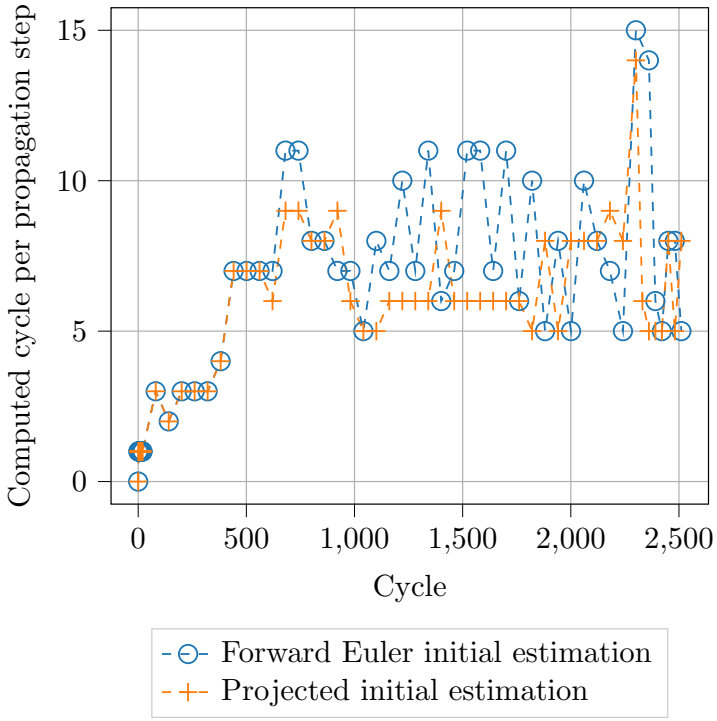

Figure 3.30: Cycle computed per propagation step with both formulations.

considering that some successive AMR steps only implies a low amount of element refinement, we can assess that this predicted variable is very close to the accurate solution in some cases. It can therefore be used to accelerate the proposed procedure.

The proposed approach to "recycle" this lost data is to use it as a first estimator of the next AMR iteration's cycle jump. Instead of using the forward Euler approach for the initiation step, a projection of the predicted fatigue internal variable on the new mesh can be used. We expected that this predicted value would be closer to the accurate results than the forward Euler estimation. Furthermore we estimated that the time gained by having a faster convergence of the cycle jump scheme (effectively increasing ΔN_{eff}), could largely surpass the time lost during the projection of the field on the new mesh. Therefore, we attempted this acceleration approach.

The same numerical sample was used with $\Delta\sigma_2$, and $\Delta N = 60$. We compared the originally proposed formulation with this recycling process, where when the mesh is refined, $\bar{\alpha}_{N+\Delta N}$ is projected along with the other fields. Then, the cycle jump procedure is initiated with this projected field, instead of the usual forward Euler estimation. We plot the number of computed cycles per propagation step in Fig. 3.30. We can see that most propagation steps converged faster (with some exceptions), with the proposed data projection. In fact, we noticed that the projected estimation is usually a better initial guess than the naive

FE estimation, since one iteration less per TI cycle jump was reported in most cases: the projected estimation yielded initial residuals magnitudes which where ten times lower than with the FE initial guess. In this regard, it does not change the convergence rate of the scheme, but it yields an initiation that is closer to the convergence threshold.

We therefore verified that the projected quantity is a better estimator. Furthermore, considering that the approach yielded a 27% gain in absolute computing time, we showed that these gains significantly outweigh the loss at the projection step, because a cycle computation is more costly than a projection step. Note that the most gains can be made when the crack propagation rate is very high, hence at the end of the propagation, because those steps usually require a larger amount of AMR loops, where we can expect to save one cycle computation per loop. Additionally, in this AMR framework, these steps are usually the most computationally expensive because since we do not coarsen the mesh, the number of degrees of freedom is the highest. It is therefore very interesting to compute less cycles at this stage.

Finally, note that, as mentioned in the previous section, by avoiding the forward Euler estimation after a projection step, the ΔN magnification of the error committed at the field transfer stage is avoided.

3.4.3 Applications

The proposed framework was applied on several numerical samples to validate that the implementation can recover crack patterns accurately. Consequently we investigated the accelerated framework on the “en-passant scenario”, the branching case scenario and the perforated plate, introduced in Section 2.4. We compared the accelerated results with the cycle by cycle results on fixed pre-refined meshes. Note that we applied the iterative trapezoidal cycle jump scheme, with the tools introduced in the previous Section 3.4.2.

3.4.3.1 "En-passant" scenario

First, we investigated the well known "en-passant" crack propagation scenario, where two crack tips interact in a specific successive shielding and attracting pattern. It ties well with the objective of being able to model complex crack patterns, with multiple cracks and mixed mode propagation. The sample is inspired by [172], [223] and [222]. The geometry used in this work was taken from Ref. [222], and was given in Fig. 3.31a.

Contrarily to most other numerical samples, the initial crack was not prescribed as double nodes, but as Dirichlet conditions $\hat{d} = 1$ on initially damaged nodes. Material

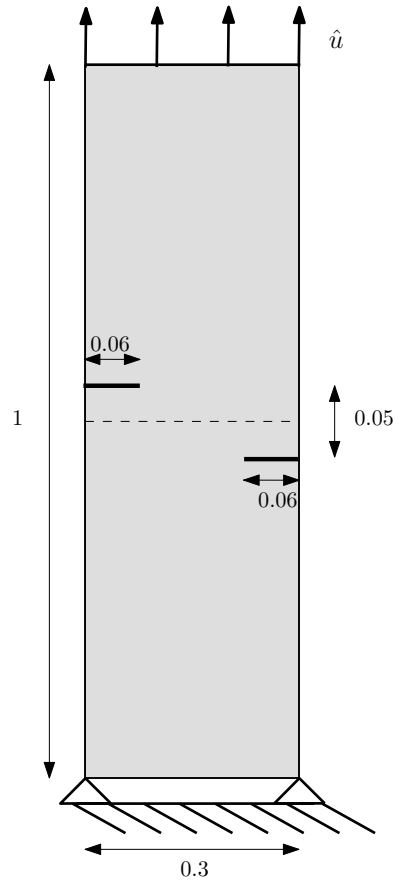

(a) Geometry (in mm) boundary conditions of "En-passant" sample.

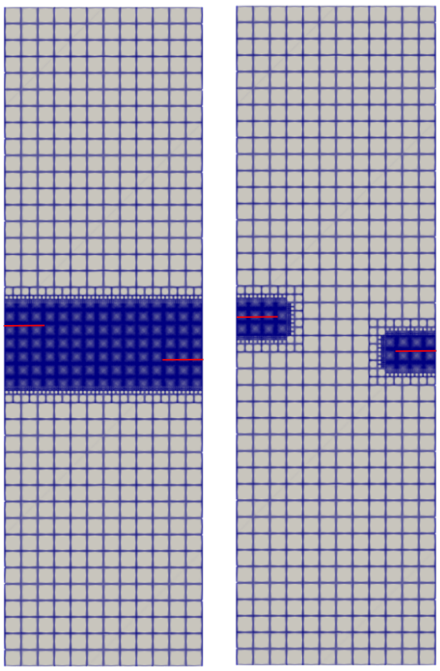

(b) Used meshes, refined prior to the simulation and using AMR, for "En-passant" sample.

Figure 3.31: Geometry, boundary conditions and meshes of the "En-passant" sample. Red markers correspond to nodes where $\hat{d} = 1$ is enforced.

properties were $G_c = 2.7$ N/mm, $l_c = 5 \cdot 10^{-3}$ mm, $\alpha_T = 540$ N/mm^2, $E = 210$ GPa and $\nu = 0.3$. A cyclic loading was applied to the upper edge of the sample, with an amplitude $\Delta u = 5 \cdot 10^{-4}$ mm and the loading ratio was 0. This yielded a fatigue behavior where the crack propagates in a stable fatigue regime. We compared an approach where the mesh was refined prior to the simulation, to an approach with cycle jumps and adaptive mesh refinement. The refinement prior to the simulation was illustrated in Fig. 3.31b for both case-studies, with $h < l_c/2$ in the refined zone. Furthermore, we plotted and compared the evolution of the crack area with respect to elapsed cycles, for those two different refinement contexts, in Fig. 3.33. Furthermore, we compared the refined meshes and damage field at different steps of this crack propagation in Fig. 3.32.

The presented framework was indeed able to capture this phenomenology, considering that the crack tips followed the shielding and attracting pattern before coalescing in

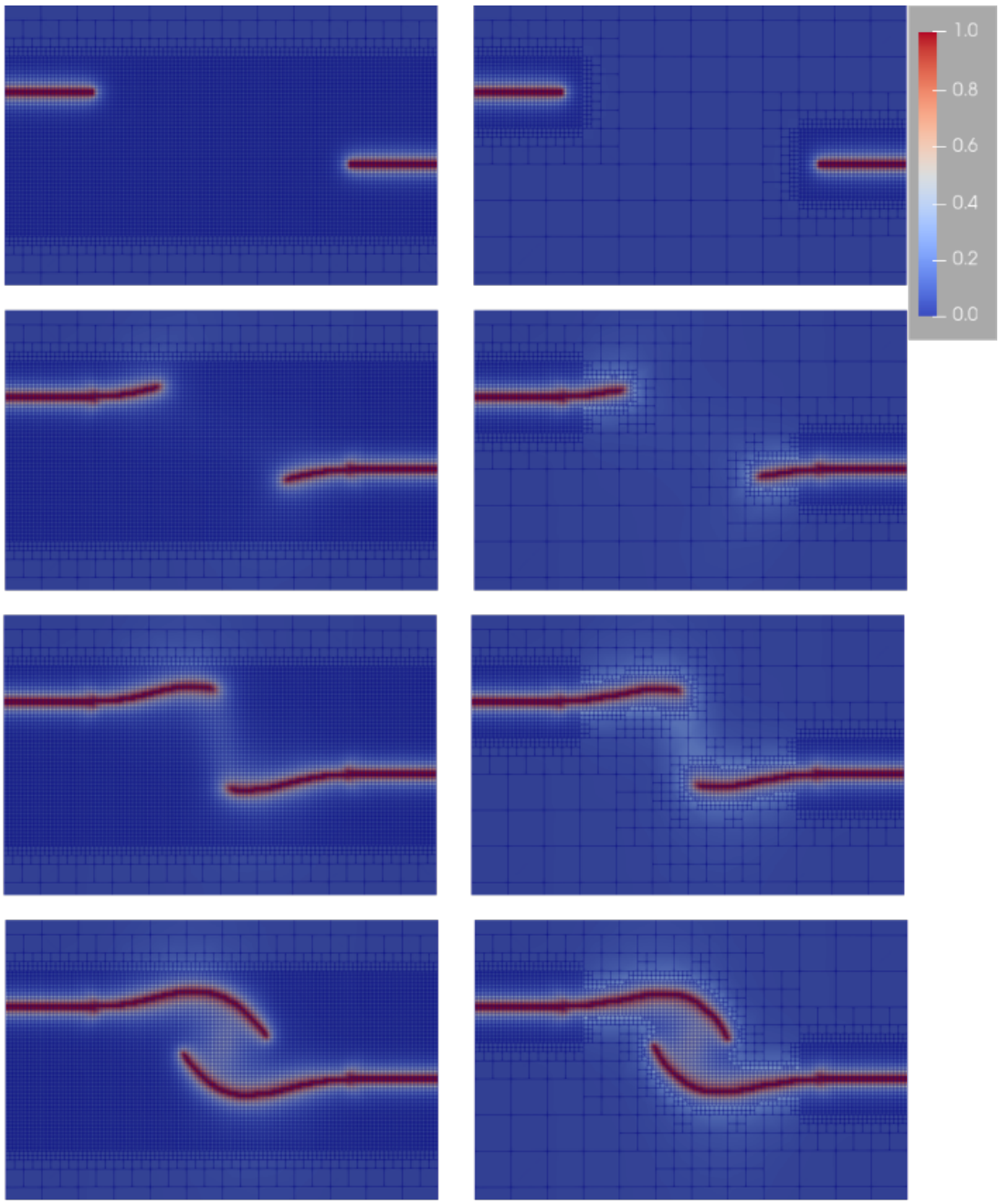

Figure 3.32: Crack pattern computed on the "En-passant" sample.

the middle of the sample. This ability of the phase-field model to recover such patterns was already shown in *e.g.,* Refs.[172, 222]. Furthermore, we have shown here that the accelerating framework *i.e.,* cycle jump and AMR, yielded only a marginal influence on the computed result, as the phenomenology was recovered with a refining mesh, the obtained damage topology is almost identical and the computed crack area is very close in both cases. Finally, it should be noted that the fully accelerated simulation (AMR and the trapezoidal iterative cycle jump, with ΔN=2000) ran more than twenty times faster than the semi-accelerated simulation (No AMR and ΔN=500). We hence validated the use of this accelerating framework in a context with multiple cracks interacting, and coalescing.

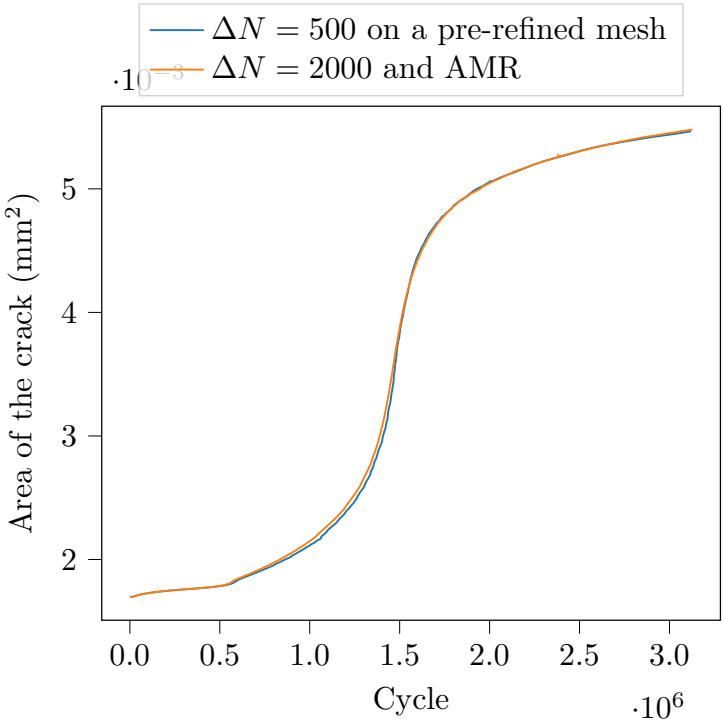

Figure 3.33: Area of the crack with respect to elapsed cycle, for the "En-passant" sample.

3.4.3.2 Crack branching

We followed-up with the crack branching sample that was set-up previously (see Section 2.4). We recall that a bi-material sample was used, inspired by Molnár & Gravouil, in order to induce crack branching, and a cyclic loading was enforced to simulate fatigue crack propagation. The geometry and boundary conditions were illustrated in Fig. 2.20a. The pre-refined mesh in Fig. 3.35a was used for cycle-by-cycle time discretization: we recall it was refined on the expected crack path and the bi-material interface with $h < l_c/2$

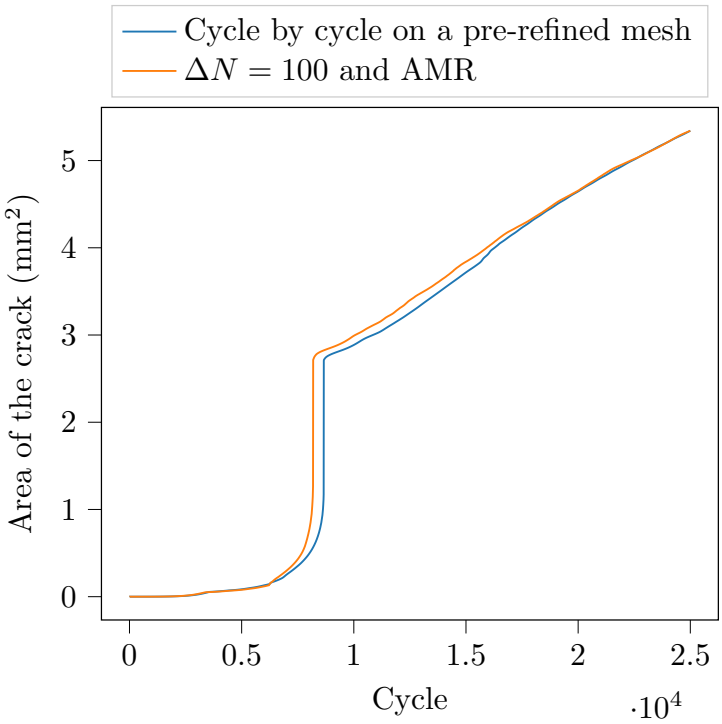

Figure 3.34: Area of the crack with and without acceleration tools, for the crack branching sample.

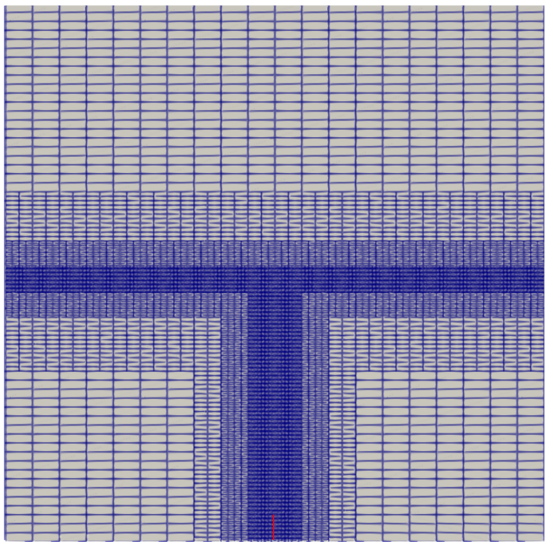

(a) Pre-refined mesh used without AMR: pre-refined on expected crack path.

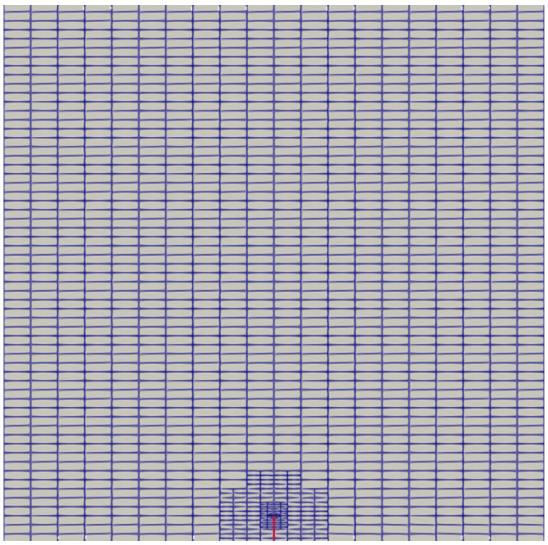

(b) Initial mesh used with AMR and cycle jump: pre-refined at the initial notch.

Figure 3.35: Comparison of the initially used meshes for the crack branching case.

in the refined zone. Then, a model with a pre-refined mesh limited to a small zone around the initial crack tip was employed, illustrated in Fig. 3.35b. A similar density of element $h_{\text{AMR}} < l_c/2$ was enforced, but the cycle by cycle treatment is exchanged for the iterative cycle jump procedure with an initial value of $\Delta N = 200$ cycles.

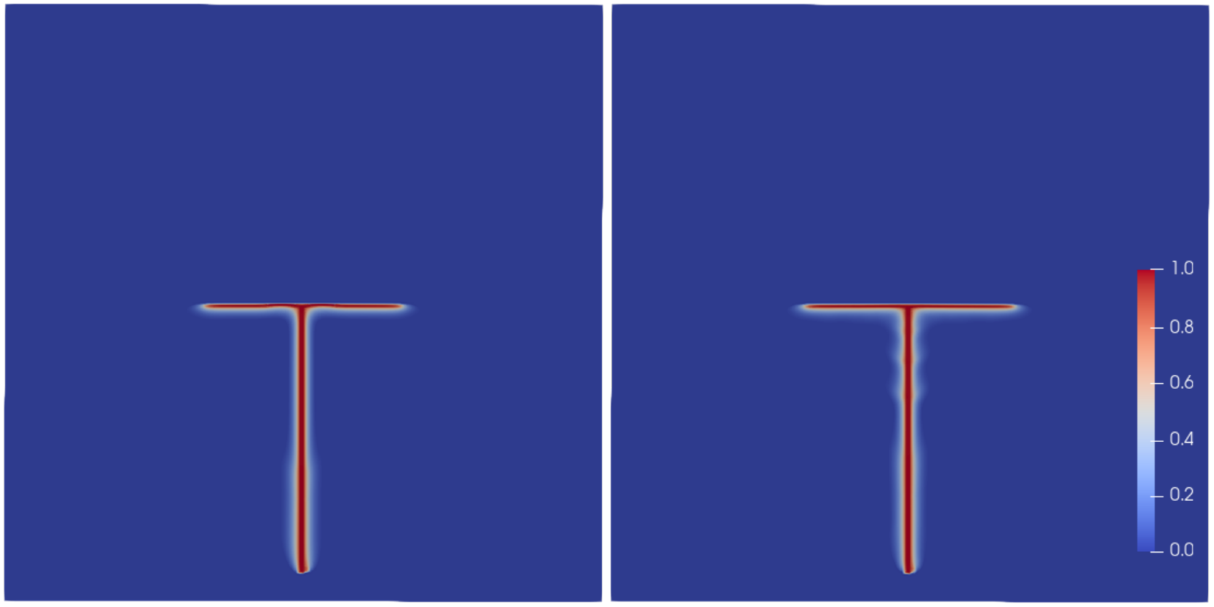

Figure 3.36: Damage field after 25000 cycles on base model (left), and accelerated model (right).

As was observed for the cycle by cycle computations, we can separate crack propagation observed on this sample in different regimes: an initial stable fatigue crack propagation in mode I from the notch, then unstable crack propagation from a critical crack length to the interface of the bi-material, followed by a fatigue stable crack propagation regime with branching along the interface. These steps are challenging to the proposed accelerating framework. Indeed, it was designed with slow fatigue crack propagation in mind. Nevertheless, we observed that it was able to capture these different crack propagation regimes very accurately as was shown in Fig. 3.36, where the computed damage fields were compared, and in Fig. 3.34, where the crack area was compared. It should however be noted that uneven damaged zones were present on the unstable crack pattern in Fig. 3.36, revealing issues in the present algorithm in the case of unstable crack propagation. Still, these spurious results seemed to have a minimal effect on precision as shown in Fig. 3.34 where a small deviation was observed at instability.

As well as recovering unstable crack propagation, the accelerated framework also recovered the crack branching phenomenon, and was able to handle the two emerging crack tips, and resulting crack propagations in a robust and accurate manner. See Fig. 3.37, for a

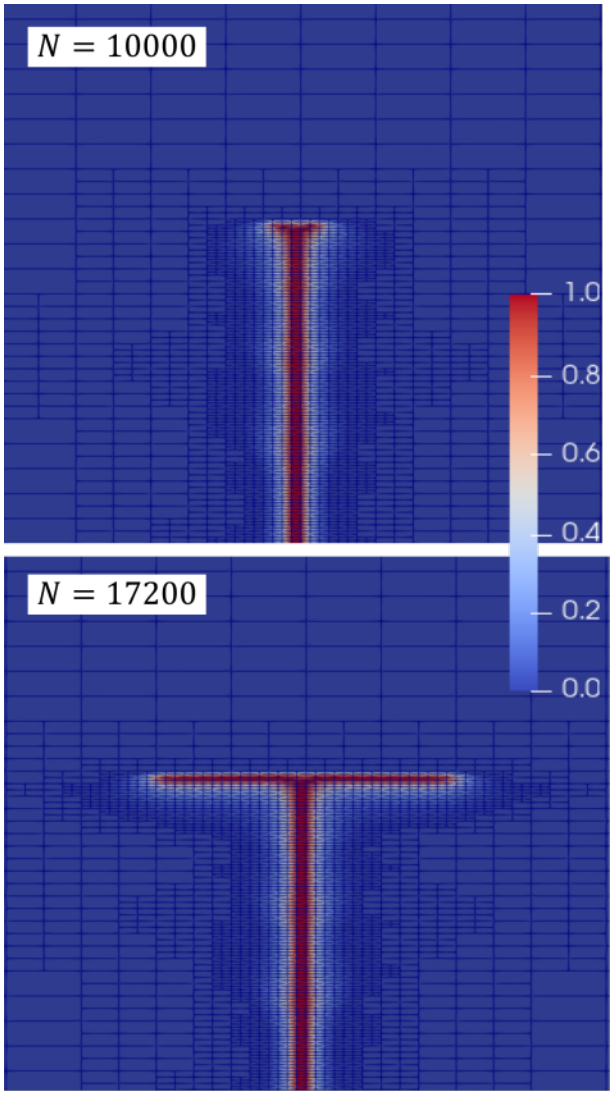

Figure 3.37: Damage field on successive meshes for the AMR and cycle jump accelerated model, for the crack branching sample.

visualization of the refining mesh and corresponding computed damage fields. Furthermore, the accelerating treatment yielded computation time that was five times lower than the initial formulation. Note that during the unstable crack propagation regime, ΔN used for cycle jumping was reduced to 1, and this value was kept for the rest of crack propagation (considering that no adaptive change of increasing ΔN was attempted in this work). This means that if no unstable crack propagation regime was reported, much larger computing gains could have been made.

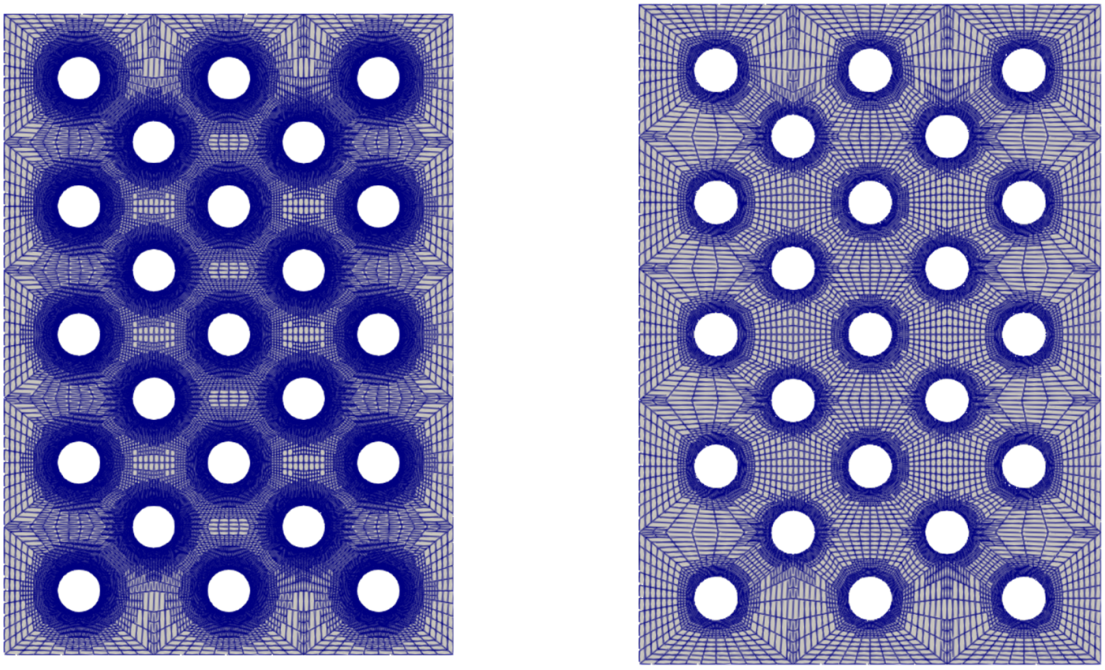

(a) Fixed mesh, refined prior to the simulation.

(b) Initial mesh, refined around the hole.

Figure 3.38: Comparison of the initial meshes used for the perforated plate.

3.4.3.3 Crack initiation

Continuing the acceleration of the numerical samples studied in Section 2.4, we proceeded on with the crack initiation sample. We recall that being able to recover fatigue crack nucleation with a fatigue crack growth model is not a trivial task, as most theoretical tools designed to model fatigue degradation separate these two domains, and hence use very distinct models for their analysis. Therefore, the proposition of a fatigue model that considers these phenomena in a unified framework could bridge the gap between those communities, and enable a unified analysis of fatigue degradation, from fatigue initiation or endurance limit determination, along with fatigue crack growth analysis for damage tolerant approaches.

The objective was to establish whether the nucleation pattern and the resulting crack growth could be recovered with a coarser initial mesh, which is adaptively refined, and cycle jump schemes to accelerate the fatigue time-integration. Therefore, conversely to the previous test, the initially used mesh was refined to $h < l_c/3$ around the holes, and $\Delta N = 50$ was chosen. We provided an illustration of both used meshes in Fig. 3.38, to give an idea of the initial refinement used in both cases.

The computed damage topology after 1600 cycles was plotted in Fig. 3.39. We can see

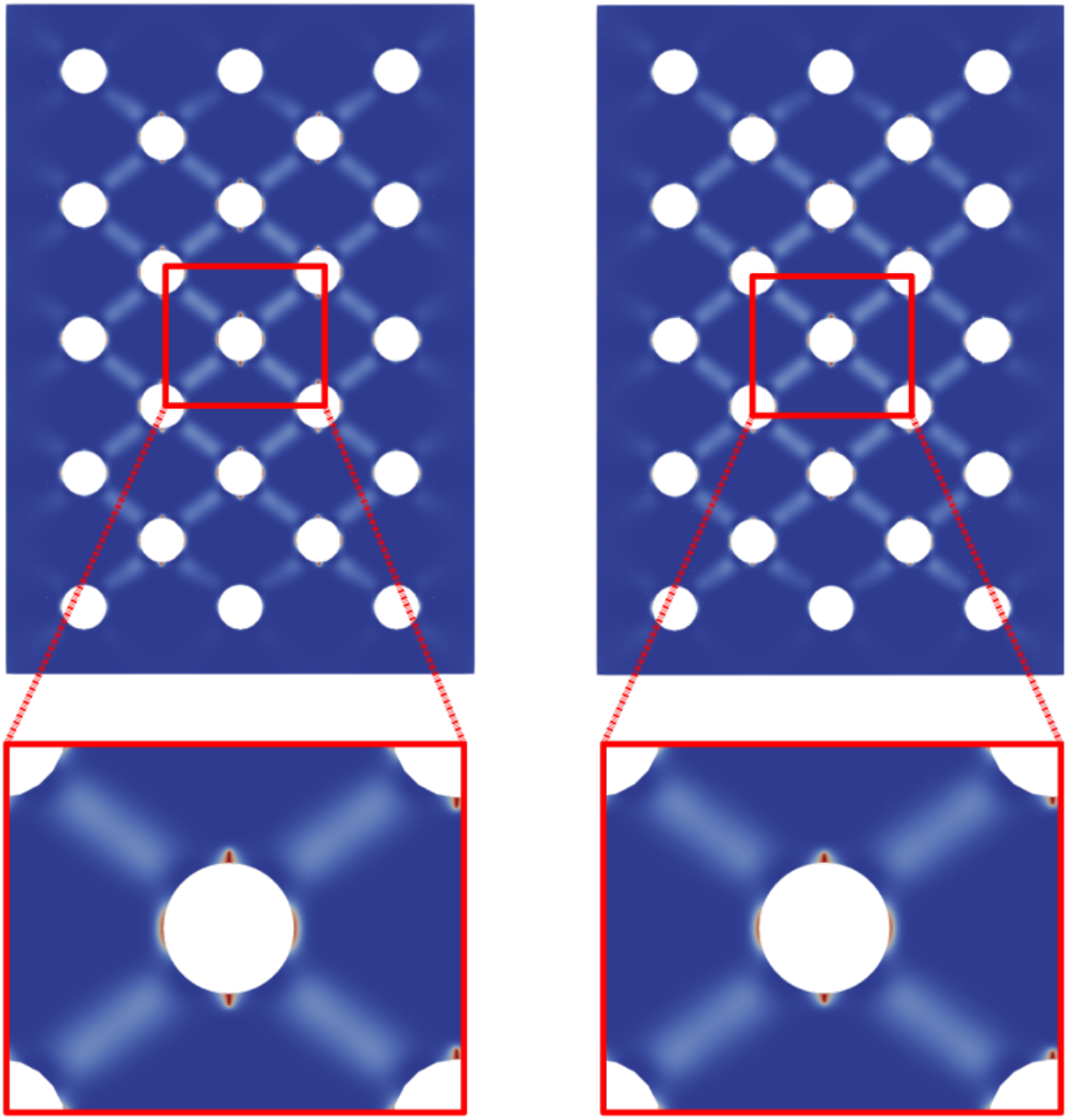

Figure 3.39: Comparison of computed damage fields on the perforated plate after 1600 cycles. Results are shown without accelerating tools on the left, and with AMR and cycle jump on the right.

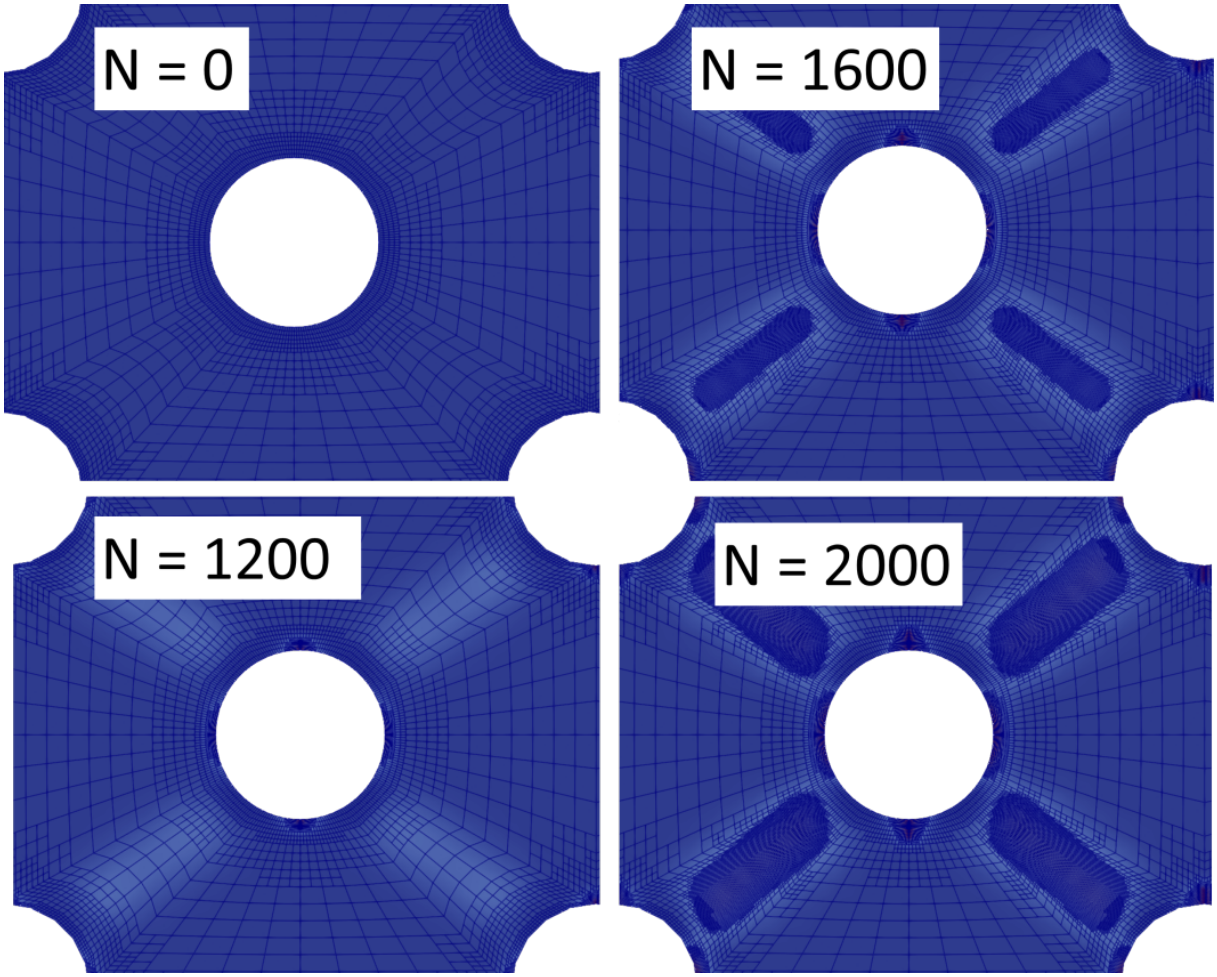

Figure 3.40: The evolution of the mesh on the perforated plate around the central hole, with background damage field color code.

that both numerical models led to very similar crack initiation patterns, in line with the literature [182], with vertical lines emerging from the holes, and damage localization lobes on the horizontal lines. Furthermore, the damage cross patterns linking the holes together were also observed. Considering the zoom on the central hole in Fig. 3.39, we can see that the accelerated results predicted a slightly slower initiation, as the computed length of the crack emerging from the notch is slightly shorter with the acceleration tools at cycle 1600. In Fig. 3.40, we provided an illustration of successive meshes with the acceleration tools, centered around the central hole. We see that even though the mesh of this sample is initially significantly coarser than the reference nucleation sample, mesh refinement is triggered in the relevant zones, leading to the recovery of the expected crack pattern. However note that using $d_{\mathrm{AMR}} = 0.1$, led to a very fine refinement of the cross pattern around the holes, in turn leading to a very large amount of degrees of freedom, in a zone where damage is not so important, and where its gradient is not critical. In fact, we see that

the cross patterns are almost identical in both tested configurations, even though the mesh of the reference example is not refined that finely between the holes. This seems to indicate that it is not necessary to refine the zone where this cross pattern emerges, even though it was selected for refinement by the chosen AMR procedure. This observation shows the issue of using the phase-field value as a mesh refinement criterion, rather than its gradient.

Nevertheless, note that the acceleration tools on these numerical experiments enabled very significant computing gains, considering that 1600 cycles were simulated in 8 days on the unaccelerated case, while the accelerated case was computed to N=2500 cycles in 1 day and 18 hours, on the same computer. We see how this kind of approach could be used to give a first idea of the crack nucleation sites, without the need for a very fine refinement of the whole mesh.

3.4.3.4 3D SEN

Finally we have applied the framework on the 3D single-edged notched tensile sample: corresponding to a cube of side 1 mm with a plane crack in its center, with an upper boundary loaded in tension. Its geometry is simply an extrusion of the previously defined SEN sample in the z axis. We applied the following parameters: $E = 210$ GPa, $\nu = 0.3$, $G_c = 2.7$ N/m, $l_c = 0.02$ mm $\alpha_T = 56.25$ N/mm^2, with a cyclic load of amplitude 10^{-3} mm and a load ratio of 1/100. The transition from 2D to 3D did not require any alteration of the presented cycle jump and AMR framework. As in the previous examples, we have compared results obtained on a fixed initially refined mesh with a cycle-by-cycle treatment, against results with AMR and cycle jumps (with $\Delta N = 20$).

The initial mesh represents an eighth of the sample using the symmetries of the geometry and loading. Furthermore, it was refined in a local zone at $h < l_c/2$ on the expected crack path for the unaccelerated version in Fig. 3.41b, and conversely only around the crack tip for the AMR and cycle jump accelerated sample, in Fig. 3.44. We plot the evolution of crack volume in Fig. 3.42. As with the 2D examples, we see that the proposed framework enable to keep the accuracy of the solution. In both cases, we observed a stable mode I propagation of the crack, with a slight delay of the crack front at the free boundary, as can be seen in Fig. 3.45.

With the proposed settings, the computations where significantly faster with AMR and cycle jumps, as illustrated in Fig. 3.43, where the computing time as a function of elapsed cycles is compared. We notice that the acceleration factor of the total computed fatigue life (until

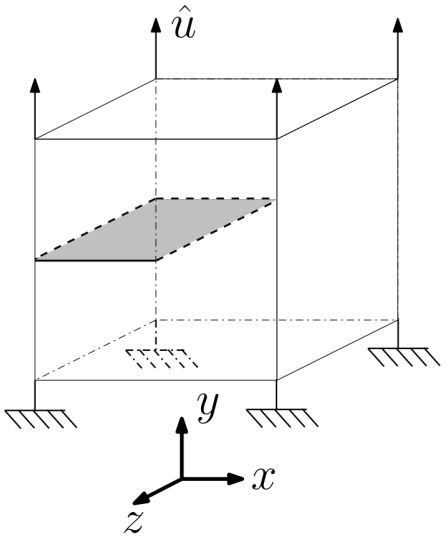

(a) Geometry and boundary conditions in mm, for the 3D SEN sample.

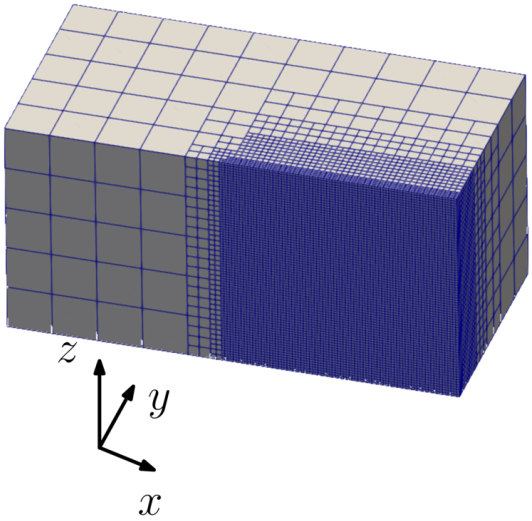

(b) Mesh used to model this 3D sample. An eighth of the structure was considered. It was adaptively refined prior to the simulation on the expected path of the crack, and then fixed during propagation.

Figure 3.41: Geometry and model put forward for the 3D SEN sample.

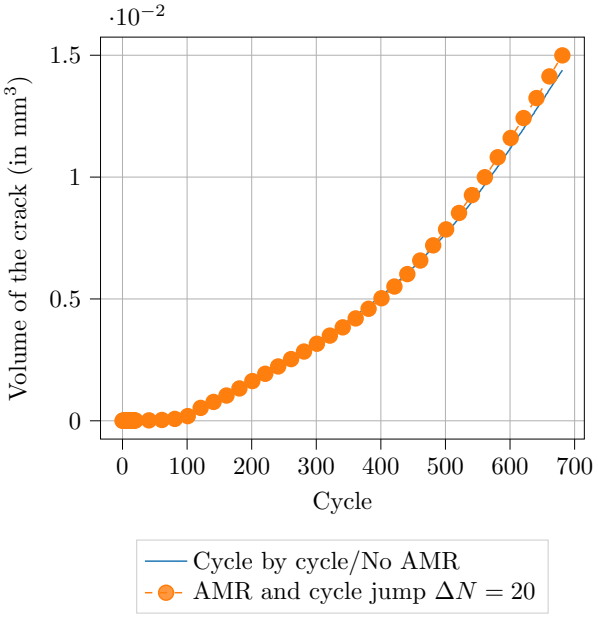

Figure 3.42: Comparison of the simulated volumes of the crack.

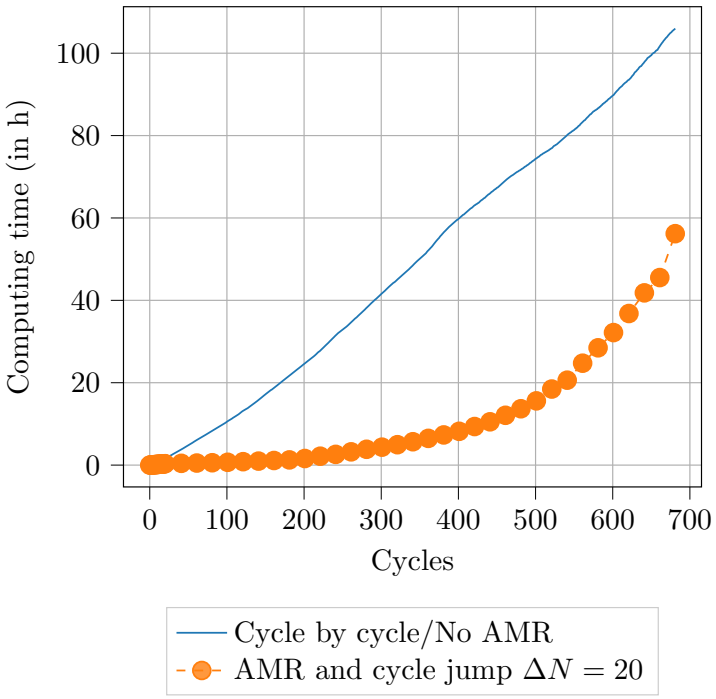

Figure 3.43: Computing time with and without AMR and cycle jumps.

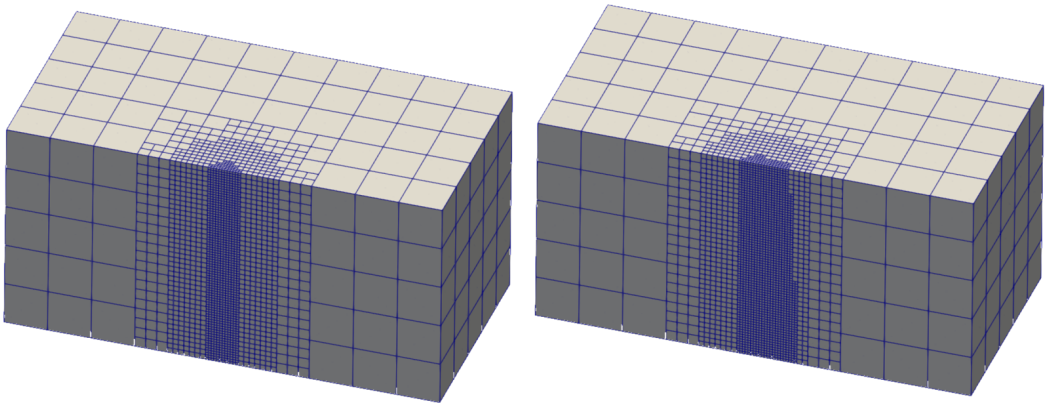

Figure 3.44: 3D Meshes used with AMR and cycle jump: Initial mesh and mesh at N=300. No crack has still initiated (d<0.95).

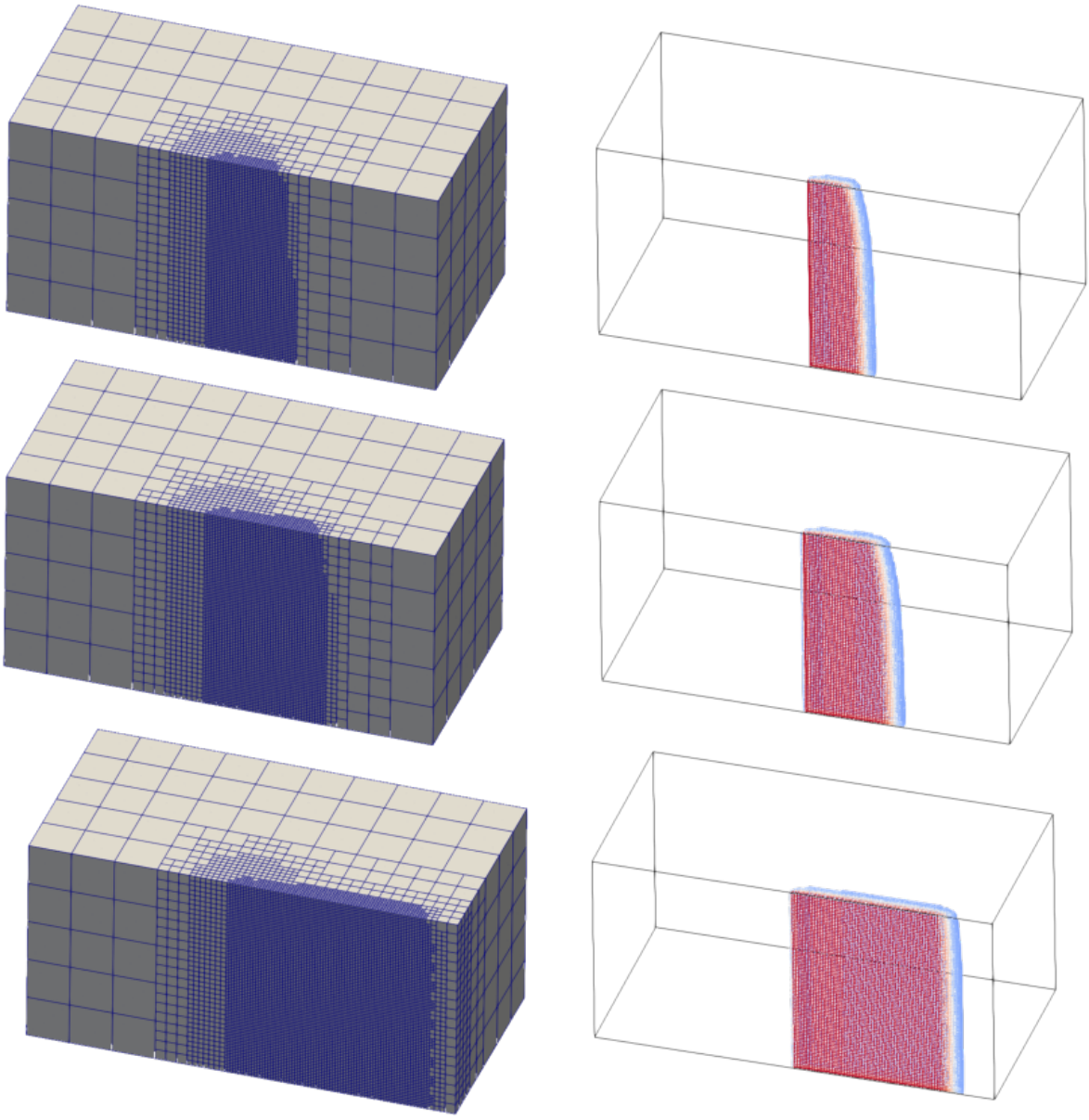

Figure 3.45: 3D Meshes used with AMR and cycle jump: At N=400, N=500, N=650, with the elements where d>0.2 are highlighted below. Red elements are close to d=1, while blue elements are close to d=0.2.

N = 681), we obtain $T^0/T^{CJ+R} = 1.89$ (106 hours to 56.8 hours on a similar computer). It can seem weak, but we notice on Fig. 3.43 that when we consider the acceleration factor to reach cycle $N = 500$, $T^0/T^{CJ+R} = 4.77$ and, to reach cycle $N = 300$, $T^0/T^{CJ+R} = 9.55$.

This can be explained with the 3D refined meshes shown in Fig. 3.44 and Fig. 3.45. Those visuals illustrate the issue associated with the transition to coarser zones of the mesh. Indeed, in Fig. 3.44, as the mesh refines in an initially fine mesh, no smoothening issues

or accuracy deviation is reported. However from cycle $N = 400$, in Fig. 3.45, when the framework reaches a coarser zone of the mesh, we see that the smoothening process does not yield a perfect "2-to-1" transition, and large patches of refinement can emerge. Those large patches eventually turn the refined mesh to a more expensive version of the initially refined mesh, fixed prior to the simulation, in Fig. 3.41b. This explains the rise in computing time at the end of the simulation: the AMR mesh has grown from 11 030 elements to 51 987 elements at the last steps. On the other hand the mesh refined prior to the simulation has stayed constant at 41 655 elements.

However, note that the transition to coarser zones only has a negligible influence on the accuracy of the solution, and the smoothening subroutine was flexible enough to find a compromise between a smooth transition and large patches of very fine element, which are the main concern of the proposed framework: maintain accuracy and keep flexibility of the phase-field model. Furthermore, even if the mesh is not perfectly optimized, we see that it is much more efficient at the initiation phase of the simulation and all throughout propagation until the last phases where the mesh becomes heavier. Note that one solution to avoid this issue would be to implement coarsening operations. Finally, if we had considered that the trajectory of the crack was not known, a fine uniform mesh would have been necessary for the whole volume, which would make for a much higher acceleration factor.

This case was the only 3D sample attempted in this work considering the enormous computing time associated with this simple example: for 41 655 elements, more than 5 days are required to compute 700 cycles. For 3D applications, considering a native parallel code with domain decomposition thus seems to be a priority to overcome this issue.

Conclusion of the chapter

In this chapter, we presented several numerical strategies that enabled faster computations for a given level of accuracy. First, we investigated for the most efficient time integration approach in the phase-field context, in order to accelerate the computation of a cycle. An implicit staggered strategy was chosen with a specific "one-loop" formulation and convergence acceleration tool. Then we worked on decreasing the number of cycle required to compute a complete fatigue lifetime, using a cycle jump strategy. An iterative cycle jump scheme was compared to the usual forward Euler scheme, each yielding important computing gains. Following this cycle jump strategy, we tackled the issue of adaptive mesh refinement in order to accelerate simulations by minimizing the number of degrees of freedom during each cycle computations, while retaining accuracy. These tools were proposed in the context of cycle jumps and applied successfully to reproduce typical benchmarks of the phase-field literature, while accelerating computing time.

Further investigations could nevertheless be led for each proposed numerical tools. For instance the time integration treatment of the cycle could further be accelerated with the BFGS staggered approach used in Ref. [129], or the constant load treatment proposed in Ref. [130], which would both be compatible with the current framework, and enable faster computation of individual cycles. Then, the search for a flexible adaptive ΔN during cycle jump needs to be extended, in order to ensure robustness and accuracy of the solution with the proposed iterative scheme (some elements on this matter where compiled in A). Finally, coarsening operations could yield even more computing gains, as they would enable to optimize further the finite element mesh.

4

Toward industrial applications

Finally, after putting forward a novel fatigue crack propagation framework and accelerating it to enable its use on industrial component, we apply the framework on multiple real life samples, to evaluate the predictive ability of the model.

Contents

In this section, we present the results of two experimental-numerical comparisons developed in this work. These applications of the proposed framework were considered to enter the industrial scope of this work, where we seek to enable the use of this model for real-life applications. Indeed, these investigations provided a platform to put in light the issues of such applications. Furthermore, they acted as proofs of concept, that the framework holds predictive abilities.

4.1 Compact tension specimen

The first experimental-numerical comparison led in this work was based on the work of Gibert [84]. In the context of his doctoral thesis, he carried out an experimental campaign of fatigue crack propagation on a CT geometry. A two-step process was applied in his work. First, he identified the Paris law parameters associated with the studied material from a mode I CT fatigue crack propagation experiment. Then he injected these identified parameters to drive crack propagation in a numerical framework, using XFEM and AMR [83], on a perforated CT geometry in order to estimate the predictive abilities of the framework on a mixed mode case.

Using these results, we applied a similar two-step process. First, we calibrated the numerical parameters associated with the phase-field fatigue model to the experimentally obtained mode I crack growth case. Then, we injected those fitted parameters in our proposed accelerated framework, on the perforated CT geometry. In a similar fashion to Gibert [84], it enabled the assessment of the predictive abilities of the framework, and provided a platform to put in light some issues associated with the real life application of the accelerated phase-field framework.

4.1.1 Geometry, loading and numerical models

The studied CT geometry was provided in Fig. 4.1, with a thickness of 12.5 mm. The material was 304L steel, typical of the nuclear industry. A loading of $F_{\max} = 20$ kN and load ratio $R = 0.1$, with a hydraulic traction/compression device from the CEA's lab, LISN (Istron 1273)[84]. Furthermore, a speckle pattern was applied on the surface of the sample in order to perform image correlation operations to identify the displacement field, and the length of the crack during crack propagation. A pre-cracking procedure was finally applied in order to initiate a 2 mm pre-crack at the notch.

Following the identification of the crack growth rate on the CT sample, the author studied

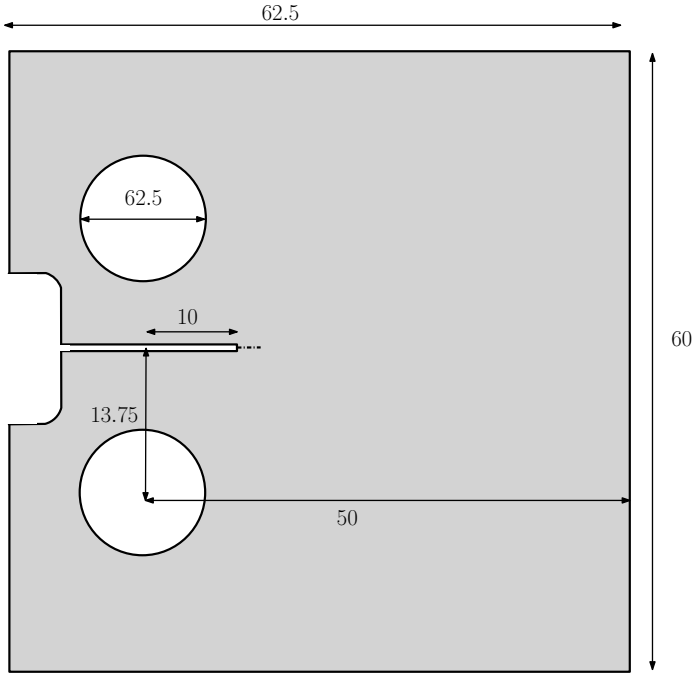

Figure 4.1: Geometry of the used CT sample.

the influence of a hole on the observed crack path. Considering the asymmetry linked with the hole, a mixed mode propagation regime was observed with the same loading ($R = 0.1$, and $F_{\max} = 20$ kN). The perforated CT were drilled using two different hole diameters, in order to observe the influence of the diameter on the crack path. The two configurations were detailed in Table 4.1, with coordinates illustrated in Fig. 4.2.

Table 4.1: Geometric properties of the holes, from Ref. [84]

	x_1	y_1	d_1
Geometry 1	18 mm	7 mm	4 mm
Geometry 2	18 mm	7 mm	5.3 mm

The first considered geometry was modeled using a 2D finite element representation illustrated in Fig. 4.3. Only half of the specimen was modeled, using the symetry of the studied case. The prescribed force was applied on a node in the center of pin hole, linked to a triangular domain, where we enforced $d = 0$. This is a very basic representation of the boundary conditions of the simulated setup, which can have a significant influence on the computed mechanical response [245]. In contrary to the sane geometry, the whole perforated geometry had to be modeled, considering that symmetry is lost with the hole. The boundary conditions were modeled with a similar application at the central node: the lowest pin was blocked, while a prescribed cyclic displacement was applied on the upper pin.

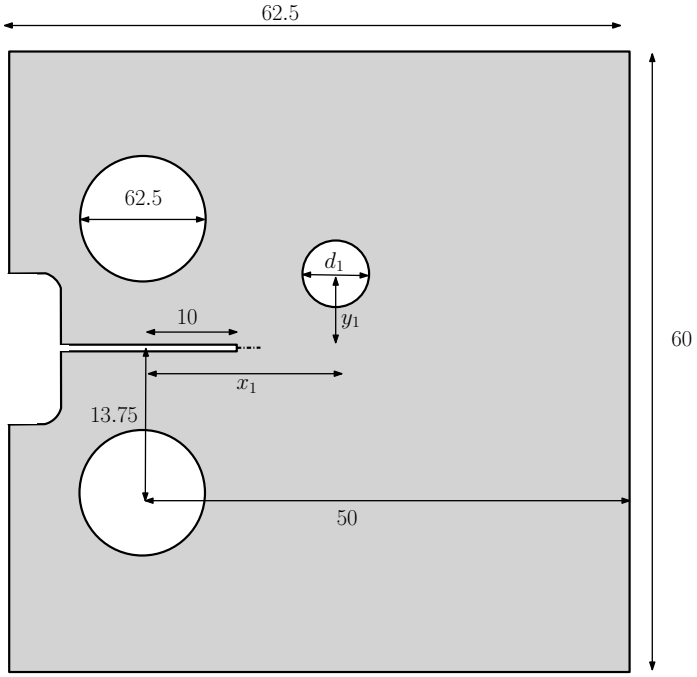

Figure 4.2: Compact tension specimen geometry, with a hole (in mm).

Note that both meshes were adaptively refined prior to the simulation. Aside from the initial notch, which is very finely refined (h$<l_c/4$) in order to reach spatial convergence at the initiation phase, we also refined finely (h$\simeq l_c \cdot 4$) the zone where the crack is expected to propagate. This adaptive discretization was chosen to reduce the maximum ratio between coarser and finer elements. Indeed, as briefly described in Section 3.3.4, if this ratio is too large, it can lead to issues with the used smoothening process. For instance, during the AMR iterations, damage can localize in the very coarse elements in the neighborhood of the damaged zone, which means that the a large patch of the domain is then refined very finely, leading to a large amount of unnecessary degrees of freedom, far from the damaged zone. In our context of the study of materials at the macroscopic scale, this is a recurring issue of the phase-field model, as the characteristic size of the studied sample are much larger than than the characteristic length used to describe the material. For instance, consider that the fitted l_c on this sample to reproduce experimental data, was 600 times smaller than the width of the sample.

4.1.2 Parameter identification

The subject of parameter identification in the phase-field literature was explored by several authors in recent years, both in a brittle context [176, 181, 241], and for fatigue extensions of the model [6, 100, 148]. In the brittle context, four parameters are necessary, E, ν, l_c, G_c.

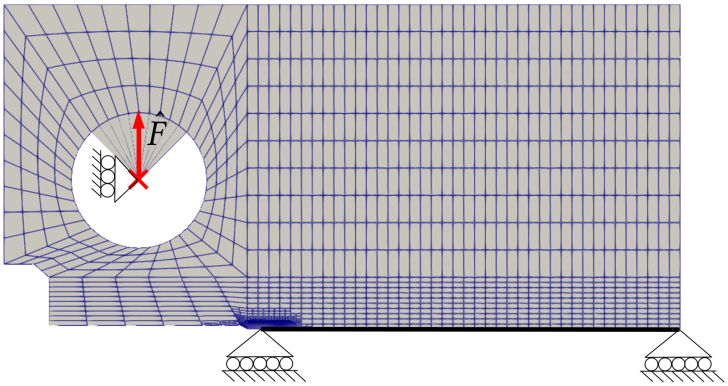

Figure 4.3: Mesh and boundary conditions of the CT sample.

With fatigue phase-field extensions, more parameters are usually introduced, for instance one more: α_T in the case of the use the fatigue degradation function (2.32), or two more, α_T and κ with the logarithmic degradation function, eq. (2.33). In this section, we used the logarithmic degradation function considering that it enabled a better fit.

Several works have quantitatively shown the link between the numerical parameters of a given phase-field fatigue model and the Paris law exponents, for instance in Refs.[44, 94, 101, 125, 162, 224]. Furthermore, some authors went further by fitting their numerical parameters to reproduce experimental tests *e.g.,* [87, 100, 148, 149].

Note however that these author's identification approaches can differ drastically. First, comes the consideration of l_c, which, as we have seen before, can be alternatively seen as a regularization parameter, or a material parameter, and can be accounted for in multiple ways in the degradation function (see Section 2.1.2.1) in order to have a l_c dependent or independent mechanical response. Furthermore, l_c has been related to material quantities in brittle fracture, by considering its influence on the critical stress on a uniaxial sample [33, 241]. Then comes the treatment of G_c, which is unanimously considered as a material parameter considering its LEFM origin. Since both of these parameters are present in the original brittle approach, some authors link them to quantities computed with monotonously loaded samples, for instance with the theoretical relation between l_c and σ_{crit} on an uniaxial case [87, 148] or experimental results with static loads [149, 151]. Then, the remaining parameters of their respective fatigue models are fitted on cyclically loaded cases.

This kind of approach is based on the consideration that the fatigue model should also recover the behaviour under monotonous loading conditions. However, such a brittle-fatigue unification does not seem easily tractable with the considered metallic material. Indeed, the present model was designed for high cycle fatigue and considering the response

of metallic material to this type of fatigue load we neglected the plastic effects, which are however not negligible under a monotonic load. For instance, the signification of G_c, and the link between l_c and σ_{crit} are not straightforward in this context. Consequently, we applied an identification process which is only based on fatigue. Therefore, the Paris exponents were fitted with l_c, G_c, as well as the additional fatigue parameters. This approach was used in Hasan et al. [100], where the fit was performed on all phase-field and fatigue parameters at once, without taking fracture toughness measurements into account for G_c, or estimating l_c beforehand.

Inspired by these works, we carried out a similar parameter investigation, by observing the influence of G_c, κ, α_T on the Paris coefficients obtained at the emerging linear regime as highlighted in Section 2.4. In this case, we applied three different loadings (of growing amplitude, $F_{\max}$=10,20,40 kN) to identify the linear regime as illustrated in Fig. 4.4: the plot of the evolution of da/dN with respect to the variation of SIF for three different load amplitude led to the identification of a linear regime. Note that $\alpha_T = 10^8$ N/m^2 $\kappa = 0.8$, $G_c = 50$ N/mm and $l_c = 0.4$ mm when it is not specified. The value for ΔK and da/dN during propagation were computed using the process described in Ref. [44], which is based on the ASME norm [111, 112]. We showed the influence of the fatigue specific numerical parameters on the extracted linear regime in Fig. 4.5. With the constitutive choices made in this work, it seems that a straightforward relationship between Paris exponents and the numerical parameters can be made, in line with observations in Ref. [225]. Indeed, denoting C and m the Paris law coefficients in Fig. 1.5, we found a correlation between α_T and C and a correlation between κ and m. For a given α_T, varying κ yields an influence on the slope of the Paris linear curve. Interestingly, this deduced slope is limited in range, as we've found exponents varying from $2 < m < 5$, in line with usual values of Paris exponents for metallic ductile material [109]. Conversely, at a given κ, the variation of α_T has an influence on the y-intercept, which can be linked to the C parameter of Paris linear regime. Note that κ also has an influence on C.

If the identified linear regime seems to be load independent, it is clear from Fig. 4.4, and Fig. 2.19b, that the lower and upper bound of the linear regime are highly dependent on the used loading. On the contrary, the described Paris law behavior, is supposedly bounded by specific values of ΔK. For instance, $\Delta K_{\text{threshold}}$ is defined as a lower bound (before which the crack growth rate is rapid and non linear), and K_{IC} is defined as an upper bound (after which crack growth rate accelerates fast and can lead to unstable crack propagation): as illustrated in the Paris crack growth rate curve in Fig. 1.5. These observations show how the fitting of the present model's phase-field fatigue parameters

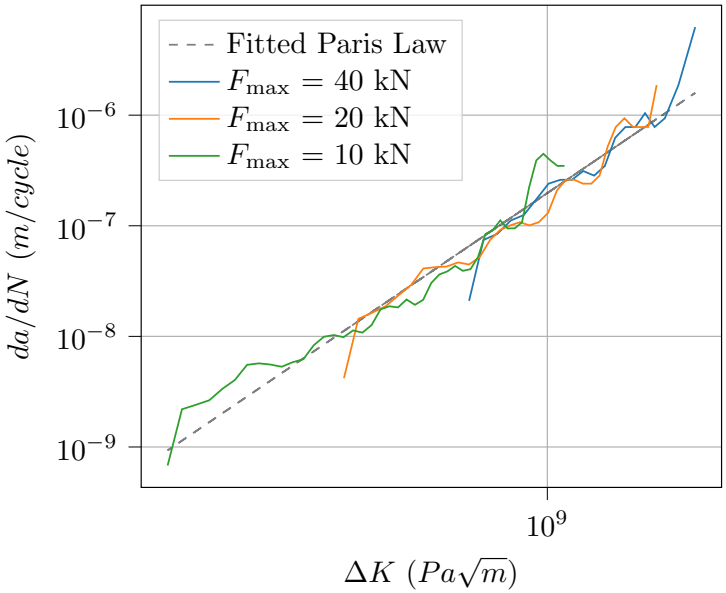

Figure 4.4: Paris' exponents identification process.

to follow a Paris Law, and brittle behavior in a unified framework is almost impossible. Indeed, K_{Ic} for example is supposed to be linked to both fracture phenomenologies, but is here evidenced to be load dependent. Similar arguments could be put forward for the lower bound $\Delta K_{\text{threshold}}$, which is related to α_T considering that it is a threshold parameter below which no fatigue can occur.

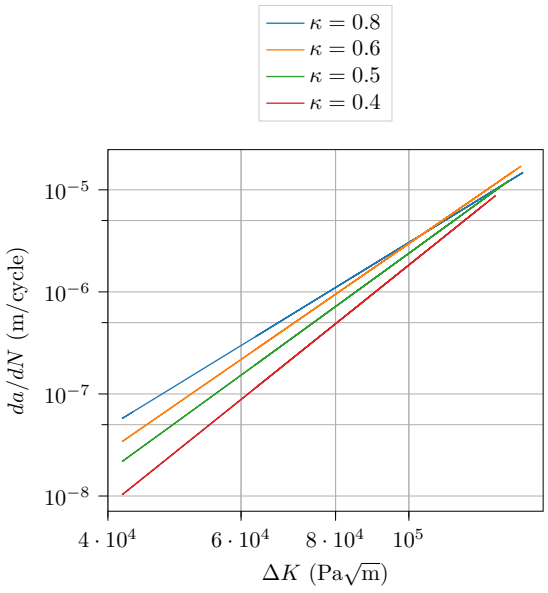

(a) Influence of κ on identified Paris law.

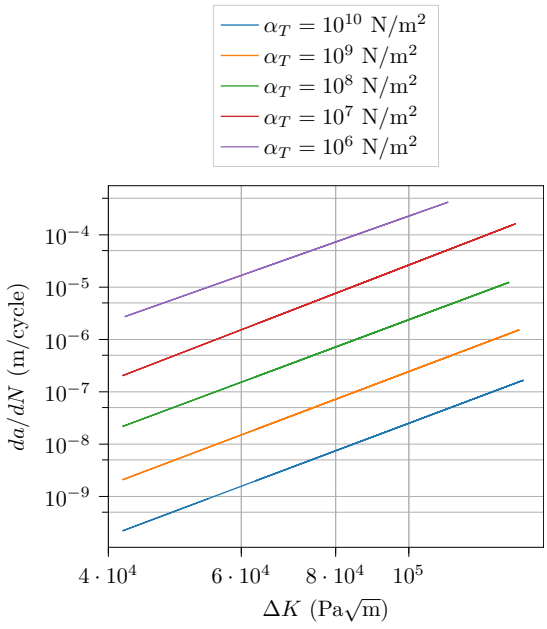

(b) Influence of α_T on identified Paris law.

Figure 4.5: Influence of α_T and κ on emerging linear regime.

The issue here is that the flexibility of the phase-field framework enables to bridge the gap between different representations of crack propagation, which are based on different theoretical tools that are complicated (or impossible) to unify. Therefore, the setup of the parameters based on material arguments is rendered difficult, as they should take all of those unified phenomenologies into account. The question is then, should we unify these fracture types, considering that they are driven by very different physical mechanisms? Considering these difficulties, we chose to fit the phase-field parameter without considering material arguments.

Therefore, using an iterative process of parameter tuning, and the clear correlations illustrated previously, we fitted our model to the experimental results of Ref. [84], with $l_c = 0.1$ mm, $G_c = 80$ N/mm, $\alpha_T = 10^9$ N/m^2 and $\kappa = 0.8$. With those fitted parameters, an applied loading of $\hat{F}_{\max} = 20$ kN and a loading ratio of 0.1, we reproduced the experimental results of crack length with respect to the elapsed cycle in Fig. 4.6.

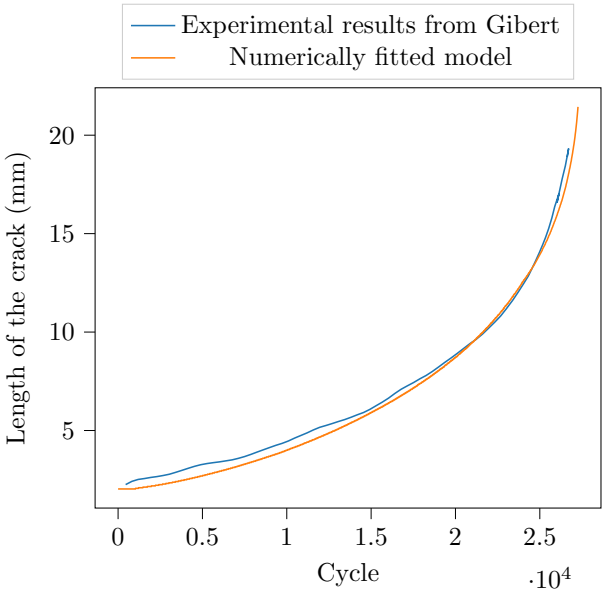

Figure 4.6: Length of the crack with the compact tension geometry, compared with Ref. [84].

As underlined in Hasan et al.'s work [100], such a fitting process is very computationally expensive because it requires the computations of several fatigue crack propagation cases. Therefore, the acceleration tools put forward in this work enabled to save a lot of computational effort during this fitting campaign.

4.1.3 Perforated CT prediction

The fitted numerical parameters were applied to the perforated CT model. The loading of $\hat{F}_{\max} = 20$ kN, and loading ratio 0.1 were employed. We recall that following Ref. [84], two hole diameters were tested on the CT geometry. We studied the influence of the hole diameter on the crack path by running two simulations of the perforated CT.

In Geometry 1, the crack deviated slightly from its usual path. In contrast, the crack was completely attracted to the hole in Geometry 2, where a larger hole had been drilled. These experimental observations were reproduced numerically with the previous fit. Fig. 4.7, illustrates this experimental-numerical comparison. On the left, we see the numerical results of the proposed model superimposed with the experimentally obtained cracks represented as black dashed lines. On the right, we picked figures from Ref. [84]. The experimentally measured displacement field is shown superimposed with the author's numerical results in white. One can see that a different initial crack height was recovered as the parameters of the hole given in Table 4.1, were slightly different from the final experimental geometry, due to usage of a low precision machining process [84]. The picture of the experimental sample for geometry one was taken at cycle $N = 27475$. The simulated results, on the other hand are shown at cycle $N = 21145$. For geometry 2, the picture was taken at cycle $N = 18787$ while our simulation is shown at $N = 15150$. Consequently, as well overestimating the influence of the hole on the simulated crack path, we overestimated the crack growth rate. This is consistent with the fact that no ductile effect were considered, leading to a more conservative prediction of crack propagation.

Finally, images of the damage field on the adaptively refined meshes are illustrated in Fig. 4.8. These numerical observations showed that a given Paris law fit could be transferred to another geometry with this model, and still yield relevant results. Moreover, the proposed acceleration tools enabled to accelerate the simulations significantly considering that the crack trajectory was not known beforehand. In this context, the model would have required a very fine mesh in the zone between the notch and the hole, with an explicit simulation of tens of thousands of cycles, which would have rendered this simulation untractable due to unmanageable computing time.

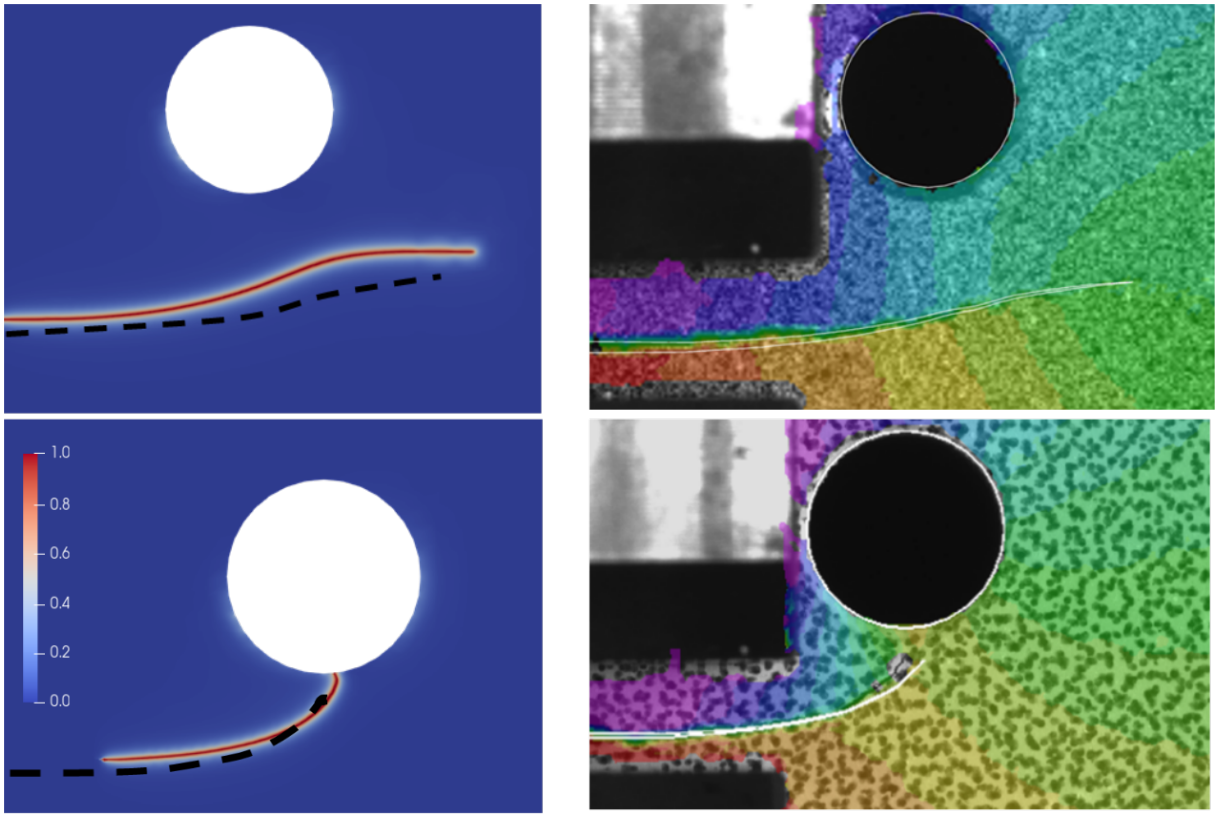

Figure 4.7: Comparison of crack paths with the numerical fitted model (left) and experimental-numerical XFEM results by Gibert [84] (right). The first row corresponds to geometry 1 and the second row to geometry 2.

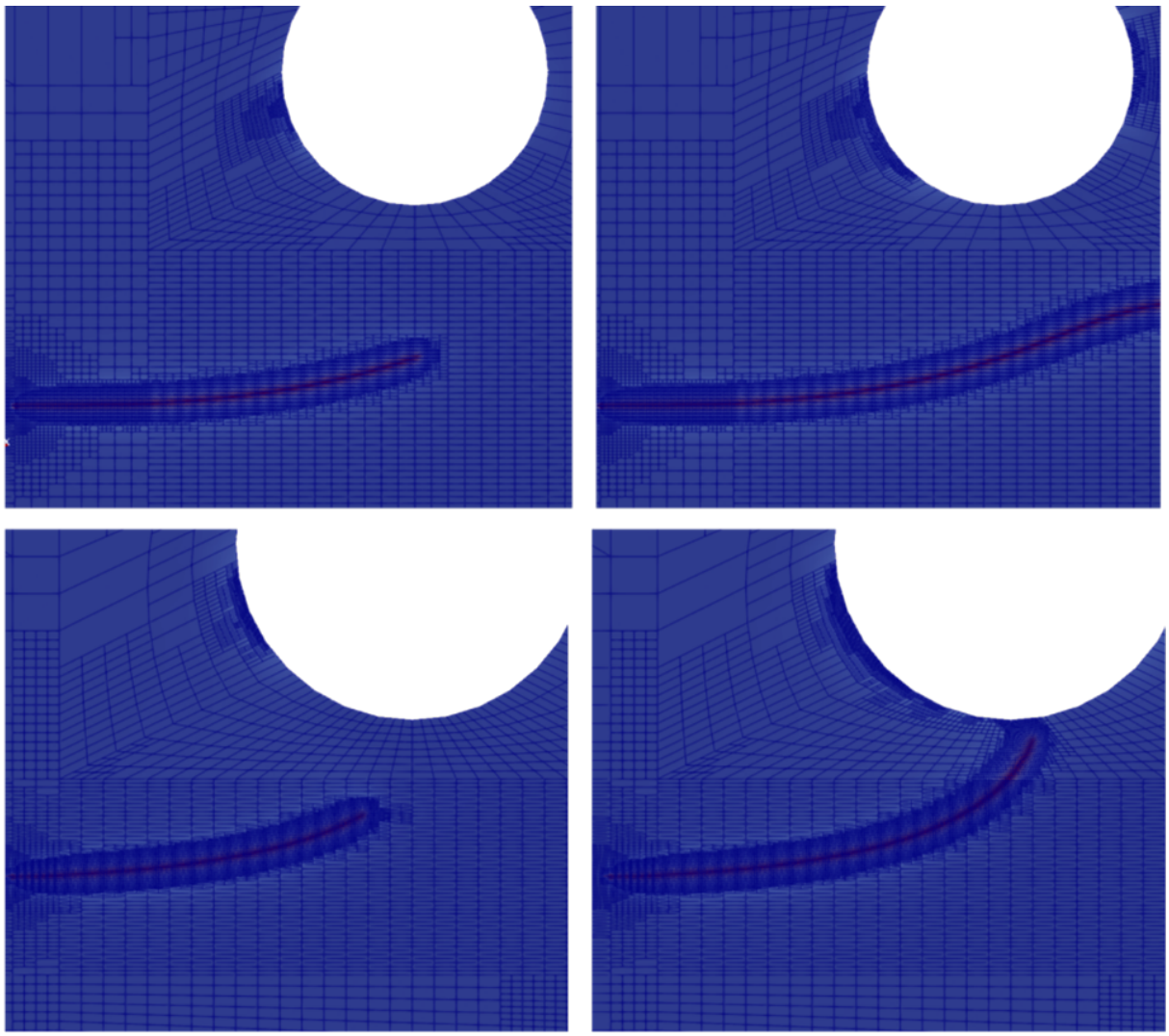

Figure 4.8: Meshes obtained with phase-field AMR and cycle jump on geometry 1 (upper row) and geometry 2 (lower row).

4.2 Participation in a benchmark activity

The second experimental-numerical comparison led in this work, was performed in the context of the seventh international conference on computational modeling of fracture and failure of materials and structures, CFRAC 2023. There a benchmark activity was organized by Julien Réthoré [209] based on experimental results by Réthoré and Seghir.

The authors have performed four experiments, on four different geometries, on the quasi-brittle failure of Plexiglas plates. These experiments were documented using high resolution imaging which led to the extraction of several precise experimental curves, of force-displacement curves, and evolution of the length of the crack, with respect to prescribed displacement.

The idea of the benchmark activity is that the participants should use two experiments to calibrate the model parameters, and then apply these fitted parameters to predict the two remaining experiments, without knowing the results beforehand.

Consequently, we structured this section in three parts. First, we described the studied geometries and the numerical models put forward to simulate them. Then, the parameter identification phase was detailed on the first two geometries. Finally, we applied these identified parameters to the remaining geometries and compared our results with the experimental ones, in order to estimate the predictive abilities of the proposed framework.

4.2.1 Preliminary work

4.2.1.1 Description of the samples

The first two geometries, onto which the calibration of parameter was performed, are the tapered double cantilever beam (TDCB), and the CLOVER geometry. They are illustrated in Fig. 4.9. The TDCB is a sample with an initial notch, from which the crack usually propagates in a stable manner. Displacement was prescribed to the geometry by moving the upper pin upward, while the lower pin was kept fixed, which induced mode I crack opening. The CLOVER sample is a plate with 4 holes. Both sides of the plate were clamped with a slight misalignment in order to force a consistent initiation on one specific side.

The next two geometries mirror the calibrating geometry, with slight differences. For instance, the TRIANGLE geometry is very similar to the TDCB experiment, with a mode I opening initiating at the initial notch. Then, the single crack drilled compression

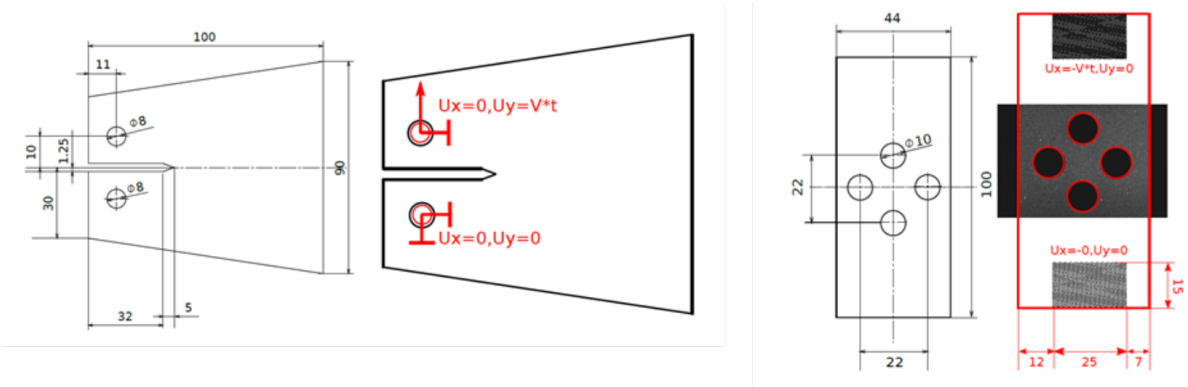

Figure 4.9: Geometries of TDCB and CLOVER from Ref. [209].

sample, (SCDC) is a perforated plate, which is compressed to initiate a crack at the notch. The geometries are illustrated in Fig. 4.10

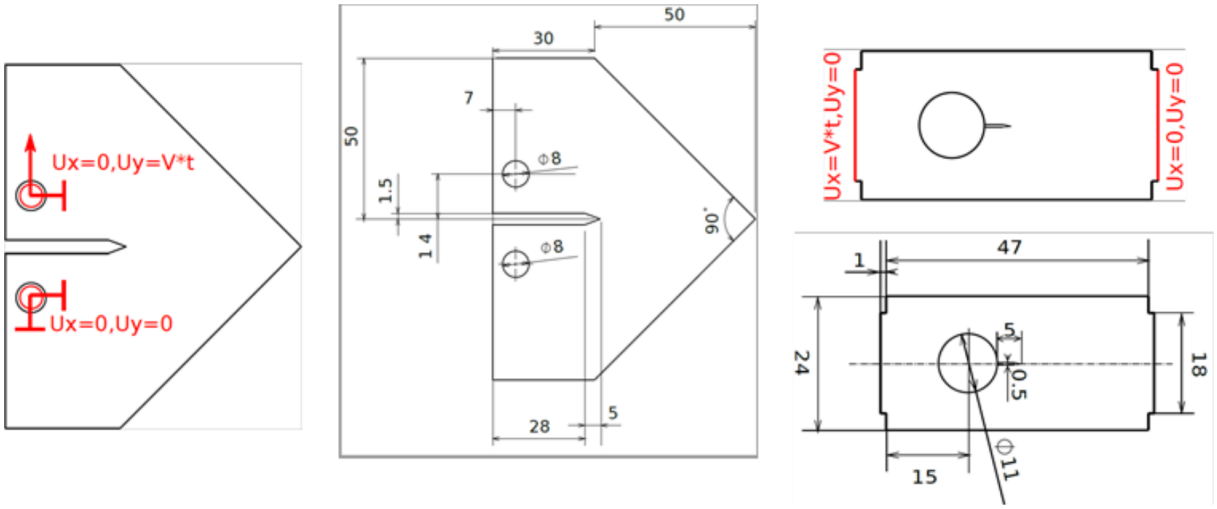

Figure 4.10: Geometries of TRIANGLE and SCDC from Ref. [209].

Four numerical models were proposed to simulate these geometries. For each of them, we proposed half specimens to reduce the size of the models by using their symmetric properties. Furthermore, we initially used fixed meshes, refined prior to the simulation on the expected crack paths, such that $h < l_c/4$. A representation of these numerical models were provided in Fig. 4.11 for CLOVER and TDCB, and in Fig. 4.12 for SCDC and TRIANGLE. On these illustrations, we indicated the boundaries onto which we prescribed the load: for TDCB and TRIANGLE, we prescribed displacement on a triangular geometry, which simulated the pin's contact in the holes with the central node used in the previous section. On the other hand, for SCDC and CLOVER, we represented the clamped as a part of the modeled domains, and prescribed displacement on these set nodes.

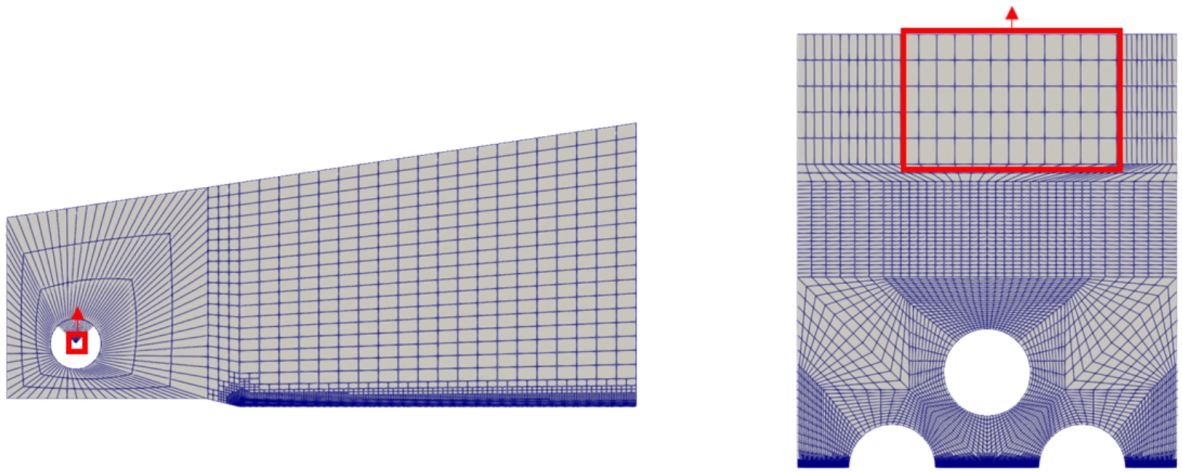

Figure 4.11: Mesh of TDCB and CLOVER. The elements that are displaced to model the loading boundary conditions are shown in red.

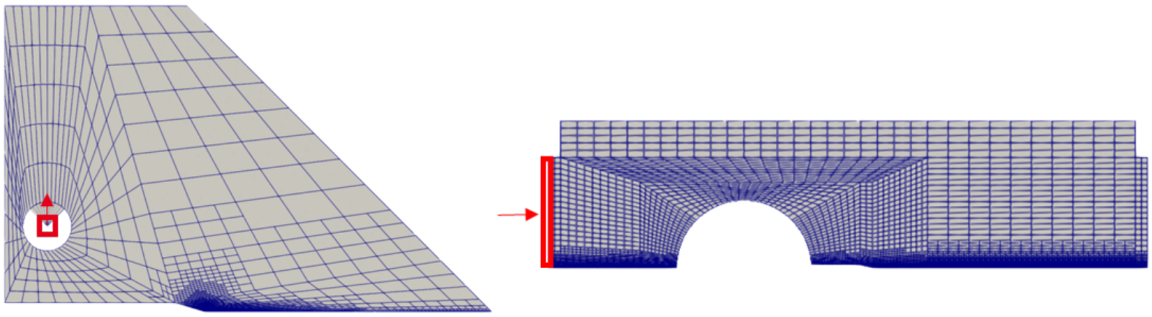

Figure 4.12: Mesh of TRIANGLE and SCDC. The elements that are displaced to model the loading boundary conditions are shown in red.

Furthermore, we decided to apply the adaptive mesh refinement procedure in order to evaluate its ability to recover results accurately in this challenging quasi-brittle context. The a-posteriori AMR procedure described in Section 3.4 was applied at each computed displacement step (without cycle jump procedures).

For the AMR cases, each of the presented numerical model were modified by setting much coarser elements on the expected crack path, except for the initial notches. Note that even though the mesh was set to be coarser, we still had to apply a relatively fine refinement ($h < l_c \cdot 2$) in the propagation zone. Indeed, as discussed previously, applying the proposed mesh refinement process on a uniform coarse mesh yields unnecessary large patches of extremely fine elements (see Section 3.3.4, and the 3D study in Section 3.4.3).

These mesh refinement experiments were in fact slower than the simulated results with the pre-refined meshes. This mostly comes from the fact that these patches of refined

elements were created, eventually leading to a less optimized mesh than the specifically tailored pre-refined one, exactly as illustrated in the 3D visualizations in Section 3.4.3. This observation once again highlights the importance of mesh coarsening in the phase-field context. Nevertheless, on all examples, the AMR process enabled significant computing gain before the number of degrees of freedom exceeded the initial mesh size. Indeed, the elastic domain, crack initiation and the initial crack growth stage were computed approximately three time faster considering.

4.2.1.2 Solver for unstable propagation

Considering that Plexiglas exhibits a quasi-brittle failure behavior, we found that the phase-field fatigue implicit cycle integration proposed in Section. 3.1, in a fatigue crack propagation context was not ideal. Indeed, quasi-brittle material can exhibit unexpected unstable crack propagation, which yields a challenging convergence of the implicit staggered scheme, and hence very long computing time. In order to avoid these convergence issues, we used the work of Molnár et al. [173], well adapted to unstable brittle crack propagation, where a time-step controlled explicit staggered approach is put forward. Contrarily to the mentioned work, we neglected inertial effect in this study. Hence, the pseudo-time is limited to the role of the evolution parameter. Brittle fracture was hence studied as fatigue was in the rest of the work: with a quasi-static formulation.

As we have shown in Section. 3.1.1, the explicit staggered approach suffers from its dependency to the prescribed displacement step. This is because no global convergence of the uncoupled sub-problem is checked. In this context, Molnár et al. [173] controlled the displacement step during propagation by enforcing a maximal variation of the history field: if the maximal variation of H is higher than a specific threshold, then the step is restarted with a lower prescribed displacement. More details on this approach are available in Refs. [173, 174]. It was used for this section, and yielded much more robust results and efficient computations, while converging to the implicit staggered solution.

4.2.2 Parameter identification

The benchmark activity's organizers have provided indications for the elastic parameters of the used Plexiglas: the value of E and ν were hence given [209]. However no indication of fracture toughness measurement, or critical stress on uniaxial samples were provided, which meant that no parameter calibration based on the arguments mentioned in the previous section could be used. Therefore, we again opted for a trial and error process, where we evaluated the variability of the mechanical response with respect to the numerical

parameter. Note that considering the quasi-brittle context, we set $f(\bar{\alpha}) = 1$ effectively cancelling fatigue effects. Therefore, no calibration of the fatigue parameters was performed.

We plotted the force-displacement curves obtained with the numerical models of TDCB and CLOVER in Figs. 4.13 and 4.14. By using varying values of l_c and G_c on both geometries we noticed a peculiar pattern: while l_c and G_c both have a significant influence on the computed mechanical response on the CLOVER sample, it seems that G_c plays a much larger role than l_c on the TDCB sample. Indeed, as can be seen on Fig. 4.13, for a given value of G_c, the critical stress reported for varying values of l_c are very close together.

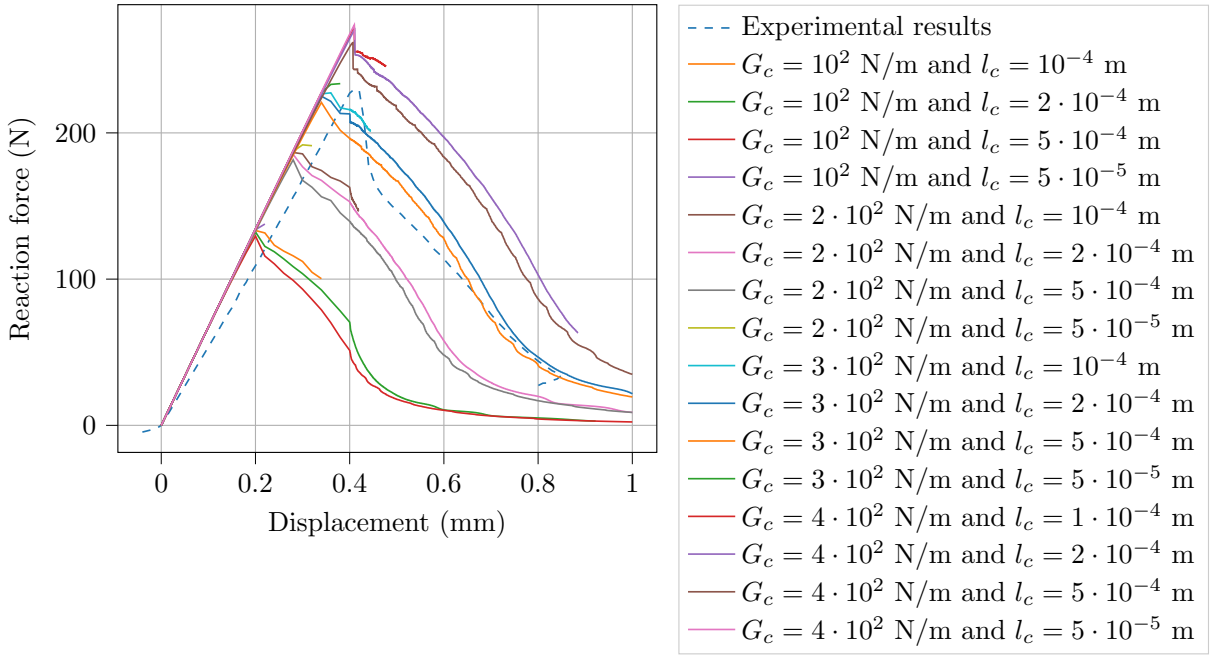

Figure 4.13: Influence of G_c, l_c on TDCB's response.

Furthermore, note that with the used elastic parameters we reported a significant deviation of the elastic response on both samples. This is because the experimental results provided here take the rigidity of the experimental device into account. Réthoré and Seghir reported the use of different experimental devices for each geometry, which meant that a specific correction had to be made on all computed results. As a first step, we calibrated the value of $F_{\max}$ without taking into account the displacement associated with this force. Then a displacement correction was applied on the computed result, in order to fit to the elastic domain found experimentally. This correction was only applied at the calibrating step, and not in the prediction phase.

Considering these initial observations, we chose to apply a two-step fitting process. First G_c was fitted for $F_{\max}$ on the TDCB geometry. Then, using this estimated G_c, we calibrated

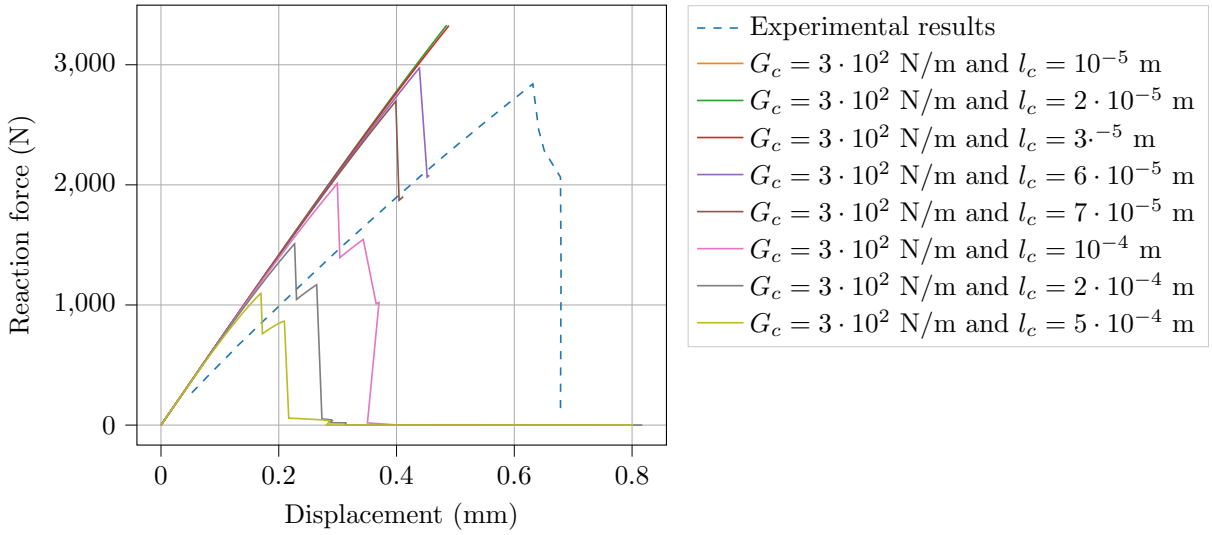

Figure 4.14: Influence of l_c on CLOVER's response.

l_c in order to recover the CLOVER's $F_{\max}$. Using this process, we found $G_c = 300\text{N/m}$ and $l_c = 0.06\text{mm}$, along with the initially set elastic parameters, $E = 1,47$ GPa and $\nu = 0.3$. The resulting fit on the calibrating samples were illustrated in Fig. 4.15.

In Fig. 4.15a we see that the TDCB sample experienced an abrupt softening phase before reaching a state of stable mode I crack propagation. The proposed fit was able to recover the stable crack propagation regime, with an underestimation of the initial jump. On the contrary, the CLOVER sample fails instantly at a given displacement. The unstable crack propagation was recovered. However, we predicted that the crack initiated at the short side of the clamps, which is not consistent with the experimental observation. This can be accounted to, among other sources of error, the simplistic modeling of the clamping device.

Note that the authors provided results of the evolution of crack length on the TDCB sample after the conference. A comparison between the fitted model (with the device's rigidity corrections) and the experimental results was provided in Fig. 4.16. Following the good recovery of experimental results with the proposed fit, we see that the crack evolution was also close to experimental result, with a steady state propagation after an initial abrupt jump.

Finally, on all these figures we have provided the results accelerated with AMR on the initially coarser numerical models. We observed a very accurate recovery of unaccelerated results. However, as previously mentioned, the simulations were slower at the final stages of crack propagation considering the large cost of the mesh without coarsening operations.

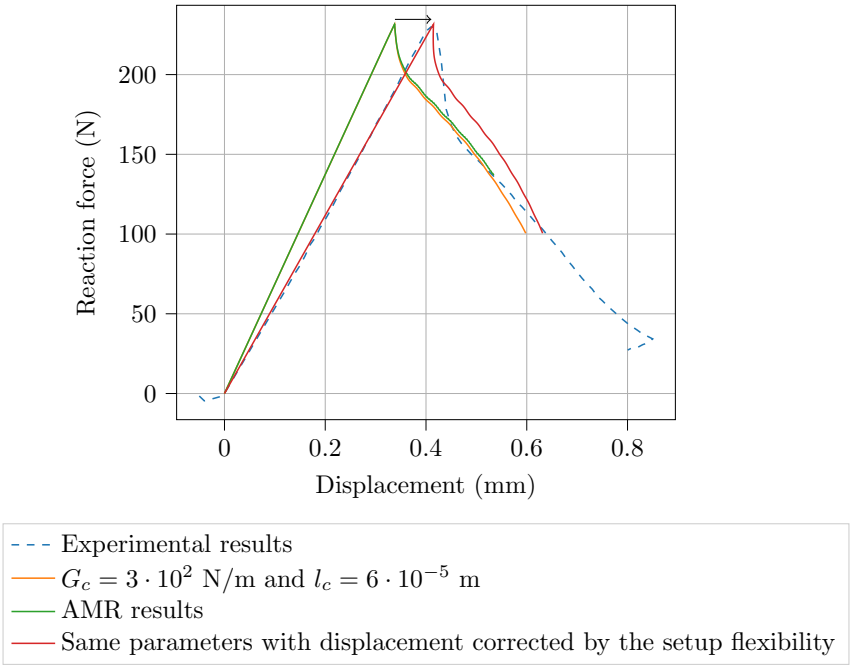

(a) Fit on TDCB with $G_c = 300\text{N/m}$ and $l_c = 0.06\text{mm}$.

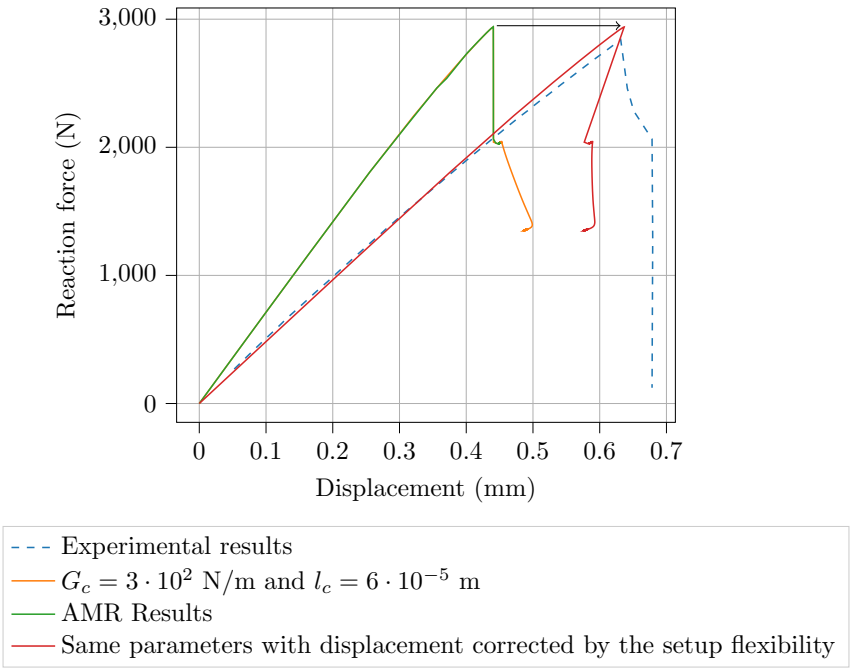

(b) Fit on CLOVER with $G_c = 300\text{N/m}$ and $l_c = 0.06\text{mm}$.

Figure 4.15: Force displacement graphs comparison of experimental results and the fitted model.

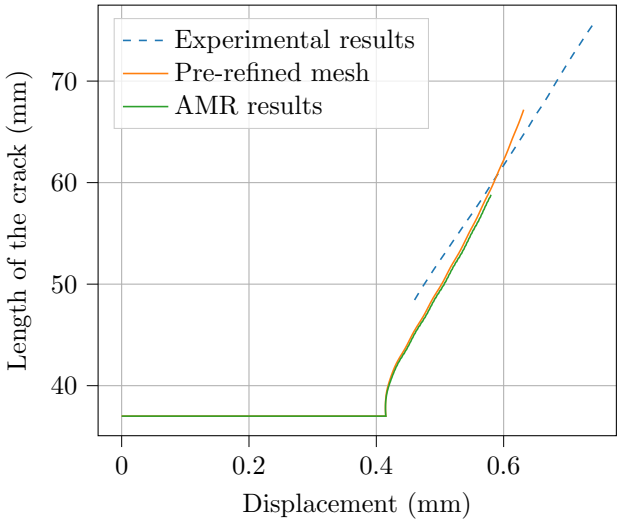

Figure 4.16: Crack propagation predicted with the fitted model on TDCB.

4.2.3 Prediction and AMR

Following this calibration process, we applied the deduced parameters to the remaining geometries. A comparison between the predicted results for force-displacement on TRIANGLE and SCDC was provided in Fig. 4.17. Furthermore, the evolution of crack length on these samples was plotted in Figs. 4.18. All of these results are given with the unaccelerated procedure, and the AMR procedure.

The predicted results on the SCDC test were not in line with experimental observations. For the compression loading prescribed, the sample experienced a progressive softening shown in Fig. 4.17a. All the while, the crack propagated in a stable manner at the notch until complete failure. With the proposed model, we have predicted a similar two-step failure: first stable crack propagation at the notch, then unstable crack propagation at the notch leading to failure on the other side of the hole. However we underestimated considerably the displacement at which fracture initiates at the notch, and overestimated the crack growth rate under this compressive loading, as shown in Fig. 4.18a. This could highlight the deficiency of the spectral split to model Plexiglas in compression. Indeed, this sample is the only one where the treatment of unilateral effects (see Section. 2.1.2.3 and 2.2) plays a key role. This highly inaccurate prediction could also come from the simple modeling of boundary conditions, and issues of device rigidity. The adaptive mesh refinement process yielded very accurate results, with a slight deviation observed at the last stages of unstable crack propagation.

On the other hand, the prediction of the TRIANGLE test were more in line with experi-

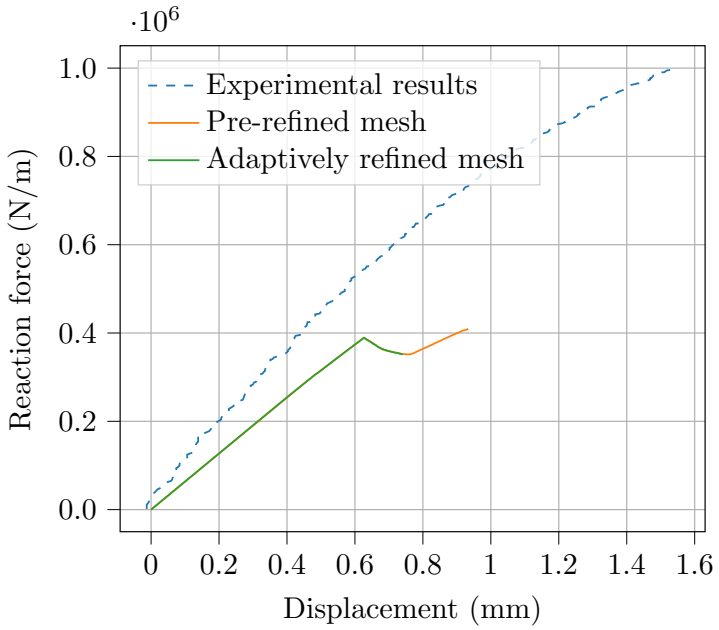

(a) Blind prediction on SCDC with $G_c = 300\text{N/m}$ and $l_c = 0.06\text{mm}$.

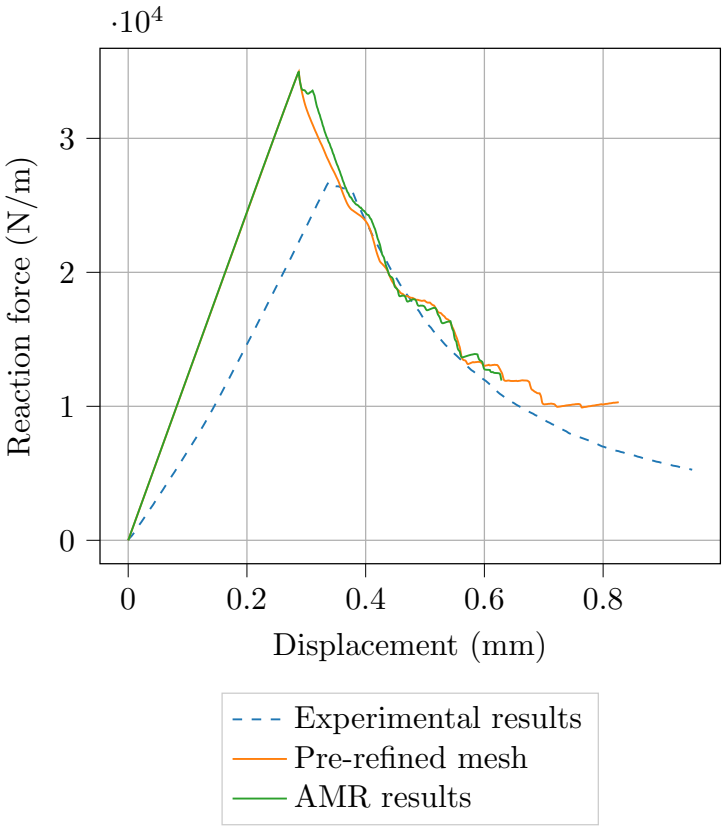

(b) Blind prediction on TRIANGLE with $G_c = 300\text{N/m}$ and $l_c = 0.06\text{mm}$.

Figure 4.17: Force displacement graphs comparison of experimental results and the fitted model.

mental results. Indeed, we see that even though $F_{\max}$ was significantly overestimated, we were able to reproduce the stable crack propagation regime observed with this sample. Moreover, this regime was captured remarkably right, with an initially fast crack growth rate, that progressively slows down, as illustrated in Fig. 4.18b. However note the strong influence of the mesh in the last stages of propagation considering the set pre-refined mesh, which used coarser elements near the further edge of the sample, in order to yield tractable computing time (Fig. 4.12). These spurious results were also found with the AMR procedure which showcases the issues of mesh dependent results in the context of very large $h_{\max}/h_{\min}$ ratios. This underlines once again the difficulty of applying the framework at the scale of structural elements where this ratio is bound to be important considering the ratio between the structure size and the characteristic length.

In the end, the precise prediction of crack propagation also depends strongly on the modeling choices. In Triclot et al. [245], the pin-hole boundary conditions, and its usual numerical representations were closely investigated, to show that in the propagation phase, none of these choices could reproduce experimental data. The authors points toward the influence of crack propagation on the movement of the contact as a possible source for this discrepancy. Here such effects are bound to have an influence on the results since the TDCB and TRIANGLE samples were loaded using a pin-hole setup. Furthermore, the CLOVER and SCDC respective clamp and contact setup must be closely investigated to improve accuracy of the model, but represents an important modeling challenge. Note additionally, that Triclot et al. [245] also report accuracy issues before the propagation phase, when using displacement loading conditions, which were consistently used here.

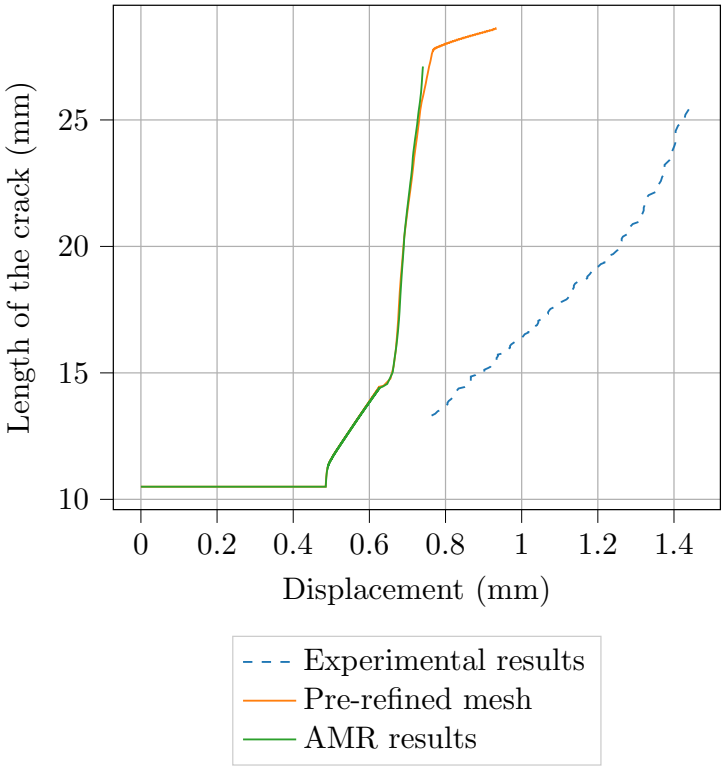

(a) Crack propagation on SCDC with the fitted model

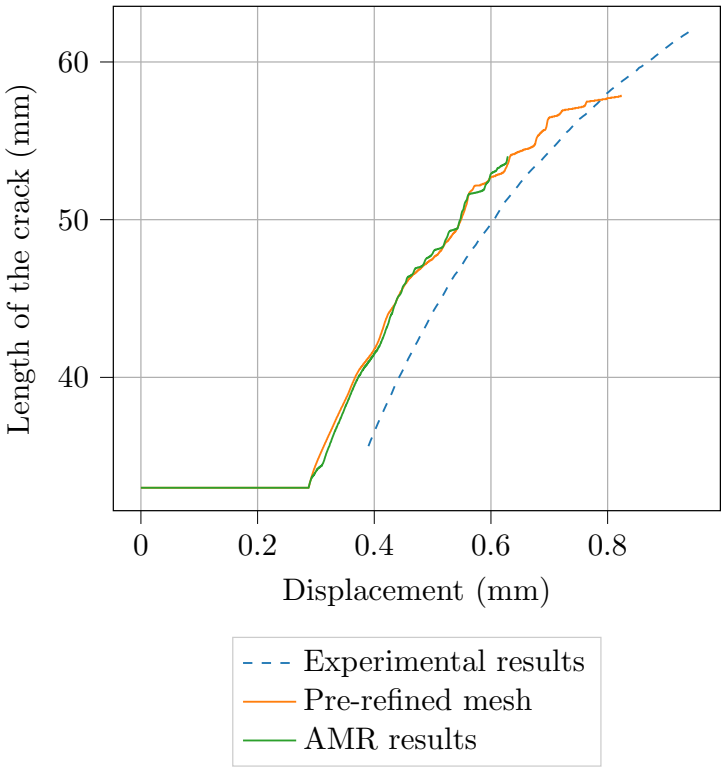

(b) Crack propagation with the fitted model

Figure 4.18: Crack propagation on TRIANGLE with the fitted model

Conclusion of the chapter

In this section, we reproduced experimental results of fatigue crack propagation and quasi-brittle failure using the proposed accelerated framework. For both cases, we identified phase-field parameters to correspond to a given experimental observation, and applied the fit to slightly different geometries. On most cases, the fitted phase-field framework provided quite good qualitative predictions, and the AMR and cycle jump tools were used to accelerate significantly all stages of the numerical campaigns. We have hence shown the applicability of the framework on real-life cases, and shown that a basic fitting process could enable the prediction of experimental crack paths.

Moreover, these applications enabled to put in light the issues of such real-life application. First, we highlighted the difficulties linked to parameter identification in a unified fatigue-brittle context. Then, several issues with the refinement of the mesh in the context of very large $h_{\max}/h_{\min}$ ratios were observed, which strongly underlined the need for coarsening operations. Additionally, we have seen the difficulty of reproducing experimental data with simplistic modeling of the boundary conditions, and the influence of the device's rigidity in measured results.

Conclusions and perspectives

In this thesis, we first proposed a brief literature review of the fatigue degradation mechanisms, as well as an overview of the different theoretical and numerical methods used to characterize it. At this point the phase-field model for fatigue was chosen, which led us to an in depth description of the different ingredients of the used phase-field model, and its implementation in a finite element method context. A special care was given to the spectral decomposition of energy, as a novel method was put forward in this work, to compute the decomposed terms and associated stiffness/stress tensor. This method enabled computing gains as well as eliminating the risk of singular values in the original expression [176]. This phase-field fatigue model was then validated by applying it on several numerical benchmarks, which enabled to showcase the possibilities of the model which can bridge the gap between crack initiation and growth, recover crack branching, and from which a Paris type crack growth rate can be extracted.

These initial tests also underlined how computing time associated with the phase-field model are not tractable for industrial use, which motivated us to add some accelerating tools in the formulation. After a brief investigation for an efficient time-integration method, a novel accelerating framework for phase-field fatigue was proposed, that makes use of adaptive mesh refinement (AMR) with cycle jump schemes. Some variants of this accelerating framework were investigated, such as different extrapolation schemes for cycle jump, settling for an iterative formulation inspired by Loew. [151]. The possible computing gains of this AMR/cycle jump approach were obtained by comparing results of initially pre-refined meshes (in itself, already more efficient than a uniform fine mesh) with results from adaptively refined meshes, which yielded an acceleration factor of around 100 in some conditions. Such an efficiency gain at a given level of accuracy shows the interesting perspective of this approach. With it, we were able to reproduce precisely complex crack propagation patterns such as the "en-passant" crack, the branching pattern, and the crack nucleation example of the perforated plate.

Thereafter, using this accelerated framework, we tried reproducing experimental data, that was collected in the work of Gibert [84], and during CFRAC 2023, by Réthoré & Seghir [209]. In both cases, a trial and error process was used to calibrate the phase-field parameter considering the inherent difficulty to link these parameters with material quantities, in a unified brittle-fatigue manner. We showed that this calibration process enabled a very good fit of the model. Furthermore, note that these calibrations required several fatigue/brittle lifetime computations, which were greatly accelerated with the proposed framework. Then, the prediction step based on these numerical fit, led to a relatively good prediction of crack paths and lifetime before failure. These predictions showcased how even a very simplistic parameter identification process could lead to satisfying predictive abilities with this model. For instance, using the Paris type crack growth rate, which is recovered by the model on a simple geometry, we were able to reproduce crack path trajectories by applying the fitted Paris Law on a different geometry. This means that the Paris Law, supposedly only dependent on the material parameters [190], could be used with success across geometries and loading conditions.

Finally, note that one objective of this work was to enable the use of the proposed phase-field framework for CEA's engineer. Therefore, we implemented the phase-field fatigue framework in this environment, and created the acceleration subroutines for cycle jump and AMR within the same package. The structure of this package was described in appendix.

Nevertheless, following these positive results of significant acceleration, at a good level of precision, and with the ability to fit experimentally obtained results, this work has enabled to showcase several issues, and thus perspectives for the phase-field model and its application for real-life settings. The rest of this section discusses some of these perspectives.

Several works have been published recently about the extension of the phase-field model for fatigue. Some proposed modifications of the functional to add more fatigue effects [6, 88], or further acceleration methods [130]. All of these additions would be interesting to implement with the current framework, in order to test it with a model that takes more fatigue effects into account, such as with the different modifications of the fatigue history variable proposed in Alessi et al.'s work [6]. Moreover, in this work, the use of a purely elastic framework hinders the application of the model in an industrial context. It would therefore be interesting to extend the model to add plastic effects, explicitly through the use of a fatigue elasto-plastic phase-field model [101, 247], or indirectly through the modification of the accumulation of the fatigue history variable, as proposed in Ref. [6].

Even though the accelerated framework provided very significant computing gains, we feel

that in order to use the framework on large scale 3D models, further gains must be made. Indeed, as illustrated by the very small amount of 3D benchmarks tested in this work, the modeling of meshes with a high number of degrees of freedom was too computationally expensive. In this regard we propose the acceleration of the cycle computation [129, 130], the development of a relevant ΔN for cycle jump schemes, and most importantly, mesh coarsening operations. Some works have proposed mesh coarsening with a phase-field model [192, 244]. But, as the phase-field's variation must still be properly captured by a fine discretization in the wake of the crack, the authors are limited to coarsening the elements which were not necessary, with an a-posteriori check. Such a treatment would enable computing gains with our proposed framework, but it would be interesting to investigate for further coarsening in the wake of the crack. This means evaluating how a coarse discretization of the crack, far from the crack tip influences the overall mechanical response and the crack's path. Alternatively, the crack could be modeled using XFEM (or any element erosion/remeshing techniques) after the wake of the crack to enable coarsening operations that would only require a fine mesh at the crack tip [83].

As mentioned in the AMR section (Section 3.3.2), irreversibility cannot be checked locally with the proposed framework, as it is based on the history field method which cannot be used rigorously with the AMR process. Therefore, even though no reversibility issues were noticed in this work, considering the utmost importance of irreversibility with continuous damage models, we advocate for a more rigorous irreversibility constraint in this context.

Finally, as discussed in the last chapter, parameter identification with a fatigue phase-field model remains an open question. In this work we only used a trial and error heuristic method to identify the phase-field parameters l_c and G_c, and the fatigue related parameters κ and α_T. The former group can be related to the critical stress with a uniaxial test, and the critical energy release rate. It would therefore be interesting to try the numerical/experimental comparisons led in this work, with these considerations in mind.

A

Tests for an adaptive ΔN for cycle jumps

In the literature, most approaches for the adaptive choice of ΔN during cycle jump operations are all based on the limitation of the variations of the extrapolated quantities. For instance in Lemaitre & Doghri [145], and other works [246] it is enforced through the ratio between the variation of quantities in one cycle, and the variation of the quantities during cycle jump. Note that we used a similar assumption previously, stating that this micro time scale variation remained small in front of the macro-time scale cumulated value, to simplify the expression of the tangeant operator (3.9). This is also analogous to the vision expressed in Abdullatif et al. [1], that considering a first order Taylor development approximation, means neglecting second order terms which leads to enforcing a very small value of ΔN compared to the ratio between the macro cumulated variables and the micro-time variation. In Yan et al. [261] the scheme is driven by the variation of damage in the control cycles, similarly to Loew et al. [151], based on the ratio between variation at N, and variation at $N + \Delta N$, which is consistent with the proposed trapezoidal scheme. A similar approach is used in Seles et al. [225], based on relative difference between variation of the fatigue internal variable at different control cycles.

A brief investigation was thus pursued to check suitable criteria for an adaptive ΔN in this AMR and cycle jump framework. We recall that the trapezoidal scheme used a simple adaptive ΔN approach, driven by the length of convergence of its iterative scheme: if convergence is too long, we restart the jump with a lower value of ΔN. This approach seemed to work correctly in the previous section, even though we have shown that in some cases, the trapezoidal criterion could yield imprecise result. Therefore we have searched for another indicator that could control ΔN during computation.

We intend to keep the flexibility of the phase-field approach, and hence dismissed adaptive methods based on crack length, or crack growth rate [43] as they would not be tractable in multi-cracks, or crack nucleation scenarios. First we investigated a criterion for the FE extrapolation scheme, considering that it has proven its ability to accelerate computing time, but is very dependent on the value of ΔN. Then we tried for an adaptive criterion based on the variation of $\Delta\bar{\alpha}$, considering the previously mentioned works in the literature, that could hence be used with both extrapolation schemes.

A.1 Trapezoidal criterion for the forward-Euler scheme

Our first idea was to use the trapezoidal criterion to drive the FE scheme. This means that we checked that the variation of $\bar{\alpha}$ is the average of $\Delta\bar{\alpha}$ computed at N, and $\Delta\bar{\alpha}$

computed at $N + \Delta N$ with $\bar{\alpha}_N$ predicted with the FE scheme. If this criterion explicited in Eq.(3.4) was not verified, the cycle jump was restarted with a lower ΔN.

Even though it seems to be a relevant criterion to bound ΔN during propagation with the FE scheme, it did not improve computing time in any significant way. First, note that it reduced ΔN_{eff} because of the computation of $\bar{\alpha}_{N+\Delta N}$ for the verification of the trapezoidal criterion. Then, it predicted very conservative values of ΔN as was illustrated in Fig. A.1. Here, we used the proposed adaptive scheme on the previous mode I sample, with $\Delta\sigma_{i=1,2,3,4}$. For the initial jump used on each respective loading, we have shown the evolution of the maximum trapezoidal residual (3.7) with respect to the used ΔN. For instance, take $\Delta\sigma_2$, where we have shown that $\Delta N = 60$ could be used to predict accurately the initial stage of fatigue crack propagation with the FE scheme. However for $\Delta N = 60$, we can see that the maximum residual is 10^4 times higher than the threshold that was used for the trapezoidal scheme (and that $\Delta N < 1$ would be used if we wanted to use the same threshold for both schemes). Similar conservative results were observed for the other loadings, and throughout crack propagation. This seems to indicate that the FE scheme prediction is not very well aligned with a trapezoidal evolution of $\bar{\alpha}$, which was expected considering the explicit nature of the scheme. Nevertheless, it can be used to provide an adaptive bound for ΔN with the FE scheme. Further investigations should be led to confirm that this adaptive bound is linked to crack growth rate, and hence robustly provides a relevant decrease of ΔN to keep accurate results. These investigations were not pursued because of the low efficiency gains reported with these initial tests.

A.2 Adaptive ΔN for trapezoidal scheme

From the previously mentioned works on the choice of an adaptive ΔN [1, 145, 151, 246, 261], we can consider multiple criteria based on the variation of $\bar{\alpha}$. For instance, we can study the value of:

1. $\Delta\bar{\alpha}_N$ the variation of the fatigue internal variable in one cycle.
2. $\Delta\bar{\alpha}_{N\to N+\Delta N}$ the variation of the fatigue internal variable in one cycle jump.
3. $\dfrac{\delta\bar{\alpha}_{N+\Delta N}}{\delta\bar{\alpha}_N}$ analoguous to Loew et al. [151] and Seles et al. [225].
4. $\dfrac{\Delta\bar{\alpha}_{N\to N+\Delta N}}{\bar{\alpha}}$ analogous to Abdullatif et al. [1].

The idea to find a relevant criterion was to assess if the variation of these quantities on a known propagation case, reflect the reality of the ΔN needed at each stages of the fatigue

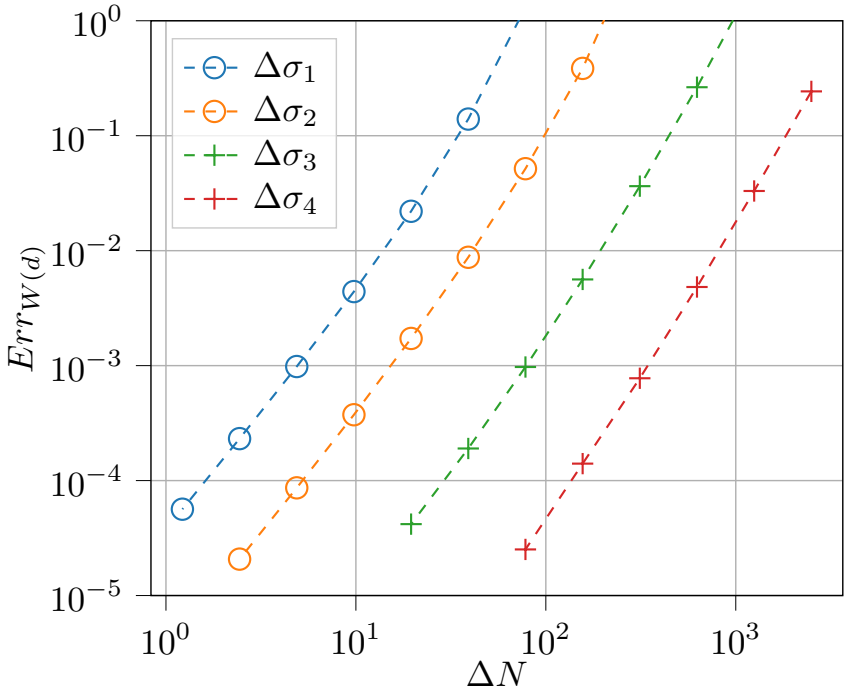

Figure A.1: Trapezoidal criterion for different values of ΔN with a Forward Euler extrapolation scheme.

life. We used the mode I crack in an infinite plane, with $\Delta\sigma_2$, as we already have all the relevant information of crack growth rate, number of iterative steps of the (TI) scheme with and without AMR. At each performed cycle jump, we computed the presented criteria, so as to observe how they evolve during crack propagation, and if they are able to quantify the need for a finer, or a larger ΔN. These criteria were hence not used to adaptively modify ΔN: a constant number of jumped cycle $\Delta N = 30$ was kept fixed during propagation.

Note that this sample was recently analyzed in Alessi et al [6], with a precise description of the fatigue crack propagation stages with a toughness degradation model. The authors report a 3 stage propagation before unstable failure: "(1) initial accumulation stage, (2) the transient evolution stage, (3) the stable propagation stage" [6].

These stages were also identified with the proposed framework. For instance, the initial accumulation stage was already mentioned previously, as the stage where $\bar{\alpha}$ evolves linearly because no toughness degradation, or damage evolution can happen. This stage is related to the threshold value of the fatigue degradation function, and can promptly be simulated using very high values of ΔN [62, 145, 225].

The second stage was also observed just after crack initiation as can be seen on plots of evolution of the crack such as Fig. 3.26a, where the evolution of the variation of area

between $250 < N < 900$ was not stable. This stage can be linked to the stage (I) of the standard Paris crack growth rate curve as illustrated in Section 1.1.1. Note that the trapezoidal scheme exhibited difficulties at this stage, as can be seen on Fig. 3.13b and Fig. 3.27, with longer convergence for $250 < N < 600$ than further, at the stable propagation stage. This can be explained by the fact that at this point, $\Delta\bar{\alpha}_{N\to N+\Delta N}/\bar{\alpha}$ is too high considering that the fatigue internal variable is still very low. As mentioned earlier, a high value of this ratio means that the neglected variation in the computation the tangent operator of the TI scheme is no longer justified. Furthermore, it means that the neglected second order terms of the FE scheme becomes important [1]. Finally, in Alessi et al. [6], the authors attribute this transient state, to the fact that "the material ahead of the crack tip degrades more before triggering fatigue crack propagation than during the steady propagation stage". This leads to a faster crack growth rate at the beginning of the transient regime than in the steady regime. We therefore expected that a relevant criterion would find this transient stage and advise a lower ΔN than in the next stage. Note however that considering the low influence of this stage on the accuracy of the solution, even with ΔN and the FE scheme, its recovery is not an absolute necessity.

Finally the stable regime was also recovered as highlighted in Section 2.4, and we therefore expected that a relevant ΔN criterion would then yield a stable regime, smoothly increasing to the last stages, where the crack growth rate rapidly grows to unstable failure.

In order to compare the variation of these criteria, we normalized their value by the range they spanned during computations, such that:

$$Crit_{\text{norm}} = \frac{Crit_N - Crit_{\min}}{Crit_{\max} - Crit_{\min}}, \tag{A.1}$$

with $Crit_{\max/\min}$ the maximal/minimal value of the criterion during propagation. Note that this normalizing operation is not possible during propagation as $Crit_{\max/\min}$ are not known beforehand. It is therefore very hard to set a general threshold in practice.

All of the considered criteria are based on the variation of $\bar{\alpha}$ which is a field defined at the integration points of the finite element mesh. Therefore, two norms were used to evaluate the criteria: the maximal value of the criteria on the domain, and the integral of the criteria on the domain.

The variation of the normalized criteria was plotted in Fig A.2. First, we illustrated the variation of the fatigue internal variable, during a cycle $\Delta\bar{\alpha}_N$, and the variation of the fatigue internal variable during a jump $\Delta\bar{\alpha}_{N\to N+\Delta N}$ in Fig A.2a We observed that

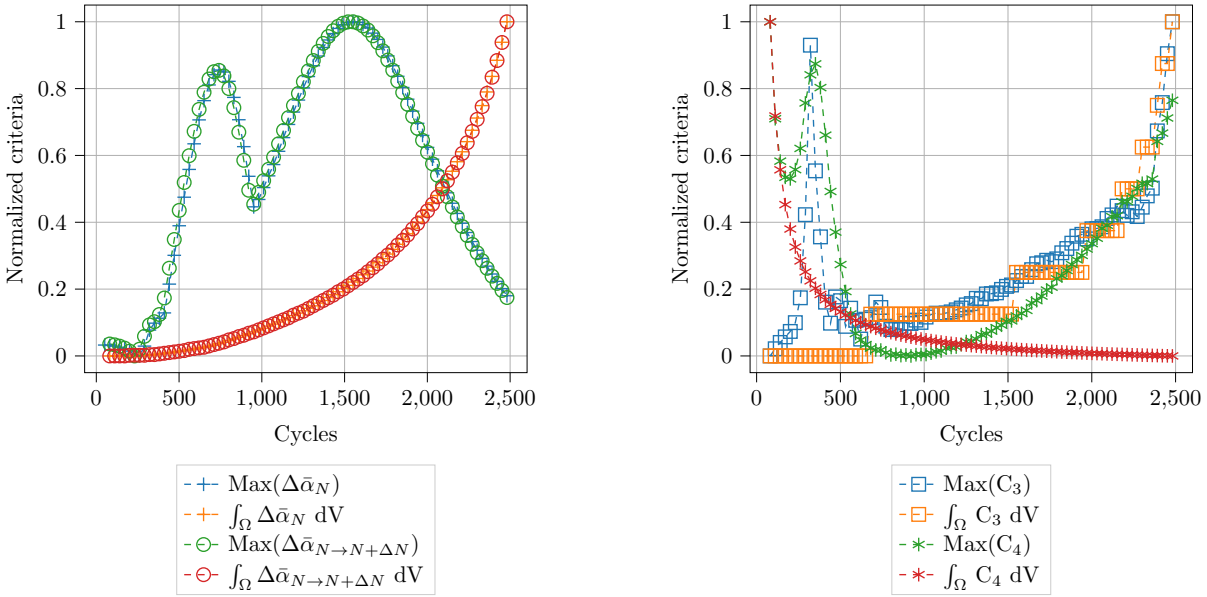

(a) Variation of the first defined criteria.

(b) Variation of the ratio.

Figure A.2: Evolution of the defined "criteria" for an adaptive ΔN.

both criteria yielded very similar result when using this normalizing approach. This was expected considering that the variation of $\bar{\alpha}$ during a cycle jump is conditioned to be a function of $\Delta\bar{\alpha}_N$ by the trapezoidal scheme. However, we noticed a large difference between the maximum value of the criterion and the integral value: The maximum criterion yielded a very irregular evolution during propagation, while the integral value can be described as a smoothly increasing evolution, apparently similar to the crack area growth. In this sense it seems that the integral value of the variation of the internal fatigue variable could be used as a reliable adaptive ΔN indicator. However, note that the transient state was not captured by either approaches.

Then, in Fig. A.2b we plotted the criteria based on the recent adaptive ΔN approaches for phase-field [151, 225], which have limited the jump using a measure of the ratio between variation at two successive control cycles. This is quite similar to driving ΔN by limiting the acceleration of the evolution of internal variables rather than their velocity of change. With this criterion, we obtained the expected result that this acceleration steadily grows during propagation, with both used norms. However, the transient state was only recovered with the consideration of the max of the criterion on the domain.

Finally the evolution of the ratio between $\Delta\bar{\alpha}_N$ and the current value of $\bar{\alpha}$ was plotted in Fig. A.2b. The integral value of this criterion yielded a poor indicator, contrarily to the maximal value which seems to recover every expected jumps of ΔN. Indeed, the

integration of this ratio on the entire domain flooded the important local information at the crack tip with the rest of the domain where this ratio is much lower. However, considering the maximum value yields the most critical point on the mesh, where the most important variation of $\bar{\alpha}$ happened and its cumulated value was the lowest: the crack tip. This enabled to find the transient state with a predicted jump of the criterion for $250 < N < 500$, as well as the stable state with a drastic reduction of ΔN, which smoothly increases as crack growth rate increases. This seemed to be the most relevant criterion investigated here.

However, note that this brief investigation for a relevant adaptive ΔN scheme was not pursued further in this work, and with the following applications. This is because, in practice, finding an appropriate threshold for each considered cases was not trivial. Therefore, considering the advantages of the TI scheme, along with the ease of use of the adaptive ΔN scheme based on length of convergence, we chose to apply it on all remaining applications in this work.

B

Cast3M implementation

B.1 Structure of the phase-field extension

In order to use a damage phase-field model in Cast3M, we added several small bits of code in several subroutines. The implementation relied on the creation of a mechanical model (modified for phase-field). Furthermore, we have extensively used the standard thermal Cast3M subroutines by considering the damage field and the associated evolution laws, analogous to the temperature scalar and the typically associated partial derivative equations.

For the mechanical phase-field model we used Ref. [51], where clear instructions on how to introduce a new mechanical model in Cast3M are compiled. As the phase-field model can be viewed as a continuous damage model, we have introduced our formulation along those models. Therefore, we changed several sources:

- NOMATE.ESO : where we can set the index of the model
- MODENDO.ESO : where we can set the keywords of the model
- IDVARI/IDVAR5/IDENDO.ESO : where we list the model's specific parameters
- COML6.ESO/COML8.ESO : where the evolution law is enforced

Those last subroutines (COMLX.ESO), are then directed towards custom subroutines created for this work, where the phase-field variable's influence on the mechanical quantities is computed. For instance, in this subroutine we compute the damaged stiffness tensor, (with the spectral decomposition when using this approach), we compute ψ_0^+ and ψ_0^-, as well as the damaged stress and finally, we check irreversibility.

The rest of the implementation work was performed in so-called "*procedures*". One procedure per operations were implemented:

- Solving for the damage sub-problem
- Solving for the mechanical sub-problem
- Computing a fatigue cycle
- Performing a cycle jump
- Checking the AMR criteria and refining
- Applying boundary conditions on the new mesh
- Propagation procedure linking all those tools

Users would then have to set an initial geometry and mesh, linked with boundary conditions. Several parameters can be adjusted, starting from the material parameters $E, \nu, G_c, l_c, \alpha_T, \kappa$, to the acceleration tools parameters $\Delta N, h_{AMR}$ and d_{AMR}. All cited objects can then directly be inputted in the main *procedure* to simulate the fatigue life of a component.

B.2 Basic example : damage problem

Here we show a basic example of the resolution of the damage problem. Adding fatigue effects simply relies on the degradation of G_c by $f(\bar{\alpha})$. Here the example enables to get Figs.2.5 and 2.6.

```
*** RESOLUTION OF A DAMAGE PROBLEM IN CAST3M ***
* mesh is the FEM mesh, nd_crack is the nodes along the crack *
* the model can be AT1 or AT2, Gc, lc must be set *

** MODEL DEFINITION **
ME = MODE mesh 'THERMIQUE';

** DIRICHLET ON CRACK D=1 **
BLD = BLOQ nd_crack 'T';
fd = DEPI BLD 1;

SI(NON AT2);
* if AT1, we enforce 0>d>1 *
  BLO2 = RELA 'MINI' 'T' mesh;
  BLO1 = RELA 'MAXI' 'T' mesh;
  BLD = BLD ET BLO1 ET BLO2;
  f1 = DEPI BLO1 1;
  f2 = DEPI BLO2 0;
  fd = fd ET f1 ET f2;
FINSI;


SI(AT2);
*AT2, Gc.lc => conduction (B^T.B), Gc/lc => capacity (N^T.N) *
  condumat = Gc * lc * 1;
  capamat = Gc/lc;
SINON;
*AT1, (3/4)*Gc.lc => conduction (B^T.B), 0 => capacity (N^T.N) *
  condumat = (3./4.) * Gc * lc;
  capamat = 0;
FINSI;

** MATERIAL DEFINITION **
```

```
MAE = MATE ME 'K' condumat 'C' capamat 'RHO' 1.;
CON = COND ME MAE0;
CAP = CAPA ME MAE0;

** RIGIDITY ASSEMBLY **
RIG_ENDO = CON ET CAP ET BLD;


** SOURCE TERMS **
SI(AT2);
* if AT2, no source terms *
  sour_end = 0;
SINON;
* if AT1, -3/8*(Gc/lc) as source terms *
  sour_end = (-1) * (3./8.) * (Gc/lc);
FINSI;
term_sour = SOUR ME sour_end mesh;

** SOURCE TERMS ASSEMBLY **
SOURC_TERM = term_sour ET fd;


** RESOLUTION STEP **
endo1 = RESO RIG_ENDO (SOURC_TERM);
```

C

Resume étendu de la thèse

Contexte

La dégradation des structures par fatigue est responsable de plus de 80% des cas de rupture dans l'industrie [61]. Toutefois, la difficulté de modélisation de ce genre de phénomène a mené à l'utilisation dans l'industrie de modèles simples accompagnés de grands coefficients de sécurité permettant de garantir l'intégrité de ces structures. Toutefois, une modélisation plus fine du phénomène d'initiation et de propagation de fissure par fatigue peut permettre de s'affranchir de ces conservatismes, et ainsi de garantir l'intégrité pour des structures plus légères, moins chères, et de façon plus durable. Ainsi, une large communauté s'intéresse à l'amélioration des méthodes numériques pour prédire la rupture en fatigue. C'est dans ce cadre que ce travail se place, au sein du Laboratoire d'Intégrité des Structures et Normalisations (LISN) au CEA, où de nombreux cas de fissuration sont étudiés, expérimentalement et numériquement pour garantir l'intégrité des structures et en définir les règles de normalisations.

La modélisation par champ de phase de problème de rupture gagne en popularité ces dernières années, étant donné sa facilité d'implémentation, sa capacité à retrouver des motifs de fissure complexes (*e.g.,* branchement, coalescence), et à unifier des communautés précédemment scindées (*e.g.,* mécanique de la rupture et mécanique de l'endommagement

ou encore initiation de fissure en fatigue, et propagation de fissure en fatigue). Par ailleurs, cette approche adopte une représentation diffuse de la fissure qui facilite grandement le traitement des fissures aux géométries complexes, en enlevant le besoin de construire (et reconstruire) un maillage qui la prend explicitement en compte. Tous ces avantages font que cette approche et son utilisation pour prédire la rupture numériquement intéressent beaucoup de groupe de chercheurs, sans pour autant qu'elle ne soit exploitée en industrie.

En effet, malgré tous les avantages listés précédemment, la modélisation de rupture par champ de phase est limitée par un coût de calcul excessif qui rend difficile son utilisation sur des cas réels. Ce coût de calcul s'explique par la nécessité d'avoir un raffinement extrêmement fin dans la zone endommagé pour garantir la convergence spatiale du champ de phase qui varie abruptement dans cette zone. Par ailleurs, il s'explique aussi par la possible longue convergence liée à la résolution du problème couplé résultant du modèle champ de phase. Cette problématique est moins critique en fatigue, où l'évolution des champs est très lente à l'échelle du cycle. Toutefois, avec la plupart des modèles champ de phase en fatigue, on aura donc besoin de calculer l'intégralité des cycles de chargement explicitement, ce qui implique un nombre de pas de calcul beaucoup trop important quand la vie en fatigue des matériaux métallique peut dépasser 10^7 cycles. Plusieurs auteurs proposent déjà des solutions à ces problèmes spécifiques à la modélisation champ de phase, comme l'utilisation de raffinement adaptatif de maillage pour optimiser le nombre de degré de liberté en temps réel [103, 107], d'accélération de la résolution d'un pas [129, 154], ou encore l'utilisation de saut de cycle pour diminuer le nombre de pas calculés [130, 151, 225]. L'objectif de ce travail est de mettre en commun ces approches d'accélération du modèle champ de phase, pour permettre de gagner du temps de calcul dans un contexte de dégradation par fatigue : sollicitation cyclique répétée, menant à la ruine pour des niveaux de chargement pouvant être très inférieurs aux niveaux attendus en chargement statiques. Il est important de noter que ce gain en temps de calcul doit se faire à un niveau de précision satisfaisant, et que les avantages de flexibilité du modèle champ de phase, c'est-à-dire sa capacité à retrouver des trajectoires de fissuration complexe, doit être conservé.

Ainsi, ce mémoire est structuré en quatre chapitres. D'abord, nous présentons les fondamentaux de la dégradation par fatigue ainsi que les différents outils, théoriques et numériques, mis en place pour sa caractérisation. Ensuite, une attention particulière est donnée au modèle champ de phase, et ses différentes formulations dans la littérature. Á partir de cet état de l'art, un modèle champ de phase en fatigue est proposé et appliqué à plusieurs géométries usuelles de la littérature champ de phase.
Le chapitre 3 présente ensuite plusieurs outils d'accélération ajoutés au modèle pour

permettre de gagner du temps de calcul tout en conservant la précision. Nous commençons par l'accélération du calcul du cycle, puis présentons plusieurs schémas de saut de cycle, couplés ensuite à des opérateurs de raffinement adaptatif de maillage.
Enfin, nous utilisons ce modèle champ de phase accéléré dans le chapitre 4 afin de mettre en évidence la capacité de l'approche à reproduire des cas expérimentaux. Ces comparaisons numérique-expérimental permettent de mettre en lumière les avantages, les inconvénients et les perspectives du modèle proposé.

Chapitre 1 : Préliminaires

Le premier chapitre est axé sur la rapide description des concepts théoriques exploités dans cette thèse. Nous commençons par détailler les différentes étapes de la dégradation par fatigue, qui se divise en étape d'initiation, de propagation de fissure macroscopique, et qui peut mener vers la ruine brutale de la structure. Un rappel historique de l'étude de la dégradation par fatigue est ensuite proposé, qui débute par la caractérisation empirique de l'enveloppe de contrainte par Wöhler sous forme de courbe "S-N". Depuis, de nombreuses loi ont vu le jour qui permettent d'approximer ces enveloppes, ou de les supplémenter pour prendre en compte, la contrainte moyenne [89, 232], ou les effets plastiques [55]. Ce type de traitement pour la fatigue ne différencie pas les différentes étapes de la fatigue, ou la présence de défaut initial, pour poser la question de la propagation de ce défaut.

Cette manière de traiter la problématique de rupture ne vient que plus tard, avec l'avènement la mécanique de la rupture [93, 113]. Griffith [93] pose les bases de ce traitement différent, en formulant le problème de rupture comme la compétition entre l'énergie relâchée par la propagation de fissure, et l'énergie nécessaire à la création de deux nouvelles surfaces de fissure. Par ce biais, il propose d'exprimer un critère de rupture avec le taux de restitution d'énergie, ou la variation d'énergie impliquée par une avancée infinitésimale de fissure, comparé à un paramètre matériau : l'énergie de surface. Par la suite, Irwin [113] introduit les facteurs d'intensité des contraintes (FIC) qu'il a vu émerger de l'expression des champs de contraintes asymptotiques en pointe de fissure [250]. Ces facteurs d'intensité des contraintes permettent de quantifier l'état de contrainte en pointe de fissure, et sont donc déterminants pour l'étude de la propagation de fissure. Irwin propose également un lien direct entre ses FIC, et le taux de restitution d'énergie introduit par Griffith [93]. Ces outils ont ensuite été exploités par Paris & Erdogan [190], qui ont l'idée de tracer la vitesse d'avancée de fissure en fatigue en fonction de la variation des FIC sur un cycle de chargement, ΔK. Nous avons représenté une courbe que l'on

obtient pour les matériaux métalliques en Fig. C.1. On y aperçoit trois domaines, pour $\Delta K < K_{\text{th}}$, on observe une avancée très rapide et irrégulière, tout comme pour $\Delta K > K_{\text{Ic}}$, où l'on s'approche du régime de fissuration en chargement statique. Entre ces deux phases irrégulière, les auteurs mettent en évidence la présence d'un régime linéaire, qu'ils approximent par une loi, dites de Paris-Erdogan, qui définit donc un régime d'avancée de fissure en fonction de la variation des FIC.

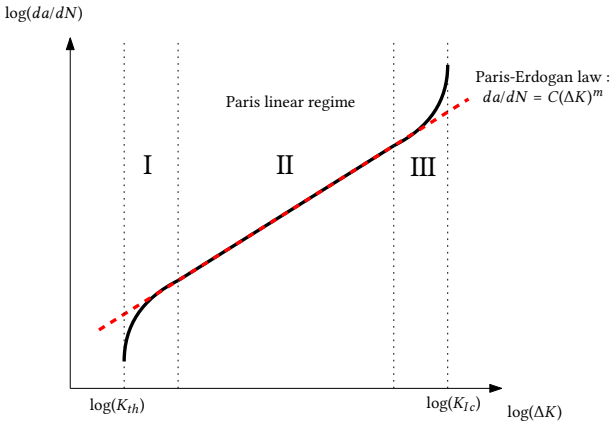

Figure C.1: Évolution typique de la vitesse de propagation de fissure en fonction de la variation des facteurs d'intensité des contraintes. Le domaine II est un régime linéaire qui peut être modèlisé par une loi type Paris-Erdogan [190]

Après avoir introduit ces concepts fondamentaux de la mécanique linéaire élastique de la rupture, nous listons quelques méthodes numériques qui s'appuient sur ces concepts pour proposer un modèle numérique de structure fissurée, et pour prédire la propagation en fatigue de la fissure sous des conditions de chargement données. Plusieurs modèles sont ainsi présentés, et différenciés en fonction de la manière dont la fissure est représentée dans le maillage élément finis. Ainsi, nous présentons d'abord les approches basées sur une représentation discrète de la fissure, les plus habituellement utilisés dans l'industrie, et qui reposent sur le calcul numérique des FIC, pour imposer une certaine vitesse d'avancée de fissure déduite de la loi de Paris. Ces approches peuvent toutefois être difficiles à utiliser pour des cas de fissuration complexe, étant donné la nécessité de construire (et souvent reconstruire) un maillage (ou les fonctions supports du maillage en XFEM) pour correspondre à la géométrie fissurée [83, 208].

Ces quelques exemples pour la modélisation numérique de la fissuration en fatigue sont ensuite mis en opposition avec des modèles basés sur une représentation diffuse de l'endommagement. Ces modèles sont tirés de la mécanique de l'endommagement [120, 142], où un scalaire représentant la fraction de matériau endommagé (ou micro-

vide), sur la fraction de matériau sain est introduit pour représenter la fissure. Sous leur forme locale, ces modèles souffrent généralement d'une dépendance pathologique des résultats à la taille de maille [20, 36]. C'est pourquoi plusieurs travaux proposent de modifier ces formulations en y ajoutant des termes non-locaux, ou le gradient du scalaire d'endommagement [119, 169, 196]. Ces approches permettent de retrouver des géométrie de fissure très complexe, et d'unifier l'étude de l'initiation et de la propagation de fissure, habituellement traités séparément [142].

Plus récemment, l'approche champ de phase pour la fissuration, gagne en popularité. Elle est basée sur l'approche variationnelle de la rupture, introduit par Francfort et Marigo [76]. Dans ce travail, les auteurs proposent de réécrire le critère de Griffith [93] sous forme variationnelle, c'est-à-dire, trouver le déplacement $\boldsymbol{u}$, et la fissure Γ, qui minimise l'énergie potentielle du solide fissurée. Suivant Griffith, les auteurs proposent d'écrire cette énergie potentielle comme la somme de deux termes : l'énergie mécanique $E(\boldsymbol{u})$ (relâchée en propagation) , et l'énergie de surface $W(\Gamma)$ (tirée du relâchement d'énergie mécanique) . Plus tard, Bourdin [38] propose une régularisation de cette fonctionnelle pour en faciliter le traitement numérique, et introduit donc le paramètre champ de phase, un scalaire représentatif de l'endommagement d. Cette régularisation implique que la fonctionnelle ressemble à un modèle d'endommagement avec un terme de gradient. Ainsi, l'approche permet de lier la mécanique linéaire élastique de la rupture (à travers le critère de Griffith) et la mécanique de l'endommagement. On écrit cette fonctionnelle régularisée comme :

$$\Pi_{int}(\boldsymbol{u}, d) = E(\boldsymbol{u}, d) + W(d). \tag{C.1}$$

Cette formulation a été créée pour la rupture fragile et ne mène à aucune dégradation dans le cas d'un chargement cyclique répété inférieur à la limite usuelle. C'est pourquoi plusieurs auteurs proposent des modifications de cette fonctionnelle pour prendre en compte la fatigue des matériaux. On peut regrouper la plupart de ces approches sous ces deux modifications de la fonctionnelle originale :

$$\Pi_{int}(\boldsymbol{u}, d) = E(\boldsymbol{u}, d) + W(d) + \int_0^t \dot{\mathcal{H}}(d, \bar{\alpha}(\tau))\ \mathrm{d}\tau\ (\textit{e.g.},\ [13, 149]) \tag{C.2}$$

$$\Pi_{int}(\boldsymbol{u}, d) = E(\boldsymbol{u}, d) + \int_0^t f(\bar{\alpha}(\tau)) \cdot \dot{W}(d)\ \mathrm{d}\tau\ (\textit{e.g.},\ [7, 44]) \tag{C.3}$$

Notre travail est basé sur la modification de l'eq. (C.3), qui introduit la fatigue par la dégradation locale de G_c, le taux de restitution d'énergie critique du matériau. Un

paramètre de fatigue est accumulé au fur et à mesure du chargement cyclique qui est injecté dans une fonction de dégradation de G_c qui va impliquer un seuil de rupture très bas, dans les zones où les champs mécaniques sont les plus importants. De cette façon, la fatigue est phénoménologiquement reproduite.

Chapitre 2 : Un modèle champ de phase pour la fatigue

Dans ce second chapitre, nous détaillons les différents ingrédients de la fonctionnelle champ de phase explicité ci-dessus. Pour chacun de ces ingrédients, nous discutons des différentes variantes explorés dans la littérature pour obtenir un certain comportement donné. Ainsi, nous pouvons reprendre les termes de la fonctionnelle (C.1), venant de l'approche variationnelle de la rupture fragile de Francfort & Marigot [76], régularisée par Bourdin [38], avec les notations de Wu et al. [259] :

$$E(\boldsymbol{u}, d) = \int_{\Omega} g(d) \cdot \psi_0^+(\boldsymbol{u}) + \psi_0^-(\boldsymbol{u})\, dV, \tag{C.4a}$$

$$W(d) = \frac{G_c}{c_w} \cdot \int_{\Omega} \frac{w(d)}{l_c} + l_c \cdot |\nabla d|^2\, dV. \tag{C.4b}$$

On voit ici le développement du terme d'énergie mécanique $E(\boldsymbol{u}, d)$, et du terme d'énergie dissipée par la rupture $W(d)$. Commençons par le terme mécanique.

$E(\boldsymbol{u}, d)$ est représentatif de l'énergie mécanique stockée par le solide étudié. Dans un cadre élastique, il est identique à la densité d'énergie élastique, habituellement constitutive de l'énergie libre d'un solide, à la différence de $g(d)$ la fonction de dégradation qui permet d'obtenir un comportement adoucissant avec l'augmentation de la variable champ de phase. Dans ce travail, nous avons choisi une formulation quadratique de la fonction de dégradation, car elle permet notamment d'avoir un problème d'endommagement linéaire dans un cadre de résolution étagée du problème couplée mécanique-endommagement. De plus, nous utilisons l'approche de Miehe et al. [166], qui consiste à ajouter une petite constante à cette fonction pour éviter les problèmes de conditionnement de matrice, en conservant une rigidité résiduelle dans les éléments totalement endommagés. On écrit donc :

$$g(d) = (1 - d)^2 + k \tag{C.5}$$

On peut également voir que la densité d'énergie élastique $\psi(\boldsymbol{u})$ dans l'eq. (C.4a) est décomposé en deux termes. L'un des deux est dégradé par la fonction $g(d)$ alors que l'autre non. Cette formulation sert à induire un comportement asymétrique de dégradation, typique des matériaux réels, qui présente généralement une ténacité, et un comportement adoucissant différents en traction et en compression. Par ailleurs, cette écriture permet de modéliser le contact entre les lèvres des fissures, et ainsi d'empêcher leur interpénétration. Dans notre travail, nous avons opté pour une décomposition spectrale de

l'énergie mécanique, c'est-à-dire que l'endommagement est piloté par les parties positives des composantes de déformation propres. On considère avec ce modèle que la traction mène à l'endommagement, alors que la compression ramène un comportement sain et ne peut pas adoucir la réponse mécanique. Afin de différencier les composantes en traction des composantes en compression, une décomposition spectrale est effectué et le signe des valeurs propres obtenus nous mène à considérer cette déformation comme de compression ou de traction. Nous avons proposé une nouvelle manière de calculer ces contributions, en passant par le calcul d'une matrice d'élasticité dégradée dans le repère principale (inspiré par Ref. [26]), que l'on peut ensuite retrouver dans le repère de travail par une simple opération de changement de base. Cette nouvelle approche a permis de réduire le coût de calcul associé à la méthode, et d'éviter des problématiques de singularité qui apparaissaient en 3D lorsque deux valeurs propres sur trois étaient identiques [26, 173, 176].

Passons ensuite au second terme, $W(d)$, représentant l'énergie dissipée par la fissuration, ou plutôt l'énergie de surface provenant de l'énergie mécanique relâché par la propagation de fissure. Celui-ci est donc composé d'un terme d'énergie de surface G_c, (le taux de restitution d'énergie critique), intégré sur la surface de fissure, qui est ici formulée selon l'intégration de sa densité de surface $\gamma(d, \nabla d) = \dfrac{w(d)}{l_c \cdot c_w} + \dfrac{l_c}{c_w} \cdot |\nabla d|^2$. On retrouve dans cette formulation, $w(d)$ la fonction de dissipation, ou fonction de géométrie de fissure, qui pilote la topologie de d qui approxime la géométrie discrète de fissure. Dans notre travail, nous avons opté pour la fonction dîtes AT2, qui permet à d d'être directement borné par 0 et 1, et participe ainsi, avec la fonction de dégradation choisie, à permettre au sous-problème d'endommagement de rester linéaire. Le modèle AT2 est $w(d) = d^2$ et $c_w = 2$. Il faut toutefois noter que ce modèle ne permet pas d'avoir un vrai seuil élastique : n'importe quel niveau de sollicitation implique l'endommagement de la structure.

Enfin, précisons que le modèle champ de phase doit garantir l'irréversibilité des fissures formées, et ainsi respecter que $\dot{d} \geq 0$. Dans notre travail, nous avons opté pour une imposition implicite de cette condition, afin de diminuer les temps de calculs de la méthode, étant donné le coût important associé aux ressources Cast3M d'optimisation sous contraintes. Ainsi, nous avons utilisé la méthode du champ d'histoire de Miehe et al. [166]. Cette approche est forcément liée à une résolution étagée du problème couplé, comme initialement proposé par Bourdin et al. [38], et comme rigoureusement formulé par Miehe et al. [166]. Une approche étagée est donc utilisée dans ce travail, mais retravaillée dans le chapitre suivant pour permettre une efficacité accrue dans un contexte de fissuration en fatigue.

Enfin, nous nous intéressons aux ingrédients de l'extension en fatigue comme indiqué dans la fonctionnelle modifiée (C.3). Deux nouveaux termes entrent en jeu : la fonction de dégradation en fatigue $f(\bar{\alpha})$ et la variable interne de fatigue cumulée, ou variable d'histoire de fatigue, $\bar{\alpha}$. Le premier terme sert à dégrader la ténacité du matériau dans les zones où un cumul important d'énergie mécanique s'est manifesté, représenté par $\bar{\alpha}$, le cumul de variable interne de fatigue α. Nous avons choisi $\alpha = g(d) \cdot \psi_0^+$ comme dans Ref. [44]. Ceci permet d'éviter des soucis de dépendance à la taille de maille observés dans Ref. [7] en prenant $\alpha = \epsilon$, et de permettre une prise en compte des effets d'asymétrie de dégradation en fatigue, ainsi que d'arrêter le cumul d'énergie dans les zones complètement endommagées.

La fin de ce chapitre s'articule ensuite sur trois points importants pour comprendre la suite des travaux : la modélisation de fissure pré-existante pour le modèle champ de phase, l'interprétation de l_c, la longueur caractéristique du modèle champ de phase, et les méthodes de résolution du problème couplé obtenu. Á partir de ces bases théoriques, une fonctionnelle pour un modèle champ de phase étendu en fatigue est proposée, et nous obtenons la formulation forte du problème couplé ainsi que sa formulation éléments finis dans un cadre étagé. Le modèle obtenu est ensuite appliqué à plusieurs benchmarks usuels de la littérature champ de phase pour valider son implémentation et mettre en avant ses capacités.

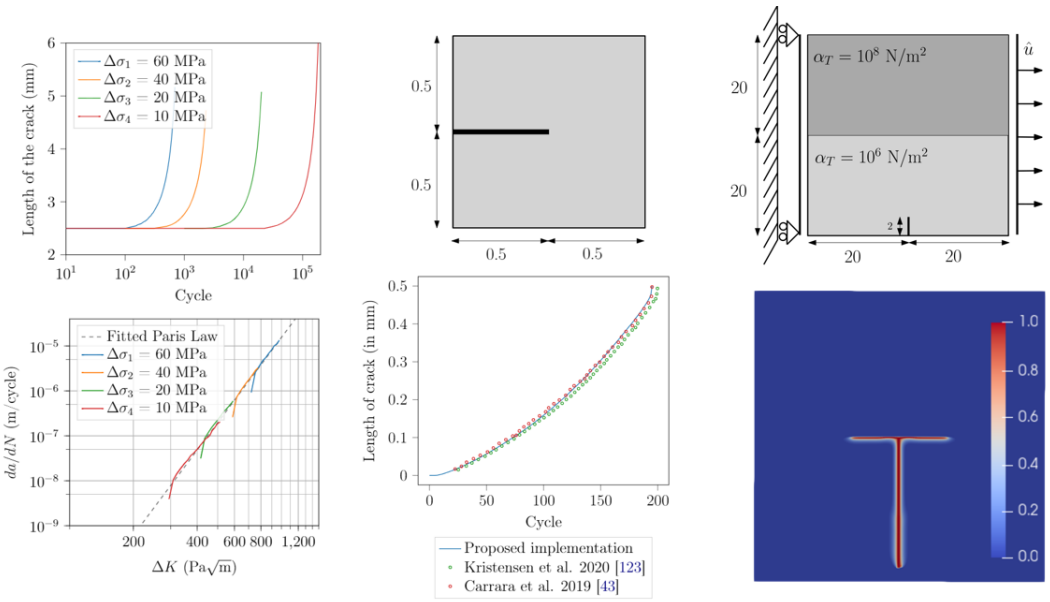

Figure C.2: De gauche à droite, étude sur cas de fissure en milieu infini, avec tracé dans le domaine de Paris, étude sur échantillon SEN et comparaison à la littérature, étude sur échantillon de branchement de fissure, avec champ de phase calculé.

Chapitre 3 : Outils d'accélération

Nous agissons sur trois leviers pour accélérer les simulations de champ de phase. Premièrement, le calcul du cycle est accéléré en investiguant différentes approches de résolution étagée, puis d'accélération de convergence. Ensuite, plusieurs procédures de saut de cycle sont testées et appliquées sur un cas de fissuration en mode I dans un espace infini. Les opérateurs de raffinement adaptatifs de maillage sont ensuite détaillés, avant d'être couplés au saut de cycle pour obtenir des gains en temps de calculs encore plus important.

La première partie du chapitre est donc centrée sur la méthode de résolution du problème couplé mécanique-champ de phase dans le cadre de fissuration en fatigue. Il existe en effet de nombreuses approches dans la littérature, basées sur une résolution monolithique du problème couplé [82, 159, 230], ou plusieurs types de résolution étagée [38, 129, 154, 166], c'est-à-dire en découplant les inconnus. Suite à quelques tests sur des géométries simples, nous avons opté pour une approche étagée dîtes *implicite*, *one-loop* inspirée par les Refs. [104, 154], qui semble être la plus efficace en fatigue. Par ailleurs, nous avons testé une approche Newton modifiée, où l'opérateur tangent du problème mécanique n'est pas recalculé à chaque itération interne du schéma de résolution. Toutefois, la non-robustesse du schéma obtenu nous a poussés à abandonner cette approche. Enfin, un schéma d'accélération de convergence de type Aitken [3, 206] a été utilisé dans la boucle du problème couplé sur les résidus mécanique successifs, en permettant de réduire encore significativement le temps de calcul.

Ensuite, nous avons traité la problématique du modèle champ de phase en fatigue choisi qui impose un calcul explicite de tous les cycles de chargement. Le calcul de chaque cycle n'est pas possible lorsque l'on parle d'expérience de fatigue qui peut en impliquer jusqu'à 10^7. Nous proposons donc l'utilisation d'une approche par saut de cycle, qui doit donc permettre d'éviter de calculer chaque cycle, tout en conservant un certain niveau de précision. L'idée des approches saut de cycle est d'utiliser des cycles dits *de contrôle*, durant lesquelles le comportement est simulé, pour estimer l'évolution des quantités d'intérêt $\Delta\alpha$ sur ΔN cycles, par un procédé d'extrapolation des $\Delta\alpha$ calculés. Dans ce travail, nous nous sommes limités à 1 cycle de contrôle, et avons testé deux procédés d'extrapolation : un procédé type Forward-Euler (FE), analogue à un développement de Taylor d'ordre 1, et un procédé itératif, d'extrapolation type trapèze (TI), qui utilise un cycle de contrôle en N et un cycle en $N + \Delta N$. Pour ces deux schémas, la variable interne de fatigue cumulée $\bar{\alpha}$ a été utilisé comme seule variable extrapolée dans le schéma saut de cycle : à partir de cette extrapolation, toutes les autres inconnues sont recalculées. Ces deux

approches par saut de cycle permettent de faire des gains de calculs considérables, tout en conservant un très bon niveau de précision. Toutefois, on remarque que la précision du schéma FE est dépendante de la valeur de ΔN choisie, contrairement au schéma TI, qui présente une précision quasi-indépendante du ΔN, jusqu'à un certain seuil à partir duquel, le schéma itératif ne converge plus, ou converge vers une solution fausse. Dans les deux cas, il est donc nécessaire de contrôler ΔN pour régler l'efficacité et la précision de l'approche. Dans le cadre de l'approche itérative avec l'extrapolation TI, nous avons donc proposé de diminuer ΔN pendant le calcul si le nombre d'itérations internes du schéma itératif dépasse un certain seuil.

Enfin, nous proposons de palier au problème du coût de calcul du modèle champ de phase par l'ajout d'une procédure de raffinement de maillage adaptatif (AMR, Adaptive Mesh Refinement). Cette approche de gestion du maillage pendant la propagation est très importante pour le modèle champ de phase étant donné la nécessite d'utiliser une maille extrêmement fine dans la zone endommagée, pour capturer la variation abrupte du champ de phase. Ainsi, on retrouve déjà plusieurs méthodes de raffinement adaptatif de maillage dans la littérature champ de phase *e.g.,* [103, 107, 244] qui permettent des gains en temps de calcul très important. Faisant suite à cette riche littérature, nous proposons d'appliquer ce type d'approche dans le cadre champ de phase en fatigue, tout en prévoyant de l'utiliser avec une approche saut de cycle. Dans cette section, nous nous attachons donc à décrire les différentes briques nécessaires au couplage AMR et saut de cycle : premièrement, nous décrivons l'outil de raffinement permettant de passer d'un maillage grossier à un maillage raffiné. Ensuite, nous discutons du transfert de champs, nécessaire pour recalculer les champs inconnus sur les nouveaux maillages raffinés. Enfin, nous précisons le critère de raffinement, basé sur la variable champ de phase, et le rapport l_c/h dans la zone considérée comme endommagée [165, 176]. Ces choix permettent au final d'avoir une approche AMR efficace, précise et robuste, qui est applicable dans un cadre fatigue et fragile.

Armés de tous ces outils d'accélération, nous proposons un algorithme de propagation de fissure qui permet leur mise en commun. Ainsi, l'objectif est de minimiser le nombre de degrés de liberté calculés à chaque cycle par l'utilisation d'AMR, tout en minimisant le nombre de cycles calculés par l'utilisation du saut de cycle. Pour garantir la robustesse et la précision du schéma couplé obtenu, une approche *à-posteriori* est utilisé, c'est-à-dire que le critère de raffinement est vérifié après chaque saut de cycle, et qu'une approche itérative est enclenchée à chacune de ces vérifications jusqu'à l'obtention d'un maillage qui respecte le critère.

Après avoir présenté cette approche couplant les outils d'accélération précédents, nous

l'appliquons sur plusieurs cas usuels de la littérature champ de phase. Premièrement, nous l'appliquons sur le cas de l'ouverture de fissure en mode I dans un milieu infini afin de comparer les deux schémas d'extrapolation (FE et TI) dans ce cadre spécifique avec AMR. Les deux approches permettent des gains importants en temps de calcul, qui sont d'autant plus important, plus le calcul de fatigue est long. Toutefois, l'approche TI est privilégiée pour le reste du travail étant donné son efficacité (à niveau de précision donné) qui semble un peu supérieure au schéma FE. Par ailleurs, l'approche TI permet l'utilisation du saut de cycle adaptatif cité plus tôt. Ceci n'est pas le cas du schéma FE qui nécessite l'introduction d'une méthode de ΔN adaptatif, brièvement investiguée, sans résultat définitif, en annexe de ce travail. Ensuite, le schéma accéléré est appliqué sur des cas de fissuration plus complexe, faisant intervenir des modes mixtes de rupture, du branchement, de la coalescence, et de l'initiation de fissure. Enfin, le seul cas tridimensionnel du travail est présenté. Tous ces cas de fissurations ont été reproduits avec le traitement décrit, permettant une accélération significative du temps de calcul tout en conservant la précision.

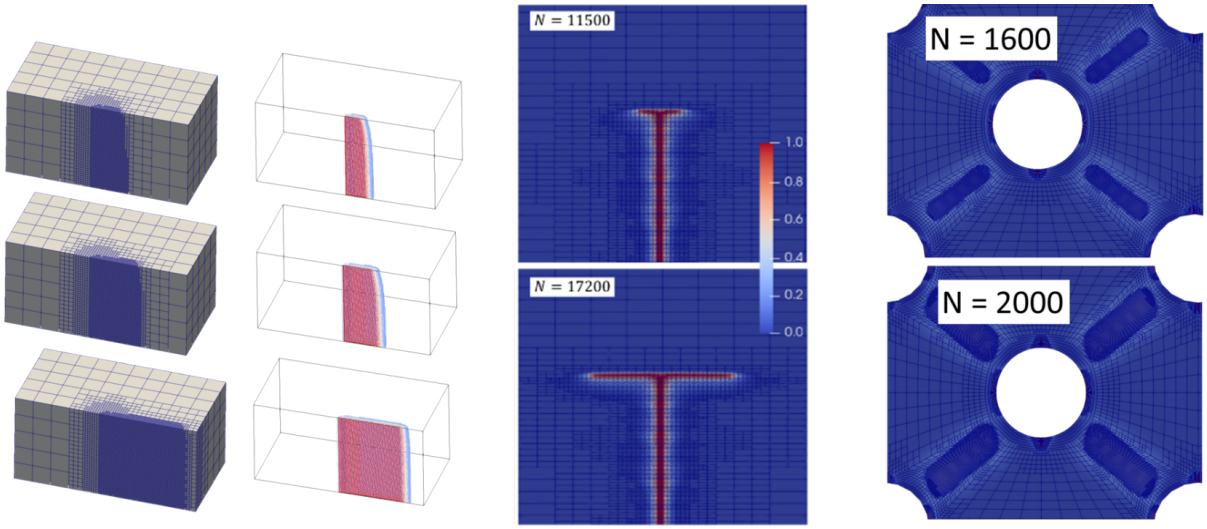

Figure C.3: De gauche à droite, maillages raffinés adaptativement sur SEN 3D, maillages raffinés sur le cas de branchement de fissure, maillages raffinés sur le cas d'initiation de fissure.

Chapitre 4 : Vers l'application industrielle

Si l'objectif du travail est d'accélérer les temps de calculs associés à la simulation numérique de propagation de fissure par champ de phase, c'est en réalité pour permettre de faciliter l'utilisation de ce modèle pour traiter des cas réels. Ainsi, après avoir étudié de nombreux cas numériques académiques, nous nous sommes penchés sur la question de la reproduction de résultats expérimentaux avec le modèle accéléré proposé dans ce travail. Pour ce faire nous nous sommes basés sur deux campagnes d'essais réalisés respectivement par G.Gibert dans le cadre de sa thèse [84], et par J.Réthore & R. Seghir dans le cadre d'une activité de benchmarking organisée à CFRAC 2023 [209], un congrès international centré sur la mécanique de la rupture. En plus de la valeur de preuve de concept de ce chapitre, la comparaison numérique-expérimentale visée permet de mettre en évidence certaines difficultés associées à l'application de ces approches.

La première campagne basée sur les travaux de thèse de G. Gibert [84], se focalise sur l'identification de paramètre grâce aux essais sur une éprouvette CT chargé en fatigue dans laquelle une fissure se propage en mode I, puis la prédiction d'une trajectoire de fissure dans un échantillon CT troué. Ainsi, nous commençons par proposer un modèle numérique de l'échantillon CT sain, et modifier les paramètres numériques de notre modèle afin d'obtenir le comportement en fatigue que l'on essaye de reproduire. Dans le chapitre 2, nous avons discuté du fait que les modèles basés sur la dégradation de ténacité peuvent reproduire des effets de fatigue, comme montré par Carrara et al. [44] qui retrouvent une vitesse de fissure corrélée linéairement à ΔK sur un intervalle, et ce, de façon supposément indépendante de la géométrie ou du chargement : un comportement type Paris. L'auteur mentionné [44] reproduit également des courbes type S-N, encore une fois, sans la nécessité d'imposer ces comportements à priori. Cette caractéristique du modèle signifie que l'on peut jouer sur les paramètres numériques afin d'obtenir des coefficients de la loi de Paris qui permettent de caractériser un certain comportement en fatigue que l'on souhaite reproduire.

Nous avons donc réalisé ce fit sur l'éprouvette CT saine, étudiée expérimentalement par G. Gibert [84]. Le modèle champ de phase en fatigue utilisé est caractérisé par quatre paramètres l_c, G_c, qui sont les paramètres numériques liés au modèle champ de phase en fragile, et κ, α_T qui pilotent la fonction de dégradation en fatigue. Malgré les travaux existant qui permettent de lier les paramètres champ de phase à des propriétés matériaux spécifiques (*e.g.,* l_c et σ_c liés par Refs. [171, 241]), nous avons opté au contraire pour une approche purement heuristique de calibration des paramètres, en effectuant des tests successifs avec différentes valeurs de paramètres numériques jusqu'à atteindre le meilleur

fit possible. Durant ces tests, nous avons pu observer des corrélations plus ou moins clairs entre les paramètres qui pilotent la fonction de dégradation en fatigue, et les coefficients de Paris obtenus, avec l'influence de α_T sur l'ordonnée à l'origine du domaine linéaire, et l'influence de κ sur la pente du domaine linéaire. Ces observations, mêlées au processus par tâtonnement, nous a mené à un fit très précis du cas CT sain.

Nous avons ensuite appliqué ces paramètres déduits sur la géométrie CT trouée étudiée par G. Gibert [84], pour voir si nous étions capables de retrouver l'influence expérimentalement observée de ce trou sur la trajectoire de la fissure. Deux diamètres de trou ont été étudiés, pour différencier l'influence de ces changements de géométrie sur la réponse mécanique. Expérimentalement, G. Gibert [84] observe que le trou le plus gros attire la fissure complètement, alors que le plus petit trou attire légèrement la fissure, qui continue ensuite sa route en mode I après avoir approché le trou. Ces observations ont été très bien reproduites qualitativement : le gros diamètre a complètement attiré la fissure, alors que le petit diamètre n'a fait que dévier légèrement la trajectoire. Toutefois, notons que la non-prise en compte de la plasticité, et la modélisation en déformation plane ne sont pas des choix très pertinents pour ce matériau et ces conditions d'expériences, pouvant ainsi expliquer la déviation importante observée avec les résultats expérimentaux.

Ensuite, nous avons participé à l'activité de Benchmark de J. Réthoré & R. Seghir, qui est basé sur la rupture quasi-fragile de quatre échantillons en PMMA. Ainsi, contrairement à la plupart des travaux entrepris dans ce mémoire, il ne s'agit pas de fissuration en fatigue. Plusieurs changements ont donc été proposés pour faciliter le traitement quasi-statique du phénomène de rupture fragile : d'abord, nous avons opté pour une résolution étagée explicite, pilotée par l'incrément du champ d'histoire H. Ceci permet d'éviter les problèmes de convergence associés au schéma implicite étagé (dans les cas de rupture instable), tout en contrôlant la précision grâce à la limitation de l'incrément de H. Ensuite, cette section n'utilise ni saut de cycle, ni dégradation en fatigue (en imposant $f(\bar{\alpha}) = 1$).

Dans la même veine que les travaux sur la CT, le processus de comparaison numérique-expérimentale s'est déroulé en deux temps. On nous a premièrement fourni les données liées à la rupture de deux échantillons de PMMA, afin de calibrer les paramètres numériques du modèle utilisé. Ensuite, à partir du modèle numérique fitté, une prédiction à l'aveugle des deux autres cas de rupture était demandé. Avec ce cas fragile, les seuls paramètres importants sont G_c, l_c, que nous avons décidé de calibrer de la même façon que pour la CT: par tâtonnement. Les valeurs de G_c, l_c ainsi choisis ont permis de reproduire très fidèlement les cas de calibration, avec un cas de fissuration stable en mode I, et un cas de rupture instable d'une plaque à quatre trous sollicitée en traction.

Les deux cas de prédiction étaient une sorte de reflet des cas de calibration, avec un cas de fissuration stable en mode I, et un cas de fissuration dans une plaque trouée (cette fois sollicitée en compression). La prédiction proposée pour le cas en mode I est plutôt fidèle avec un pic de contrainte avant rupture qui mène à une propagation de fissure stable dans l'axe de symétrie de la géométrie. Le pic de chargement fut toutefois beaucoup surestimé, alors que la phase de propagation stable a été très bien reproduite. Inversement, la prédiction du dernier échantillon (plaque trouée en compression) fut très mauvaise à tous les niveaux. On peut imaginer que l'utilisation de l'approche de décomposition spectrale pour modéliser le comportement du PMMA sous compression n'est pas pertinente, ou encore qu'un modèle trop simple des conditions aux limites a été pris en compte.

Á noter que ces deux essais de comparaison numérique-expérimental ont été réalisés avec des outils d'accélération, AMR et saut de cycle pour le cas CT, et seulement AMR pour le cas des échantillons en PMMA. Ces outils sont particulièrement utiles dans ce genre de cas où le procédé d'identification par tâtonnement implique le calcul de plusieurs dizaines de cas de fissuration. Toutefois, dans ces conditions, on a pu mettre en évidence la difficulté de calibration du schéma AMR, et notamment l'outil de lissage, dans les cas où le rapport entre la taille éléments très fins et les éléments très grossiers devient important. Dans ce contexte, des outils de déraffinement, nous semblent très importants pour permettre d'optimiser les procédures proposées.

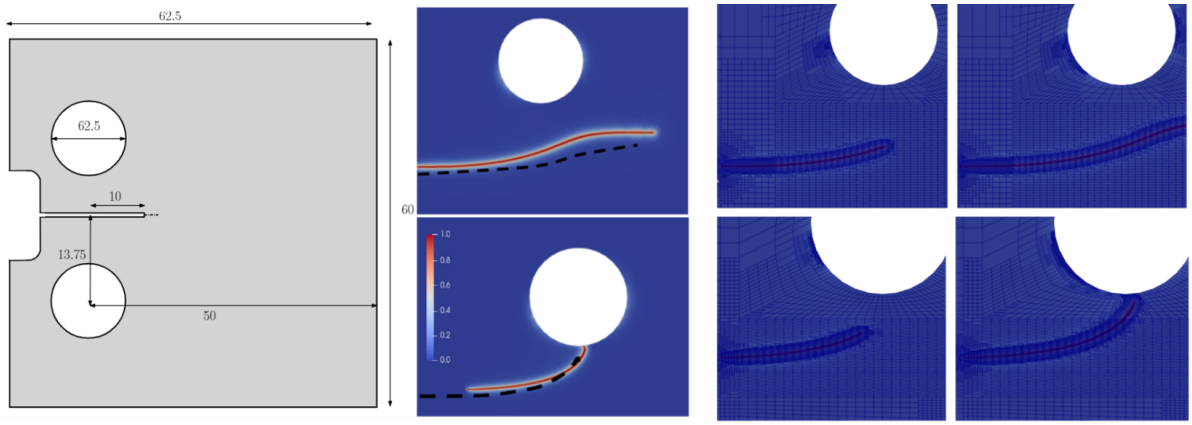

Figure C.4: De gauche à droite, la géométrie de CT trouée d'après Ref. [84], puis comparaison numérique expérimentale de trajet de fissure sur CT trouée (pointillés noir correspond à la vraie fissure), puis comparaison de maillages raffinés.

Conclusions et Perspectives

Ce travail a commencé par l'introduction du phénomène de fatigue des matériau et les différents outils, théoriques et numériques, mis en place pour le caractériser et prédire le comportement des structures face à un chargement de fatigue à grand nombre de cycles. Le modèle champ de phase a été choisi pour tirer profit de la flexibilité du modèle, qui permet de traiter aisément des cas de fissuration complexe (modes mixtes, branchement, coalescence, initiation). L'approche a donc été décrit, avec un état de l'art des différents ingrédients de la fonctionnelle régularisé, une description de l'extension en fatigue choisie, et le détail de l'implémentation numérique utilisé pour résoudre le problème couplé obtenu. Une attention particulière fut portée sur la méthode utilisée pour induire le comportement en dégradation asymétrique et les effets de refermeture de fissure. Inspirés par plusieurs approches de décomposition spectrale [26, 165, 173], nous avons proposé une méthode par changement de base qui a permis d'améliorer son efficacité et sa robustesse. Finalement, l'implémentation proposée a été validée sur plusieurs cas usuels de la littérature champ de phase. Le modèle de fatigue tiré de Carrara et al. [44] a été utilisé pour traiter des cas de fissuration avec chargement cyclique, et un régime linéaire type Paris [190] indépendant du niveau de chargement fut illustré. Ces applications nous ont permis de montrer la flexibilité du modèle champ de phase, mais son coût en temps de calcul prohibitif nous a poussé à développer des outils d'accélérations, propres à ce modèle en fatigue à grand nombre de cycles.

C'est pourquoi une accélération en trois axes a été proposée. D'abord, le calcul du cycle a été travaillé pour permettre une implémentation étagée, précise et efficace, adapté au comportement obtenu avec le modèle de fatigue. Ensuite, plusieurs schémas de saut de cycle ont été proposés pour éviter la nécessité de calculer explicitement des dizaines de millions de cycles pour estimer l'évolution non-linéaire de la variable d'histoire de fatigue. Finalement, un outil de raffinement adaptatif de maillage est mis en place, pour permettre de coupler tous les outils d'accélérations et ainsi obtenir une optimisation simultanée de la discrétisation spatiale et temporelle. Une approche itérative de saut de cycle inspiré par Loew et al. [151] est proposée, avec vérification a-posteriori de critères de raffinement adaptatif adaptés au modèle champ de phase. Ce cadre accéléré fut ensuite appliqué sur plusieurs cas numériques usuels 2D-3D de la littérature champ de phase, montrant ainsi sa robustesse, et son efficacité à une précision donnée. Finalement, nous avons proposé plusieurs comparaisons numérique-expérimentale, permettant de mettre en lumière certaines étapes, et problématiques de l'utilisation du modèle sur des cas réels.

Finalement, nous avons donc implémenté un modèle de champ de phase, avec prise en compte d'effets de fatigue, accompagné d'outils d'accélération adaptées permettant d'importants gain en temps de calcul. Ce modèle et ses outils ont été intégralement réalisés sur le code éléments finis du CEA, Cast3M [46]. Ces résultats positifs ouvrent plusieurs perspectives pour améliorer l'applicabilité du modèle à des cas réels et son efficacité numérique. Premièrement, il est nécessaire de prendre plus d'effets en compte, comme la plasticité, ou différents effets propres à la fatigue, comme l'influence de la contrainte moyenne ou les effets de refermeture. La littérature qui concerne l'extension en fatigue du modèle champ de phase est déjà riche et florissante, permettant d'ajouter ces effets déterminants pour la prédiction des phénomènes réels. Ensuite, un travail additionnel sur le coût numérique de la méthode est nécessaire, en exploitant les approches astucieuses proposées par le reste des auteurs travaillant sur la question. Citons par exemple l'approche BFGS pour la résolution du système couplé [129], ou l'approche type quart de cycle pour la prise en compte du chargement [130, 225], qui pourraient être ajoutés au cadre accéléré proposé sans grande difficulté. Finalement le déraffinement de maillage nous a semblé nécessaire pour permettre une accélération significative. Ce type d'opération pourrait être rendu possible si le manque de discrétisation derrière le front de fissure n'influence pas la réponse mécanique. On pourrait aussi envisager un changement de représentation de la fissure derrière le front pour permettre d'utiliser des éléments très grossiers.

Bibliography

[1] A. Abdul-Latif, D. Razafindramary, and J. Rakotoarisoa, "New hybrid cycle jump approach for predicting low-cycle fatigue behavior by a micromechanical model with the damage induced anisotropy concept," *International Journal of Mechanical Sciences*, vol. 160, pp. 397–411, Sep. 2019.

[2] V. Agrawal and B. Runnels, "Block structured adaptive mesh refinement and strong form elasticity approach to phase field fracture with applications to delamination, crack branching and crack deflection," *Computer Methods in Applied Mechanics and Engineering*, vol. 385, p. 114 011, Nov. 2021.

[3] A. C. Aitken, "On bernoulli's numerical solution of algebraic equations," *Proceedings of the Royal Society of Edinburgh*, vol. 46, pp. 289–305, 1927.

[4] S. Alameddin, M. Bhattacharyya, A. Fau, U. Nackenhorst, D. Néron, and P. Ladevèze, "Large time increment approach for fatigue damage computations," *PAMM*, vol. 17, no. 1, pp. 231–232, Dec. 2017.

[5] R. Alessi, J.-J. Marigo, C. Maurini, and S. Vidoli, "Coupling damage and plasticity for a phase-field regularisation of brittle, cohesive and ductile fracture: One-dimensional examples," *International Journal of Mechanical Sciences*, vol. 149, pp. 559–576, Dec. 2018.

[6] R. Alessi and J. Ulloa, "Endowing griffth's fracture theory with the ability to describe fatigue cracks," Preprint submitted to Elsevier, 2023.

[7] R. Alessi, S. Vidoli, and L. D. Lorenzis, "A phenomenological approach to fatigue with a variational phase-field model: The one-dimensional case," *Engineering Fracture Mechanics*, vol. 190, pp. 53–73, Mar. 2018.

[8] O. Allix and J.-F. Deü, "Delay-damage modelling for fracture prediction of laminated composites under dynamic loading," *Engineering Transactions*, vol. 45, pp. 29–46, Jan. 1997.

[9] M. Ambati, T. Gerasimov, and L. D. Lorenzis, "Phase-field modeling of ductile fracture," *Computational Mechanics*, vol. 55, no. 5, pp. 1017–1040, Apr. 2015.

[10] M. Ambati, T. Gerasimov, and L. De Lorenzis, "A review on phase-field models of brittle fracture and a new fast hybrid formulation," *Computational Mechanics*, vol. 55, Dec. 2014.

[11] M. Ambati, R. Kruse, and L. D. Lorenzis, "A phase-field model for ductile fracture at finite strains and its experimental verification," *Computational Mechanics*, vol. 57, no. 1, pp. 149–167, Nov. 2015.

[12] L. Ambrosio and V. M. Tortorelli, "Approximation of functional depending on jumps by elliptic functional via t-convergence," *Communications on Pure and Applied Mathematics*, vol. 43, no. 8, pp. 999–1036, Dec. 1990.

[13] G. Amendola, M. Fabrizio, and J. Golden, "Thermomechanics of damage and fatigue by a phase field model," *J. Therm. Stresses*, vol. 39, 2018.

[14] H. Amor, "Variational approach of griffith and paris laws via non-local damage models : Theoretical study and numerical implementation," Jun. 2008.

[15] H. Amor, J.-J. Marigo, and C. Maurini, "Regularized formulation of the variational brittle fracture with unilateral contact: Numerical experiments," *Journal of the Mechanics and Physics of Solids*, vol. 57, no. 8, pp. 1209–1229, 2009.

[16] A. de-Andrés, J. Pérez, and M. Ortiz, "Elastoplastic finite element analysis of three-dimensional fatigue crack growth in aluminum shafts subjected to axial loading," *International Journal of Solids and Structures*, vol. 36, no. 15, pp. 2231–2258, May 1999.

[17] M. Artina, M. Fornasier, S. Micheletti, and S. Perotto, "Anisotropic mesh adaptation for crack detection in brittle materials," *SIAM Journal on Scientific Computing*, vol. 37, no. 4, B633–B659, Jan. 2015.

[18] H. Badnava, M. A. Msekh, E. Etemadi, and T. Rabczuk, "An h-adaptive thermo-mechanical phase field model for fracture," *Finite Elements in Analysis and Design*, vol. 138, pp. 31–47, Jan. 2018.

[19] C. Bathias, "There is no infinite fatigue life in metallic materials," *Fatigue & Fracture of Engineering Materials Structures*, vol. 22, no. 7, pp. 559–565, Jul. 1999.

[20] Z. P. Bazant, T. Belytschko, and T.-P. Chang, "Continuum theory for strain-softening," *Journal of Engineering Mechanics-asce*, vol. 110, pp. 1666–1692, 1984.

[21] Z. Bažant, *International Journal of Fracture*, vol. 83, no. 1, pp. 19–40, 1997.

[22] T. Belytschko and T. Black, "Elastic crack growth in finite elements with minimal remeshing," *International Journal for Numerical Methods in Engineering*, vol. 45, no. 5, pp. 601–620, Jun. 1999.

[23] A. Benoit, M. Maitournam, L. Rémy, and F. Oger, "Cyclic behaviour of structures under thermomechanical loadings: Application to exhaust manifolds," *International Journal of Fatigue*, vol. 182, no. 4, pp. 65–74, May 2012.

[24] A. Berard, "Transferts de champs entre maillages de type éléments finis et applications numériques en mécanique non linéaire des structures," Ph.D. dissertation, Université de Franche Comté, 2011.

[25] A. Bergara, J. Dorado, A. Martin-Meizoso, and J. Martínez-Esnaola, "Fatigue crack propagation in complex stress fields: Experiments and numerical simulations using the extended finite element method (XFEM)," *International Journal of Fatigue*, vol. 103, pp. 112–121, Oct. 2017.

[26] P.-E. Bernard, N. Moës, and N. Chevaugeon, "Damage growth modeling using the thick level set (TLS) approach: Efficient discretization for quasi-static loadings," *Computer Methods in Applied Mechanics and Engineering*, vol. 233, pp. 11–27, 2012.

[27] M. Bhattacharyya, A. Fau, U. Nackenhorst, D. Néron, and P. Ladevèze, "A LATIN-based model reduction approach for the simulation of cycling damage," *Computational Mechanics*, vol. 62, no. 4, pp. 725–743, Nov. 2017.

[28] J. Bleyer and R. Alessi, "Phase-field modeling of anisotropic brittle fracture including several damage mechanisms," *Computer Methods in Applied Mechanics and Engineering*, vol. 336, pp. 213–236, Jul. 2018.

[29] J. Bleyer and J.-F. Molinari, "Microbranching instability in phase-field modelling of dynamic brittle fracture," *Applied Physics Letters*, vol. 110, no. 15, Apr. 2017.

[30] J. Boldrini, E. B. de Moraes, L. Chiarelli, F. Fumes, and M. Bittencourt, "A non-isothermal thermodynamically consistent phase field framework for structural damage and fatigue," *Computer Methods in Applied Mechanics and Engineering*, vol. 312, pp. 395–427, Dec. 2016.

[31] M. J. Borden, T. J. Hughes, C. M. Landis, A. Anvari, and I. J. Lee, "A phase-field formulation for fracture in ductile materials: Finite deformation balance law derivation, plastic degradation, and stress triaxiality effects," *Computer Methods in Applied Mechanics and Engineering*, vol. 312, pp. 130–166, Dec. 2016.

[32] M. J. Borden, T. J. Hughes, C. M. Landis, and C. V. Verhoosel, "A higher-order phase-field model for brittle fracture: Formulation and analysis within the isogeometric analysis framework," *Computer Methods in Applied Mechanics and Engineering*, vol. 273, pp. 100–118, May 2014.

[33] M. J. Borden, C. V. Verhoosel, M. A. Scott, T. J. Hughes, and C. M. Landis, "A phase-field description of dynamic brittle fracture," *Computer Methods in Applied Mechanics and Engineering*, vol. 217-220, pp. 77–95, Apr. 2012.

[34] R. de Borst and C. V. Verhoosel, "Gradient damage vs phase-field approaches for fracture: Similarities and differences," *Computer Methods in Applied Mechanics and Engineering*, vol. 312, pp. 78–94, Dec. 2016.

[35] R. D. Borst and H.-B. Mühlhaus, "Gradient-dependent plasticity: Formulation and algorithmic aspects," *International Journal for Numerical Methods in Engineering*, vol. 35, no. 3, pp. 521–539, Aug. 1992.

[36] R. D. Borst, L. J. Sluys, H.-B. Mühlhaus, and J. Pamin, "Fundamental issues in finite element analyses of localization of deformation," *Engineering Computations*, vol. 10, pp. 99–121, 1993.

[37] P. Bouchard, F. Bay, and Y. Chastel, "Numerical modelling of crack propagation: Automatic remeshing and comparison of different criteria," *Computer Methods in Applied Mechanics and Engineering*, vol. 192, no. 35-36, pp. 3887–3908, Aug. 2003.

[38] B. Bourdin, G. Francfort, and J.-J. Marigo, "Numerical experiments in revisited brittle fracture," *Journal of the Mechanics and Physics of Solids*, vol. 48, no. 4, pp. 797–826, 2000.

[39] B. Bourdin, C. J. Larsen, and C. L. Richardson, "A time-discrete model for dynamic fracture based on crack regularization," *International Journal of Fracture*, vol. 168, no. 2, pp. 133–143, Nov. 2010.

[40] A. Braides, *Gamma-Convergence for Beginners*. Oxford University Press, Jul. 2002.

[41] D. Brancherie, P. Villon, and A. Ibrahimbegovic, "On a consistent field transfer in non linear inelastic analysis and ultimate load computation," *Computational Mechanics*, vol. 42, no. 2, pp. 213–226, Jul. 2007.

[42] H. Bui, *Mécanique de la rupture fragile*, fre. Masson, 1977.

[43] Q. Caradec, M. Breuzé, H. Maitournam, B. Prabel, and J.-L. Fayard, "Finite element simulation of high cycle fretting wear using an implicit adaptive cycle jump," *Wear*, vol. 522, p. 204 703, Jun. 2023.

[44] P. Carrara, M. Ambati, R. Alessi, and L. D. Lorenzis, "A framework to model the fatigue behaviour of brittle materials on a variational phase-field approach," *Computer Methods in Applied Mechanics and Engineering*, 2019.

[45] B. J. Carter, P. A. Wawrzynek, and A. R. Ingraffea, "Automated 3-d crack growth simulation," *International Journal for Numerical Methods in Engineering*, vol. 47, no. 1-3, pp. 229–253, Jan. 2000.

[46] CEA, *Cast3m - finite element software developed by the french alternative energies and atomic energy commission*, 2022. [Online]. Available: cast3m.cea.fr.

[47] J. L. Chaboche and P. M. Lesne, "A non linear continuous fatigue damage model," *Fatigue & Fracture of Engineering Materials and Structures*, vol. 11, no. 1, pp. 1–17, Jan. 1988.

[48] A. Chambolle, G. Francfort, and J.-J. Marigo, "When and how do crack propagate?" *Journal of The Mechanics and Physics of Solids*, vol. 57, Apr. 2009.

[49] A. Chambolle, "An approximation result for special functions with bounded deformation," *Journal de Mathématiques Pures et Appliquées*, vol. 83, no. 7, pp. 929–954, Jul. 2004.

[50] A. Chambolle, S. Conti, and G. A. Francfort, "Approximation of a brittle fracture energy with a constraint of non-interpenetration," *Archive for Rational Mechanics and Analysis*, vol. 228, no. 3, pp. 867–889, Dec. 2017.

[51] T. CHarras and J. Kichenin, "Développer dans cast3m - implémentation d'une nouvelle loi de comportement," 2011.

[52] V. Chiaruttini, D. Geoffroy, V. Riolo, and M. Bonnet, "An adaptive algorithm for cohesive zone model and arbitrary crack propagation," *European Journal of Computational Mechanics*, vol. 21, no. 3-6, pp. 208–218, 2012.

[53] V. Chiaruttini, V. Riolo, and F. Feyel, "Advanced remeshing techniques for complex 3d crack propagation," *The 13th International Conference on Fracture*, 2013.

[54] H. Choi, K. Park, and G. H. Paulino, "Mixed-mode fatigue crack growth using cohesive zone modeling," *Engineering Fracture Mechanics*, vol. 240, p. 107 234, Dec. 2020.

[55] L. F. Coffin, "A study of the effects of cyclic thermal stresses on a ductile metal," *Journal of Fluids Engineering*, vol. 76, no. 6, pp. 931–949, Aug. 1954.

[56] D. COJOCARU and A. KARLSSON, "A simple numerical method of cycle jumps for cyclically loaded structures," *International Journal of Fatigue*, vol. 28, no. 12, pp. 1677–1689, Dec. 2006.

[57] D. Colombo and M. Giglio, "A methodology for automatic crack propagation modelling in planar and shell FE models," *Engineering Fracture Mechanics*, vol. 73, no. 4, pp. 490–504, Mar. 2006.

[58] G. Crossland, "Effect of large hydrostatic pressures on the torsional fatigue strength of an alloy steel," *Proc of the Int. Conf. of Fatigue of Metals*, 1956.

[59] V. Davies, "Discussion of "the strength of metals under combined alternating stresses by h.j gough and h.v. pollard," *Institution of Mechanical Engineers*, vol. 131, no. 3, 1935.

[60] L. De Lorenzis and T. Gerasimov, "Numerical implementation of phase-field models of brittle fracture," in Feb. 2020, pp. 75–101.

[61] S. Degallaix and B. Ilschner, "Caractérisation expérimentale des matériaux: Propriétés physisques, thermiques et mécaniques; chapitre 8," 2007.

[62] R. Desmorat, "Damage and fatigue. continuum damage mechanics modeling for fatigue of materials and structures.," *Revue Europeenne de Genie Civil*, pp.849–878, 2006.

[63] P. Destuynder, "Quelques remarques sur la mecanique de la rupture elastique," *Journal de mecanique theorique et appliquee*, vol. 2, no. 1, pp.113–135, 1983.

[64] A. Devulder, D. Aubry, and G. Puel, "Two-time scale fatigue modelling: Application to damage," *Computational Mechanics*, vol. 45, no. 6, pp. 637–646, Feb. 2010.

[65] F. P. Duda, A. Ciarbonetti, P. J. Sánchez, and A. E. Huespe, "A phase-field/gradient damage model for brittle fracture in elastic/plastic solids," *International Journal of Plasticity*, vol. 65, pp. 269–296, Feb. 2015.

[66] D. Dugdale, "Yielding of steel sheets containing slits," *Journal of the Mechanics and Physics of Solids*, vol. 8, no. 2, pp. 100–104, May 1960.

[67] W. Elber, "Fatigue crack closure under cyclic tension," *Engineering Fracture Mechanics*, vol. 2, no. 1, pp. 37–45, 1970.

[68] T. Elguedj, "Simulation numérique de la propagation de fissure en fatigue par la méthode des éléments finis étendus : Prise en compte de la plasticité et du contact-frottement," Ph.D. dissertation, INSA Lyon, 2006.

[69] T. Elguedj, A. Gravouil, and A. Combescure, "Appropriate extended functions for x-FEM simulation of plastic fracture mechanics," *Computer Methods in Applied Mechanics and Engineering*, vol. 195, no. 7-8, pp. 501–515, Jan. 2006.

[70] F. Erdogan and G. C. Sih, "On the crack extension in plates under plane loading and transverse shear," *Journal of Basic Engineering*, vol. 85, no. 4, pp. 519–525, Dec. 1963.

[71] P. Farrell and C. Maurini, "Linear and nonlinear solvers for variational phase-field models of brittle fracture," *International Journal for Numerical Methods in Engineering*, vol. 109, no. 5, pp. 648–667, Jul. 2016.

[72] J. Fish and Q. Yu, "Computational mechanics of fatigue and life predictions for composite materials and structures," *Computer Methods in Applied Mechanics and Engineering*, vol. 191, no. 43, pp. 4827–4849, Sep. 2002.

[73] S. Forest, "Micromorphic approach for gradient elasticity, viscoplasticity, and damage," *Journal of Engineering Mechanics*, vol. 135, no. 3, pp. 117–131, Mar. 2009.

[74] R. G. Forman, V. E. Kearney, and R. M. Engle, "Numerical analysis of crack propagation in cyclic-loaded structures," *J. Basic Eng.*, vol. 89, no. 3, pp. 459–463, Sep. 1967.

[75] P. Forsyth, "A two stage fatigue fracture mechanism," *Cranfield Symposium on Fatigue Crack Propagation*, vol. 76, no. 1, 1961.

[76] G. Francfort and J.-J. Marigo, "Revisiting brittle fracture as an energy minimization problem," *Journal of the Mechanics and Physics of Solids*, vol. 46, no. 8, pp. 1319–1342, 1998.

[77] G. Francfort and J.-J. Marigo, "Revisiting brittle fracture as an energy minimization problem," *Journal of the Mechanics and Physics of Solids*, vol. 46, no. 8, pp. 1319–1342, Aug. 1998.

[78] F. Freddi and L. Mingazzi, "Mesh refinement procedures for the phase field approach to brittle fracture," *Computer Methods in Applied Mechanics and Engineering*, vol. 388, p. 114 214, Jan. 2022.

[79] F. Freddi and G. Royer Carfagni, "Regularized variational theories of fracture: A unified approach," *Journal of the Mechanics and Physics of Solids*, vol. 58, pp. 1154–1174, Aug. 2010.

[80] F. Freddi and G. Royer-Carfagni, "Regularized variational theories of fracture: A unified approach," *Journal of the Mechanics and Physics of Solids*, vol. 58, no. 8, pp. 1154–1174, Aug. 2010.

[81] T. Gerasimov and L. De Lorenzis, "On penalization in variational phase-field models of brittle fracture," *Computer Methods in Applied Mechanics and Engineering*, vol. 354, pp. 990–1026, 2019.

[82] T. Gerasimov and L. De Lorenzis, "A line search assisted monolithic approach for phase-field computing of brittle fracture," *Computer Methods in Applied Mechanics and Engineering*, vol. 312, Dec. 2015.

[83] G. Gibert, B. Prabel, A. Gravouil, and C. Jacquemoud, "A 3D automatic mesh refinement x-fem approach for fatigue crack propagation," *Finite Elements in Analysis and Design*, vol. 157, 2019.

[84] G. Gibert, "Propagation de fissures en fatigue par une approche x-fem avec raffinement automatique de maillage," Ph.D. dissertation, INSA de Lyon, 2019.

[85] C. Gilbert, R. Dauskardt, and R. Ritchie, "Microstructural mechanisms of cyclic fatigue-crack propagation in grain-bridging ceramics," *Ceramics International*, vol. 23, no. 5, pp. 413–418, Jan. 1997.

[86] R. V. Gol'dstein and R. L. Salganik, "Brittle fracture of solids with arbitrary cracks," *International Journal of Fracture*, vol. 10, no. 4, pp. 507–523, Dec. 1974.

[87] A. Golahmar, P. K. Kristensen, C. F. Niordson, and E. Martínez-Pañeda, "A phase field model for hydrogen-assisted fatigue," *International Journal of Fatigue*, vol. 154, p. 106 521, Jan. 2022.

[88] A. Golahmar, C. F. Niordson, and E. Martínez-Pañeda, "A phase field model for high-cycle fatigue: Total-life analysis," *International Journal of Fatigue*, vol. 170, p. 107 558, May 2023.

[89] J. Goodman, "Mechanics applied to engineering," *Longman London*, 1899.

[90] M. Gosz, J. Dolbow, and B. Moran, "Domain integral formulation for stress intensity factor computation along curved three-dimensional interface cracks," *International Journal of Solids and Structures*, vol. 35, no. 15, pp. 1763–1783, 1998.

[91] H. Gough and H. Pollard, "A two stage fatigue fracture mechanism," *Cranfield Symposium on Fatigue Crack Propagation*, vol. 131, no. 3, 1935.

[92] A. Gravouil, N. Moës, and T. Belytschko, "Non-planar 3d crack growth by the extended finite element and level sets-part II: Level set update," *International Journal for Numerical Methods in Engineering*, vol. 53, no. 11, pp. 2569–2586, Jan. 2002.

[93] A. Griffith, "The phenomena of rupture and flow in solids," *Philosophical transaction of the royal society of London - Series A*, vol. 221, 1921.

[94] B. E. Grossman-Ponemon, A. Mesgarnejad, and A. Karma, "Phase-field modeling of continuous fatigue via toughness degradation," *Engineering Fracture Mechanics*, vol. 264, p. 108 255, Apr. 2022.

[95] T. Guennouni, "Sur une méthode de calcul de structures soumises a des chargements cycliques : L'homogénéisation en temps," fre, *ESAIM: Mathematical Modelling and Numerical Analysis - Modelisation Mathematique et Analyse Numerique*, vol. 22, no. 3, pp. 417–455, 1988.

[96] G. Guinea, J.Planas, and M. Elices, "K1 evaluation by the displacement extrapolation," *Eng. Fract. Mech.*, vol. 66, 2000.

[97] A. Gupta, U. M. Krishnan, T. K. Mandal, R. Chowdhury, and V. P. Nguyen, "An adaptive mesh refinement algorithm for phase-field fracture models: Application to brittle, cohesive, and dynamic fracture," *Computer Methods in Applied Mechanics and Engineering*, vol. 399, p. 115 347, Sep. 2022.

[98] V. Hakim and A. Karma, "Laws of crack motion and phase-field models of fracture," *Journal of the Mechanics and Physics of Solids*, vol. 57, no. 2, pp. 342–368, Feb. 2009.

[99] P. W. Harper and S. R. Hallett, "A fatigue degradation law for cohesive interface elements development and application to composite materials," *International Journal of Fatigue*, vol. 32, no. 11, pp. 1774–1787, Nov. 2010.

[100] M. M. Hasan and T. Baxevanis, "A phase-field model for low-cycle fatigue of brittle materials," *International Journal of Fatigue*, vol. 150, p. 106 297, 2021.

[101] G. Haveroth, M. Vale, M. Bittencourt, and J. Boldrini, "A non-isothermal thermodynamically consistent phase field model for damage, fracture and fatigue evolutions in elasto-plastic materials," *Computer Methods in Applied Mechanics and Engineering*, vol. 364, p. 112 962, Jun. 2020.

[102] Q.-C. He and Q. Shao, "Closed-form coordinate-free decompositions of the two-dimensional strain and stress for modeling tension/compression dissymmetry," *Journal of Applied Mechanics*, vol. 86, no. 3, Jan. 2019.

[103] T. Heister, M. F. Wheeler, and T. Wick, "A primal-dual active set method and predictor-corrector mesh adaptivity for computing fracture propagation using a phase-field approach," *Computer Methods in Applied Mechanics and Engineering*, vol. 290, pp. 466–495, Jun. 2015.

[104] T. Helfer, B. Bary, O. Fandeur, and L. Ye, "Un schéma numérique efficace pour le traitement de la fissuration fragile des matériaux quasi-fragiles par champ de phase," *Congrès Français de Mécanique*, vol. 24, pp. 648–667, Jul. 2019.

[105] H. Henry and H. Levine, "Dynamic instabilities of fracture under biaxial strain using a phase field model," *Physical Review Letters*, vol. 93, no. 10, Sep. 2004.

[106] C. Hesch *et al.*, "A framework for polyconvex large strain phase-field methods to fracture," *Computer Methods in Applied Mechanics and Engineering*, vol. 317, pp. 649–683, Apr. 2017.

[107] H. Hirshikesh, A. Pramod, H. Waisman, and S. Natarajan, "Adaptive phase field method using novel physics based refinement criteria," *Computer Methods in Applied Mechanics and Engineering*, vol. 383, p. 113 874, Sep. 2021.

[108] Hirshikesh, C. Jansari, K. Kannan, R. Annabattula, and S. Natarajan, "Adaptive phase field method for quasi-static brittle fracture using a recovery based error indicator and quadtree decomposition," *Engineering Fracture Mechanics*, vol. 220, p. 106 599, Oct. 2019.

[109] Z. S. Hosseini, M. Dadfarnia, B. P. Somerday, P. Sofronis, and R. O. Ritchie, "On the theoretical modeling of fatigue crack growth," *Journal of the Mechanics and Physics of Solids*, vol. 121, pp. 341–362, Dec. 2018.

[110] J. Hutchinson, "Singular behaviour at the end of a tensile crack in a hardening material," *Journal of the Mechanics and Physics of Solids*, vol. 16, no. 1, pp. 13–31, 1968.

[111] A. International, "E1820-01 standard test method for measurement of fatigue crack growth rates," 2008.

[112] A. International, "E647-05 standard test method for measurement of fatigue crack growth rates," 2005.

[113] G. R. Irwin, "Analysis of stresses and strains near the end of a crack traversing a plate," *Journal of Applied Mechanics*, vol. 24, 1957.

[114] G. R. Irwin, "Fracture," in *Elasticity and Plasticity / Elastizität und Plastizität*, S. Flügge, Ed. Berlin, Heidelberg: Springer Berlin Heidelberg, 1958, pp. 551–590.

[115] A. Jaccon, B. Prabel, G. Molnár, J. Bluthé, and A. Gravouil, "Adaptive mesh refinement and cycle jumps for phase-field fatigue fracture modeling," *Finite Elements in Analysis and Design*, vol. 224, p. 104 004, Oct. 2023.

[116] A. Jaubert and J. .-. Marigo, "Justification of paris-type fatigue laws from cohesive forces model via a variational approach," *Continuum Mechanics and Thermodynamics*, vol. 18, no. 1-2, pp. 23–45, May 2006.

[117] D. Jeulin, "Towards crack paths simulations in media with a random fracture energy," *International Journal of Solids and Structures*, vol. 184, pp. 279–286, Feb. 2020.

[118] Y. Jiang and M. Feng., "Modeling of fatigue crack propagation," *Journal of Engineering and Material Technologies*, vol. 126, 2004.

[119] M. Jirásek, "Nonlocal models for damage and fracture: Comparison of approaches," *International Journal of Solids and Structures*, vol. 35, no. 31-32, pp. 4133–4145, Nov. 1998.

[120] L. M. Kachanov, "Fatigue damage," in *Introduction to continuum damage mechanics*. Dordrecht: Springer Netherlands, 1986, pp. 121–128.

[121] L. Kachanov, "Rupture time under creep conditions," *Otdelenie Tekhnicheskich Nauk*, 1958.

[122] A. Karma, D. A. Kessler, and H. Levine, "Phase-field model of mode iii dynamic fracture," *Phys. Rev. Lett.*, vol. 87, p. 045 501, 4 2001.

[123] A. Karma and A. E. Lobkovsky, "Unsteady crack motion and branching in a phase-field model of brittle fracture," *Physical Review Letters*, vol. 92, no. 24, Jun. 2004.

[124] A. Karma and A. E. Lobkovsky, "Unsteady crack motion and branching in a phase-field model of brittle fracture," *Physical Review Letters*, vol. 92, no. 24, Jun. 2004.

[125] Z. Khalil, A. Y. Elghazouli, and E. Martínez-Pañeda, "A generalised phase field model for fatigue crack growth in elasticplastic solids with an efficient monolithic solver," *Computer Methods in Applied Mechanics and Engineering*, vol. 388, p. 114 286, Jan. 2022.

[126] H. Kiewel, J. Aktaa, and D. Munz, "Application of an extrapolation method in thermocyclic failure analysis," *Computer Methods in Applied Mechanics and Engineering*, vol. 182, no. 1-2, pp. 55–71, Feb. 2000.

[127] H.-Y. Kim and H.-G. Kim, "A novel adaptive mesh refinement scheme for the simulation of phase-field fracture using trimmed hexahedral meshes," *International Journal for Numerical Methods in Engineering*, vol. 122, no. 6, pp. 1493–1512, Dec. 2020.

[128] M. Klinsmann, D. Rosato, M. Kamlah, and R.-M. McMeeking, "An assessment of the phase field formulation for crack growth," *Computer Methods in Applied Mechanics and Engineering*, vol. 294, pp. 313–330, 2015.

[129] P. K. Kristensen and E. Martínez-Pañeda, "Phase field fracture modelling using quasi-newton methods and a new adaptive step scheme," *Theoretical and Applied Fracture Mechanics*, vol. 107, p. 102 446, 2020.

[130] P. K. Kristensen, A. Golahmar, E. Martínez-Pañeda, and C. F. Niordson, "Accelerated high-cycle phase field fatigue predictions," *European Journal of Mechanics - A/Solids*, vol. 100, p. 104 991, Jul. 2023.

[131] P. K. Kristensen and E. Martinez-Pañeda, *Quasi-newton implementation of the phase-field method for fracture and fatigue in abaqus - documentation*, 2020. [Online]. Available: www.empaneda.com/codes/.

[132] C. Kuhn and R. Müller, "A continuum phase field model for fracture," *Engineering Fracture Mechanics*, vol. 77, no. 18, pp. 3625–3634, Dec. 2010.

[133] C. Kuhn, A. Schlüter, and R. Müller, "On degradation functions in phase field fracture models," *Computational Materials Science*, vol. 108, pp. 374–384, Oct. 2015.

[134] D. Kujawski and F. Ellyin, "A fatigue crack propagation model," *Engineering Fracture Mechanics*, vol. 20, no. 5, pp. 695–704, 1984.

[135] M. Kuna. Springer, 2013.

[136] P. Ladevèze, "New advances in the large time increment method," *New advances in computational structural mechanics. Elsevier, Amsterdam*, pp. 3–21, 1991.

[137] P. Ladevèze, "On a family of algorithms for structural mechanics," *Comptes Rendus Académie des Sciences Paris*, vol. 300, no. 2, pp. 41–44, 1985.

[138] P. Ladevèze, "The large time increment method for the analysis of structures with non-linear behavior described by internal variables," *Comptes rendus de l'academie des sciences serie II*, vol. 309, no. 11, pp. 1095–1099, 1989.

[139] G. Lancioni and G. Royer-Carfagni, "The variational approach to fracture mechanics. a practical application to the french panthéon in paris," *Journal of Elasticity*, vol. 95, no. 1-2, pp. 1–30, Jan. 2009.

[140] S. Lee, M. F. Wheeler, and T. Wick, "Pressure and fluid-driven fracture propagation in porous media using an adaptive finite element phase field model," *Computer Methods in Applied Mechanics and Engineering*, vol. 305, pp. 111–132, Jun. 2016.

[141] C. Lemaignan, *La rupture des matériaux*. EDP Sciences, Jul. 2003.

[142] J. Lemaitre and J.-L. Chaboche, *A Course on Damage Mechanics (2nd edn)*. Springer: Berlin, 1996.

[143] J. Lemaitre and R. Desmorat, *Engineering Damage Mechanics*. Springer-Verlag, 2005.

[144] J. Lemaitre, J. Sermage, and R. Desmorat, *International Journal of Fracture*, vol. 97, no. 1/4, pp. 67–81, 1999.

[145] J. Lemaitre and I. Doghri, "Damage 90: A post processor for crack initiation," *Computer Methods in Applied Mechanics and Engineering*, vol. 115, no. 3-4, pp. 197–232, May 1994.

[146] B. Li, C. Peco, D. Millán, I. Arias, and M. Arroyo, "Phase-field modeling and simulation of fracture in brittle materials with strongly anisotropic surface energy," *International Journal for Numerical Methods in Engineering*, vol. 102, no. 3-4, pp. 711–727, Jul. 2014.

[147] T. Li, J.-J. Marigo, D. Guilbaud, and S. Potapov, "Gradient damage modeling of brittle fracture in an explicit dynamics context," *International Journal for Numerical Methods in Engineering*, vol. 108, no. 11, pp. 1381–1405, May 2016.

[148] Y.-S. Lo, M. J. Borden, K. Ravi-Chandar, and C. M. Landis, "A phase-field model for fatigue crack growth," *Journal of the Mechanics and Physics of Solids*, vol. 132, p. 103 684, Nov. 2019.

[149] P. J. Loew, B. Peters, and L. A. Beex, "Fatigue phase-field damage modeling of rubber using viscous dissipation: Crack nucleation and propagation," *Mechanics of Materials*, vol. 142, p. 103 282, Mar. 2020.

[150] P. J. Loew, B. Peters, and L. A. Beex, "Rate-dependent phase-field damage modeling of rubber and its experimental parameter identification," *Journal of the Mechanics and Physics of Solids*, vol. 127, pp. 266–294, Jun. 2019.

[151] P. J. Loew, L. H. Poh, B. Peters, and L. A. Beex, "Accelerating fatigue simulations of a phase-field damage model for rubber," *Computer Methods in Applied Mechanics and Engineering*, vol. 370, p. 113 247, Oct. 2020.

[152] E. Lorentz and V. Godard, "Gradient damage models: Toward full-scale computations," *Computer Methods in Applied Mechanics and Engineering*, vol. 200, no. 21-22, pp. 1927–1944, May 2011.

[153] L. D. Lorenzis and C. Maurini, "Nucleation under multi-axial loading in variational phase-field models of brittle fracture," *International Journal of Fracture*, vol. 237, no. 1-2, pp. 61–81, Jun. 2021.

[154] Y. Lu, T. Helfer, B. Bary, and O. Fandeur, "An efficient and robust staggered algorithm applied to the quasi-static description of brittle fracture by a phase-field approach," *Computer Methods in Applied Mechanics and Engineering*, vol. 370, p. 113 218, 2020.

[155] S. Maiti and P. H. Geubelle, "Cohesive modeling of fatigue crack retardation in polymers: Crack closure effect," *Engineering Fracture Mechanics*, vol. 73, no. 1, pp. 22–41, Jan. 2006.

[156] H. Maitournam, fre. Editions Ecole Polytechnique, 2017.

[157] M. Maitournam, B. Pommier, and J.-J. Thomas, "Détermination de la réponse asymptotique d'une structure anélastique sous chargement thermomécanique cyclique," *Comptes Rendus Mécanique*, vol. 330, no. 10, pp. 703–708, Oct. 2002.

[158] K. Mang, M. Walloth, T. Wick, and W. Wollner, "Mesh adaptivity for quasi-static phase-field fractures based on a residual-type a posteriori error estimator," *GAMM-Mitteilungen*, vol. 43, no. 1, Aug. 2019.

[159] S. May, J. Vignollet, and R. de Borst, "A new arc-length control method based on the rates of the internal and the dissipated energy," *Engineering Computations*, vol. 33, no. 1, pp. 100–115, Mar. 2016.

[160] J. Mazars, Y. Berthaud, and S. Ramtani, "The unilateral behaviour of damaged concrete," *Engineering Fracture Mechanics*, vol. 35, no. 4-5, pp. 629–635, Jan. 1990.

[161] J. Mediavilla, R. Peerlings, and M. Geers, "A robust and consistent remeshing-transfer operator for ductile fracture simulations," *Computers & Structures*, vol. 84, no. 8-9, pp. 604–623, Mar. 2006.

[162] A. Mesgarnejad, A. Imanian, and A. Karma, "Phase-field models for fatigue crack growth," *Theoretical and Applied Fracture Mechanics*, vol. 103, p. 102 282, Oct. 2019.

[163] S. R. Mettu *et al.*, "Nasgro 3.0: A software for analyzing aging aircraft," 1999.

[164] C. Miehe, M. Hofacker, L.-M. Schänzel, and F. Aldakheel, "Phase field modeling of fracture in multi-physics problems. part II. coupled brittle-to-ductile failure criteria and crack propagation in thermo-elasticplastic solids," *Computer Methods in Applied Mechanics and Engineering*, vol. 294, pp. 486–522, Sep. 2015.

[165] C. Miehe, F. Welschinger, and M. Hofacker, "Thermodynamically consistent phase-field models of fracture: Variational principles and multi-field FE implementations," *International Journal for Numerical Methods in Engineering*, vol. 83, no. 10, pp. 1273–1311, 2010.

[166] C. Miehe, M. Hofacker, and F. Welschinger, "A phase field model for rate-independent crack propagation: Robust algorithmic implementation based on operator splits," *Computer Methods in Applied Mechanics and Engineering*, vol. 199, no. 45–48, pp. 2765–2778, 2010.

[167] M. Miner, "Cumulative fatigue damage," *Journal of Applied Mechanics*, vol. 12, 1945.

[168] N. Moës, A. Gravouil, and T. Belytschko, "Non-planar 3d crack growth by the extended finite element and level sets-part i: Mechanical model," *International Journal for Numerical Methods in Engineering*, vol. 53, no. 11, pp. 2549–2568, Jan. 2002.

[169] N. Moës, C. Stolz, P.-E. Bernard, and N. Chevaugeon, "A level set based model for damage growth: The thick level set approach," *International Journal for Numerical Methods in Engineering*, vol. 86, no. 3, pp. 358–380, Dec. 2010.

[170] N. Moës, J. Dolbow, and T. Belytschko, "A finite element method for crack growth without remeshing," *International Journal for Numerical Methods in Engineering*, vol. 46, no. 1, pp. 131–150, Sep. 1999.

[171] G. Molnár, A. Doitrand, R. Estevez, and A. Gravouil, "Toughness or strength? regularization in phase-field fracture explained by the coupled criterion," *Theoretical and Applied Fracture Mechanics*, vol. 109, p. 102 736, 2020.

[172] G. Molnár and A. Gravouil, "2D and 3D abaqus implementation of a robust staggered phase-field solution for modeling brittle fracture," *Finite Elements in Analysis and Design*, vol. 130, pp. 27–38, 2017.

[173] G. Molnár, A. Gravouil, R. Seghir, and J. Réthoré, "An open-source abaqus implementation of the phase-field method to study the effect of plasticity on the

instantaneous fracture toughness in dynamic crack propagation," *Computer Methods in Applied Mechanics and Engineering*, vol. 365, p. 113 004, 2020.

[174] G. Molnár, *Documentation for automatic time integration*, 2020. [Online]. Available: www.molnar-research.com/tutorials.

[175] G. Molnár, *Documentation for the anisotropic/asymmetric energy degradation element*, 2020. [Online]. Available: www.molnar-research.com/tutorials.

[176] G. Molnár, A. Doitrand, A. Jaccon, B. Prabel, and A. Gravouil, "Thermodynamically consistent linear-gradient damage model in abaqus," *Engineering Fracture Mechanics*, vol. 266, p. 108 390, May 2022.

[177] A. Muixí, S. Fernández-Méndez, and A. Rodríguez-Ferran, "Adaptive refinement for phase-field models of brittle fracture based on nitsche's method," *Computational Mechanics*, vol. 66, no. 1, pp. 69–85, Mar. 2020.

[178] D. Mumford and J. Shah, "Optimal approximations by piecewise smooth functions and associated variational problems," *Communications on Pure and Applied Mathematics*, vol. 42, no. 5, pp. 577–685, Jul. 1989.

[179] S. Nagaraja, M. Elhaddad, M. Ambati, S. Kollmannsberger, L. D. Lorenzis, and E. Rank, "Phase-field modeling of brittle fracture with multi-level hp-FEM and the finite cell method," *Computational Mechanics*, vol. 63, no. 6, pp. 1283–1300, Oct. 2018.

[180] O. Nguyen, E. Repetto, M. Ortiz, and R. Radovitzky, "A cohesive model of fatigue crack growth," *International Journal of Fracture*, vol. 110, no. 4, pp. 351–369, 2001.

[181] T. T. Nguyen *et al.*, "On the choice of parameters in the phase field method for simulating crack initiation with experimental validation," *International Journal of Fracture*, vol. 197, no. 2, pp. 213–226, Feb. 2016.

[182] T. Nguyen, J. Yvonnet, Q.-Z. Zhu, M. Bornert, and C. Chateau, "A phase field method to simulate crack nucleation and propagation in strongly heterogeneous materials from direct imaging of their microstructure," *Engineering Fracture Mechanics*, vol. 139, pp. 18–39, May 2015.

[183] T. Nguyen, J. Yvonnet, Q.-Z. Zhu, M. Bornert, and C. Chateau, "A phase-field method for computational modeling of interfacial damage interacting with crack propagation in realistic microstructures obtained by microtomography," *Computer Methods in Applied Mechanics and Engineering*, vol. 312, pp. 567–595, Dec. 2016. [Online]. Available: https://doi.org/10.1016/j.cma.2015.10.007.

[184] T.-T. Nguyen, J. Réthoré, J. Yvonnet, and M.-C. Baietto, "Multi-phase-field modeling of anisotropic crack propagation for polycrystalline materials," *Computational Mechanics*, vol. 60, no. 2, pp. 289–314, Apr. 2017.

[185] T.-T. Nguyen, J. Yvonnet, D. Waldmann, and Q.-C. He, "Implementation of a new strain split to model unilateral contact within the phase field method," *International Journal for Numerical Methods in Engineering*, vol. 121, no. 21, pp. 4717–4733, Aug. 2020.

[186] T. Nishihara and M. Kawamoto, "The strength of metals under combined alternating bending and torsion.," *Journal of the Society of Mechanical Engineers, Japan*, vol. 44, pp. 722–723, 1941.

[187] W. V. Paepegem and J. Degrieck, "Fatigue degradation modelling of plain woven glass/epoxy composites," *Composites Part A: Applied Science and Manufacturing*, vol. 32, no. 10, pp. 1433–1441, Oct. 2001.

[188] E. Pali, A. Gravouil, A. Tanguy, D. Landru, and O. Kononchuk, "Three-dimensional x-fem modeling of crack coalescence phenomena in the smart cuttm technology," *Finite Elements in Analysis and Design*, vol. 213, p. 103 839, 2023.

[189] I. Papadopoulos, "Fatigue polycyclique des métaux," Ph.D. dissertation, Ecole Nationale des Ponts et Chaussées, 1987.

[190] P. Paris and F. Erdogan, "A critical analysis of crack propagation laws," *Journal of Basic Engineering*, vol. 85, no. 4, pp. 528–533, Dec. 1963.

[191] J.-C. Passieux, J. Réthoré, A. Gravouil, and M.-C. Baietto, "Local/global non-intrusive crack propagation simulation using a multigrid x-FEM solver," *Computational Mechanics*, vol. 52, no. 6, pp. 1381–1393, Jun. 2013.

[192] R. Patil, B. Mishra, and I. Singh, "An adaptive multiscale phase field method for brittle fracture," *Computer Methods in Applied Mechanics and Engineering*, vol. 329, pp. 254–288, Feb. 2018. [Online]. Available: https://doi.org/10.1016/j.cma.2017.09.021.

[193] S. Pearson, "Initiation of fatigue cracks in commercial aluminium alloys and the subsequent propagation of very short cracks," *Engineering Fracture Mechanics*, vol. 7, no. 2, pp. 235–247, 1975.

[194] R. H. J. Peerlings, R. D. Borst, W. A. M. Brekelman, and J. H. P. D. Vree, "Gradient enhanced damage for quasi-brittle materials," *International Journal for Numerical Methods in Engineering*, vol. 39, no. 19, pp. 3391–3403, Oct. 1996.

[195] R. H. J. Peerlings, W. A. M. Brekelmans, R. de Borst, and M. G. D. Geers, "Gradient-enhanced damage modelling of high-cycle fatigue," *International Journal for Numerical Methods in Engineering*, vol. 49, no. 12, pp. 1547–1569, 2000.

[196] R. Peerlings, M. Geers, R. de Borst, and W. Brekelmans, "A critical comparison of nonlocal and gradient-enhanced softening continua," *International Journal of Solids and Structures*, vol. 38, no. 44-45, pp. 7723–7746, Nov. 2001.

[197] M. Peigney and C. Stolz, "An optimal control approach to the analysis of inelastic structures under cyclic loading," *Journal of the Mechanics and Physics of Solids*, vol. 51, no. 4, pp. 575–605, Apr. 2003.

[198] D. Perić, C. Hochard, M. Dutko, and D. Owen, "Transfer operators for evolving meshes in small strain elasto-placticity," *Computer Methods in Applied Mechanics and Engineering*, vol. 137, no. 3-4, pp. 331–344, Nov. 1996.

[199] K. Pham, H. Amor, J.-J. Marigo, and C. Maurini, "Gradient damage models and their use to approximate brittle fracture," *International Journal of Damage Mechanics*, vol. 20, no. 4, pp. 618–652, Nov. 2010.

[200] S. Pietruszczak and Z. Mróz, "Finite element analysis of deformation of strain-softening materials," *International Journal for Numerical Methods in Engineering*, vol. 17, no. 3, pp. 327–334, Mar. 1981.

[201] G. Pijaudier-Cabot and Z. P. Bažant, "Nonlocal damage theory," *Journal of Engineering Mechanics*, vol. 113, no. 10, pp. 1512–1533, Oct. 1987.

[202] B. Prabel, "Modélisation avec la methode X-FEM de la propagation dynamique et de l'arret de fissure de clivage dans un acier de cuve rep.," Ph.D. dissertation, INSA Lyon, 2007.

[203] E. C. J. R. C. I. for the Protection and the Security of the Citizen., *Adaptivity in CEA's fluid elements in EUROPLEXUS*. Publications Office, 2014.

[204] G. Puel and D. Aubry, "Methode d homogeneisation temporelle : Application a la simulation numerique de la fatigue," May 2011.

[205] F. Rabold, M. Kuna, and T. Leibelt, "Procrack: A software for simulating three-dimensional fatigue crack growth," in *Advanced Finite Element Methods and Applications*, Springer Berlin Heidelberg, 2013, pp. 355–374.

[206] I. Ramière and T. Helfer, "Iterative residual-based vector methods to accelerate fixed point iterations," *Computers Mathematics with Applications*, vol. 70, no. 9, pp. 2210–2226, Nov. 2015.

[207] J. Rannou *et al.*, "Three dimensional experimental and numerical multiscale analysis of a fatigue crack," *Computer Methods in Applied Mechanics and Engineering*, vol. 199, no. 21-22, pp. 1307–1325, Apr. 2010.

[208] K. Rege and H. G. Lemu, "A review of fatigue crack propagation modelling techniques using FEM and XFEM," *IOP Conference Series: Materials Science and Engineering*, vol. 276, p. 012 027, Dec. 2017.

[209] J. Rethoré and R. Seghir, *Fracture benchmark*, 2023. [Online]. Available: mech.fsv.cvut.cz/cfrac/cfrac_benchmark.php.

[210] R. Ribeaucourt, M.-C. Baietto-Dubourg, and A. Gravouil, "A new fatigue frictional contact crack propagation model with the coupled x-FEM/LATIN method," *Computer Methods in Applied Mechanics and Engineering*, vol. 196, no. 33-34, pp. 3230–3247, Jul. 2007.

[211] J. R. Rice, "A path independent integral and the approximate analysis of strain concentration by notches and cracks," *Journal of Applied Mechanics*, vol. 35, no. 2, pp. 379–386, Jun. 1968.

[212] J. Rice and G. Rosengren, "Plane strain deformation near a crack tip in a power-law hardening material," *Journal of the Mechanics and Physics of Solids*, vol. 16, no. 1, pp. 1–12, Jan. 1968.

[213] R. Ritchie, "Mechanisms of fatigue crack propagation in ductile and brittle solids," *International journal of fracture*, vol. 100, 1999.

[214] R. Romani, "Rupture en compression des structures hétérogènes à base de matériau quasi-fragiles," Ph.D. dissertation, Université Pierre et Marie Curie, 2013.

[215] H. Saberi, H. Saberi, T. Q. Bui, Y. Heider, and M. N. Nguyen, "A multi-level adaptive mesh refinement method for phase-field fracture problems," *Theoretical and Applied Fracture Mechanics*, vol. 125, p. 103 920, Jun. 2023.

[216] O. Sally, F. Laurin, C. Julien, R. Desmorat, and F. Bouillon, "An efficient computational strategy of cycle-jumps dedicated to fatigue of composite structures," *International Journal of Fatigue*, vol. 135, p. 105 500, Jun. 2020.

[217] D. Santillán, R. Juanes, and L. Cueto-Felgueroso, "Phase field model of fluid-driven fracture in elastic media: Immersed-fracture formulation and validation with analytical solutions," *Journal of Geophysical Research: Solid Earth*, vol. 122, no. 4, pp. 2565–2589, Apr. 2017.

[218] J. M. Sargado, E. Keilegavlen, I. Berre, and J. M. Nordbotten, "High-accuracy phase-field models for brittle fracture based on a new family of degradation functions," *Journal of the Mechanics and Physics of Solids*, vol. 111, pp. 458–489, Feb. 2018.

[219] M. Schöllmann, M. Fulland, and H. Richard, "Development of a new software for adaptive crack growth simulations in 3d structures," *Engineering Fracture Mechanics*, vol. 70, no. 2, pp. 249–268, 2003.

[220] C. Schreiber, C. Kuhn, and R. Müller, "On phase field modeling in the context of cyclic mechanical fatigue," *PAMM*, vol. 19, no. 1, Nov. 2019.

[221] C. Schreiber, C. Kuhn, and R. Müller, "Phase field modeling of fatigue crack initiation and growth under various loading situations," *PAMM*, vol. 20, no. 1, Jan. 2021.

[222] C. Schreiber, R. Müller, and C. Kuhn, "Phase field simulation of fatigue crack propagation under complex load situations," *Archive of Applied Mechanics*, vol. 91, no. 2, pp. 563–577, Nov. 2020.

[223] M.-É. Schwaab, T. Biben, S. Santucci, A. Gravouil, and L. Vanel, "Interacting cracks obey a multiscale attractive to repulsive transition," *Physical Review Letters*, vol. 120, no. 25, Jun. 2018.

[224] M. Seiler, T. Linse, P. Hantschke, and M. Kästner, "An efficient phase-field model for fatigue fracture in ductile materials," *Engineering Fracture Mechanics*, vol. 224, p. 106 807, Feb. 2020.

[225] K. Seleš, F. Aldakheel, Z. Tonković, J. Sorić, and P. Wriggers, "A general phase-field model for fatigue failure in brittle and ductile solids," *Computational Mechanics*, vol. 67, no. 5, pp. 1431–1452, Mar. 2021.

[226] P. Shanthraj, B. Svendsen, L. Sharma, F. Roters, and D. Raabe, "Elasto-viscoplastic phase field modelling of anisotropic cleavage fracture," *Journal of the Mechanics and Physics of Solids*, vol. 99, pp. 19–34, Feb. 2017.

[227] C. F. Shih, B. Moran, and T. Nakamura, "Energy release rate along a three-dimensional crack front in a thermally stressed body," *International Journal of Fracture*, vol. 30, no. 2, pp. 79–102, Feb. 1986.

[228] G. C. Sih, "Strain-energy-density factor applied to mixed mode crack problems," *International Journal of Fracture*, vol. 10, no. 3, pp. 305–321, Sep. 1974.

[229] M. Simoes and E. Martínez-Pañeda, "Phase field modelling of fracture and fatigue in shape memory alloys," *Computer Methods in Applied Mechanics and Engineering*, vol. 373, p. 113 504, Jan. 2021.

[230] N. Singh, C. Verhoosel, R. de Borst, and E. van Brummelen, "A fracture-controlled path-following technique for phase-field modeling of brittle fracture," *Finite Elements in Analysis and Design*, vol. 113, pp. 14–29, Jun. 2016.

[231] I. B. ška and J. M. Melenk, "The partition of unity method," *International Journal for Numerical Methods in Engineering*, vol. 40, no. 4, pp. 727–758, Feb. 1997.

[232] R. C. Soderberg, "Working stresses," *Trans. ASME*, vol. 55, 1933.

[233] K. V. Spiliopoulos and K. D. Panagiotou, "A direct method to predict cyclic steady states of elastoplastic structures," *Computer Methods in Applied Mechanics and Engineering*, vol. 223-224, pp. 186–198, Jun. 2012.

[234] C. Steinke and M. Kaliske, "A phase-field crack model based on directional stress decomposition," *Computational Mechanics*, vol. 63, no. 5, pp. 1019–1046, Sep. 2018.

[235] M. Strobl and T. Seelig, "A novel treatment of crack boundary conditions in phase field models of fracture," *PAMM*, vol. 15, no. 1, pp. 155–156, Oct. 2015.

[236] M. Strobl and T. Seelig, "On constitutive assumptions in phase field approaches to brittle fracture," *Procedia Structural Integrity*, vol. 2, pp. 3705–3712, 2016.

[237] A. Suffis, T. A. Lubrecht, and A. Combescure, "Damage model with delay effect," *International Journal of Solids and Structures*, vol. 40, no. 13-14, pp. 3463–3476, Jun. 2003.

[238] N. Sukumar, N. Moës, B. Moran, and T. Belytschko, "Extended finite element method for three-dimensional crack modelling," *International Journal for Numerical Methods in Engineering*, vol. 48, no. 11, pp. 1549–1570, 2000.

[239] S. Suresh, in *Fatigue of Materials*, Cambridge University Press, Oct. 1998.

[240] C. Tang, R. Wong, K. Chau, and P. Lin, "Modeling of compression-induced splitting failure in heterogeneous brittle porous solids," *Engineering Fracture Mechanics*, vol. 72, no. 4, pp. 597–615, Mar. 2005.

[241] E. Tanné, T. Li, B. Bourdin, J.-J. Marigo, and C. Maurini, "Crack nucleation in variational phase-field models of brittle fracture," *Journal of the Mechanics and Physics of Solids*, vol. 110, Sep. 2017.

[242] S. Teichtmeister, D. Kienle, F. Aldakheel, and M.-A. Keip, "Phase field modeling of fracture in anisotropic brittle solids," *International Journal of Non-Linear Mechanics*, vol. 97, pp. 1–21, Dec. 2017.

[243] V. F. Terentev, "On the problem of the fatigue limit of metallic materials," *Metal Science and Heat Treatment*, vol. 46, no. 5/6, pp. 244–249, May 2004.

[244] F. Tian, X. Tang, T. Xu, J. Yang, and L. Li, "A hybrid adaptive finite element phase-field method for quasi-static and dynamic brittle fracture," *International Journal for Numerical Methods in Engineering*, vol. 120, no. 9, pp. 1108–1125, Aug. 2019.

[245] J. Triclot, T. Corre, A. Gravouil, and V. Lazarus, "Key role of boundary conditions for the 2D modeling of crack propagation in linear elastic compact tension tests," *Engineering Fracture Mechanics*, vol. 277, p. 109 012, Jan. 2023.

[246] A. Turon, J. Costa, P. Camanho, and C. Dávila, "Simulation of delamination in composites under high-cycle fatigue," *Composites Part A: Applied Science and Manufacturing*, vol. 38, no. 11, pp. 2270–2282, Nov. 2007.

[247] J. Ulloa, J. Wambacq, R. Alessi, G. Degrande, and S. François, "Phase-field modeling of fatigue coupled to cyclic plasticity in an energetic formulation," *Computer Methods in Applied Mechanics and Engineering*, vol. 373, p. 113 473, Jan. 2021.

[248] K. D. Van, B. Griveau, and O. Message, "On a new multiaxial fatigue limit criterion: Theory and application. biaxial and multuaxial fatigue," *Ed. Brown/Miller*, 1989.

[249] B. Weber, "Modélisation avec la methode X-FEM de la propagation dynamique et de l'arret de fissure de clivage dans un acier de cuve rep.," Ph.D. dissertation, 1999.

[250] H. Westergaard, "Bearing pressures and cracks," *Journal of Applied Mechanics*, vol. 38, 1939.

[251] M. Wheeler, T. Wick, and W. Wollner, "An augmented-lagrangian method for the phase-field approach for pressurized fractures," *Computer Methods in Applied Mechanics and Engineering*, vol. 271, pp. 69–85, Apr. 2014.

[252] O. E. Wheeler, "Spectrum loading and crack growth," *Journal of Basic Engineering*, vol. 94, no. 1, pp. 181–186, Mar. 1972.

[253] T. Wick, "Goal functional evaluations for phase-field fracture using PU-based DWR mesh adaptivity," *Computational Mechanics*, vol. 57, no. 6, pp. 1017–1035, Mar. 2016.

[254] A. Wöhler, "Versuche über die festigkeit der eisenbahnwagenachsen," *Bauwesen*, vol. 10, 1860.

[255] J.-Y. Wu, "A unified phase-field theory for the mechanics of damage and quasi-brittle failure," *Journal of the Mechanics and Physics of Solids*, vol. 103, pp. 72–99, Jun. 2017.

[256] J.-Y. Wu, "Robust numerical implementation of non-standard phase-field damage models for failure in solids," *Computer Methods in Applied Mechanics and Engineering*, vol. 340, pp. 767–797, 2018.

[257] J.-Y. Wu and M. Cervera, "A novel positive/negative projection in energy norm for the damage modeling of quasi-brittle solids," *International Journal of Solids and Structures*, vol. 139-140, pp. 250–269, 2018.

[258] J.-Y. Wu and V. P. Nguyen, "A length scale insensitive phase-field damage model for brittle fracture," *Journal of the Mechanics and Physics of Solids*, vol. 119, pp. 20–42, 2018.

[259] J.-Y. Wu, V. P. Nguyen, C. Thanh Nguyen, D. Sutula, S. Bordas, and S. Sinaie, "Phase field modelling of fracture," *Advances in Applied Mechanics*, vol. 53, Sep. 2019.

[260] J.-Y. Wu, V. P. Nguyen, H. Zhou, and Y. Huang, "A variationally consistent phase-field anisotropic damage model for fracture," *Computer Methods in Applied Mechanics and Engineering*, vol. 358, p. 112 629, 2020.

[261] S. Yan, C. Schreiber, and R. Müller, "An efficient implementation of a phase field model for fatigue crack growth," *International Journal of Fracture*, vol. 237, no. 1-2, pp. 47–60, Apr. 2022.

[262] B. Yin and M. Kaliske, "Fatigue phase-field modeling for elastomeric materials," *PAMM*, vol. 22, no. 1, Mar. 2023.

[263] Z. Zhan, W. Hu, B. Li, Y. Zhang, Q. Meng, and Z. Guan, "Continuum damage mechanics combined with the extended finite element method for the total life prediction of a metallic component," *International Journal of Mechanical Sciences*, vol. 124-125, pp. 48–58, May 2017.

[264] X. Zhang, S. W. Sloan, C. Vignes, and D. Sheng, "A modification of the phase-field model for mixed mode crack propagation in rock-like materials," *Computer Methods in Applied Mechanics and Engineering*, vol. 322, pp. 123–136, Aug. 2017.

[265] S. Zhou and X. Zhuang, "Adaptive phase field simulation of quasi-static crack propagation in rocks," *Underground Space*, vol. 3, no. 3, pp. 190–205, Sep. 2018.

[266] V. Ziaei-Rad, M. Mollaali, T. Nagel, O. Kolditz, and K. Yoshioka, "Orthogonal decomposition of anisotropic constitutive models for the phase field approach to fracture," *Journal of the Mechanics and Physics of Solids*, vol. 171, p. 105 143, Feb. 2023.

[267] O. C. Zienkiewicz and J. Z. Zhu, "A simple error estimator and adaptive procedure for practical engineerng analysis," *International Journal for Numerical Methods in Engineering*, vol. 24, no. 2, pp. 337–357, Feb. 1987.

FOLIO ADMINISTRATIF

THESE DE L'INSA LYON, MEMBRE DE L'UNIVERSITE DE LYON

NOM : JACCON DATE de SOUTENANCE : 07/11/2023

Prénoms : Adrien, Jean-Michel

TITRE : Méthodes d'accélérations numériques dédiées à la fissuration en fatigue à grand nombre de cycle par champ de phase

NATURE : Doctorat Numéro d'ordre : 2023ISAL0084

Ecole doctorale : ED MEGA 162

Spécialité : Mécanique

RESUME :
La prédiction de l'initiation et de la propagation de fissure de fatigue dans les structures constitue un enjeu majeur de l'industrie, qui cherche à limiter les approches habituellement conservatives pour diminuer les coûts, optimiser les formes, et garantir l'intégrité des structures sur des durées plus longues. Un nombre important de méthodes numériques peuvent être exploité dans ce contexte, et notamment l'approche champ de phase, qui bénéficie d'une grande flexibilité pour traiter des cas de fissuration complexe, et considérer l'initiation et la propagation de fissure de façon unifiée. Cependant, le coût numérique associé à l'application de ce modèle sur des cas réels est aujourd'hui trop important et limite donc son application à des cas académiques. L'objectif de ce mémoire est de proposer plusieurs approches d'accélération pour diminuer ce coût de calcul prohibitif, tout en maintenant le niveau de précision et de robustesse, dans le but de rendre possible l'application sur des cas réels du modèle champ de phase.
Pour ce faire, un modèle champ de phase étendu en fatigue est implémenté dans le code éléments finis Cast3M. Une approche par dégradation de la ténacité est choisie et validée sur plusieurs cas usuels de la littérature champ de phase. Par ailleurs, une nouvelle méthode de décomposition de l'énergie est également mise en place, permettant d'en améliorer l'efficacité et la robustesse. Nous proposons ensuite plusieurs modifications de cette implémentation initiale qui permet d'accélérer les calculs. D'abord, le calcul de cycle est optimisé à travers l'introduction d'un schéma de résolution étagée adapté au cadre en fatigue. Ensuite, nous introduisons plusieurs schémas de saut de cycle permettant de minimiser le nombre de cycles calculés. Enfin, une approche de raffinement adaptatif de maillage est mise en place, afin de permettre d'optimiser le nombre de degrés de liberté pris en compte pendant la simulation. Ces outils répondent en fait aux différentes raisons pour lesquelles le coût de calcul du modèle champ de phase en fatigue est prohibitif: la résolution d'un problème non-linéaire, sur un nombre très important de cycles, avec un maillage extrêmement fin dans la zone endommagée.
Ce cadre champ de phase accéléré est ensuite exploité sur plusieurs cas académiques usuels pour valider son implémentation, et montrer les gains en temps de calcul possibles. Puis, deux cas de comparaisons numériques-expérimentales utilisant l'approche accélérée sont proposés. Ces essais mettent en évidence les capacités du modèle accéléré tout en soulignant d'autres difficultés liées à l'application du modèle sur des cas réels.

MOTS-CLÉS : Propagation de fissure, initiation de fissure, fatigue, champ de phase, méthode des éléments finis, raffinement adaptatif de maillage, saut de cycle
Laboratoire (s) de recherche : LaMCoS

Directeur de thèse: GRAVOUIL, Anthony

Président de jury :

Composition du jury :

LORENTZ, Éric	Ingénieur HDR	EDF	Rapporteur
LEGRAIN, Grégory	Professeur	Centrale Nantes	Rapporteur
DE LORENZIS, Laura	Professeur	ETH-Zürich	Examinatrice
BERINGHIER, Marianne	Maître de conférence	ISAE-ENSAM	Examinatrice
YVONNET, Julien	Professeur	Université Gustave Eiffel	Examinateur
GRAVOUIL, Anthony	Professeur	INSA Lyon	Directeur de thèse
MOLNÁR, Gergely	Chargé de recherche	CNRS-LaMCoS	Co-directeur de thèse
PRABEL, Benoit	Ingénieur HDR	CEA Paris Saclay	Encadrant